Universität Rostock Traditio et Innovatio

A study of $\overline{B}^0 \to D^0 p\overline{p}$ decays with the LHCb experiment

Dissertation
zur
Erlangung des akademischen Grades
doctor rerum naturalium (Dr. rer. nat.)
der Mathematisch-Naturwissenschaftlichen Fakultät
der Universität Rostock

vorgelegt von
Miriam Heß, geb. am 25. Oktober 1987 in Bad Oldesloe

Rostock, 13. April 2018

urn:nbn:de:gbv:28-diss2018-0143-1

Gutachter: **Priv.-Doz. Dr. Roland Waldi**
Institut für Physik, Universität Rostock
Albert-Einstein-Str. 23
D-18059 Rostock

Prof. Dr. Ulrich Uwer
Physikelisches Institut, Universität Heidelberg
Im Neuenheimer Feld 226
D-69120 Heidelberg

eingereicht am: 13. April 2018
verteidigt am: 14. September 2018

Zusammenfassung

Im Rahmen dieser Doktorarbeit wurde der Zerfall $\overline{B}^0 \to D^0 p\overline{p}$ anhand der Daten des LHCb Experimentes untersucht. Die Daten der Proton-Proton-Kollisionen wurden mit dem LHCb Detektor bei Schwerpunktsenergien von 7 TeV und 8 TeV aufgenommen. Dies entspricht einer integrierten Luminosität von etwa $3\,\text{fb}^{-1}$. Das Verzweigungsverhältnis des Zerfalls $\overline{B}^0 \to D^0 p\overline{p}$ ist bereits durch Messungen der Experimente *BABAR* und Belle bekannt und wird mit der höheren Statistik der LHCb Daten überprüft. Das relative Verzweigungsverhältnis von $\overline{B}^0 \to D^0 p\overline{p}$ Zerfällen zu $\overline{B}^0 \to D^0\pi^+\pi^-$ Zerfällen ist

$$\frac{\mathcal{B}\left(\overline{B}^0 \to D^0 p\overline{p}\right)}{\mathcal{B}\left(\overline{B}^0 \to D^0\pi^+\pi^-\right)} = (9.2 \pm 0.7\,(\text{stat}) \pm 0.6\,(\text{syst})) \times 10^{-2}\,.$$

Mit dem Weltmittelwert des Verzweigungsverhältnisses von $\overline{B}^0 \to D^0\pi^+\pi^-$ Zerfällen ergibt sich hieraus ein Verzweigungsverhältnis von

$$\mathcal{B}\left(\overline{B}^0 \to D^0 p\overline{p}\right) = (0.81 \pm 0.06\,(\text{stat}) \pm 0.06\,(\text{syst}) \pm 0.05(\text{norm})) \times 10^{-4}$$

für $\overline{B}^0 \to D^0 p\overline{p}$ Zerfälle. Die Verzweigungsverhältnismessung weicht weniger als 2σ von der Messung des *BABAR*-Experimentes ab.
Die invariante Baryon-Antibaryon-Massenverteilung der $\overline{B}^0 \to D^0 p\overline{p}$ Zerfälle zeigt das erwartete Verhalten der Anreicherung an der unteren Massenschwelle und in der Winkelverteilung für das ruhende $p\overline{p}$-System lässt sich ein asymmetrisches Verhalten beobachten. Zudem werden Strukturen in der invarianten $D^0 p$ Massenverteilung beobachtet.

Abstract

This thesis presents the results of the study of $\overline{B}^0 \to D^0 p\overline{p}$ decays with the LHCb experiment. The data of proton-proton collisions were taken with the LHCb detector at centre-of-mass energies of 7 TeV and 8 TeV, corresponding to an integrated luminosity of about $3\,\text{fb}^{-1}$. The branching fraction of $\overline{B}^0 \to D^0 p\overline{p}$ decays has been already measured by the B Factories *BABAR* and Belle and will be verified with the higher statistics of the LHCb data. The relative branching fraction of $\overline{B}^0 \to D^0 p\overline{p}$ decays to $\overline{B}^0 \to D^0\pi^+\pi^-$ decays is measured to be

$$\frac{\mathcal{B}\left(\overline{B}^0 \to D^0 p\overline{p}\right)}{\mathcal{B}\left(\overline{B}^0 \to D^0\pi^+\pi^-\right)} = (9.2 \pm 0.7\,(\text{stat}) \pm 0.6\,(\text{syst})) \times 10^{-2}\,.$$

Using the world average of the $\overline{B}^0 \to D^0\pi^+\pi^-$ branching fraction results in a branching fraction of

$$\mathcal{B}\left(\overline{B}^0 \to D^0 p\overline{p}\right) = (0.81 \pm 0.06\,(\text{stat}) \pm 0.06\,(\text{syst}) \pm 0.05(\text{norm})) \times 10^{-4}$$

for $\overline{B}^0 \to D^0 p\overline{p}$ decays. This is a deviation of less than 2σ from *BABAR*'s branching fraction measurement.

The invariant baryon-antibaryon mass of $\overline{B}^0 \to D^0 p\overline{p}$ shows the expected behaviour of the so-called threshold enhancement for small invariant masses and an asymmetric behaviour of the angular distribution of the $p\overline{p}$ system at rest. Further structures are observed for the invariant $D^0 p$ mass.

Acknowledgements

I would like to thank and express my very great appreciation to all the people who directly or indirectly made this thesis possible.
First of all, I would like to thank my supervisor Priv.-Doz. Dr. Roland Waldi for his expert advice and academic support. He made my stays at CERN possible and enabled me to take part at conferences of the particle physics community to discuss physics topics with colleagues. Furthermore, I'd like to thank him and Prof. Dr. Stephanie Hansmann-Menzemer for their support with my scholarship of the 'Landesgraduiertenförderung Mecklenburg-Vorpommern'. I would also like to thank my fellow doctoral candidates for their support, the joyful time, and the discussions we had.
Another thank go to CERN, the LHCb Collaboration and the University of Rostock for providing the required infrastructure and resources to make my doctoral research possible. I also like to thank the Landesgraduiertenförderung for the financial support.
Warm thanks should be given to my parents who unconditionally supported me not only during the time of my doctoral thesis but also during the whole period of my physics studies. Last, but not least, I would like to thank Anna-Maria Liebhoff and Ernesto Isaac Ramírez Silva for their emotional and practical support.

Contents

CHAPTER 1

Introduction

Since the end of the last century, a part of the high energy physics research has been focusing on baryonic B meson decays. The ARGUS [1] and the CLEO [2] experiments published first studies and observations in this field. The ARGUS Collaboration observed that approximately 7% of all B meson decays have baryons in their final states [3].

During the last decade, the B Factories *BABAR* and Belle dominated this research field observing many new baryonic B decay modes [4] and new phenomena that occur concurrently with these particular decay modes [5]. One decay mode that caught the attention of theorists was *BABAR*'s study on $\overline{B}^0 \to D^0 p\overline{p}$ decays [6]. Not only peaks the invariant mass of the proton-antiproton pair near threshold (threshold enhancement) but also the invariant mass of the D^0 meson and the proton shows a structure near threshold leading to predictions of charmed resonances [7]. A Dalitz analysis is therefore of keen interest to learn more about charmed resonances in $\overline{B}^0 \to D^0 p\overline{p}$ decays and to verify theory models describing the threshold enhancement.

In 2010/2011 started the operation of the Large Hadron Collider (LHC) with a centre-of-mass energy of 7 TeV, to further increase it to 8 TeV in 2012 and 13 TeV in 2015/2016. LHCb is one of the main experiments at the LHC with the focus on CP-violation measurements, the violation of charge conjugation and parity symmetry, and studies of b- and c-hadron decays. A highlight of the LHCb experiment regarding baryonic B decays is the evidence for CP-violation in $B^+ \to p\overline{p}K^+$ decays [8]. A large number of B mesons produced in the LHCb detector allows the LHCb experiment to search for more yet unknown phenomena in baryonic B decays and to rerun measurements with higher statistics as the B Factories.

However, baryonic B decay modes are less explored than decays to meson-only final states. The threshold enhancement, for instance, can be described by theory [9–18] but still needs more experimental data to be understood. To address the lack of knowledge of baryonic B decays, the branching fraction measurements for $\overline{B}^0 \to D^0 p\overline{p}$ decays of *BABAR* and Belle [6, 19] are compared with the branching fraction measured with LHCb data. Special interest is given to the unknown structures in the Dalitz plane of $\overline{B}^0 \to D^0 p\overline{p}$ decays. In this work, these measurements will be performed as a first step into a time-dependent CP-violation measurement in $\overline{B}^0 \to D^0 p\overline{p}$ decays.

Outline of this thesis

The outline of this thesis is as follows. Chapter 2 briefly summarises the Standard Model of particle physics including the phenomenon of CP-violation and B^0-$\overline{B}^0$ mixing, which led to the idea of this thesis. The following Chapters will then describe the first steps towards a time-dependent CP-violation measurement in the decay $\overline{B}^0 \to D^0 p\overline{p}$. Chapter 3 gives an overview of the LHC particle collider and one of its experiments, LHCb. The data collected by the LHCb experiment are then selected and analysed in Chapter 4 to measure the branching fraction of $\overline{B}^0 \to D^0 p\overline{p}$ decays relative to $\overline{B}^0 \to D^0 \pi^+ \pi^-$ decays to reduce the uncertainty of this measurement. The successful selection of $\overline{B}^0 \to D^0 p\overline{p}$ is used in Chapter 5 to discuss the structures in the Dalitz plane. Chapter 6 summarises the results of the previous Chapters and gives an outlook to future measurements.

CHAPTER 2

The Standard Model and *CP*-violation in the *B*-system

The Standard Model of elementary particle physics (SM) [20–22] has been developed over several years with significant developments in the mid-1970s [23]. These developments were always accompanied by experimental discoveries. Starting with the discovery of the electron by J. J. Thomson in 1987 [24], the proton by E. Rutherford in the beginning of the 20th century [25] and the neutron in 1932 by J. Chadwick [26] up to the discovery of mesons (1947) [27], neutrinos (1956) [28] and the *Higgs* particle (2012) [29,30]. The SM describes a large part of what we know today about the matter and forces in the Universe. The theoretical framework of the SM includes a successful description of three fundamental forces in Nature: the electromagnetic, weak, and strong nuclear interaction. Even though all experimental tests of the SM are in good agreement with their predictions and the SM is one of the most successful theories in modern physics, there are some weaknesses which demonstrate the incompleteness of the SM theory. Gravity, one of the known fundamental forces, is not included in the SM but can be described by Einstein's theory of general relativity [31]. The SM fails to explain some of the following phenomena: the origin of the neutrino masses [32], the matter-antimatter asymmetry of our Universe [33], or dark matter [34] and dark energy [35]. More deficiencies result from the inability to provide satisfactory answers to the hierarchy problem [36] and the strong *CP*-problem [37]. The search for physics beyond the Standard Model (New Physics), *e.g.* new fundamental particles or new types of interactions, can help to find a more comprehensive theory.

This Chapter briefly summarises particles and interactions of the SM without discussing every aspect of the theory, to later explain the mechanism of *CP*-violation (violation of charge conjugation symmetry and parity symmetry) in the *B* meson system.

2.1 Particles and interactions of the Standard Model

The Standard Model is a relativistic quantum field theory [38], where particles are represented by quantum fields: fermionic fields and bosonic fields. The quanta of the fermionic field are called fermions (spin-1/2 particles). Fermionic fundamental particles are divided into leptons and quarks. Electrically neutral leptons are called neutrinos; charged leptons have an electric charge, $-1e$. Leptons consist of electrons (e), muons (μ), tauons (τ) and their associated neutrinos (ν). The six leptons carry properties like charge and lepton numbers. Their antiparticles, the antileptons, have all the properties reversed except mass. In total, there are 12 leptons. Quarks, unlike leptons, have a property called colour charge associated with the strong interaction. The colour charge can be either red, green or blue. They also carry an electric charge associated with the electromagnetic interaction which allows separating quarks into up-type quarks with charge $+2/3e$ and down-type quarks with charge $-1/3e$. The known quark flavours are the up (u), down (d), strange (s), charm (c), bottom (b), and top (t) quark. Antiparticles, called antiquarks, again have opposite quantum numbers. In total, there are 36 quarks. The elementary fermions can be grouped into three generations; each generation contains an up-type quark, a down-type quark, a charged lepton, and a neutrino.

The SM Lagrangian $\mathcal{L}$ is a function of the field variables and their derivatives; it describes the dynamics of the quantum state and the fundamental fermionic fields. The SM is a gauge theory; therefore, the SM Lagrangian is invariant under a continuous group of local symmetry transformations. This gauge invariance leads to the introduction of bosons (integer-spin particle). These gauge fields describe the interactions between the fermions. As a result, they represent the fundamental forces. The forces of the SM are associated with the symmetry group

$$\mathrm{SU}(3)_C \times \mathrm{SU}(2)_L \times \mathrm{U}(1)_Y \,. \tag{2.1}$$

The first term, the $\mathrm{SU}(3)_C$ gauge group, refers to the theory of the strong interaction (Quantum Chromodynamics, QCD [39]). The mediators of the strong interaction are called gluons (g). Gluons themselves carry colour and build a colour octet. The colour confinement in QCD indicates that the colour-charged particles cannot be observed isolated. They must form colourless bound states. Colourless composite particles of quarks are called hadrons. Hadrons can be divided into two classes: the baryons and the mesons. Baryons consist of three quarks and are fermions with half-integer spin, whereas mesons are quark-antiquark combinations and bosons with integer-spin. Rel-

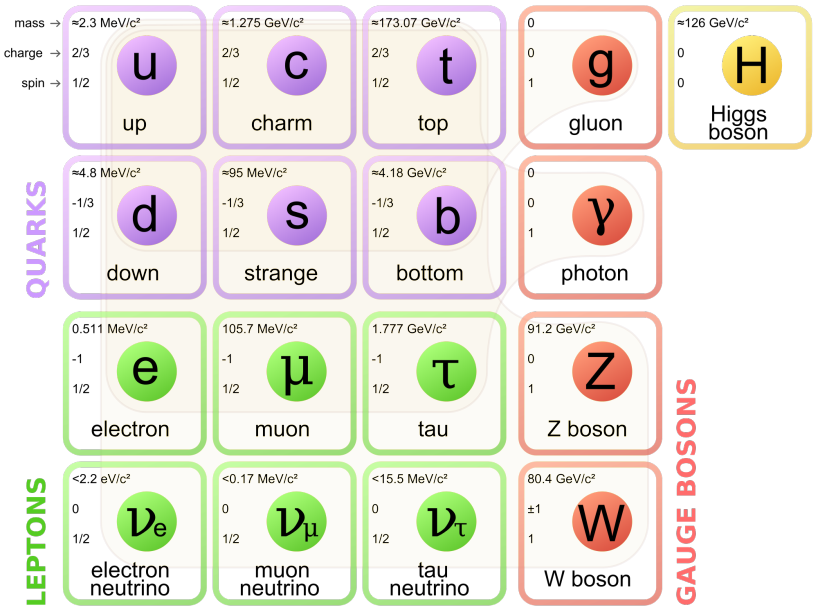

Figure 2.1: Summary of the Standard Model particles and their properties. The purple coloured particles are the six quarks, the green coloured particles the six leptons. Every interaction has a mediator coloured here in orange, and the yellow coloured particle is the *Higgs* particle. The first column of quarks and leptons is called first generation, the second column second generation, and the third column third generation, respectively. Figure is taken from [40].

evant for this thesis are B mesons. They are composed of a heavy $\overline{b}$ antiquark and a lighter u (B^-) / d ($\overline{B}^0$) / s ($\overline{B}^0_s$) / c (B^-_c) quark. Colourless combinations of gluons are called glueballs.

The remaining term, the $\mathrm{SU}(2)_L \times \mathrm{U}(1)_Y$ gauge group, where L stands for left and Y refers to the hypercharge, describes the unified electroweak interaction. The generators of the $\mathrm{SU}(2)_L \times \mathrm{U}(1)_Y$ group build the mediators of the weak interaction ($W^\pm$ bosons and Z boson) and the mediating particle of the electromagnetic field (photon γ). In total, there are 12 mediators of forces. Quarks couple to all three mentioned forces, whereas charged leptons interact via the electromagnetic and the weak force; neutrinos only interact via the weak force. Figure 2.1 shows the summary of the interactions and particles of the SM.

The $\mathrm{SU}(2)_L \times \mathrm{U}(1)_Y$ electroweak sector is spontaneously broken at low energy via the *Higgs* mechanism [41,42] to $\mathrm{U}(1)_{em}$, giving masses to the $W^\pm$ and the Z vector-bosons while allowing the electromagnetic photon to be massless. The result is a scalar (spin-0) particle called *Higgs* boson. The *Higgs* mechanism also generates masses for the fermions without violating the gauge invariance of the SM theory and can explain the observed features of quark mixing.

Even though symmetry is a fundamental principle in theoretical physics, symmetry breaking is an essential concept in particle physics. The idea to study the decay

$\overline{B}^0 \to D^0 p\overline{p}$ originates from the observation of CP-violation in B decays, and the question of CP-violation in baryonic B meson decays. CP-violation plays a major role in cosmology and the study of weak interactions in particle physics because the weak interaction is the only interaction that violates parity-symmetry and charge conjugation-parity symmetry. In cosmology, CP-violation is one of the criteria used to explain baryogenesis, which is the imbalance of matter and antimatter observed in the Universe. A. Sakharov formulated three conditions [43] that would lead to the absence of antimatter in the universe: baryon number violation, charge and CP-violation, and interactions outside of the thermal equilibrium.

2.2 CP-violation in the Standard Model

CP-violation was first discovered in the neutral kaon system [44]. The observed CP-violation is a small effect. In 1973 M. Kobayashi and T. Maskawa incorporated this phenomenon into the SM theory of the quark mixing matrix introduced by Cabibbo [45]. Their theory explains CP-violation with a complex phase in the quark-mixing matrix and three families of quarks and leptons [46]. Years later, in 1981, Carter and Sanda pointed out that CP-violation should also be observable for neutral B mesons [47]. The B Factories at SLAC (U.S.A.) [48] and KEK (Japan) [49] were built to test the predictions of CP-violation. By 2001, both experiments announced the observation of CP-violation in the neutral B meson system [50, 51]. Since then, several other measurements on symmetry violation by these and other experiments have been published. Recent contributions to the sector of flavour physics have been made by the LHCb experiment.

The following subsections briefly summarise the mechanism of CP-violation in the SM.

2.2.1 The Cabibbo-Kobayashi-Maskawa matrix

Glashow, Weinberg and Salam proposed a theory [20–22] that provides a successful description of the weak interaction using a unified description of weak and electromagnetic interactions. The mechanism of spontaneous symmetry breaking of the electroweak group results in the appearance of a *Higgs* scalar and generates the fermion masses and mixings, among other effects. The Lagrangian which describes the W couplings to quarks in terms of mass eigenstates (u_L, d_L, left-handed up-type and down-type quarks, respectively) is written as

$$\mathcal{W} = \frac{g_W}{\sqrt{2}} \left(W_\mu^+ \, \overline{u}_L \, \gamma^\mu \, V_{CKM} \, d_L + W_\mu^- \, \overline{d}_L \, \gamma^\mu \, V_{CKM}^\dagger \, u_L \right), \tag{2.2}$$

where g_W is the weak coupling constant, W_μ corresponds to the field of the intermediate $W^\pm$ boson, γ^μ are Dirac's matrices, and V_{CKM} is the Cabibbo-Kobayashi-Maskawa (CKM) mixing matrix [45, 46]. The CKM matrix is

$$V_{CKM} = \begin{pmatrix} V_{ud} & V_{us} & V_{ub} \\ V_{cd} & V_{cs} & V_{cb} \\ V_{td} & V_{ts} & V_{tb} \end{pmatrix}. \tag{2.3}$$

The Cabibbo-Kobayashi-Maskawa parametrisations

There are several representations of the 3×3 unitary CKM matrix that can be found in the literature. An initial parametrisation of the CKM matrix was proposed by Kobayashi and Maskawa [46]. Today this form of the CKM matrix is rarely used. A representation that is commonly-used is the standard parametrisation [52]

$$\begin{aligned} V_{CKM} &= \begin{pmatrix} 1 & 0 & 0 \\ 0 & c_{23} & s_{23} \\ 0 & -s_{23} & c_{23} \end{pmatrix} \begin{pmatrix} c_{13} & 0 & s_{13}e^{-i\delta} \\ 0 & 1 & 0 \\ -s_{13}e^{i\delta} & 0 & c_{13} \end{pmatrix} \begin{pmatrix} c_{12} & s_{12} & 0 \\ -s_{12} & c_{12} & 0 \\ 0 & 0 & 1 \end{pmatrix} \\ &= \begin{pmatrix} c_{12}c_{13} & s_{12}c_{13} & s_{13}e^{-i\delta} \\ -s_{12}c_{23} - c_{12}s_{23}s_{13}e^{i\delta} & c_{12}c_{23} - s_{12}s_{23}s_{13}e^{i\delta} & s_{23}c_{13} \\ s_{12}s_{23} - c_{12}c_{23}s_{13}e^{i\delta} & -c_{12}c_{23} - s_{12}c_{23}s_{13}e^{i\delta} & c_{23}c_{13} \end{pmatrix}, \end{aligned} \tag{2.4}$$

where $c_{ij} = \cos\theta_{ij}$ and $s_{ij} = \sin\theta_{ij}$ for $i < j = 1, 2, 3$. The angles θ_{12}, θ_{13} and θ_{23} are three Euler angles representing the mixing angles between the three quark generations. The weak phase δ is responsible for CP-violation.

The matrix elements of the CKM matrix are experimentally well determined [4]. The diagonal matrix elements are found to be close to unity, while the off-diagonal matrix elements are smaller and continue decreasing the further they are away from the diagonal elements. A representation that uses this behaviour is the Wolfenstein parametrisation [53]. The matrix element V_{us} is set to the parameter $\lambda \equiv s_{12} = \sin\theta_{12} \sim 0.22$, and the matrix is expanded in powers of λ

$$V_{CKM} = \begin{pmatrix} 1-\lambda^2/2 & \lambda & A\lambda^3(\rho - i\eta) \\ -\lambda & 1-\lambda^2/2 & A\lambda^2 \\ A\lambda^3(1-\rho-i\eta) & -A\lambda^2 & 1 \end{pmatrix} + \mathcal{O}(\lambda^4), \tag{2.5}$$

with the substitutions

$$\begin{aligned} s_{23} &\equiv A\lambda^2 \\ s_{13}e^{-i\delta} &\equiv A\lambda^3(\rho - i\eta). \end{aligned} \tag{2.6}$$

The parameter A is of order unity while ρ and η are smaller than one. It follows that

$$\rho = \frac{s_{13}}{s_{12}\,s_{23}}\cos\delta \qquad \text{and} \qquad \eta = \frac{s_{13}}{s_{12}\,s_{23}}\sin\delta\,. \tag{2.7}$$

The last parameter η quantifies the size of CP-violating effects in the SM.

The unitarity triangles

The unitarity condition of the CKM matrix $V_{CKM}^{\dagger}V_{CKM} = \mathbb{1}$, where $\mathbb{1}$ is the identity matrix, results in six orthogonality relations between the CKM matrix elements

$$V_{us}^{*}V_{us} + V_{cd}^{*}V_{cs} + V_{td}^{*}V_{ts} = 0 \qquad \left[\mathcal{O}(\lambda) + \mathcal{O}(\lambda) + \mathcal{O}\left(\lambda^5\right) = 0\right] \tag{2.8}$$

$$V_{ud}^{*}V_{cd} + V_{us}^{*}V_{cs} + V_{ub}^{*}V_{cb} = 0 \qquad \left[\mathcal{O}(\lambda) + \mathcal{O}(\lambda) + \mathcal{O}\left(\lambda^5\right) = 0\right] \tag{2.9}$$

$$V_{us}^{*}V_{ub} + V_{cs}^{*}V_{cb} + V_{ts}^{*}V_{tb} = 0 \qquad \left[\mathcal{O}\left(\lambda^4\right) + \mathcal{O}\left(\lambda^2\right) + \mathcal{O}\left(\lambda^2\right) = 0\right] \tag{2.10}$$

$$V_{cd}^{*}V_{td} + V_{cs}^{*}V_{ts} + V_{cb}^{*}V_{tb} = 0 \qquad \left[\mathcal{O}\left(\lambda^4\right) + \mathcal{O}\left(\lambda^2\right) + \mathcal{O}\left(\lambda^2\right) = 0\right] \tag{2.11}$$

$$V_{td}^{*}V_{ud} + V_{ts}^{*}V_{us} + V_{tb}^{*}V_{ub} = 0 \qquad \left[\mathcal{O}\left(\lambda^3\right) + \mathcal{O}\left(\lambda^3\right) + \mathcal{O}\left(\lambda^3\right) = 0\right] \tag{2.12}$$

$$V_{ub}^{*}V_{ud} + V_{cb}^{*}V_{cd} + V_{tb}^{*}V_{td} = 0 \qquad \left[\mathcal{O}\left(\lambda^3\right) + \mathcal{O}\left(\lambda^3\right) + \mathcal{O}\left(\lambda^3\right) = 0\right] \tag{2.13}$$

These six relations can be represented as triangles in the complex plane, known as unitarity triangles. The shapes of these six triangles differ from each other, as suggested by the powers of λ from the Wolfenstein parametrisation in equation 2.5. The unitarity triangles resulting from the first four equations (2.8 to 2.11) are relatively flat triangles compared to those resulting from the last two equations (2.12 to 2.13). The triangle sides for the last two equations are of the same order so that the angles of the triangles are relatively large. The triangle from the last equation (2.13) is also often called "the" unitarity triangle since its elements are those involved in B meson processes. Unitarity triangles are usually drawn with two fixed vertices. This means, *e.g.* for the triangle of equation 2.13, that the phase of $V_{cb}^{*}V_{cd}$ is conventionally chosen to be real and that each triangle side is divided by its magnitude. The triangle for the $\overline{b} \to d$ transition, shown in Figure 2.2, has three vertices at $(0,0)$, $(1,0)$ and $(\bar{\rho},\bar{\eta})$. The last coordinate $(\bar{\rho},\bar{\eta})$ comes from the Wolfenstein parametrisation including up to $\mathcal{O}\left(\lambda^5\right)$ [54] and is defined as

$$\bar{\rho} = \rho\left(1 - \lambda^2/2\right) \qquad \bar{\eta} = \eta\left(1 - \lambda^2/2\right)\,. \tag{2.14}$$

The three angles α, β and γ of the triangle are defined as

$$\alpha \equiv \arg\left[-\frac{V_{tb}^{*}V_{td}}{V_{ub}^{*}V_{ud}}\right] \qquad \beta \equiv \arg\left[-\frac{V_{cb}^{*}V_{cd}}{V_{tb}^{*}V_{td}}\right] \qquad \gamma \equiv \arg\left[-\frac{V_{ub}^{*}V_{ud}}{V_{cb}^{*}V_{cd}}\right]\,. \tag{2.15}$$

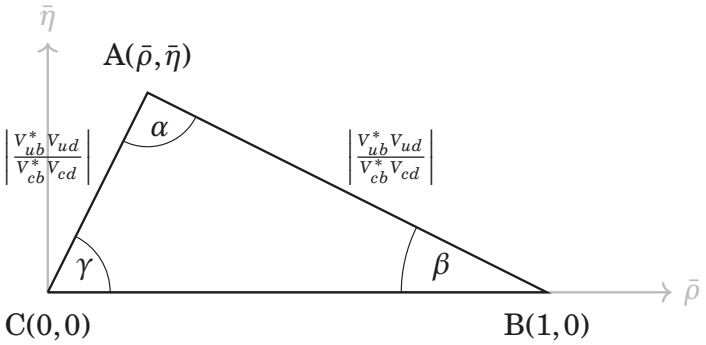

Figure 2.2: Illustration of the unitarity triangle from equation 2.13.

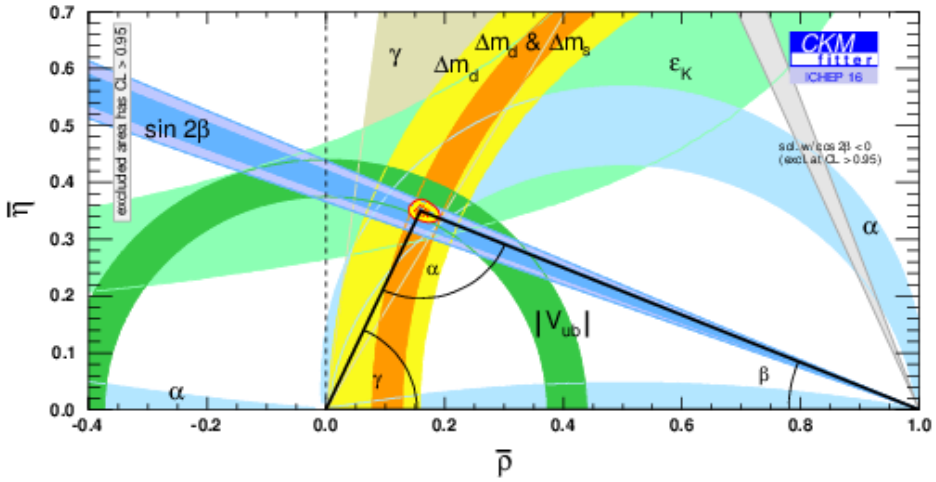

Figure 2.3: Status of the measurements of the angles and sides of the unitarity triangle [55].

The CKM matrix using the Wolfenstein parametrisation can also be rewritten as:

$$V_{CKM,\text{Wolfenstein}} = \begin{pmatrix} |V_{ud}| & |V_{us}| & |V_{ub}|e^{-i\gamma} \\ -|V_{cd}| & |V_{cs}| & |V_{cb}| \\ |V_{td}|e^{-i\beta} & |V_{ts}|e^{i\beta_s} & |V_{tb}| \end{pmatrix} + \mathcal{O}\left(\lambda^5\right), \tag{2.16}$$

where $\beta_s \equiv \arg\left[-V_{tb}^* V_{ts} / V_{cb}^* V_{cs}\right]$.

Figure 2.3 shows the current status of the most recent measurements of the angles and sides of the unitarity triangle. Details about the measurements of the CKM matrix elements and the angles of the unitarity triangles can be found in the literature [4].

2.2.2 Discrete symmetries in the Standard Model

The relation between symmetries and conserved quantities is expressed by Noether's theorem [56]. Three discrete transformations exist in the SM theory:

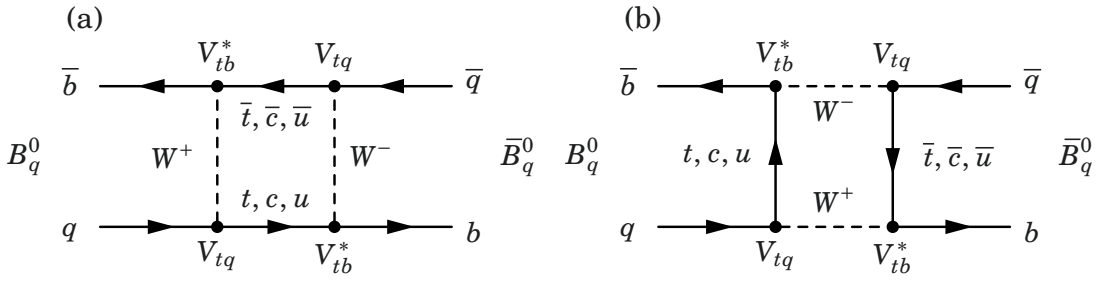

Figure 2.4: Feynman box diagrams for neutral B meson mixing.

- **Parity** (P): Parity involves a discrete transformation of the space coordinates $\vec{x}$. The parity operator reflects all three space coordinates simultaneously (space reflection) $(t,\vec{x}) \mapsto (t,-\vec{x})$ and requires the eigenstates to be ± 1 ($\mathbf{P}^2 = 1$). It inverts the particle's momentum $(E,\vec{p}) \mapsto (E,-\vec{p})$ while leaving its orbital angular momentum unchanged.

- **Charge conjugation** (C): The charge conjugation operator transforms a particle into its antiparticle. It changes the electric charge of the particle but leaves the momentum, the energy and the spin of the particle unchanged. As for the parity transformation, two applications of the charge conjugation transformation bring the particle back to its original state $\mathbf{C}^2 = 1$, and only eigenvalues ± 1 are possible.

- **Time reversal** (T): The time reversal transformation flips the sign of the time coordinate t $(t,\vec{x}) \mapsto (-t,\vec{x})$. This operation also reverses the particle's momentum and its orbital angular momentum.

Besides the Lorentz invariance, a continuous symmetry of space-time, the CPT invariance is one of the most fundamental symmetries in Nature. None of both invariances has yet been observed to be violated. The proof of the CPT invariance is based on Lorentz invariance and the locality of the interaction of quantum fields [57]. The CPT theorem states that CPT is the only combination of the C, P and T operation that is symmetric in any interaction. Any of the discrete symmetries C, P, T or a combination of two of them may be violated.

2.2.3 Mixing of neutral B mesons

Neutral B mesons can transform into their antiparticles before they decay and vice versa. The mixing of neutral B mesons has been observed experimentally [58] and plays an important role in the phenomenon of CP-violation. The Feynman box diagrams for the B^0-$\bar{B}^0$-mixing are shown in Figure 2.4.

An arbitrary quantum mechanical state Ψ can be expanded in terms of its eigenstates. Given a pure B^0 or $\bar{B}^0$ initial state at $t = 0$, the state $\Psi(t)$ can be expressed as

a two-component wave function $|\Psi(t)\rangle = \psi_1(t)|B^0\rangle + \psi_2(t)|\bar{B}^0\rangle$, or as column vector

$$|\Psi(t)\rangle = \begin{pmatrix}\psi_1(t)\\ \psi_2(t)\end{pmatrix}, \tag{2.17}$$

where the states $|B^0\rangle$ and $|\bar{B}^0\rangle$ are eigenstates of the strong and the electromagnetic interaction, called flavour eigenstates. The time evolution of this quantum state is described by the time-dependent Schrödinger equation

$$\mathrm{i}\hbar\frac{\mathrm{d}}{\mathrm{d}t}\begin{pmatrix}\psi_1(t)\\ \psi_2(t)\end{pmatrix} = \mathcal{H}\begin{pmatrix}\psi_1(t)\\ \psi_2(t)\end{pmatrix}, \tag{2.18}$$

where $\mathcal{H}$ is the effective non-Hermitian Hamiltonian. The Hamiltonian can be split into a Hermitian and anti-Hermitian part

$$\mathcal{H} = \mathcal{M} - \frac{\mathrm{i}}{2}\Gamma, \tag{2.19}$$

where both matrices $\mathcal{M}$ (mass matrix) and Γ (decay matrix) are Hermitian. The CPT invariance requires the diagonal matrix elements to be equal: $M_{11} = M_{22}$ and $\Gamma_{11} = \Gamma_{22}$. CPT gives no information about the off-diagonal matrix elements (M_{12}, M_{21}, Γ_{12}, and Γ_{21}).

The states $|B_{L,H}\rangle$, where L and H indicate the lighter and heavier eigenstates respectively, are the eigenstates of the effective Hamiltonian $\mathcal{H}$ with complex eigenvalues $\lambda_{L,H}$

$$\mathcal{H}|B_{L,H}\rangle = \lambda_{L,H}|B_{L,H}\rangle \qquad \lambda_{L,H} \equiv m_{L,H} - \mathrm{i}\Gamma_{L,H}/2\,, \tag{2.20}$$

where $m_{L,H}$ are the masses and $\Gamma_{L,H}$ the decay widths. The time-dependence of the mass eigenstates is expressed as follows

$$|B_{L,H}(t)\rangle = e^{-\mathrm{i}m_{L,H}t}e^{-\Gamma_{L,H}t/2}|B_{L,H}(0)\rangle\,. \tag{2.21}$$

A general expression for the mass eigenstates is

$$|B_L\rangle = p|B^0\rangle + q|\bar{B}^0\rangle \qquad |B_H\rangle = p|B^0\rangle - q|\bar{B}^0\rangle\,, \tag{2.22}$$

where p and q are complex parameters, normalized by $|p|^2 + |q|^2 = 1$. Solving the Schrödinger equation (2.18) helps to find a relation between q and p

$$\frac{q}{p} = \sqrt{\frac{M_{12}^* - \frac{\mathrm{i}}{2}\Gamma_{12}^*}{M_{12} - \frac{\mathrm{i}}{2}\Gamma_{12}}} = \frac{\Delta m - \frac{\mathrm{i}}{2}\Delta\Gamma}{2\left(M_{12} - \frac{\mathrm{i}}{2}\Gamma_{12}\right)}\,, \tag{2.23}$$

with $M_{21} = M_{12}^*$ and $\Gamma_{21} = \Gamma_{12}^*$ because $\mathcal{M}$ and Γ are Hermitian. The two differences Δm and $\Delta\Gamma$ are defined as $\Delta m \equiv m_H - m_L$ and $\Delta\Gamma \equiv \Gamma_H - \Gamma_L$ respectively. The following set of equations for the time evolution of the quantum states is valid for the B^0 system when approximating $\Delta\Gamma << \Delta m$:

$$|B^0(t)\rangle = f_+(t)|B^0(0)\rangle + \frac{q}{p} f_-(t)|\bar{B}^0(0)\rangle \tag{2.24}$$

$$|\bar{B}^0(t)\rangle = \frac{q}{p} f_+(t)|B^0(0)\rangle + f_-(t)|\bar{B}^0(0)\rangle \tag{2.25}$$

with

$$f_+(t) = e^{-imt} e^{-\Gamma t/2} \cos(\Delta m t/2) \qquad f_-(t) = e^{-imt} e^{-\Gamma t/2} i \sin(\Delta m t/2) \tag{2.26}$$

and $m = (m_H + m_L)/2$ and $\Gamma = (\Gamma_H + \Gamma_L)/2$, which are the average mean and width, respectively. The parameter $\Delta m \equiv m_H - m_L$ is the oscillation frequency of the two flavour eigenstates.

Another possibility is to describe the B^0-$\bar{B}^0$ system by CP-eigenstates $|B_+\rangle$ and $|B_-\rangle$

$$|B_\pm\rangle = \frac{1}{\sqrt{2}} \left(e^{-i\xi_{CP}/2} |B^0\rangle \pm e^{i\xi_{CP}/2} |\bar{B}^0\rangle \right), \tag{2.27}$$

with $CP|B_\pm\rangle = \pm|B_\pm\rangle$. The phase ξ_{CP} between $|B^0\rangle$ and $|\bar{B}^0\rangle$ is arbitrary and can be chosen to be equal to 0 so that the CP eigenvalue is $\eta_{CP} = +1$

$$CP|B^0\rangle = +|\bar{B}^0\rangle \qquad CP|\bar{B}^0\rangle = +|B^0\rangle\,. \tag{2.28}$$

2.2.4 CP-violation in the B meson system

Let the decay amplitudes of a neutral B meson to the final state f be defined as

$$\begin{aligned} \langle f|\mathcal{T}|B\rangle &= A_f \qquad & \langle f|\mathcal{T}|\bar{B}\rangle &= \bar{A}_f \\ \langle \bar{f}|\mathcal{T}|B\rangle &= A_{\bar{f}} \qquad & \langle \bar{f}|\mathcal{T}|\bar{B}\rangle &= \bar{A}_{\bar{f}}\,. \end{aligned} \tag{2.29}$$

where $\mathcal{T}$ is the transition matrix. There are three different types of CP-violation that can occur in the system of the B^0 meson: CP-violation in decay (direct CP-violation), CP-violation in mixing, and CP-violation in the interference.

Direct CP-violation refers to CP-violation in the decay amplitudes. It occurs if $|A_f| \neq |\bar{A}_{\bar{f}}|$; the decay amplitudes of the meson $B \to f$ and the antimeson $\bar{B} \to \bar{f}$ differ, or if $|A_{\bar{f}}| \neq |\bar{A}_f|$; the decay amplitudes of the meson $B \to \bar{f}$ and the antimeson $\bar{B} \to f$ differ. Assuming a meson decay with two contributing amplitudes A_1 and A_2, with only the weak phases changing sign under CP transformation, the behaviour of the amplitudes

under CP transformation is then

$$\begin{aligned} A_f(B \to f) &= |A_1| e^{i(\phi_1+\delta_1)} + |A_2| e^{i(\phi_2+\delta_2)} \\ \bar{A}_{\bar{f}}(\overline{B} \to \bar{f}) &= |A_1| e^{i(-\phi_1+\delta_1)} + |A_2| e^{i(-\phi_2+\delta_2)} , \end{aligned} \tag{2.30}$$

where the weak phase ϕ_i is a CP-odd phase and the strong phase δ_i is a CP-even phase. The difference in the transition rates is now

$$|\bar{A}_{\bar{f}}|^2 - |A_f|^2 = 2|A_1||A_2| \sin(\phi_1 - \phi_2) \sin(\delta_1 - \delta_2) . \tag{2.31}$$

So direct CP-violation requires the presence of at least two interfering decay amplitudes with different phases. This phenomenon can be observed for charged and neutral mesons. The LHCb experiment lately found evidence for direct CP-violation for the baryonic B decay $B^+ \to p\overline{p}K^+$ [8].

CP-violation in mixing is present when $|q| \neq |p|$, see equation 2.22, so that the composition of the physical states is not flavour symmetric. It can only occur for neutral mesons since mixing is forbidden for charged particles by charge conservation.

CP-violation in the interference between decay and mixing, also called mixing-induced CP-violation, can be observed when both flavour eigenstates decay to the same final state f as shown in Figure 2.5, even if $|p| = |q|$ and $|\bar{A}_f| = |A_f|$. The time-dependent rate asymmetry for the interference of decay and mixing can be written with the help of the decay rates as

$$A_{CP}(t) = \frac{\Gamma\left(B^0(t) \to f\right) - \Gamma\left(\overline{B}^0(t) \to f\right)}{\Gamma\left(B^0(t) \to f\right) + \Gamma\left(\overline{B}^0(t) \to f\right)} , \tag{2.32}$$

where $B^0(t)$ and $\overline{B}^0(t)$ are the states into which the particles, produced at time $t = 0$ as B^0 and $\overline{B}^0$ respectively, have evolved when decaying at time t. The method to identify the particles' initial flavour is called flavour tagging. Using equation 2.24 and 2.25 simplifies the time-dependent asymmetry to

$$A_{CP}(t) = C \cos(\Delta m\, t) - S \sin(\Delta m\, t) \tag{2.33}$$

with

$$C = \frac{1 - |\lambda|^2}{1 + |\lambda|^2} , \quad S = \frac{2\Im(\lambda)}{1 + |\lambda|^2} , \quad \text{and} \quad \lambda = \frac{q}{p}\frac{\bar{A}_f}{A_f} . \tag{2.34}$$

The rate asymmetry $A_{CP}(t)$ depends only on the complex parameter λ. CP-violation in the interference between mixing and decay can be observed if the imaginary part is non-zero: $\Im(\lambda) \neq 0$.

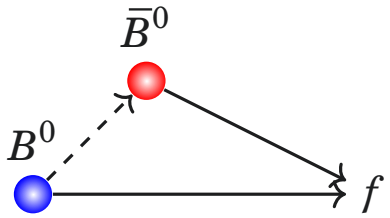

Figure 2.5: Diagram for the interference of mixing and decay in the B^0 and $\overline{B}^0$ system. This can only appear when both flavour eigenstates decay to the same final state f.

2.2.5 *CP*-violation in the $\overline{B}^0 \to D^0 p\overline{p}$ system and search for New Physics

Many searches for and measurements on *CP*-violation have been done and published so far, mainly by the experiments *BABAR*, Belle and LHCb. The effect of *CP*-violation in baryonic B decay modes is less explored than the appearance of *CP*-violation in B meson decays with meson-only final states. As mentioned before the most recent measurement of *CP*-violation in this field has been published by LHCb for the decay $B^+ \to p\overline{p}K^+$ [8]. Further measurements on *CP*-violation and the deviation from existing measurements could give hints to New Physics.

In this thesis, the decay of interest is $\overline{B}^0 \to D^0 p\overline{p}$. The mixing angle describing the *CP*-violation in the interference with and without B^0-$\overline{B}^0$ mixing for $\overline{B}^0 \to D^0 p\overline{p}$ decays is β (see Figures 2.6 and 2.4)

$$\beta \equiv \arg\left[-(V_{ud}V_{cb}^*)/(V_{td}V_{tb}^*)\right] . \tag{2.35}$$

This CKM quark mixing angle is precisely known from $\sin 2\beta$ measurements of the decay mode $B^0 \to J/\psi K_S^0$ [4]. In contrast to Feynman diagrams of the decay $\overline{B}^0 \to D^0 p\overline{p}$, $B^0 \to J/\psi K_S^0$ decays also have contributions from so-called penguin diagrams [59]. These penguin amplitude contributions are expected to be very small and negligible so that $\beta_{B^0 \to J/\psi K_S^0} \approx \beta$. As the penguin amplitude contributions are expected to be small, they are also neglected in SM prediction of the mixing angles [60]. A difference between the $\sin 2\beta$ measurements of the $B^0 \to J/\psi K_S^0$ decay and the $\overline{B}^0 \to D^0 p\overline{p}$ decay could be a hint for New Physics. Another decay which allows measuring $\sin 2\beta$ without penguin pollution is $\overline{B}^0 \to D^0\pi^+\pi^-$ [61] which also allows measuring $\cos 2\beta$ using the interference of $\overline{B}^0 \to D_2^{*-}\pi^+$ and $\overline{B}^0 \to D^0\rho^0$ in the Dalitz plane [62, 63].

The time-dependent *CP*-violation measurement would be done with $\overline{B}^0 \to D^0{}_{CP} p\overline{p}$, where $D^0{}_{CP}$ stands for a D^0 meson which decays into a *CP*-eigenstate, *e.g.* $\pi^+\pi^-$ or K^-K^+, so that the final states are the same for B^0 and $\overline{B}^0$ meson decays. Since the initial flavour of the mother particle cannot be identified by the final state particles, the

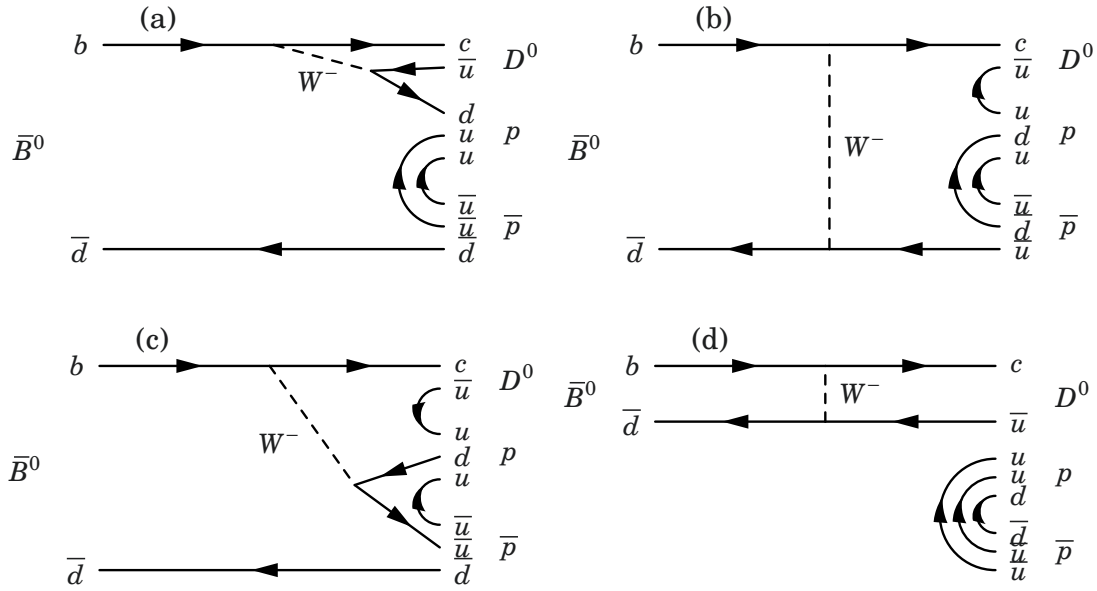

Figure 2.6: Feynman diagrams for the decay $\overline{B}^0 \to D^0 p\overline{p}$: tree-type on the left side and box-type on the right side.

flavour of the particle needs to be identified using the so-called flavour tagging [64–67]. LHCb has different types of tagging algorithms which are used to determine the B flavour in the event. The tagging method is called Same Side (SS) when the tagging algorithm looks for particles produced with the B meson during the hadronisation of a b quark [68]. For neutral B mesons, the particle produced at the fragmentation process of the B signal is a charged pion; the B^0 meson is more likely to be accompanied by a π^+ meson, whereas the $\overline{B}^0$ meson is more likely to be accompanied by a π^- meson. Other tagging algorithms are called Opposite Side (OS) taggers. OS tagging algorithms rely on the $b\overline{b}$ quark production and determine the flavour of the initial B meson using the other non-signal b-hadron. The variables which define the performance of the flavour tagging algorithm are the tagging efficiency, ϵ_{tag}, the mistag fraction, ω, and the dilution factor, $\mathcal{D} = 1 - 2\omega$. For a simple tagging algorithm with decisions B^0, $\overline{B}^0$ and untagged, these variables are defined as

$$\epsilon_{\text{tag}} = \frac{N_{\text{r}} + N_{\text{w}}}{N_{\text{r}} + N_{\text{w}} + N_{\text{u}}}, \quad \omega = \frac{N_{\text{w}}}{N_{\text{r}} + N_{\text{w}}}, \quad \mathcal{D} = \frac{N_{\text{r}} - N_{\text{w}}}{N_{\text{r}} + N_{\text{w}}}, \tag{2.36}$$

where N_{r} is the number of rightly tagged particles, N_{w} the number of wrongly tagged particles and N_{u} the number of untagged particles.

Using flavour tagging, the observed time-dependent CP-violation is diluted by the

fraction of events which are wrongly tagged

$$A_{CP\ \mathrm{obs}}(t) = \frac{\Gamma_{\mathrm{obs}}\left(B^0(t)\to f\right) - \Gamma_{\mathrm{obs}}\left(\overline{B}^0(t)\to f\right)}{\Gamma_{\mathrm{obs}}\left(B^0(t)\to f\right) + \Gamma_{\mathrm{obs}}\left(\overline{B}^0(t)\to f\right)} \tag{2.37}$$

$$= \frac{(1-\omega)\Gamma\left(B^0(t)\to f\right) + \omega\Gamma\left(\overline{B}^0(t)\to f\right) - (1-\omega)\Gamma\left(\overline{B}^0(t)\to f\right) - \omega\Gamma\left(B^0(t)\to f\right)}{(1-\omega)\Gamma\left(B^0(t)\to f\right) + \omega\Gamma\left(\overline{B}^0(t)\to f\right) + (1-\omega)\Gamma\left(\overline{B}^0(t)\to f\right) + \omega\Gamma\left(B^0(t)\to f\right)} \tag{2.38}$$

$$= (1-2\omega)A_{CP}(t) \tag{2.39}$$

The statistical uncertainty of the CP asymmetry measurement depends on the effective tagging efficiency (tagging power) ϵ_{eff}, defined as

$$\epsilon_{\mathrm{eff}} = \epsilon_{\mathrm{tag}}\mathcal{D}^2\,. \tag{2.40}$$

The tagging efficiency at LHCb is about $\epsilon_{\mathrm{eff}} \approx 2.5\%$ [65] or higher, depending on the tagging algorithms used.

CHAPTER 3

Large Hadron Collider and LHCb experiment

The Large Hadron Collider beauty (LHCb) is one of the detectors which can be used to study baryonic B decays. It collected the data on which this thesis is based to study the decay $\overline{B}^0 \to D^0 p\overline{p}$. Built by a large international collaboration of physicists, the detector is located around the Large Hadron Collider (LHC) [69] near the village of Ferney-Voltaire in France. It is designed to record information about particles produced by colliding protons. Several subdetectors deliver information about the characteristics of an individual particle, *e.g.* identity, trajectory, momentum and energy.

This Chapter gives a brief overview of the performance of the accelerator and the LHCb experiment. A more detailed description of the experiment can be found in [69–71].

3.1 Large Hadron Collider

The Large Hadron Collider (LHC) is currently the world's most powerful machine created for the analysis of particle physics. It operates with protons and heavy ions (Pb). The lead ion operation mode is not relevant for the $\overline{B}^0 \to D^0 p\overline{p}$ analysis and therefore will not be covered any further. The European Organisation for Nuclear Research (CERN) built the LHC in the tunnel constructed in the 1980s for the Large Electron-Positron Collider (LEP) near Geneva in Switzerland. Protons and heavy ions are accelerated to energies of multi-TeV in the 26.7 km-long LHC tunnel which is the last element of several pre-acceleration stages. Figure 3.1 shows a schematic view of the accelerator complex to study atoms and elementary particles.

Hydrogen is the lightest element of the periodic table and consists of a proton and an electron. Therefore, hydrogen gas is used as a proton source. The hydrogen's electrons are stripped off by an electric field so that only protons enter the first accelerator stage, the Linear Accelerator 2 (Linac2). The linear accelerator uses radiofrequency cavities to accelerate the protons to an energy of 50 MeV and sorts them into discrete packets, called bunches, before they enter the Proton Synchrotron Booster (PSB). Four superimposed synchrotron rings accelerate the particle to 1.4 GeV before injecting them

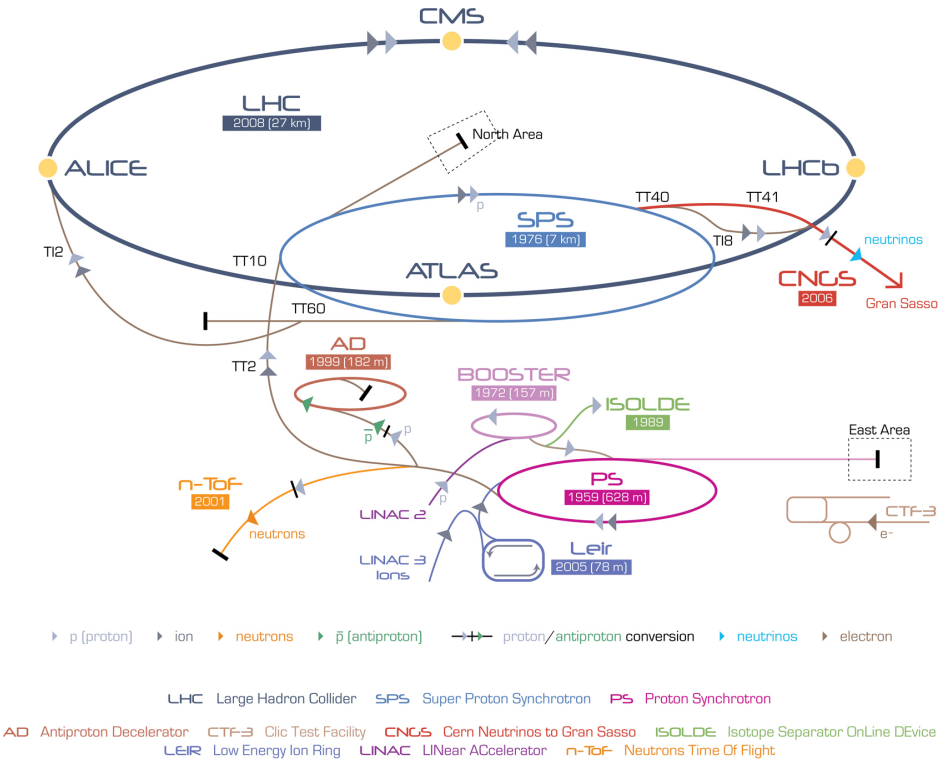

Figure 3.1: Schematic view of the CERN accelerator complex [72]. Injector chain for protons: Linear Accelerator 2 (Linac2) — Proton Synchrotron Booster (PSB) — Proton Synchrotron (PS) — Super Proton Synchrotron (SPS) — Large Hadron Collider (LHC)

into the Proton Synchrotron (PS). In the PS protons gain energies up to 25 GeV before they are sent to the Super Proton Synchrotron (SPS) where they reach energies up to 450 GeV. The SPS provides the beams for the LHC. Two beams, each in an ultrahigh vacuum tube, travel in opposite directions, guided by superconducting electromagnets and accelerated to the desired energy. A beam can have up to 2808 proton bunches consisting of up to 1.15×10^{11} protons per bunch. In 2010 and 2011 the LHC was operating at a maximum energy of 3.5 TeV which was increased to 4 TeV in 2012. During this first run period, the proton bunches crossed every 50 ns. In 2015, after a first long shutdown, the LHC started operating at beam energies up to 6.5 TeV and a bunch spacing of 25 ns. The LHC is designed for a maximum beam energy of 7 TeV. The LHC design luminosity is $10^{34}\,\mathrm{cm}^{-2}\,\mathrm{s}^{-1}$, which is defined in terms of machine parameters as

$$L = \frac{N_1 N_2 k_b f \gamma}{4\pi\epsilon_n \beta^*} F, \tag{3.1}$$

where N_1 and N_2 are the average numbers of protons per bunch of both beams, k_b the number of bunches, f the revolution frequency, $\gamma = 1/\sqrt{1-(v/c)^2}$ the relativistic factor, ϵ_n the normalised transverse emittance, β^* the value of the betatron function at the interaction point, and F the reduction factor caused by the crossing angle [73].

The LHC has collision points around the ring, where the four main detectors ATLAS (A Toroidal LHC ApparatuS), ALICE (A Large Ion Collider Experiment), CMS (Compact Muon Solenoid) and LHCb (Large Hadron Collider beauty) are located. The major goals of each experiment are diverse and complementary. ATLAS [74] and CMS [75] are the two high luminosity experiments and have general purpose detectors. They focus on the search for the *Higgs* boson, the study of its properties and search for physics beyond the Standard Model, like supersymmetry. In 2012, the aim of the *Higgs* boson search was achieved by announcing a *Higgs*-like particle [29, 30]. The ALICE experiment [76] focuses on research of the quark-gluon plasma, a state of matter appearing in heavy-ion collisions. The LHCb experiment [70, 71] is built to make precision measurements of CP-violation and search for rare B-hadron decays. Both experiments, ALICE and LHCb, operate at a lower luminosity level than ATLAS and CMS. The lower luminosity guarantees a good data quality and prevents the detector material of premature ageing. Therefore, a transverse beam offset is used to level the luminosity [77, 78].

3.1.1 B-production in proton-proton-collisions

In pp-collisions, b quarks are predominantly produced as $b\overline{b}$ quark pairs. The main production processes are quark-antiquark annihilation $q\overline{q} \rightarrow b\overline{b}$ and gluon-gluon fusion $gg \rightarrow b\overline{b}$ [79, 80] shown in the top row of Figure 3.2. Examples of second-order processes in the form of $gg \rightarrow b\overline{b}g$ for the $b\overline{b}$ production in pp-collisions are shown in the bottom row of Figure 3.2. Each produced $b\overline{b}$ pair hadronises independently into b-hadrons. The fraction of produced b-hadrons within the LHCb detector acceptance is as follows [81]:

- B^+/B^- production $\approx 39\%$
- $B^0/\overline{B}^0$ production $\approx 38\%$
- $B_s^0/\overline{B}_s^0$ production $\approx 11\%$
- b baryon and B_c^+ meson production $\approx 12\%$.

3.2 LHCb detector

Unlike the general purpose detectors ATLAS and CMS, the LHCb detector is constructed in forward direction as a single-arm spectrometer (Figure 3.3), which leads to a fixed-target-like structure. The detector geometry is chosen bacause at the high energies of the LHC, the produced $b\overline{b}$-pairs are highly boosted in the direction of the

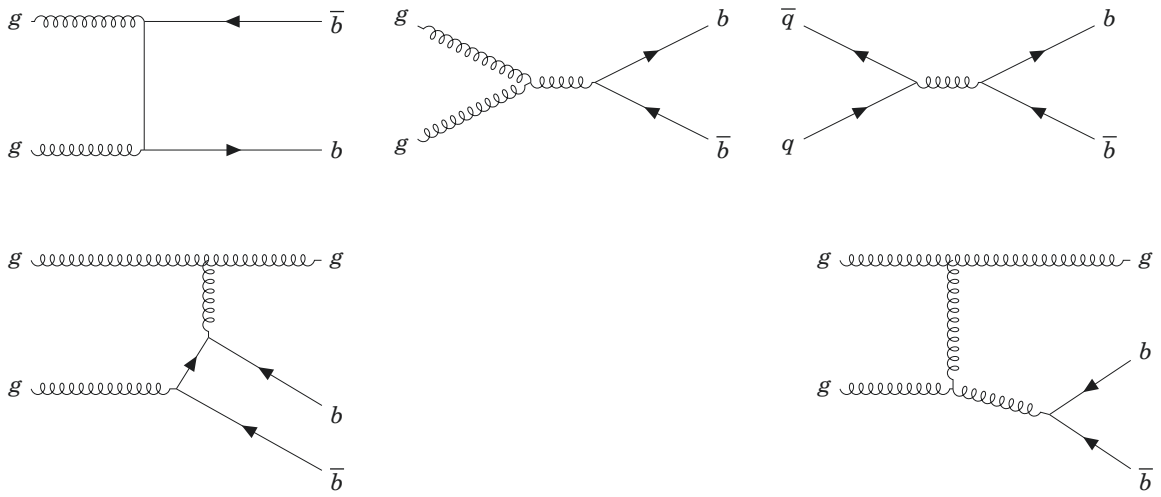

Figure 3.2: Feynman diagrams for first (top row) and second (bottom row) order QCD processes of $b\bar{b}$ pair production of the LHC.

beam axis. The LHCb detector covers a pseudorapidity range of $2 < \eta < 5$, where the pseudorapidity is defined as $\eta \equiv -\log(\tan(\theta/2))$ with the angle θ between the particle track and the beam axis. This covers an area from 15 mrad to 300 (250) mrad in the bending (non-bending) plane. The LHCb subdetectors can be classified into two categories: The tracking system and the particle identification system.

3.2.1 Tracking system

A tracking system is necessary for the reconstruction of the particle's trajectories inside the detector and to determine the momenta of the tracks. The probability that a particle passed through the whole tracking system and its trajectory is reconstructed, is called the tracking efficiency. The averaged efficiency is above 96% in the momentum range $5\,\text{GeV}/c < p < 200\,\text{GeV}/c$ and in the pseudorapidity range $2 < \eta < 5$. Subdetectors that contribute to the tracking system are the Vertex Locator (VELO) and four tracking stations. The VELO is surrounding the collision point. The first tracking station is the Tracker Turicensis (TT), located between the first Cherenkov detector (RICH1) and the LHCb dipole magnet. The other three stations are located between the magnet and the second Cherenkov detector (RICH2). These three tracking stations (T1, T2, T3) consist of two different detector technologies: silicon detectors (IT) and straw tube detectors (OT).

Vertex locator

The Vertex Locator [82] (VELO) is the detector closest to the pp collision point. It surrounds the LHCb interaction point to determine the position of the primary and

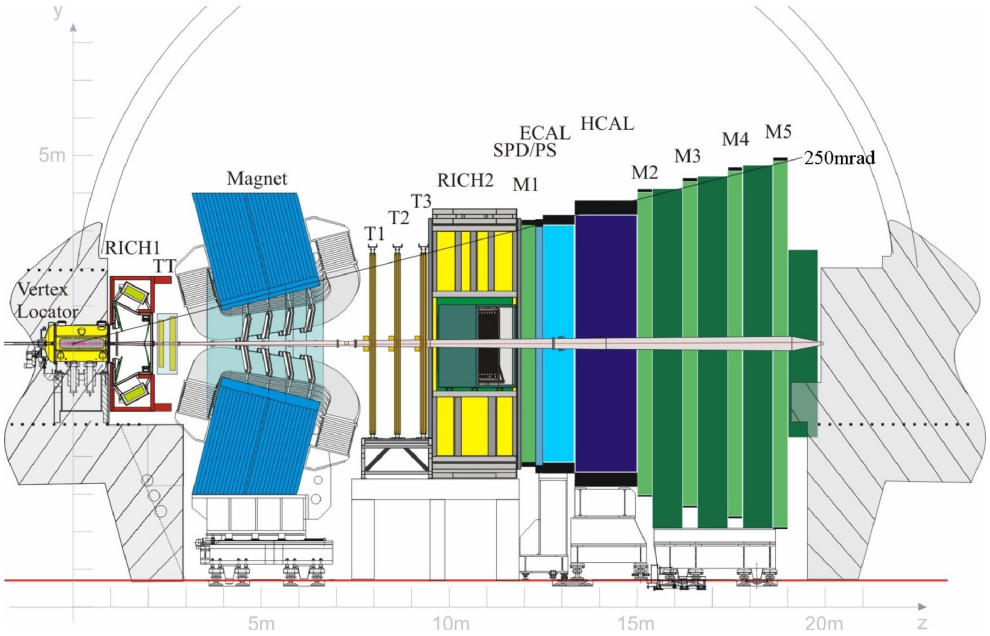

Figure 3.3: Layout of the LHCb detector [71].

the secondary decay vertices of the b-hadrons and provides a high-efficiency trigger on displaced vertices, the signature for B-meson decays. The VELO is the main tracking device upstream of the magnet and is also designed for precise measurements of the b-hadron proper lifetime (in the order of 50 fs).

The silicon detector consists of 21 micro-strip tracking modules arranged along the beam axis close to the interaction point each with two retractable semi-circular detector halves (Figure 3.4). These 300 µm thick n^+-on-n sensors measure the geometry in cylindrical polar coordinates, r and ϕ. The diameter of the beam during the injection of a new LHC fill is much larger than it is in stable operation. In open position the detector halves have a distance of 30 mm; in closed position at stable beam condition, the distance to the beamline reaches only 7 mm.

Magnet

To fulfil the requirement of a precise momentum measurement for charged particles, the LHCb dipole magnet has an integrated magnetic field of 4 Tm for tracks originating near the primary interaction point. The warm iron (non-superconducting) magnet is placed between the TT and the T1 stations. The field polarity can have two directions, up and down, and is used to study the right-left asymmetry of the detector. An iron shield is used to protect the photon detectors of the first Cherenkov detector against the stray field of the magnet.

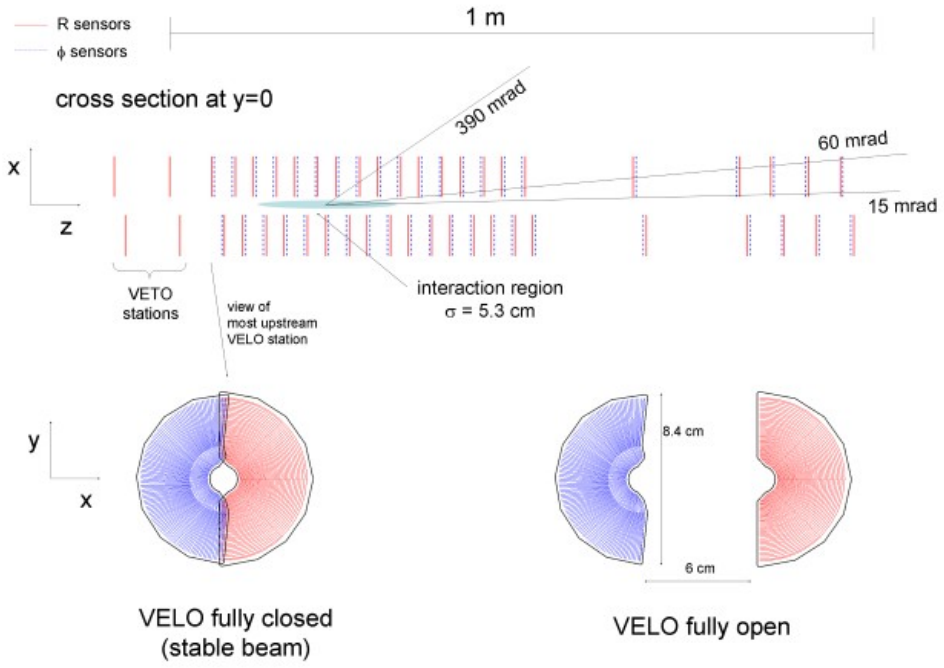

Figure 3.4: Cross section of the VELO silicon sensors in the (x,z) plane with the detector in the fully closed position. Illustration of the first VELO module in both the closed (left) and open (right) positions [70].

Tracker Turicensis

The Tracker Turicensis [83] (TT) is located downstream of RICH1 and in front of the magnet. Its information is used for the offline reconstruction of final state particles of long-lived neutral particles, which decay outside the VELO and for the offline reconstruction of low momentum particles, which leave the detector after passing through the magnet and therefore do not reach the T-stations. Furthermore, it is used in the trigger for the estimation of the track's transverse momentum.

The TT is made of silicon microstrip detectors. The active area covers the full LHCb acceptance with an area of 130 cm (height) $\times$150 cm (width). The four detection layers are grouped in pairs (TTa and TTb), arranged in x-u-v-x layers (Figure 3.5). The first and the last planes have vertical strips; the inner ones are rotated by stereo angles of -5° (u-layer) and $+5^\circ$ (v-layer), respectively. This arrangement allows a three-dimensional reconstruction of the tracks. The silicon sensors, single-sided p^+-on-n sensors, have a thickness of 500 µm and provide a spatial resolution of about 50 µm.

Inner Tracker

The Inner Tracker [83] (IT) uses similar technology as the TT, silicon microstrips with a four-layer x-u-v-x configuration. There are three stations arranged around the

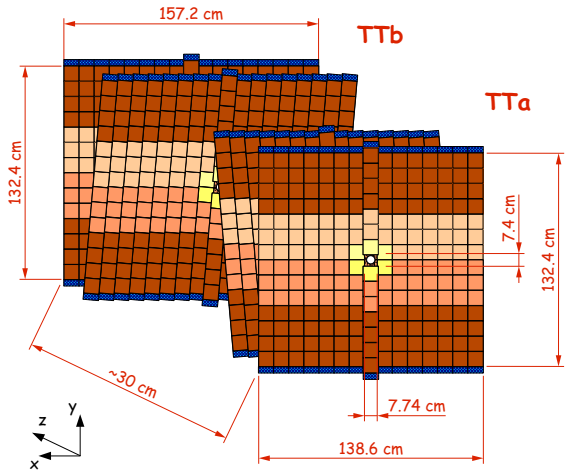

Figure 3.5: TT *x*-*u*-*v*-*x* detection layer [83]. The different shadings indicate different readout sectors; the dark blue parts are the readout electronics outside the LHCb acceptance.

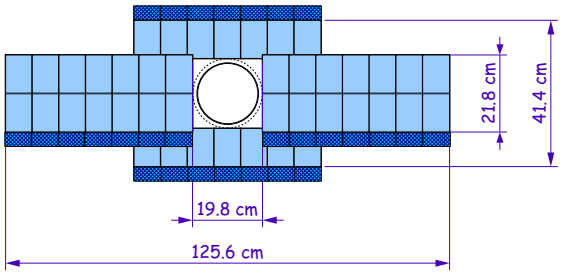

Figure 3.6: Layout of the *x* detection layer of an IT station, surrounding the LHC beam pipe [83]. The dark blue parts are the readout hybrids.

beam pipe, which do not cover the full LHCb acceptance (Figure 3.6), but a region of high track density. The IT covers a 120 cm wide and 40 cm high cross-shaped region in the centre of the three T-stations, which are located downstream of the detectors magnet. The station consists of four detector boxes containing the microstrip detectors which are organised in groups of seven modules. Depending on their location, the modules have slightly different sensor configurations. The sensors cover an area of 7.6 cm × 11 cm and are either 320 µm or 410 µm thick to have an acceptable signal-to-noise ratio for each module.

Outer Tracker

The Outer Tracker [84] (OT) together with the IT builds the tracking stations T1, T2 and T3. It has the same *x*-*u*-*v*-*x* geometry (Figure 3.7(b)) as the TT and the IT. The *x*-layer modules are oriented vertically, and the *u* and *v* layers have stereo angles of ±5°. The OT is a drift chamber and is used in a detector area of low particle dens-

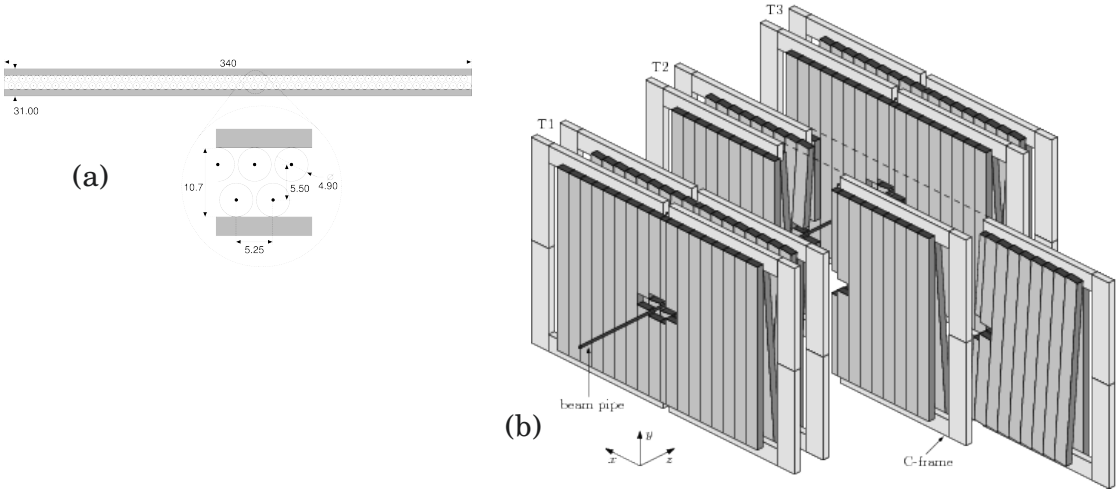

Figure 3.7: OT module cross section (a) and arrangement of the OT straw-tube modules in layers and stations [84].

ity. The total active area of the gaseous straw tube detector is about 5 m × 6 m. It is composed of modules with two staggered layers (monolayers) of drift tubes. The straw tubes (Figure 3.7(a)) are 2.4 m long with 4.9 mm inner diameter and filled with a gas mixture of Ar(70%), CO_2(28.5%) and O_2(1.5%). This guarantees a fast drift time (below 50 ns) and a drift-coordinate resolution of about 200 µm. The outer boundary of the OT corresponds to an acceptance of 300 mrad in the magnet bending plane (horizontal) and 250 mrad in the non-bending plane (vertical).

3.2.2 Particle identification system

Different types of detectable particles pass through the detector using components for particle identification information to distinguish them. Four different detectors contribute to the particle identification system of the LHCb detector: the calorimeter system, the two Ring Imaging Cherenkov (RICH) detectors and the muon stations. The two RICH detectors are used to identify charged pions and charged kaons. The electromagnetic calorimeter (ECAL) identifies electrons and photons and determines their energy. A similar function has the hadronic calorimeter (HCAL), used to identify hadrons, *e.g.* pions, kaons, and protons, and to determine their energy. The last detector, the muon system, is for identifying muons and determining their momentum. Information from the muon system is also used for the trigger system.

Cherenkov detectors

The Ring Imaging Cherenkov (RICH) [85] system allows to distinguish between pions, kaons and protons and is important to increase the signal-to-noise ratio in

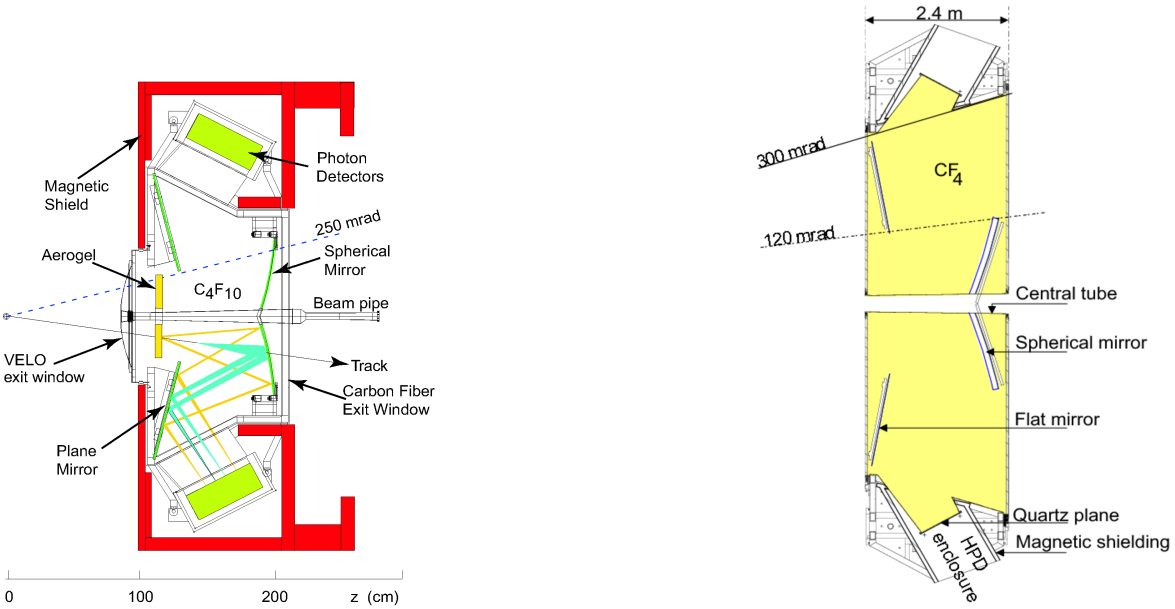

Figure 3.8: Schematic layout of the RICH1 (left) and RICH2 (right) detector [70].

B-meson decays. It contains two RICH detectors (see Figure 3.8), one (RICH1) placed upstream of the detector's magnet between the VELO and the TT and the other one (RICH2) placed downstream the magnet and the tracking stations. To cover a wide momentum range, the RICH detectors use different refractive indices n to identify the particles. The RICH1 uses silica aerogel radiator ($n = 1.03$) for the identification of low momentum particles in the range of $1.5 - 10\,\text{GeV}/c$ and C_4F_{10} gas ($n = 1.0015$) for particles with an intermediate momentum range of up to $40\,\text{GeV}/c$. The RICH2 uses CF_4 ($n = 1.0005$) gas as a radiator for high momentum particles with momenta up to $100\,\text{GeV}/c$ (see Figure 3.9).

Charged particles passing the RICH detectors are faster than the speed of light in the detector radiator material. A cone of light is formed around the particle's trajectory, which is emitted at an angle to the direction of motion. This angle θ depends on the particle's velocity $\cos(\theta) = 1/(n\beta)$, where n is the refractive index of the detector material and $\beta = v/c$ is the ratio between the particle's velocity and the speed of light. It is mass independent. Combining the information of the RICH detectors (velocity) with the information of the tracking system (momentum and entry point) leads to the particle's mass and therefore to its identity and allows to separate particles with different mass. At LHCb, the emitted Cherenkov photons are collected by spherical mirrors which are then focused onto an array of Hybrid Photon Detectors (HPDs). The HPDs are located outside of the LHCb acceptance, isolated from the magnetic field.

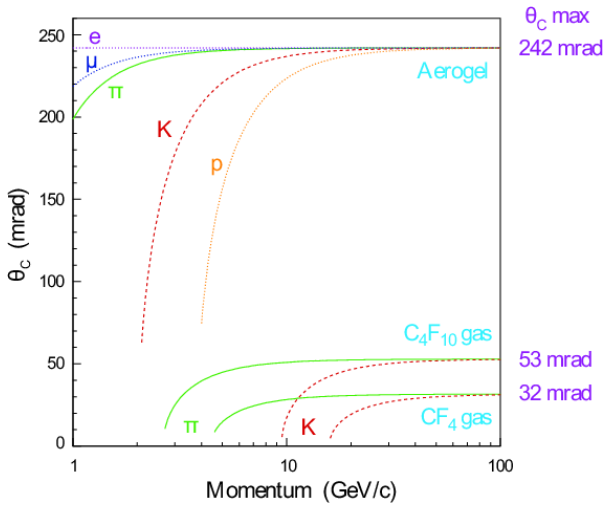

Figure 3.9: Cherenkov angle versus particle momentum for the RICH radiators [70].

Calorimeter

The purpose of the calorimeter system [86] is to measure the transverse energy E_T, the total energy and position of hadrons, electrons and photons, as well as identifying them. The transverse energy measurement is used for the first trigger level (L0).

The LHCb calorimeter system is subdivided into four systems: a Scintillator Pad Detector (SPD), a PreShower (PS), an electromagnetic calorimeter (ECAL) and a hadronic calorimeter (HCAL). All are located downstream of the RICH2 detector and follow the same detection principle: scintillation light is transmitted to a standard photo-multiplier tube (PMT) by wavelength-shifting (WLS) fibres and heavy material (lead). Depending on the particle type and its energy, the incoming particle will, after a certain distance, interact with the detector material, lose energy and create a particle shower. These photons are then collected by photo-multipliers and transformed into electrical signals. Particle types can be distinguished by the amount of energy deposited in each calorimeter and by the shape of the shower they produce.

Scintillator Pad Detector and PreShower

The Scintillator Pad Detector (SPD) and the PreShower (PS) are almost identical planes of rectangular scintillator pads and placed before and after a thin lead converter (15 mm). The thickness of the lead converter corresponds to 2.5 radiation lengths X_0. The radiation length is defined as the layer thickness that decreases the energy by a factor $1/e$ due to radiative losses only. Both detectors have an active area of 7.6 m × 6.2 m, divided into three sections: inner, middle and outer section. This division is required to achieve a one-to-one projective correspondence with the ECAL segmentation. The multianode photo-multiplier tubes (MAPMT) to detect the photons are located outside the detector acceptance.

Particles can be distinguished using the information of the SPD and the PS. Hadrons are seen as minimum ionising particles (MIPs) in the SPD as well as in the PS. Electrons are seen as MIPs in the SPD and showers in the PS whereas photons are not seen in the SPD but as showers in the PS.

Electromagnetic calorimeter

The electromagnetic calorimeter (ECAL), positioned downstream of the SPD and the PS, uses the so-called *shashlik* geometry of scintillator modules (4 mm thick) and lead absorber (2 mm thick). The total thickness of the ECAL corresponds to $25X_0$ to guarantee the full containment of the showers from high energy photons. The length is also comparable to 1.1 interaction lengths λ_{int}, the distance a hadron travels before it interacts with the material. The total size of the detector is an area of 7.8 m × 6.3 m, separated into three sections like the SPD and the PS. This covers a detector acceptance of 25 mrad $< \theta_x <$ 300 mrad in x-direction and 25 mrad $< \theta_y <$ 250 mrad in y-direction. The expected energy resolution is $\sigma_E/E = 10\%/\sqrt{E} \oplus 1\%$ (E in GeV), where the first term stands for statistics-related fluctuations, the second for the non-uniformity of the detector and calibration uncertainties. The $\oplus$ sign indicates that the two errors add in quadrature.

Hadron calorimeter

The hadron calorimeter (HCAL) consists of scintillator and steel tiles but oriented along the z-axis and is placed downstream of the ECAL. The structure of the HCAL is the following: in lateral direction, the scintillator tiles are separated by 1 cm of iron which is equal to the radiation length X_0; lengthwise corresponds the length of the scintillator tiles and iron absorbers to the hadron interaction length in iron. The total length is 1.2 m which corresponds to 5.6 interaction lengths. The measured energy resolution of the HCAL is $\sigma_E/E = (69 \pm 5)\%/\sqrt{E} \oplus (9 \pm 2)\%$ (E in GeV).

Muon system

The muon system [87] is used for triggering and offline muon identification. It consists of five stations (M1-M5), covering an area of 435 m^2 and a geometrical acceptance of about ±300 mrad in the bending and ±250 mrad in the non-bending plane. Each station consists of several multi-wire proportional chambers (MWPCs). The first muon station M1 also uses triple Gas Electron Multiplier (GEM) in the innermost region. It is located upstream of the SPD/PS and is only used for the L0 trigger; M2 to M5 are placed downstream of the calorimeter system between thick iron absorbers to stop the

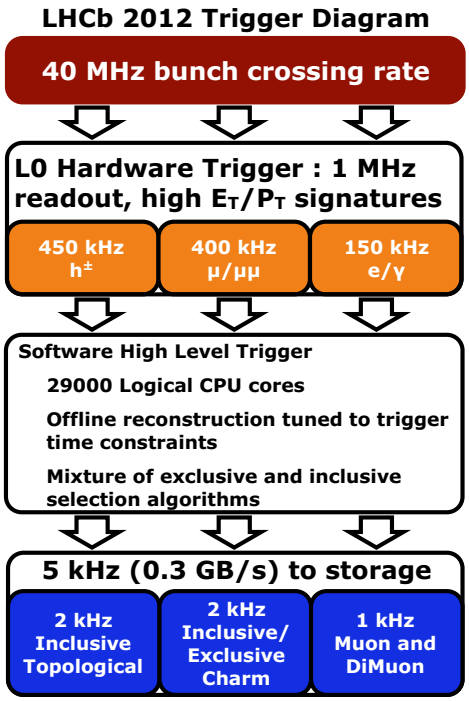

Figure 3.10: LHCb trigger system scheme of first run data in 2012 illustrating the data flow for the different trigger stages [91].

muons.

3.2.3 Trigger system

The nominal machine bunch crossing frequency of the LHC is 20 MHz, including empty bunches, whereas the rate of visible interactions, interactions with at least five tracks in the LHCb detector acceptance, is ~ 15 MHz. The amount of data coming from 15 million events per second is too large to read out all the information and to store it. Therefore the LHCb trigger system [88–90] consists of two stages to reduce the readout rate: the first Trigger is hardware-based (L0), and the second, the High-Level Trigger (HLT), is software-based. A schematic view of the trigger system is shown in Figure 3.10.

When searching for a specific decay, *e.g.* the baryonic B meson decay $\overline{B}^0 \to D^0 p\overline{p}$, there are two ways the trigger can be activated. Events can be triggered on the signal (`TOS`) or independently of the signal (`TIS`). The pp-collisions at the LHC can produce $b\overline{b}$-pairs which hadronise into hadrons, *e.g.* a B^0 meson and a $\overline{B}^0$ meson with $\overline{B}^0 \to D^0 p\overline{p}$. If the $\overline{B}^0$ meson, being the decay of interest, triggers the trigger information is `TOS`. In the other case of any other decay causing the trigger, the information is set to `TIS`. The trigger information `TIS` and `TOS` are not disjoint.

Hardware trigger

The First-Level Trigger (L0) has a customised hardware system with a latency of 4 µs. It consists of three independent trigger systems: the L0-Calorimeter trigger, the L0-Muon trigger and the L0-PileUp trigger. The first two trigger systems are used to reduce the rate to 1 MHz whereas the L0-PileUp trigger helps to determine the luminosity [92]. The L0-Muon trigger uses information from the five muon stations (M1-M5) and triggers on high transverse momentum (p_T) muons. The L0-Calorimeter trigger uses information from the SPD, PS, ECAL and HCAL and triggers on large transverse energy (E_T) deposition in the calorimeter. The transverse energy deposit is calculated in clusters of 4 cells (2×2) with the same size, as the calorimeter has smaller cells in the inner part and larger in the outer part. The transverse energy $E_T = E \sin\theta$ deposit can be computed using the energy deposited in one cell E and the polar angle θ with respect to the z-axis of the position of the centre of the cell and corresponds to the polar angle of a neutral particle coming from the interaction point and hitting the calorimeter in the centre of the cell [93]. Events with at least one candidate above a certain threshold are accepted. Hadron candidates (`L0Hadron`) are selected by the highest E_T HCAL cluster or by a sum of the highest E_T ECAL and HCAL cluster if the highest E_T ECAL cluster is in front of the HCAL cluster. A photon candidate is built by the highest E_T ECAL cluster and has hits in the PS cells in front of the ECAL cluster but none in the SPD corresponding to the hit in the PS. The same requirements as for the photon candidates apply to electron candidates, but they have a corresponding hit in the SPD. The highest E_T of the candidate has to be above a certain threshold to set the trigger. The `L0Global` decision combines the information from the L0-Calorimeter trigger and the L0-Muon trigger.

Software trigger

The second trigger level is the High-Level Trigger (HLT) which is divided into two stages: HLT1 and HLT2. The software trigger is based on a C++ application and uses the same software as used throughout LHCb data processing and simulation [94].

The first software trigger level, HLT1, uses partial event reconstruction and inclusive signal candidate selection to reduce the rate to 40 kHz and 80 kHz in 2011 and 2012, respectively. Information from the tracking stations and the VELO is used for muon-less lines to calculate the impact parameter (IP) with respect to the primary vertex (PV), the proton-proton vertex. Additional cuts on the quality of each VELO track are applied. A specific HLT1 line is `Hlt1TrackAllL0`. It is an inclusive beauty and charm trigger line that selects the candidates based on a good track quality using their p_T and the displacement from the PV.

The last trigger level, HLT2, performs a full reconstruction of the event reducing the rate to a few kHz, which is stored for the offline analysis. Specific HLT2 lines used in this thesis are the multi-body topological trigger lines, `Hlt2Topo(N)Body`, based on boosted decision tree (BDT) classifiers [95, 96]. These use topological variables, *e.g.* the n-body invariant mass (m) or the χ^2-value of the flight distance (χ^2_{FD}) to select the candidates. Variables used in this thesis are explained in more detail in Appendix B.

3.2.4 LHCb software framework

The LHCb data processing is based on an object-oriented C++ framework, called GAUDI [97], which provides a common infrastructure and environment for various software applications, *e.g.* the simulation of events, the reconstruction and the analysis itself. The main software applications will be summarised below. A more detailed description of the LHCb software framework can be found in the references [94, 98].

BRUNEL is the LHCb application for subdetector and global reconstruction. It builds tracks and clusters by using pattern recognition and provides information of the particle identification. The analysis framework is called DAVINCI. It is used for the physics selection and allows to store the event information in ROOT files. ROOT [99, 100] is an object-oriented program for the data analysis. The LHCb event simulation [101] uses two applications called GAUSS and BOOLE. The GAUSS application generates the initial event and the interactions within the LHCb detector. The PYTHIA program [102] supports GAUSS with the generation of pp-collisions whereas simulated B-meson decays are described using the EVTGEN package [103]. The GEANT4 simulation toolkit [104] helps to simulate the propagation of particles through the detector and the interaction with the material. The digitisation application BOOLE reproduces responses of the different subdetectors and their digitisation to convert the simulated data to the same format as the experiment electronics and the data acquisition system. Simulated events are then treated as data using BRUNEL and DAVINCI.

CHAPTER 4

Branching fraction measurement of $\overline{B}^0 \to D^0 p\overline{p}$

This Chapter describes the measurement of the branching fraction of $\overline{B}^0 \to D^0 p\overline{p}$ decays, as well as its charge conjugated decay $B^0 \to \overline{D}^0 \overline{p} p$, using the full dataset of an integrated luminosity of about $3\,\text{fb}^{-1}$ collected by the LHCb detector during the first physics run of the LHC.

B mesons can decay into various final state particles. The frequency of a decay is measured by the branching fraction. The branching fraction $\mathcal{B}$ of a decay can be interpreted as the probability that a particle, *e.g.* a B^0 meson, decays into a certain final state Y. It is related to the partial and total width by:

$$\mathcal{B}\left(B^0 \to Y\right) \equiv \frac{\Gamma\left(B^0 \to Y\right)}{\Gamma\left(B^0\right)}\,, \tag{4.1}$$

where $\Gamma(B^0 \to Y)$ is the partial width of the B^0 meson into the final state Y, and $\Gamma\left(B^0\right)$ is the total width of the B^0 meson. Experimentally, the branching fraction can be calculated using the ratio of the number of particles decaying into an individual mode n_Y and the total number of produced B^0 mesons n_{B^0}:

$$\mathcal{B} = \frac{n_Y}{n_{B^0}}\,. \tag{4.2}$$

The total number of produced B^0 mesons in pp-collisions at the LHC (see Section 3.1.1) depends on the luminosity $\mathcal{L}$ integrated over the data taking period and the cross-section for the B^0 meson production $\sigma_{pp\to B^0+X}$

$$n_X = \mathcal{L} \times \sigma_{pp\to B^0+X}\,. \tag{4.3}$$

When reconstructing the tracks of the final state Y, only those detected in the LHCb detector volume can be reconstructed. Selections that are applied to improve the signal-to-background ratio can also reduce the number of observable particles in the final state. The observed number of particles in the final state n'_Y is then smaller than the number of particles produced by the decay of B^0 mesons. The ratio of both values

is called efficiency, $\epsilon = n'_Y/n_Y$. The branching fraction can, therefore, be expressed as

$$\mathcal{B}\left(B^0 \to Y\right) = \frac{n'_Y}{\epsilon \times \mathcal{L} \times \sigma_{pp\to B^0+X}} \,. \tag{4.4}$$

The cross-section measurement at LHCb is not very precise, *e.g.* the measurement of $\sigma_{pp\to B^0+X}$ has an error of about 16% [81]. This error is quite large to make a precise measurement of the $\overline{B}^0 \to D^0 p\overline{p}$ branching fraction and to compete with the measurements of the *BABAR* and Belle experiment [6, 19].

To minimise the error of the branching fraction measurement, a normalisation channel is used. The $\overline{B}^0 \to D^0 p\overline{p}$ branching fraction will be measured relative to the decay $\overline{B}^0 \to D^0\pi^+\pi^-$. This normalisation channel $\overline{B}^0 \to D^0\pi^+\pi^-$ was already studied by the experiments LHCb [61] and Belle [105]. A branching fraction measurement of $B^0 \to Y$ relative to $B^0 \to Z$ can be simplified to

$$\frac{\mathcal{B}\left(B^0 \to Y\right)}{\mathcal{B}\left(B^0 \to Z\right)} = \frac{n'_Y \times \epsilon\left(B^0 \to Z\right)}{n'_Z \times \epsilon\left(B^0 \to Y\right)} \,, \tag{4.5}$$

moreover, this relative branching fraction measurement is now independent of the number of produced B^0 mesons in pp-collisions. The only values that need to be determined for the branching fraction measurement are: the number of signal events from the decay of which thesis branching fraction is going to be measured, n'_Y, the number of signal events from the normalisation channel, n'_Z, the total efficiency of the decay of interest, $\epsilon\left(B^0 \to Y\right)$, and the total efficiency of the normalisation channel, $\epsilon\left(B^0 \to Z\right)$. Systematic uncertainties will partly cancel in the branching faction ratio measurement and improve the precision of the result.

The following Sections will explain the steps towards the branching fraction measurement of $\overline{B}^0 \to D^0 p\overline{p}$ decays relative to $\overline{B}^0 \to D^0\pi^+\pi^-$ decays.

4.1 Data

Two types of data are used to reconstruct and analyse $\overline{B}^0 \to D^0 p\overline{p}$ and $\overline{B}^0 \to D^0\pi^+\pi^-$ and their charge conjugated decays: data taken with the LHCb detector under various conditions in 2011 and 2012 and simulated data where particles are generated and then propagated through a simulated LHCb detector volume, including a simulation of the interaction with the detector material.

Table 4.1: Integrated luminosity for the dataset of reconstructed $\overline{B}^0 \to D^0 p\overline{p}$ candidates.

	$\overline{B}^0 \to D^0 p\overline{p}$	
	2011	2012
MagUp $[\,\mathrm{pb}^{-1}]$	422.16 ± 7.22	1000.59 ± 11.61
MagDown $[\,\mathrm{pb}^{-1}]$	563.61 ± 9.64	992.59 ± 11.52
MagUp + *MagDown* $[\,\mathrm{pb}^{-1}]$	985.77 ± 12.05	1993.18 ± 16.35
total $[\,\mathrm{pb}^{-1}]$	2978.95 ± 20.31	

Table 4.2: Integrated luminosity for the dataset of reconstructed $\overline{B}^0 \to D^0 \pi^+ \pi^-$ candidates.

	$\overline{B}^0 \to D^0 \pi^+ \pi^-$	
	2011	2012
MagUp $[\,\mathrm{pb}^{-1}]$	422.16 ± 7.22	1000.64 ± 11.61
MagDown $[\,\mathrm{pb}^{-1}]$	563.61 ± 9.64	989.25 ± 11.48
MagUp + *MagDown* $[\,\mathrm{pb}^{-1}]$	985.77 ± 12.05	1989.89 ± 16.33
total $[\,\mathrm{pb}^{-1}]$	2975.66 ± 20.29	

4.1.1 LHCb dataset

The measurements described here use data taken with the LHCb detector in 2011 and 2012, respectively, under different beam, detector, and trigger conditions. Data in 2011 were taken at a centre-of-mass energy of $\sqrt{s} = 7\,\mathrm{TeV}$, in 2012 at a centre-of-mass energy of $\sqrt{s} = 8\,\mathrm{TeV}$. For the reconstruction of the decays, an integrated luminosity of $0.99\,\mathrm{fb}^{-1}$ is available for 2011 data and $1.99\,\mathrm{fb}^{-1}$ for 2012 data. A detailed list considering the magnet polarities (*MagUp* and *MagDown*) can be found Tables 4.1 and 4.2. LHCb uses a centralised selection of reconstructed events, called *Stripping*. The *Stripping* versions for $\overline{B}^0 \to D^0 p\overline{p}$ and $\overline{B}^0 \to D^0 \pi^+ \pi^-$ decays are different for data taken in 2012 which is the reason for the difference in the total luminosity for that year.

Small differences between the datasets of 2011 and 2012 are expected due to the increased centre-of-mass energy in 2012; this can be significantly seen for the number of tracks (n_{tracks}) in an event. But since the detector has not changed and the reconstruction algorithm, as well as the selection criteria (*Stripping*) are the same for both years, the datasets are used as a coherent sample. A comparison of 2011 and 2012 data is shown in Appendix A.2 using *sWeighted* events [106].

Good momentum, invariant mass and vertex resolutions are essential for the LHCb physics program. Therefore, the detector components need to be aligned [107]. The commissioning procedure of the detector alignment and the knowledge of the mag-

netic field are not perfect and have an impact on the momentum measurement. At LHCb, a tool (`TrackScaleState`) has been developed to perform a momentum scale calibration [108, 109]. Well-known resonances had been used to calibrate the momentum measurement of the tracks. This calibration method was used to correct the momentum of $\overline{B}^0 \to D^0 p\overline{p}$ decays and $\overline{B}^0 \to D^0 \pi^+ \pi^-$ decays. For example, the mass of the B^0 meson from $\overline{B}^0 \to D^0 p\overline{p}$ decays is about $3.5\,\text{MeV}/c^2$ larger than its corresponding PDG value [4].

4.1.2 Samples of simulated events

Simulated events are used to study signal and background channels and to estimate the reconstruction and the selection efficiency. The advantage of simulated events is that the initial conditions are known, *e.g.* the generation of a $\overline{B}^0$ meson decaying to the $D^0 p\overline{p}$ final state. Samples of simulated events are also called Monte Carlo (MC) samples. All simulations used in this analysis are listed in Appendix A.1. At event-generation level (EvtGen) [103], a cut is applied to require that all final state particles are produced within the LHCb acceptance. All charged daughters in the generated decay have to be produced within $10\,\text{mrad} < \theta_{\text{charged}} < 400\,\text{mrad}$ of the z-axis and neutral ones within $5\,\text{mrad} < \theta_{\text{neutral}} < 400\,\text{mrad}$ of the z-axis. Considering the decay $0 \to 1\,2\,3$, there are two ways of generating particles uniformly in the phase-space of a decay: The `PHSP` model is used to uniformly populate the phase-space $\left(m_{12}^2, m_{23}^2\right)$ of the generated decay, where m_{ij} is the invariant mass of final state particles i and j; the `sqDalitz` model [5] is used to uniformly populate the square Dalitz plane $\left(\mathrm{m}', \theta'\right)$, where m' and θ' are defined as

$$\mathrm{m}' = \frac{1}{\pi} \arccos\left(2 \frac{\mathrm{m}_{23} - m_{23}^{min}}{\mathrm{m}_{23}^{max} - m_{23}^{min}} - 1 \right), \tag{4.6}$$

$$\theta' = \frac{\theta}{\pi}. \tag{4.7}$$

The angle θ is the angle between final state particles 1 and 3 in the rest frame of particle 2 and 3 (helicity angle), and $m_{23}^{min} = m_2 + m_3$ and $\mathrm{m}_{23}^{max} = m_0 - m_1$ are the boundary values for the invariant mass of particles 2 and 3.

Resonant structures were not incorporated in the decay generations. The conditions under which the decays were simulated were those from the data taking period 2012 using Pythia 8 [102]. Simulated events are treated like *real* data, therefore *Stripping* selections (see Section 4.2.1) are also applied to simulation. To calculate the particle identification (PID) efficiency (more information about PID in Section 3.2.2), a modified *Stripping* selection without PID variable cut is applied when necessary. To correct for differences between data and simulation the `TrackSmearState` tool is used

for simulated events to smear the momentum of the final state particles. Another tool for simulated events is the BKGCAT tool [110] which helps to categorise simulated events. The relevant categories can be found in Appendix A.4.

4.2 Event selection

To reconstruct the candidates from $\overline{B}^0 \to D^0 p\overline{p}$ and $\overline{B}^0 \to D^0 \pi^+\pi^-$ and their charge conjugated decays, several stages of selections are necessary: *Stripping*, trigger and offline selections. The selections made to get a general collection of the candidates of interest are called *Stripping* selection. Loose cuts are applied to reduce the number of collected candidates since *Stripping*-lines have a finite bandwidth during the data processing. The cuts are chosen to preserve as much signal as possible while minimising the background to keep the retention of candidates within the acceptable limit. A rigid selection of trigger requirements is enforced in this analysis such that the efficiency of the trigger selections can be reliably measured. Finally, further selections are made to improve the selection of the *Stripping* for the specific needs of this analysis, called the offline selection. This includes a multivariate selection for the reduction of background events.

4.2.1 *Stripping* selection

The first selection step for decays of interest is called *Stripping*. The cuts applied to the reconstructed candidates are very loose to remove background events (mostly combinatorial background) and preserve signal candidates. The selection criteria of the *Stripping*-lines for the $\overline{B}^0 \to D^0 p\overline{p}$ decay and the $\overline{B}^0 \to D^0 \pi^+\pi^-$ decay are listed in Table 4.3. Both *Stripping*-lines use the same reconstruction method and the same selection criteria. The B^0 meson is reconstructed as $B \to D^0 X$ with $X \to p\overline{p}$ and $X \to \pi^+\pi^-$ for $\overline{B}^0 \to D^0 p\overline{p}$ and $\overline{B}^0 \to D^0 \pi^+\pi^-$ decays, respectively. The D^0 candidate is reconstructed as $D^0 \to K\pi$, $D^0 \to KK$ or $D^0 \to \pi\pi$ to allow different measurements such as a branching fraction or *CP* violation measurement. No mass constraints are applied to the candidates.

The track multiplicity (number of tracks in the vertex) in an LHCb event is high due to the hadronic production environment. Therefore, the main goal of the selection is to keep the signal events while reducing the combinatorial background and prompt background tracks originating directly from the primary vertex. It is required that the number of long tracks in the event (`# long track`) does not exceed a certain number and there is at least 1 primary vertex (PV) in the event. Information of the software trigger HLT2 is available for all inclusive ϕ lines (`Hlt2IncPhi`*) and

Table 4.3: Selection criteria of the *Stripping* for $\overline{B}^0 \to D^0 p\overline{p}$ and $\overline{B}^0 \to D^0\pi^+\pi^-$ candidates. Candidates are reconstructed as a 2-body decay $B \to D^0 X$ with $D^0 \to hh$, where h is a kaon or a pion. The pseudo-particle X is allowed to decay as $X \to hh$ denoting a combination of $p\overline{p}$ or $\pi^+\pi^-$ respectively. The abbreviations used in this table are explained in detail in Appendix B.

Particle	Quantity	Criteria
Event	# long track	< 250
	#PV	> 0
	`Hlt2Topo.*Decision` or `Hlt2IncPhi.*Decision`	true
All tracks	Min χ^2_{IP}	> 4
	ghost probability	< 0.3
D^0	$\sum p_{\text{T}}$	$> 1800\,\text{MeV}/c^2$
	$\delta M(D^0)$	$< 100\,\text{MeV}/c^2$
	DOCA	$< 0.5\,\text{mm}$
	Vertex χ^2/ndf	< 10
	BPVVD χ^2	> 36
	BPVDDIRA	> 0
all D^0 daughters	Track χ^2/ndf	< 3
	p_{T}	$> 100\,\text{MeV}/c$
	p	$> 1000\,\text{MeV}/c$
at least one D^0 daughter	Track χ^2/ndf	< 2.5
	p_{T}	$> 500\,\text{MeV}/c$
	p	$> 5000\,\text{MeV}/c$
X	$\sum p_{\text{T}}$	$> 1000\,\text{MeV}/c$
	invariant mass	$< 5200\,\text{MeV}/c^2$
	DOCA	$< 0.5\,\text{mm}$
	Vertex χ^2/ndf	< 16
	BPVVD χ^2	> 16
	BPVDDIRA	> 0
all X daughters	Track χ^2/ndf	< 3
	p_{T}	$> 100\,\text{MeV}/c$
	p	$> 2000\,\text{MeV}/c$
at least one X daughter	Track χ^2/ndf	< 2.5
	p_{T}	$> 500\,\text{MeV}/c$
	p	$> 5000\,\text{MeV}/c$
B^0	$\sum p_{\text{T}}$	$> 5000\,\text{MeV}/c$
	invariant mass	$[4750, 6000]\,\text{MeV}/c^2$
	Vertex χ^2/ndf	< 10
	BPVLTIME	$> 0.2\,\text{ps}$
	BPVIPCHI2	< 25
	BPVDIRA	> 0.999
One Daughter	Track χ^2/ndf	< 2.5
	p_{T}	$> 1700\,\text{MeV}/c$
	p	$> 10000\,\text{MeV}/c$
	Min χ^2_{IP}	> 16
	Min IPDV	$> 0.1\,\text{mm}$
More than one daughter	Track χ^2/ndf	< 2.5
	p_{T}	$> 500\,\text{MeV}/c$
	p	$> 5000\,\text{MeV}/c$

all topological lines for 2-, 3- and 4-body decays (`Hlt2Topo(2|3|4)Body`*). To reduce the background of prompt production, all tracks are required to have a minimal $\chi 2$ of the impact parameter (Min χ^2_{IP}) greater than a certain value, meaning that the minimum $\chi 2$ distance of a particle's trajectory to any set of vertices must be greater this value. To reduce the number of fake tracks, the probability that the particle track is a ghost (ghost probability) is required to be small. For combined particles (D^0, X, and B^0), requirements on the sum of the transverse momenta of the daughter particles ($\sum p_{\mathrm{T}}$), the transverse momentum of the daughter particle itself (p_{T}) and the momentum of the daughter particles (p) are applied. Additionally, requirements on the Min χ^2_{IP}, the minimum distance of a particle's trajectory to any set of primary vertices (Min IPDV), and the χ^2 per degree of freedom of the track fit (Track:χ^2/nDof) of the daughter particle are used to reduce background. The D^0 meson has a mass of $(1864.84 \pm 0.05)\,\mathrm{MeV}/c^2$ [4]. The difference between the measured mass of the D^0 meson and this value ($\delta M(D^0)$) is required to be smaller than $100\,\mathrm{MeV}/c^2$, which allows having enough D^0 mass sidebands for background studies. For the virtual X particle, the invariant mass is chosen to be smaller than a value that is greater than the allowed phase space value from $\overline{B}^0 \to D^0 p\overline{p}$ or $\overline{B}^0 \to D^0\pi^+\pi^-$ decays. The B^0 meson's mass is $(5279.61 \pm 0.16)\,\mathrm{MeV}/c^2$ [4]; the mass range of the combined finale state particles also allows to use the B^0 mass sidebands for background studies. Further background reduction is achieved by using the distance of closest approach between all possible pairs of particles (DOCA), the χ^2 per degree of freedom of the vertex of the particle (Vertex:χ^2/nDof), and the χ^2-separation for the distance from the end vertex of the particle and the related primary vertex (BPVVD χ^2). The end vertex of a reconstructed particle is the location of its decay vertex, whereas the primary vertex is the proton-proton interaction point. The cosine of the angle between the momentum of the particle and the direction of flight from the best PV to the decay vertex (BPVDDIRA, DIRA) is close to 1 for the decaying B^0 meson. The B^0 meson decay vertex is a few mm away from the primary interaction vertex due to the proper lifetime (BPVLTIME) of the B^0 meson. The loose cut on the IP χ^2 on the related PV (BPVIPCHI2) requires the IP of the B^0 meson with respect to the primary vertex not to be too large.

In addition to the listed *Stripping*-line cuts, a loose cut on the particle identification (PID) variable is applied to the protons of the $\overline{B}^0 \to D^0 p\overline{p}$ candidates, $\mathrm{DLL}_{p\pi} > -5$ (see Appendix D.1), to reduce the retention rate of the *Stripping*-line while removing a large number of combinations of unrelated tracks.

4.2.2 Trigger selection

In this analysis, trigger decision requirements to select hadronic decays are made as in similar studies. The hardware level trigger L0 should select hadron candid-

ates which are triggered on the signal, `L0Hadron_TOS`, or where the rest of the event triggered any L0-line, `L0Global_TIS`. The High-Level Trigger HLT1 is required to have the inclusive line `Hlt1TrackAllL0` triggered on the signal (`TOS`), as well as the multi-body topological HLT2 trigger lines `Hlt2Topo(2|3|4)BodyBBDTDecision`. Details about the LHCb trigger requirements during the first physics run of the LHC can be found elsewhere [90].

4.2.3 Offline selection

The *Stripping* selection allows having different D^0 decay modes. For the following analyses, only the $D \to K\pi$ decay mode is used. The branching fraction of the Cabibbo-favoured decay mode is $\mathcal{B}\left(D^0 \to K^-\pi^+\right) = (3.93 \pm 0.04) \times 10^{-2}$, the branching fraction for the doubly Cabibbo-suppressed mode is $\mathcal{B}\left(D^0 \to K^+\pi^-\right) = (1.398 \pm 0.027) \times 10^{-4}$ [4]. During the reconstruction of the decays $\overline{B}^0 \to D^0 p\overline{p}$ and $\overline{B}^0 \to D^0\pi^+\pi^-$ it is not possible to distinguish the decay of a B^0 meson or a $\overline{B}^0$ meson without flavour-tagging. Since the doubly Cabibbo-suppressed $D \to K\pi$ has a contribution of less than 0.4% to $D \to K\pi$ decays, it is assumed that only the Cabibbo-favoured decay mode contributes. When ever the decays $\overline{B}^0 \to D^0 p\overline{p}$ and $\overline{B}^0 \to D^0\pi^+\pi^-$ decays are mentioned in the following part, the charge conjugated decays are included.

Before using a multivariate analysis to reduce the background in reconstructed $\overline{B}^0 \to D^0 p\overline{p}$ and $\overline{B}^0 \to D^0\pi^+\pi^-$ decays, a few more cuts are applied to suppress the background. For the $\overline{B}^0$ meson, the $\chi^2_{\text{vtx}}/\text{ndf}$ cut is tightened to $\chi^2_{\text{vtx}}/\text{ndf} < 6$ to have a better vertex quality. The angle between the momentum of the $\overline{B}^0$ meson candidate and the direction of flight from the best PV to the decay vertex is very small and close to zero. Hence its cosine ($\cos\theta_{\text{DIRA}}$) is close to one. Therefore the cut on the direction angle is tightened to $\cos\theta_{\text{DIRA}} > 0.99995$. To guarantee valid kinematics for the B^0 daughters, the `DecayTreeFitter` tool [111] is used. Typical pattern recognition methods use the bottom-up approach. They start with the final state particles to reconstruct intermediate particles and work backwards to reconstruct upstream decays. In contrast, the `DecayTreeFitter` tool fits the entire decay chain simultaneously using information on momenta and vertex position. It can include constraints on particle masses and vertex positions. For the measurement of the branching fraction a D^0 mass constraint is used. The decay tree fit for the D^0 mass constraint and the D^0 and $\overline{B}^0$ mass constraint are required to be successful.

As for the $\overline{B}^0$ mesons, the D^0 meson $\chi^2_{\text{vtx}}/\text{ndf}$ cut is tightened to $\chi^2_{\text{vtx}}/\text{ndf} < 6$ for a better vertex quality. The decay vertex of the D^0 meson is displaced from the PV due to the lifetime of the D^0 meson. To require the D^0 mesons not to come from the PV, a cut on the flight distance greater than 2 mm is applied. Additionally, the significance of the vertex distance between the D^0 meson and the $\overline{B}^0$ meson along the z-axis is

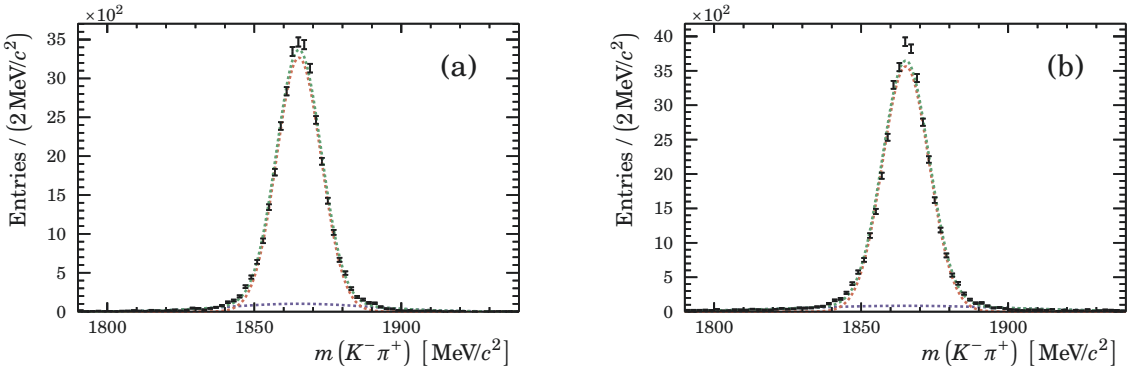

Figure 4.1: $D^0 \to K\pi$ mass distribution for truth-matched simulated signal events for (a) $\overline{B}^0 \to D^0 p\overline{p}$ and (b) $\overline{B}^0 \to D^0\pi^+\pi^-$ decays. The blue function is the first Gaussian of the double Gaussian fit function; the red one is the second Gaussian, the green function is the total fit function.

Table 4.4: Fit parameters from the fit to the D^0 mass of simulated $\overline{B}^0 \to D^0 p\overline{p}$ and $\overline{B}^0 \to D^0\pi^+\pi^-$ events. The fits are shown in Figure 4.1

parameter	$\overline{B}^0 \to D^0 p\overline{p}$	$\overline{B}^0 \to D^0\pi^+\pi^-$
μ [MeV/c^2]	1865.18 ± 0.05	1865.19 ± 0.05
σ_1 [MeV/c^2]	24.5 ± 0.6	36.8 ± 1.1
σ_2 [MeV/c^2]	7.95 ± 0.06	7.96 ± 0.05
r_G	0.091 ± 0.005	0.0096 ± 0.0031

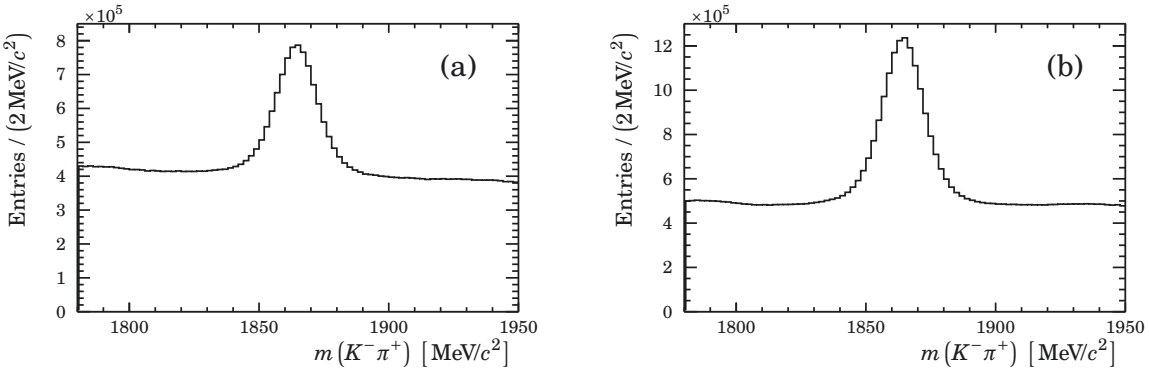

Figure 4.2: $D^0 \to K\pi$ mass data distribution for (a) $\overline{B}^0 \to D^0 p\overline{p}$ and (b) $\overline{B}^0 \to D^0\pi^+\pi^-$ candidates after *Stripping*.

used to make sure that the D^0 meson is produced downstream

$$z_{D^0} - z_{\overline{B}^0} > 0\,, \tag{4.8}$$

where z_x is the particle's vertex position along the z-axis. The D^0 mass has a resolution of about $8\,\text{MeV}/c^2$. A fit to the D^0 mass distribution of simulated events with a double Gaussian fit function is shown in Figure 4.1 (see Appendix E.1 for the definition of the double Gaussian fit function); these events are truth-matched (see Appendix A.4). The fit parameters are listed in Table 4.4. To remove the background of misidentified particle combinations, the D^0 mass window is tightened to $\delta M\left(D^0\right) < 25\,\text{MeV}/c^2$ which is an interval of about $\pm 3\sigma$. This removes the lower D^0 mass sideband with $D^0 \to KK$ decays where one kaon is misidentified as a pion and the upper sideband with $D^0 \to \pi\pi$ decays where one pion is misidentified as a kaon. Figure 4.2 shows the D^0 mass distribution of data after the *Stripping* selection.

Information from the particle identification (PID) system is used to separate pions, kaons, and protons. Due to the performance of the RICH detectors, only tracks with a momentum p smaller than $100\,\text{GeV}/c$ and pseudo-rapidity η in the range of $[1.89, 4.90]$ are used. Loose cuts on the neural network based particle identification variables ProbNN_x (see Appendix D.1) are applied to reduce the background of unrelated tracks. As a preliminary PID cut, the corresponding neural network based particle identification variable is required to be larger than 0.1 for each final state particle. At a later stage, the PID cut for the proton and the antiproton (charged pions) originating directly from the $\overline{B}^0$ meson might be tightened to get a better signal to background ratio. Particle tracks are required to have RICH information and are required not to be identified as a muon.

In addition to the selection criteria mentioned above, some veto cuts are applied for the reconstruction of $\overline{B}^0 \to D^0\pi^+\pi^-$ decays. The decay $\overline{B}^0 \to D^0\pi^+\pi^-$ has a large contribution from $\overline{B}^0 \to D^{*+}(2010)\pi^-$ decays with $D^{*+}(2010) \to D^0\pi^+$. The branching

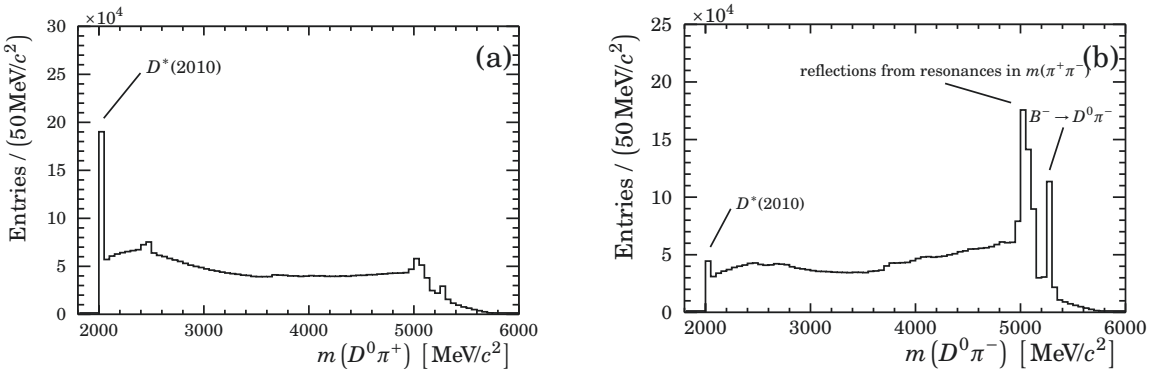

Figure 4.3: Invariant $D^0\pi$ mass distributions for $\overline{B}^0 \to D^0\pi^+\pi^-$ decays with $m(\overline{B}^0) > 5200\,\text{MeV}/c^2$: (a) invariant $D^0\pi^+$ mass distribution, (b) invariant $D^0\pi^-$ mass distribution.

fractions are [4]:

$$\mathcal{B}\left(\overline{B}^0 \to D^0\pi^+\pi^-\right) = (8.8 \pm 0.5) \times 10^{-4} \tag{4.9}$$

$$\mathcal{B}\left(\overline{B}^0 \to D^{*+}(2010)\pi^-\right) = (2.74 \pm 0.13) \times 10^{-3} \tag{4.10}$$

$$\mathcal{B}\left(D^{*+}(2010) \to D^0\pi^+\right) = (67.7 \pm 0.5)\,\% \tag{4.11}$$

Neither the Belle measurement [105] nor the LHCb measurement [61] of the $\overline{B}^0 \to D^0\pi^+\pi^-$ branching fraction measurement does include $\overline{B}^0 \to D^{*+}(2010)\pi^-$ contributions. The same kinematic cuts as for the LHCb measurement of this decay are applied. The $D^{*+}(2010)$ peak is visible in the invariant $D^0\pi^+$ mass distribution as well as the invariant $D^0\pi^-$ mass distribution (see Figure 4.3). The contributions in the invariant $D^0\pi^-$ mass result from doubly mis-identified background and doubly Cabbibo-suppressed background. Therefore, the invariant $D^0\pi^\pm$ mass is required to be larger than $2100\,\text{MeV}/c^2$. As shown in Figure 4.3 the invariant $D^0\pi^-$ mass distribution shows background from $B^- \to D^0\pi^-$ decays. This background is removed by requiring the invariant $D^0\pi^\pm$ mass to be smaller than $5200\,\text{MeV}/c^2$. The other dominant peak in the $D^0\pi^\pm$ mass distribution is a reflection of resonances in the invariant $\pi^+\pi^-$ mass.

4.2.4 Multivariate selection

Multivariate analyses are powerful tools for signal and background classification. The multivariate selection uses the input of several variables describing the decay process and combines the information to a single variable. The framework used for the multivariate analysis (MVA) is `TMVA` [112, 113] which provides a broad set of techniques. A Fisher discriminant [114, 115] with Gauss-transformed variables (FisherG)

and a boosted decision tree [116, 117] with gradient boost (BDTG) were trained to distinguish signal and background events for $\overline{B}^0 \to D^0 p\overline{p}$ and $\overline{B}^0 \to D^0\pi^+\pi^-$ decays (see Appendix C for a summary of these techniques). Cut-based approaches ignore the correlation between variables, whereas multivariate methods use this effect to explore the full discriminating potential. Even though the BDTG classifier is more likely to have a better discriminating power, the FisherG classifier will be favoured since it is less sensitive to overtraining. The input variables for the MVA are kinematic and topological ones only and all transformed with a natural logarithm for a better discrimination power. The notation for the decay is the same as used for the *Stripping*-line $B \to D^0 X$ with $X \to p\overline{p}$ and $X \to \pi^+\pi^-$ for $\overline{B}^0 \to D^0 p\overline{p}$ and $\overline{B}^0 \to D^0\pi^+\pi^-$ decays, respectively. The input variables are (for a detailed explanation see Appendix B)

- B χ^2_{FD}: the χ^2-value of the flight distance (FD) of the B^0 meson,
- B χ^2_{IP}: the χ^2-separation of the IP for the B^0 meson,
- B θ_{DIRA}: the direction angle of the B^0 meson,
- Bp: the reconstructed total momentum of the B^0 meson,
- D χ^2_{FD}: the χ^2-value of the flight distance (FD) of the D^0 meson,
- Dp: the reconstructed total momentum of the D^0 meson,
- D τ: the proper lifetime of the D^0 meson,
- D daughters min χ^2_{IP}: the smallest χ^2_{IP} of the D daughters,
- X daughters min χ^2_{IP}: the smallest χ^2_{IP} of the baryons/pions originating directly from the B^0 meson,
- X daughters sum p_{T}: the sum of the transverse momentum of the baryons/pions originating directly from the B^0 meson.

These variables are all uncorrelated to the B^0 mass. Signal and background events behave differently for $\overline{B}^0 \to D^0 p\overline{p}$ decays and $\overline{B}^0 \to D^0\pi^+\pi^-$ decays. For $\overline{B}^0 \to D^0\pi^+\pi^-$ decays, a good separation of signal and background events can be achieved using 6 of the 10 input variables used for $\overline{B}^0 \to D^0 p\overline{p}$ decays. Variables which do not improve discriminating power for the FisherG Classifier of $\overline{B}^0 \to D^0\pi^+\pi^-$ decays will not be used in training; these are Bp, Dp, D daughters min χ^2_{IP}, X daughters sum p_{T}. Consequently, the input variable for $\overline{B}^0 \to D^0\pi^+\pi^-$ decays are B χ^2_{FD}, B χ^2_{IP}, B θ_{DIRA}, D χ^2_{FD}, D τ, and X daughters min χ^2_{IP}.

Two different samples are used to train the discriminators: a sample to describe the

Table 4.5: Number of events in the training and test sample for $\overline{B}^0 \to D^0 p\overline{p}$ decays and $\overline{B}^0 \to D^0\pi^+\pi^-$ decays.

	$\overline{B}^0 \to D^0 p\overline{p}$		$\overline{B}^0 \to D^0\pi^+\pi^-$	
	signal	background	signal	background
training	9876	16452	10665	53340
testing	9876	16452	10665	53340
total	19748	32896	21330	106680

behaviour of the signal and a sample to describe the behaviour of the background. The background sample contains candidates from the upper sideband of the $\overline{B}^0 \to D^0 p\overline{p}$ ($\overline{B}^0 \to D^0\pi^+\pi^-$) mass distribution of 2011 and 2012 data to describe the background behaviour. Candidates from the upper sideband are B^0 candidates with $5350\,\text{MeV}/c^2 < m(B) < 5600\,\text{MeV}/c^2$ for $\overline{B}^0 \to D^0 p\overline{p}$ candidates and $5550\,\text{MeV}/c^2 < m\left(B^0\right) < 5800\,\text{MeV}/c^2$ for $\overline{B}^0 \to D^0\pi^+\pi^-$ candidates, respectively. These regions are expected to have a negligible level of peaking background. The signal sample for $\overline{B}^0 \to D^0 p\overline{p}$ contains phase-space simulated events where reconstructed candidates match the true $\overline{B}^0 \to D^0 p\overline{p}$ decay to describe the signal behaviour. The matching is done by using the `BKGCAT` tool, where the particles have to be in category 10. Not all variables have a good data-simulation agreement and are therefore corrected as described in Appendix A.3. The corrected distributions are taken as input for the MVA. For $\overline{B}^0 \to D^0\pi^+\pi^-$ decays, phase-space simulated signal events with truth-matching are used. A reweighting is not necessary.

The number of available events after the pre-selection for the training and testing of the different discriminators are listed in Table 4.5. The samples for signal and background are divided randomly into two halves; one used to perform the training of the discriminator and the other to perform the test of the training. A Kolmogorov-Smirnov test (see Appendix C.3) is performed to test for possible overtraining. Overtraining in machine learning occurs when the trained method describes random variations or noise instead of the real behaviour. The sensitivity to overtraining depends on the model itself. The more complex a statistical method is, the more likely the method can be overtrained.

Figures 4.4 and 4.5 show the variable behaviours for signal and background events of the training samples of $\overline{B}^0 \to D^0 p\overline{p}$ and $\overline{B}^0 \to D^0\pi^+\pi^-$ decays, respectively. The linear correlation between these topological and kinematical variables of the training samples is shown in Figure C.3 for $\overline{B}^0 \to D^0 p\overline{p}$ decays and in Figure C.4 for $\overline{B}^0 \to D^0\pi^+\pi^-$ decays. The linear correlation coefficients do not represent all possible correlations, such as the non-linear correlations. Non-linear correlations between variables justify the use of the BDT technique since the BDT technique performs bet-

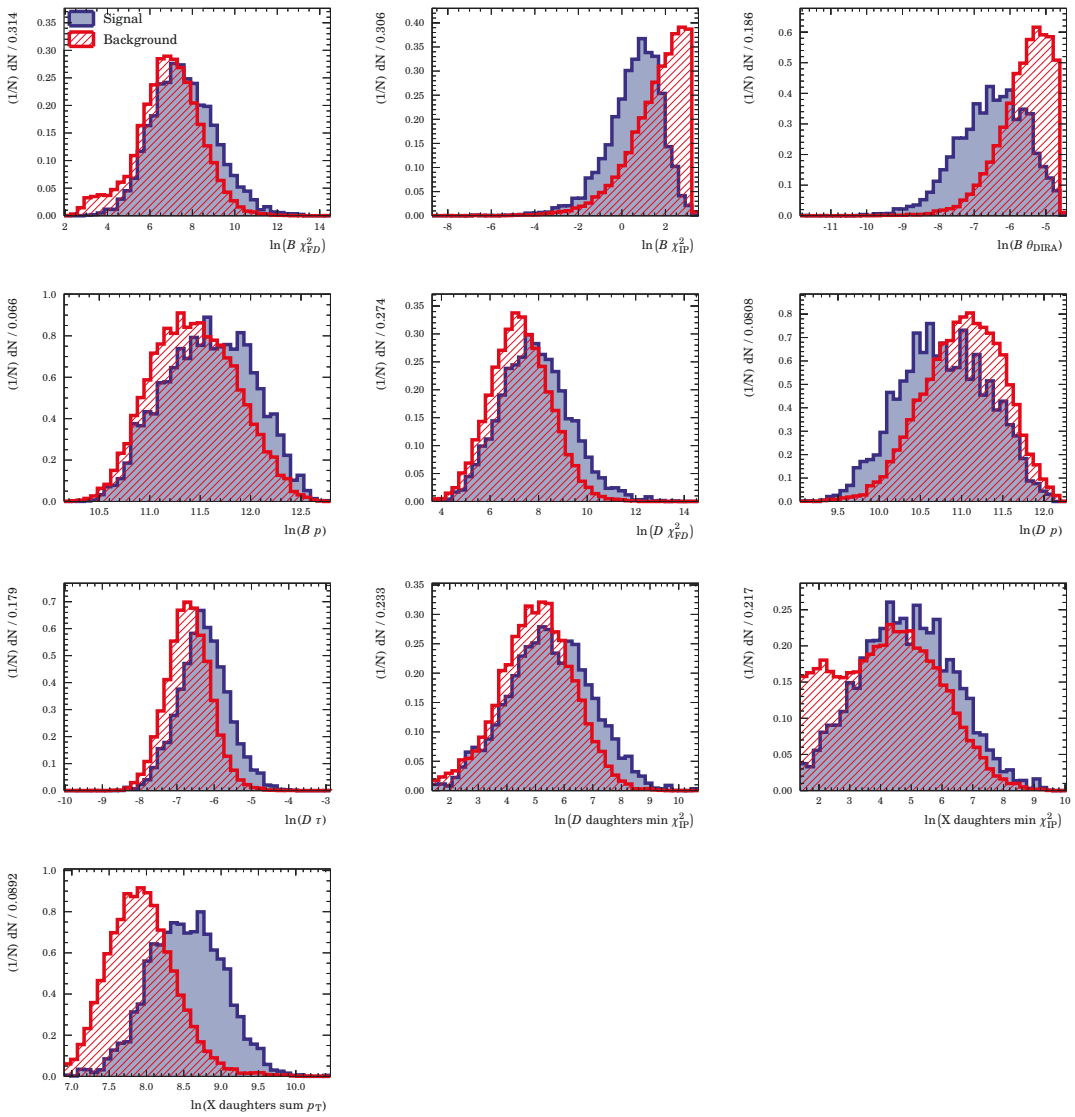

Figure 4.4: Comparison between signal (blue) and background (red) distributions for the training samples of $\overline{B}^0 \to D^0 p\overline{p}$ events for all variables used to train the discriminators. Signal refers to reweighted phase-space simulated signal events and background to events from the upper B^0 mass sideband.

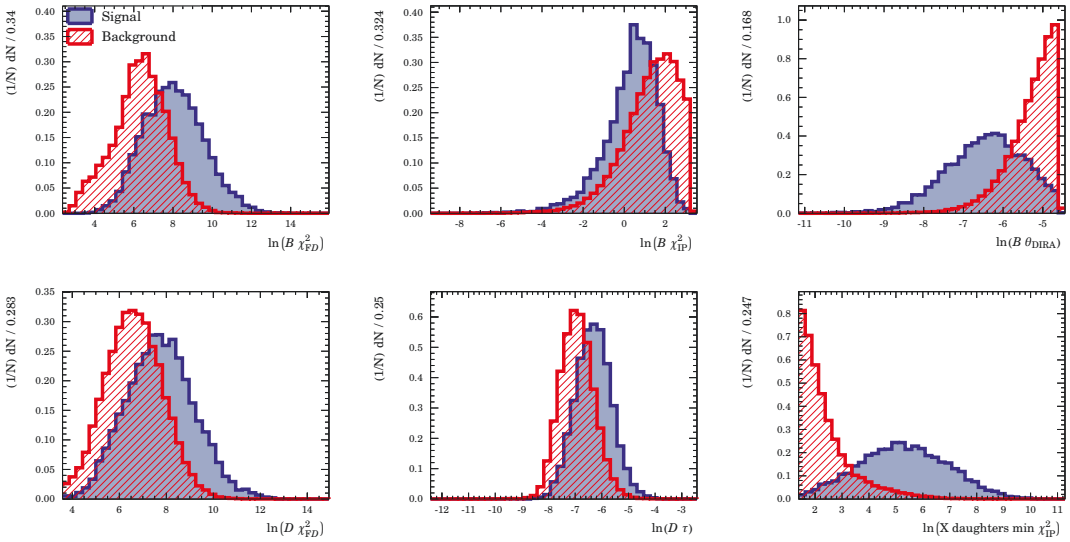

Figure 4.5: Comparison between signal (blue) and background (red) distributions for the training samples of $\overline{B}^0 \to D^0\pi^+\pi^-$ events for all variables used to train the discriminators Signal refers to phase-space simulated signal events and background to events from the upper B^0 mass sideband.

ter with non-linear correlations than the Fisher discriminant. Figure 4.6 shows the so-called receiver operating characteristic (ROC) curve for the test sample of $\overline{B}^0 \to D^0 p\overline{p}$ and $\overline{B}^0 \to D^0\pi^+\pi^-$ decays. It is a plot of the background rejection against the signal efficiency for different cut points. The larger the area under the curve the better is the discriminating power of the discriminator. Even though the BDTG classifier seems to have a better discriminating power, when applied to data in combination with PID variables, both classifiers appear to have a similar performance for $\overline{B}^0 \to D^0 p\overline{p}$ decays. Since the FisherG classifier is less sensitive to overtraining, this classifier will be used to select $\overline{B}^0 \to D^0 p\overline{p}$ and $\overline{B}^0 \to D^0\pi^+\pi^-$ decays. The classifier output distribution for the FisherG discriminant is shown in Figure 4.7.

4.2.5 Selection optimisation

The particle identification (PID) variables are not well modelled by simulated events because the simulation cannot describe all features of the event correctly. The simulation of the detectors contributing to the PID system is not trivial, and the PID variables highly depend on the kinematics of the event. For this reason, PID variables were excluded from training a classifier but are essential to reduce the background of unrelated tracks. The PID information of the tracks from the baryons/pions originating directly from the $\overline{B}^0$ meson ($p\overline{p}$ or $\pi^+\pi^-$) and the output of the Fisher response are therefore used simultaneously to find a cut which provides a good signal-to-background ratio. It is assumed that the PID variables for the positively and neg-

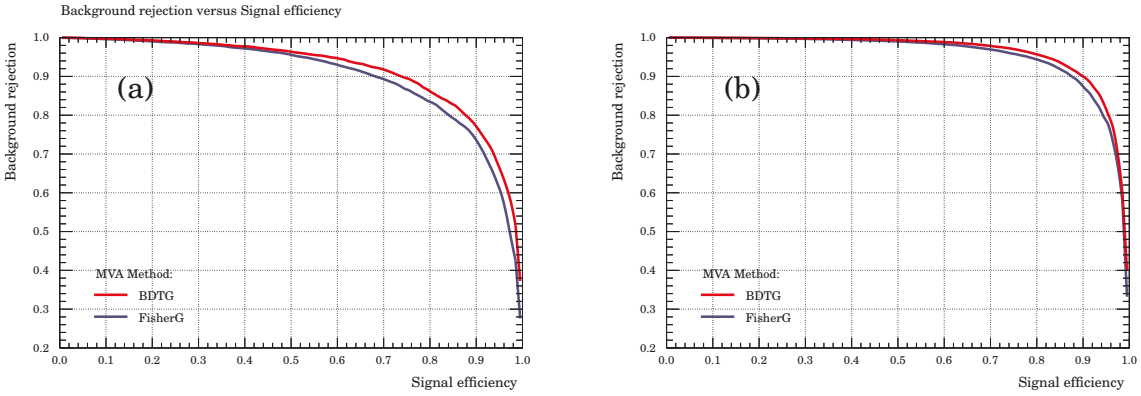

Figure 4.6: ROC curves for the Fisher and gradient boosted BDT discriminant for (a) $\overline{B}^0 \to D^0 p\overline{p}$ and (b) $\overline{B}^0 \to D^0 \pi^+ \pi^-$ decays.

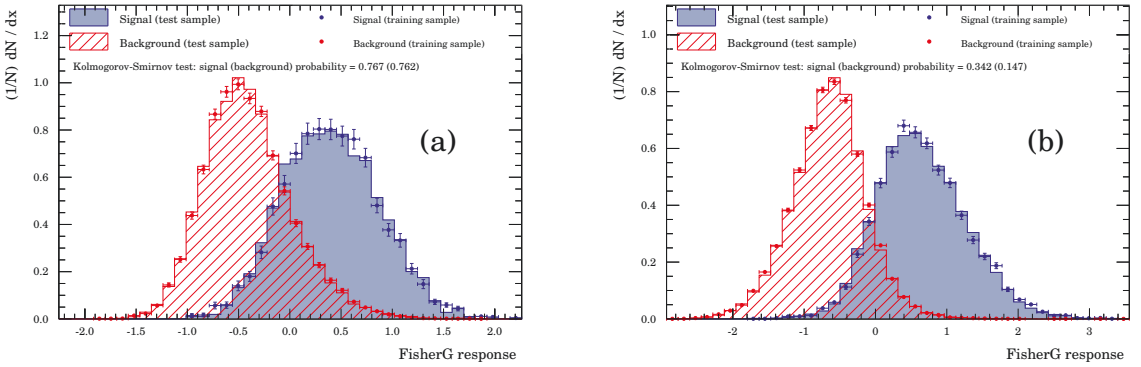

Figure 4.7: Test for overtraining between training and test sample for (a) $\overline{B}^0 \to D^0 p\overline{p}$ and (b) $\overline{B}^0 \to D^0 \pi^+ \pi^-$ events. Fisher classifier output distributions for phase space simulated signal (red) and background (blue) events from the upper mass sideband in data.

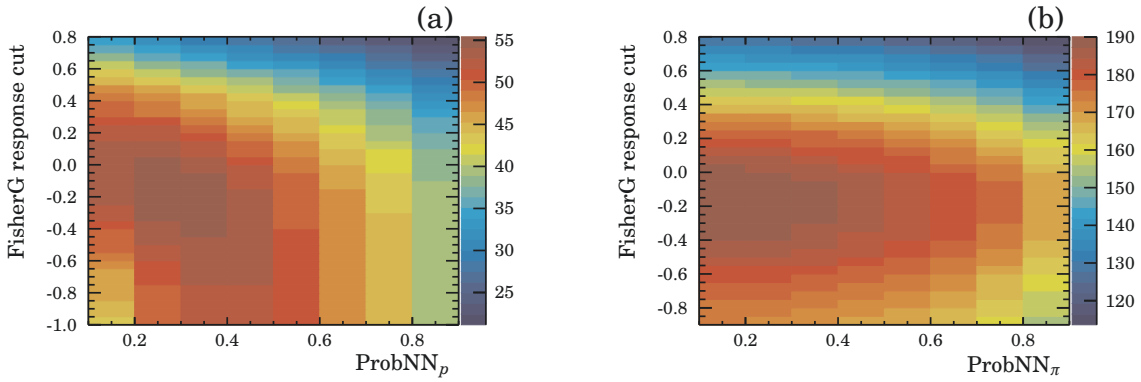

Figure 4.8: Selection optimization for (a) $\overline{B}^0 \to D^0 p\overline{p}$ events and (b) $\overline{B}^0 \to D^0 \pi^+ \pi^-$ events.

atively charged tracks of the baryons/pions originating directly from the $\overline{B}^0$ meson behave similarly and the cut on the PID variable is the same for both tracks. The variable that is optimised using data is

$$\mathcal{S} = \frac{n_{\mathrm{S}}}{\sqrt{n_S + n_B}}, \tag{4.12}$$

where $\mathcal{S}$ is the signal significance, and n_{S} and n_{B} are the number of signal and background events, respectively. The number of signal and background events is extracted in the region $m\left(\overline{B}^0\right) \in [5250, 5310]\,\mathrm{MeV}/c^2$ using the sideband-subtraction method. The background under the signal is approximated by fitting the lower and upper mass sideband with a first-order polynomial; no assumption to the shape of the signal is made. Figure 4.8 shows the result of the optimisation for $\overline{B}^0 \to D^0 p\overline{p}$ decays and $\overline{B}^0 \to D^0\pi^+\pi^-$ decays. To check whether this method may bias a branching fraction measurement or not, the $\overline{B}^0 \to D^0 p\overline{p}$ and the $\overline{B}^0 \to D^0\pi^+\pi^-$ sample is divided pseudo-randomly into two samples, and the method is repeated. These Figures are shown in Section 4.6.2. The cut chosen is a FisherG response cut higher than -0.2, and a ProbNN$_p$ PID variable cut greater than 0.2 for the proton and the antiproton of the $\overline{B}^0 \to D^0 p\overline{p}$ decay. For $\overline{B}^0 \to D^0\pi^+\pi^-$ decays, the FisherG response cut is higher than -0.2 and the pion ProbNN$_\pi$ PID variable has to be greater than 0.2. The number of multiple candidates after applying all selection criteria are about 1% for $\overline{B}^0 \to D^0 p\overline{p}$ events and 3% for $\overline{B}^0 \to D^0\pi^+\pi^-$ events. Since the percentage of multiple candidates is negligible, multiple candidates are removed by taking the first candidate in the event.

4.3 Backgrounds

The goal of this part of the thesis is to measure the branching fraction of $\overline{B}^0 \to D^0 p\overline{p}$ decays relative to $\overline{B}^0 \to D^0\pi^+\pi^-$ decays. Therefore, a clean signal region is needed to reduce the systematic uncertainties resulting from the background description. Sources for background components can come from charmless background, misidentified background, partially reconstructed background and combinatorial background. These sources for background components will be explained in this Section. To all distributions of simulated events and data, the selection described before is applied.

4.3.1 Combinatorial background

Combinatorial background results from random combinations of the final state particles and is present over the full mass window. The distribution of combinatorial background can be modelled by a first or second order polynomial or an exponential func-

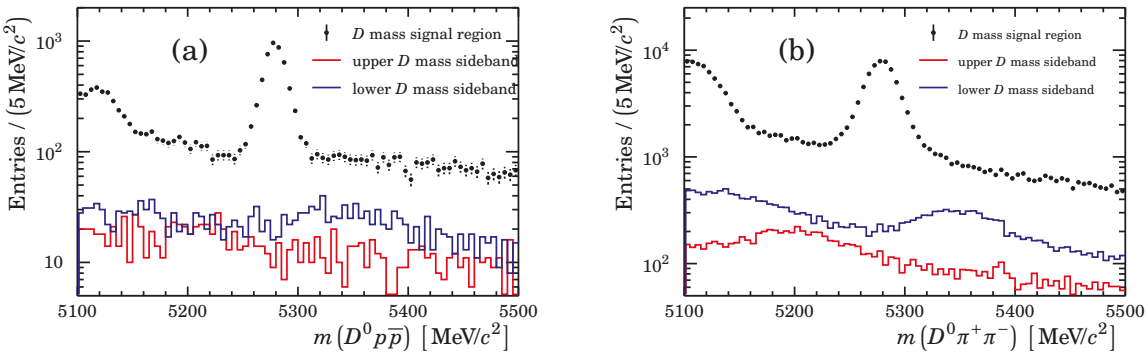

Figure 4.9: $\overline{B}^0$ mass distribution for selected $\overline{B}^0$ signal candidates and candidates from the lower and upper D^0 mass sideband for (a) $\overline{B}^0 \to D^0 p\overline{p}$ events and (b) $\overline{B}^0 \to D^0\pi^+\pi^-$ events.

tion. The part of the mass window without other background components helps to fix the shape of the combinatorial background. For both decays, $\overline{B}^0 \to D^0 p\overline{p}$ and $\overline{B}^0 \to D^0\pi^+\pi^-$, the upper B mass sideband is expected to only have contributions from combinatorial background components or a negligible level of other background components.

4.3.2 Charmless background

Charmless background refers to background peaking at the $\overline{B}^0$ mass but not containing a charmed particle, *e.g.* $\overline{B}^0 \to K^-\pi^+ p\overline{p}$ and $\overline{B}^0 \to K^-\pi^+\pi^+\pi^-$. The upper and lower D^0 mass sidebands are suitable for investigating the contribution of charmless background. The upper sideband ($m(D^0) \in [1920, 1960]\,\text{MeV}/c^2$) and lower sideband ($m(D^0) \in [1770, 1810]\,\text{MeV}/c^2$) do also have contributions from misidentified D^0 decays. A kaon from $D \to KK$ decays identified as a pion shifts the D^0 mass to lower invariant masses; a pion from $D \to \pi\pi$ decays identified as a kaon shifts the D^0 mass to higher invariant masses. The charmless $\overline{B}^0$ decay is linearly distributed over the D^0 mass range and does therefore also appear in the D^0 mass sidebands. The charmless background contribution, if present, would be visible as a peak at the $\overline{B}^0$ mass when looking at the D^0 mass sidebands. Figure 4.9 shows the $\overline{B}^0$ mass distribution for the D^0 signal region and the lower and upper sideband. No significant contribution of charmless background is observable for $\overline{B}^0 \to D^0 p\overline{p}$ as well as for $\overline{B}^0 \to D^0\pi^+\pi^-$ decays. The visible peaks result from misidentification in the D^0 decay.

4.3.3 Misidentified background

Background with misidentification refers to events where one or more final state particles are identified as another type of particle. Misidentified D^0 daughter particles

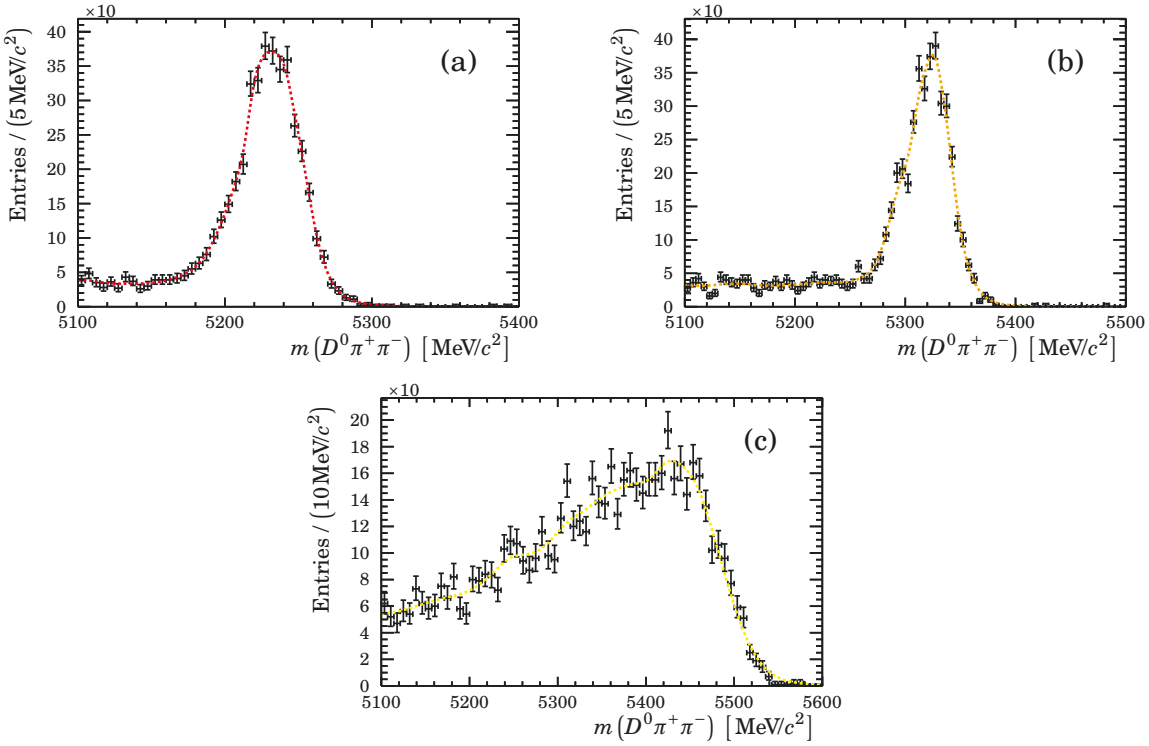

Figure 4.10: $\overline{B}^0 \to D^0 K^- \pi^+$ (a), $\overline{B}^0_s \to D^0 K^+ \pi^-$ (b) and $\Lambda^0_b \to D^0 p \pi^-$ (c) decays reconstructed as $\overline{B}^0 \to D^0 \pi^+ \pi^-$ decays each with a non-parametric PDFs overlaid.

do not influence the $\overline{B}^0$ mass distribution since misidentification shifts the D^0 to the upper and lower D^0 mass sidebands which are removed by the cut on the D^0 mass.

For $\overline{B}^0 \to D^0 p \overline{p}$ events misidentified background can come from a misidentified antiproton. The mother particle would then be a Λ^0_b baryon decaying to $\Lambda^0_b \to D^0 p \pi^-$ or $\Lambda^0_b \to D^0 p K^-$. The Λ^0_b baryon has a mass of 5619.51 MeV/c^2. The reconstruction of $\Lambda^0_b \to D^0 p \pi^-$ or $\Lambda^0_b \to D^0 p K^-$ decays as $\overline{B}^0 \to D^0 p \overline{p}$ shifts the mass peak to higher values than the Λ^0_b mass. The mass of the Λ^0_b baryon is not in the fit region used in Section 4.4 and does not need to be considered when extracting the number of $\overline{B}^0 \to D^0 p \overline{p}$ decays.

Decay modes that contribute to the misidentified background of $\overline{B}^0 \to D^0 \pi^+ \pi^-$ candidates are $\overline{B}^0 \to D^0 K^- \pi^+$ decays, $\overline{B}^0_s \to D^0 K^+ \pi^-$ decays, and $\Lambda^0_b \to D^0 p \pi^-$ decays. Decays with double misidentification, *e.g.* $\overline{B}^0 \to D^0 K K$ and $\overline{B}^0_s \to D^0 K K$, are not considered because their contribution is very small. Simulated events of decays that contribute to the misidentified background of $\overline{B}^0 \to D^0 \pi^+ \pi^-$ candidates are shown in Figure 4.10. The distributions are modelled using non-parametric probability density functions (PDFs) from the RooFit toolkit [118], called *RooKeysPdf* (see Appendix E.1). The distribution of $\Lambda^0_b \to D^0 p \pi^-$ shown in Figure 4.10(c) is without the tightened PID variable cut on the pions originating directly from the $\overline{B}^0$ meson to increase the statistics.

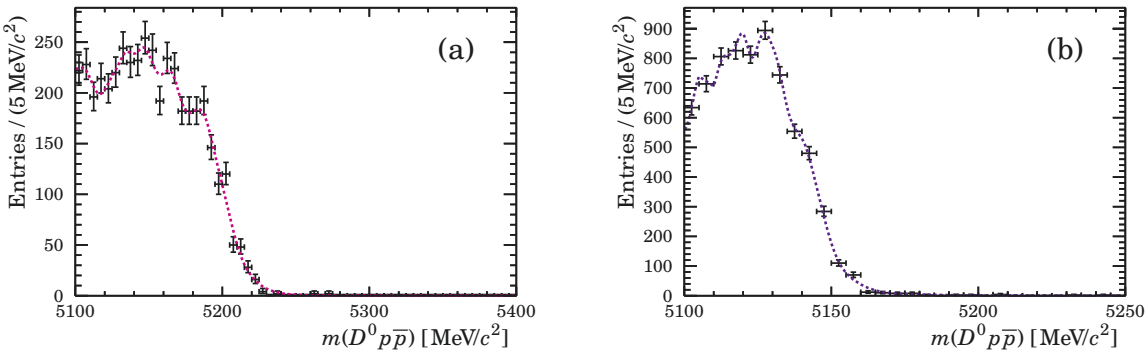

Figure 4.11: The decays $\overline{B}^0 \to D^{*0} p\overline{p}$ with (a) $D^{*0} \to D^0\gamma$ and (b) $D^{*0} \to D^0\pi^0$ reconstructed as $\overline{B}^0 \to D^0 p\overline{p}$ decays each with a non-parametric PDFs overlaid.

4.3.4 Partially reconstructed background

Partially reconstructed background events are those where one or more particles in the decay chain are not reconstructed. These are for example decays with a D^{*0} where the D^{*0} decays either to $D^{*0} \to D^0\pi^0$ or $D^{*0} \to D^0\gamma$ final states. The distributions for $\overline{B}^0 \to D^{*0} p\overline{p}$ decays are shown in Figure 4.11 and for $\overline{B}^0 \to D^{*0}\pi^+\pi^-$ decays in Figure 4.12. The distributions are also modelled using non-parametric PDFs. $B^- \to D^0 p\overline{p}\pi^-$ decays are not used for modelling partially reconstructed background in $\overline{B}^0 \to D^0 p\overline{p}$ decays. The missing pion in the reconstruction of $B^- \to D^0 p\overline{p}\pi^-$ decays as $\overline{B}^0 \to D^0 p\overline{p}$ decays broadens the mass distribution and shifts it to invariant masses smaller than $5200\,\text{MeV}/c^2$. A large fraction of these events is cut by the fit range $m(D^0 p\overline{p}) > 5120\,\text{MeV}/c^2$ so that the contribution of $B^- \to D^0 p\overline{p}\pi^-$ decays is considered to be negligible. In addition to $\overline{B}^0 \to D^{*0}\pi^+\pi^-$ decays, $\overline{B}^0_s \to D^{*0}K^+\pi^-$ decays might also be observable in mass distribution of reconstructed $\overline{B}^0 \to D^0\pi^+\pi^-$ decays. The distribution is also shown in Figure 4.12. The tightened PID variable cuts on the charged pions originating directly from the B^0 meson are not applied to $\overline{B}^0_s \to D^{*0}K^+\pi^-$ decays to increase the statistics.

4.3.5 Estimation of background contributions

The yields of background events can be estimated using simulated events. The fraction of background events can be calculated using the following ratio

$$\frac{N_{\text{bkg}}}{N_{Dhh}} = \frac{\mathcal{B}\left(\overline{B}^0_q \to X_{\text{bkg}}\right)}{\mathcal{B}\left(\overline{B}^0 \to D^0 hh\right)} \times \frac{f_q}{f_d} \times \frac{\epsilon_{\text{bkg}}}{\epsilon_{Dhh}}, \tag{4.13}$$

where $\mathcal{B}\left(\overline{B}^0 \to X\right)$ is the branching fraction of a specific decay, f_q/f_d is the b-hadron production ratio, and ϵ_X is the efficiency of a specific decay. This method is only used to

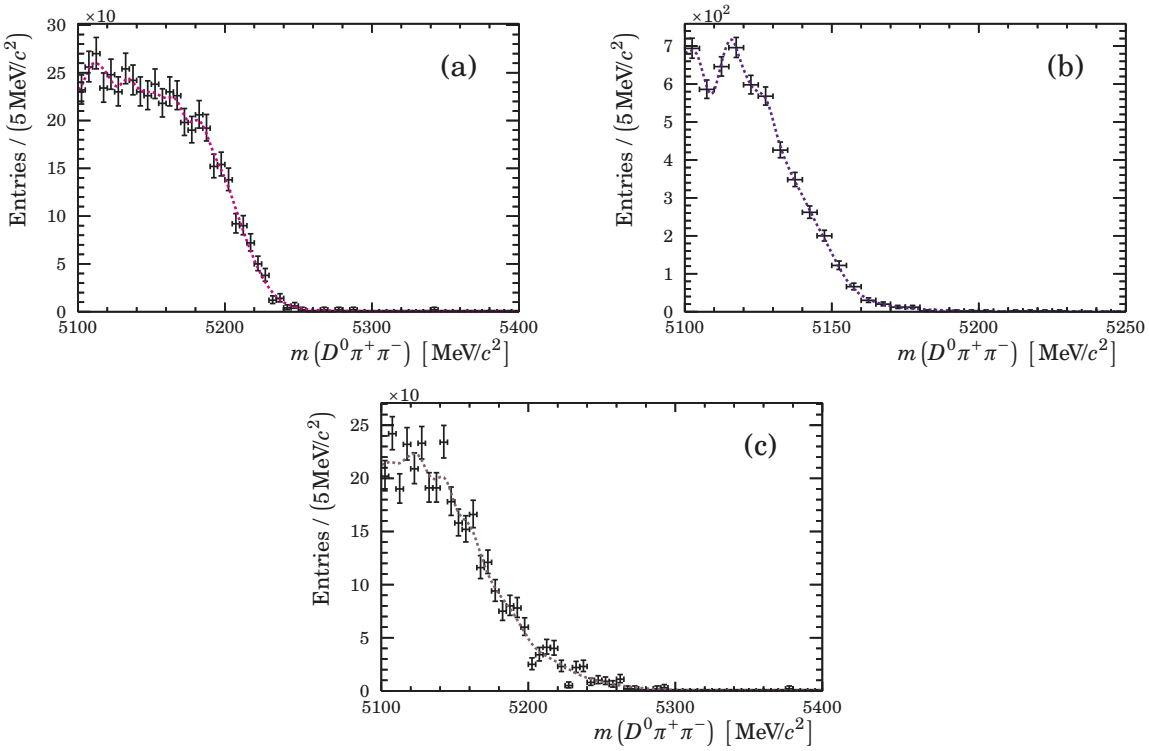

Figure 4.12: The decays $\overline{B}^0 \to D^{*0}\pi^+\pi^-$ with (a) $D^{*0} \to D^0\gamma$ and (b) $D^{*0} \to D^0\pi^0$ and (c) $\overline{B}^0_s \to D^{*0}K^+\pi^-$ reconstructed as $\overline{B}^0 \to D^0\pi^+\pi^-$ decays each with a non-parametric PDFs overlaid.

estimate the number of background events in the fit region. The result is not used for the fit to data. The efficiencies are calculated as described in Section 4.5 not correcting for structures in the Dalitz plane. The results can be found in Table 4.6 and Table 4.7. The branching fractions of the $\overline{B}^0 \to D^{*0}p\overline{p}$ decays are calculated using the PDG value [4] for this branching fraction and multiplying it either with the branching fraction for $D^{*0} \to D^0\pi^0$ decays or with the branching fraction of $D^{*0} \to D^0\gamma$ decays.

The relative branching fraction $\mathcal{B}\left(\overline{B}^0 \to D^0K^-\pi^+\right) / \mathcal{B}\left(\overline{B}^0 \to D^0\pi^+\pi^-\right)$, as well as the relative branching fraction $\mathcal{B}\left(\overline{B}^0_s \to D^0K^+\pi^-\right) / \mathcal{B}\left(\overline{B}^0 \to D^0\pi^+\pi^-\right)$ measured with the LHCb experiment [119] is used to estimate the background yields in $\overline{B}^0 \to D^0\pi^+\pi^-$ decays from $\overline{B}^0 \to D^0K^-\pi^+$ decays and $\overline{B}^0_s \to D^0K^+\pi^-$ decays. The f_s/f_d b-hadron production ratio is measured for 7 TeV pp-collisions at LHCb and is 0.259 ± 0.015 [120]. The production ratio of the Λ^0_b baryon depends on the transverse momentum p_T of the baryon [121, 122]

$$\frac{f_{\Lambda^0_b}}{f_d}(p_\mathrm{T}) = a + \exp(b + c \times p_\mathrm{T}\,[\mathrm{GeV}/c])\,, \tag{4.14}$$

Table 4.6: Estimated backgrounds for $\overline{B}^0 \to D^0 p\overline{p}$ decays.

decay mode	branching fraction ($\times 10^{-4}$)	f_q/f_d	ϵ ($\times 10^{-4}$)	$N_{\text{bkg}}/N_{Dp\overline{p}}$
$\overline{B}^0 \to D^0 p\overline{p}$	1.04 ± 0.07	1	13.18 ± 0.77	–
$\overline{B}^0 \to [D^{*0} \to D^0\pi^0]\, p\overline{p}$	0.64 ± 0.07	1	6.1 ± 0.5	0.282 ± 0.047
$\overline{B}^0 \to [D^{*0} \to D^0\gamma]\, p\overline{p}$	0.35 ± 0.04	1	6.8 ± 1.4	0.172 ± 0.044

where the parameters from Reference [122] are

$$a = +0.151 \pm 0.016^{+0.024}_{-0.025}\,, \tag{4.15}$$

$$b = -0.573 \pm 0.040^{+0.101}_{-0.097}\,, \tag{4.16}$$

$$c = (-0.095 \pm 0.007 \pm 0.014)\,[\text{GeV}/c]^{-1}\,. \tag{4.17}$$

This measurement is valid for $1.5\,\text{GeV}/c < p_{\text{T}} < 40\,\text{GeV}/c$ and $2 < \eta < 5$. The mean transverse momentum for Λ_b^0 baryons in simulation is almost 10 GeV. This value will be used to estimate the production ratio for Λ_b^0 baryons $f_{\Lambda_b^0}/f_d(10\,\text{GeV}/c) \simeq 0.369 \pm 0.009$. The only branching ratio for the decay $\Lambda_b^0 \to D^0 p\pi^-$ has been measured by the LHCb experiment [123]

$$\frac{\mathcal{B}\left(\Lambda_b^0 \to D^0 p\pi^-\right) \times \mathcal{B}\left(D^0 \to K^-\pi^+\right)}{\mathcal{B}\left(\Lambda_b^0 \to \Lambda_c^+\pi^-\right) \times \mathcal{B}\left(\Lambda_c^+ \to pK^-\pi^+\right)} = 0.0806 \pm 0.0042\,. \tag{4.18}$$

The branching fraction for the $\Lambda_b^0 \to D^0 p\pi^-$ decay can then be calculated using the averaged branching fractions for $D^0 \to K^-\pi^+$ decays, $\Lambda_b^0 \to \Lambda_c^+\pi^-$ decays, and $\Lambda_c^+ \to pK^-\pi^+$ decays. Currently, there are no branching fraction measurements for $\overline{B}^0 \to D^{*0}\pi^+\pi^-$ decays and $\overline{B}_s^0 \to D^{*0}K^+\pi^-$ decays. It is assumed that the branching fraction $\mathcal{B}\left(\overline{B}^0 \to D^{*0}\pi^+\pi^-\right)$ is approximately as large as the branching fraction $\mathcal{B}\left(\overline{B}^0 \to D^0\pi^+\pi^-\right)$ and that the branching fraction $\mathcal{B}\left(\overline{B}_s^0 \to D^{*0}K^+\pi^-\right)$ is in the order of the branching fraction $\mathcal{B}\left(\overline{B}_s^0 \to D^0K^+\pi^-\right)$. The results from Table 4.6 and Table 4.7 are only used to estimate the impact in the fit in Section 4.4. The fit fractions will no be fixed in the fit to data.

4.4 Likelihood fit

The signal and background yields are extracted from the data by finding the best fit to the data points. The program used to implement the fit to data is the ROOT toolkit [99,100] with the RooFit package [118]. The fit method chosen is the maximum

Table 4.7: Estimated backgrounds for $\overline{B}^0 \to D^0\pi^+\pi^-$ decays.

decay mode	branching fraction ($\times 10^{-4}$)	f_q/f_d	ϵ ($\times 10^{-4}$)	$N_{\text{bkg}}/N_{D\pi\pi}$ ($\times 10^{-2}$)
$\overline{B}^0 \to D^0\pi^+\pi^-$	8.95 ± 0.54	1	18.51 ± 0.46	–
$\overline{B}^0 \to D^0K^-\pi^+$	0.95 ± 0.12	1	4.01 ± 1.04	2.30 ± 0.58
$\overline{B}^0_s \to D^0K^+\pi^-$	10.56 ± 1.33	0.259 ± 0.015	4.87 ± 0.68	8.05 ± 3.15
$\Lambda^0_b \to D^0p\pi^-$	6.39 ± 0.70	0.369 ± 0.009	5.03 ± 0.13	7.16 ± 2.43
$\overline{B}^0 \to [D^{*0} \to D^0\pi^0]\,\pi^+\pi^-$	5.79 ± 0.36	1	4.76 ± 0.20	16.65 ± 4.34
$\overline{B}^0 \to [D^{*0} \to D^0\gamma]\,\pi^+\pi^-$	3.16 ± 0.21	1	6.34 ± 0.53	12.09 ± 3.35
$\overline{B}^0_s \to D^{*0}K^+\pi^-$	10.40	0.259 ± 0.015	2.12 ± 0.31	3.45 ± 0.56

likelihood method. For a dataset of multiple data points, the likelihood is defined as the product of probability density functions

$$\mathcal{L}(\vec{a}) = \prod_{i=1}^{n} f(m_i|\vec{a}) \,, \tag{4.19}$$

where $\vec{a}$ are the parameters that are going to be measured, $f(m_i|\vec{a})$ is the probability density function which is normalised to one, m_i are the measured parameters of the ith event, and n is the number of events. To find the maximum of $\mathcal{L}(a)$ it is often easier to use the negative logarithm of the likelihood, called log-likelihood,

$$-\ln\mathcal{L}(\vec{a}) = -\sum_{i=1}^{n} \ln f(m_i|\vec{a}) \tag{4.20}$$

Maximising $\mathcal{L}(\vec{a})$ is equivalent to minimising $-\ln\mathcal{L}(\vec{a})$. The type of the maximum likelihood fit is an extended maximum likelihood fit. This means that the function does not depend on a fixed sample size for normalisation so that the extended likelihood is defined as [124]

$$\mathcal{L}(\mathcal{N}, \vec{a}) = e^{-\mathcal{N}} \frac{\mathcal{N}^n}{n!} \prod_{i=1}^{n} f(m_i|\vec{a}) \tag{4.21}$$

$$\ln\mathcal{L}(\mathcal{N}, \vec{a}) = \sum_{i=1}^{n} f(m_i|\vec{a}) + n\ln\mathcal{N} - \mathcal{N} + \text{const.} \,, \tag{4.22}$$

where $\mathcal{N}$ is the number of events found by the fit to data.

To get the signal shape for the fit function in data, truth-matched simulated events are fitted with a double Crystal Ball function, as defined in Appendix E.1. The fit to simulated events is shown in Figure 4.13, and the fit parameters are listed in Table 4.8. The parameter n_1 (n_2) influences the left (right) power-law tail of the double

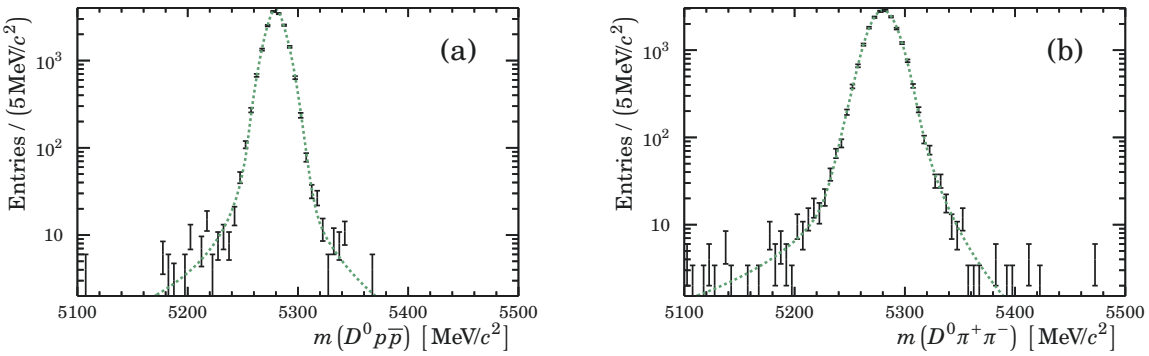

Figure 4.13: Fit to the mass distribution of simulated events of (a) $\overline{B}^0 \to D^0 p\overline{p}$ and (b) $\overline{B}^0 \to D^0\pi^+\pi^-$ decays with a double Crystal Ball function.

Table 4.8: Fitted parameters for the double Crystal Ball function from $\overline{B}^0 \to D^0 p\overline{p}$ and $\overline{B}^0 \to D^0\pi^+\pi^-$ truth-matched simulated events.

	$\overline{B}^0 \to D^0 p\overline{p}$	$\overline{B}^0 \to D^0\pi^+\pi^-$
$\bar{m}$ [MeV/c^2]	5279.740 ± 0.103	5280.25 ± 0.11
σ_1 [MeV/c^2]	10.08 ± 0.22	11.7 ± 0.5
α_1	2.50 ± 0.10	2.12 ± 0.17
n_1	1.53 ± 0.20	1.67 ± 0.27
σ_2 [MeV/c^2]	5.3 ± 0.6	15.8 ± 0.8
α_2	-1.35 ± 0.29	-1.93 ± 0.13
n_2	2.4 ± 0.4	3.9 ± 0.7
r_{CB}	0.813 ± 0.004	0.50 ± 0.11

Table 4.9: Fit parameters obtained from the fit to data of reconstructed $\overline{B}^0 \to D^0 p\overline{p}$ and $\overline{B}^0 \to D^0\pi^+\pi^-$ decays.

	$\overline{B}^0 \to D^0 p\overline{p}$	$\overline{B}^0 \to D^0\pi^+\pi^-$
$\Delta m_{\overline{B}^0 \to D^0 hh}$ $[\mathrm{MeV}/c^2]$	-0.85 ± 0.19	-1.8 ± 0.1
σ_1 $[\mathrm{MeV}/c^2]$	10.2 ± 0.4	11.2 ± 0.6
σ_2 $[\mathrm{MeV}/c^2]$	6.5 ± 0.9	17.41 ± 0.98
r_{CB}	0.72 ± 0.10	0.45 ± 0.11
a_{comb}	-0.273 ± 0.030	-0.002666 ± 0.000035
$\Delta m_{\overline{B}^0 \to D^{*0} hh}$ $[\mathrm{MeV}/c^2]$	-4.9 ± 0.5	-4.61 ± 0.14
$N_{\overline{B}^0 \to D^0 hh}$	4089 ± 83	50283 ± 391
$N_{comb.bkg}$	7251 ± 140	91801 ± 698
$N_{\overline{B}^0 \to D^{*0} hh, D^{*0} \to D^0\gamma}$	574 ± 93	6461 ± 386
$N_{\overline{B}^0 \to D^{*0} hh, D^{*0} \to D^0\pi^0}$	754 ± 51	16693 ± 208
$N_{\overline{B}^0 \to D^0 K^-\pi^+}$	–	1537 ± 358
$N_{\overline{B}^0_s \to D^0 K^+\pi^-}$	–	2387 ± 284

Crystal Ball function. The fit parameters n_i, α_i are fixed to the values from the fit to simulated events when fitting the data; mean and widths are allowed to float. The combinatorial background is described by a first-order polynomial or an exponential function and other background components by the functions described in Section 4.3. Because of the momentum calibration problem mentioned before, the mean values of the functions are allowed to float along the x-axis. The fit to data is shown in Figure 4.14, with logarithmic ordinate in Figure 4.15. The fit parameters for the signal description are listed in Table 4.9.

The fit function for $\overline{B}^0 \to D^0 p\overline{p}$ candidates includes the description for the $\overline{B}^0 \to D^0 p\overline{p}$ signal, the description for the partially reconstructed backgrounds of $\overline{B}^0 \to D^{*0} p\overline{p}$ events with $D^{*0} \to D^0\gamma$ and $D^{*0} \to D^0\pi^0$ and a first-order polynomial to describe the combinatorial background. The functions for the B decays are allowed to shift along the abscissa. The shift of the $\overline{B}^0 \to D^0 p\overline{p}$ signal along the B mass is determined with respect to the mean value $\bar{m}$ of the double Crystal Ball function obtained in simulated events, which is the mass of the B meson for simulated events. The PDFs of $\overline{B}^0 \to D^{*0} p\overline{p}$ events are allowed to have a different shift value because in both $\overline{B}^0 \to D^{*0} p\overline{p}$ decay modes is a particle missing when reconstructing it as $\overline{B}^0 \to D^0 p\overline{p}$ decays, and non-resonant decay channels can affect the shape of the decays in these regions. The number of $\overline{B}^0 \to D^0 p\overline{p}$ signal events in the fit range $[5120, 5500]\,\mathrm{MeV}/c^2$ is 4089 ± 83.

The fit function for $\overline{B}^0 \to D^0\pi^+\pi^-$ candidates includes the description for the $\overline{B}^0 \to D^0\pi^+\pi^-$ signal, the description of misidentified background from $\overline{B}^0 \to D^0 K^-\pi^+$ and

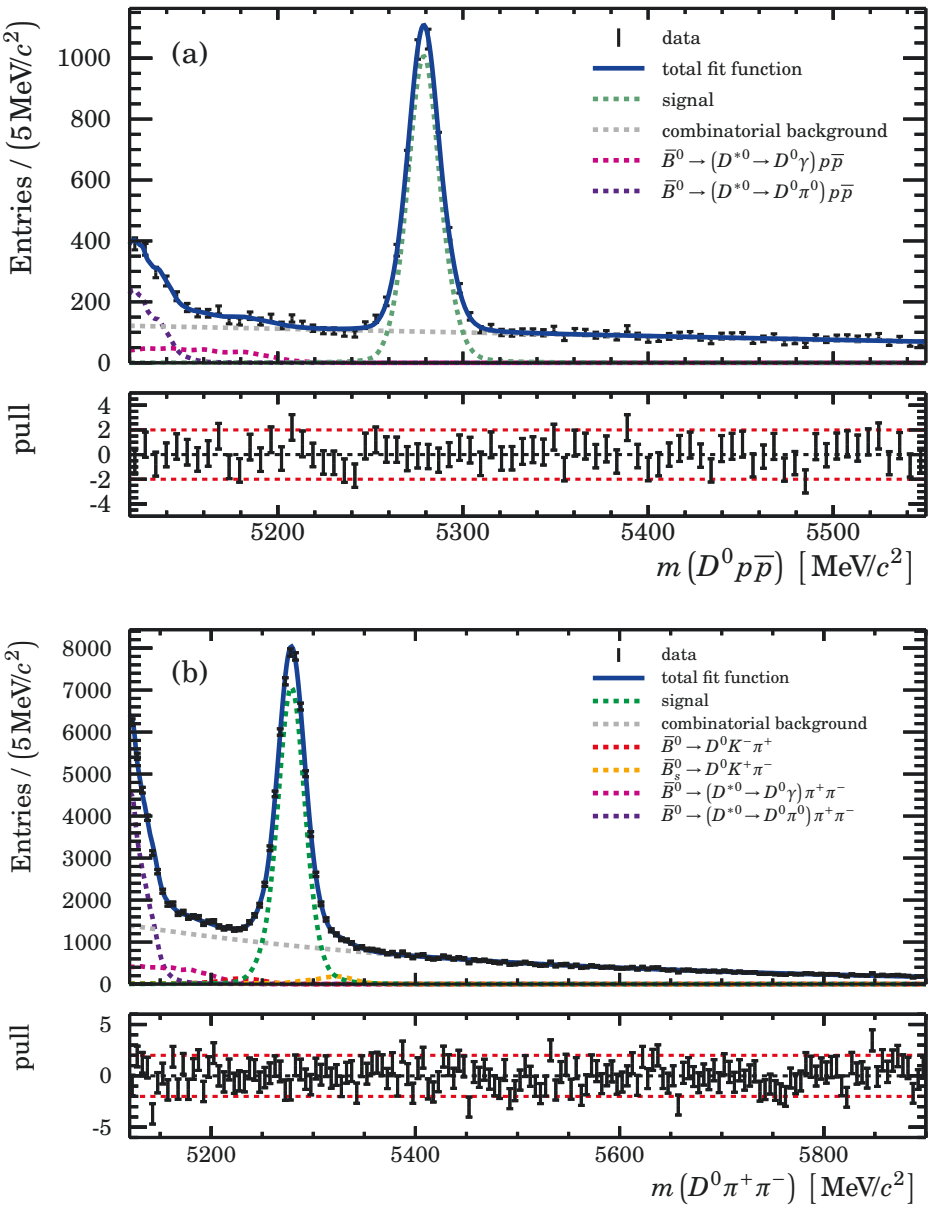

Figure 4.14: Fit to data for reconstructed (a) $\overline{B}^0 \to D^0 p\overline{p}$ and (b) $\overline{B}^0 \to D^0\pi^+\pi^-$ decays and pull-distribution.

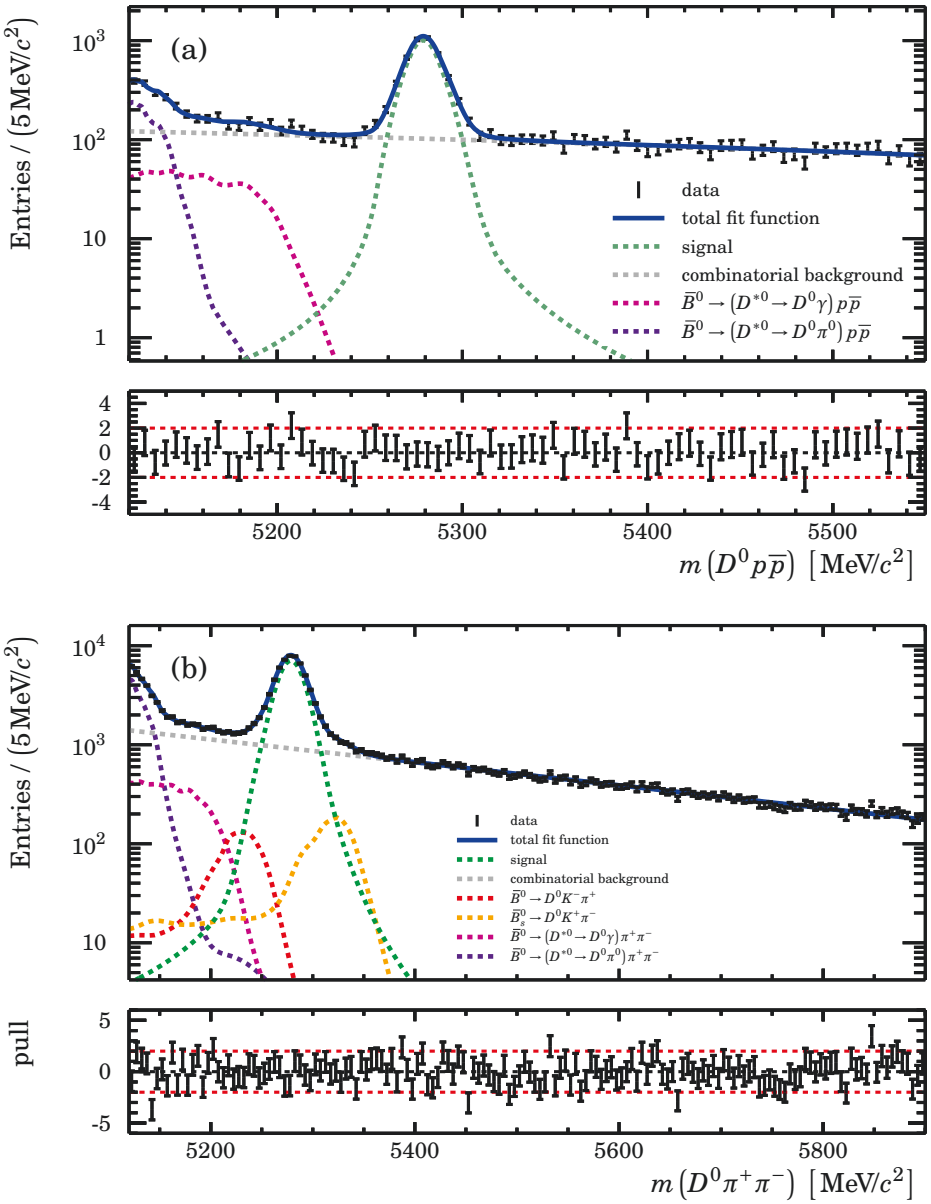

Figure 4.15: Fit to data for reconstructed (a) $\overline{B}^0 \to D^0 p\overline{p}$ and (b) $\overline{B}^0 \to D^0\pi^+\pi^-$ decays with logarithmic y-axis and pull-distribution

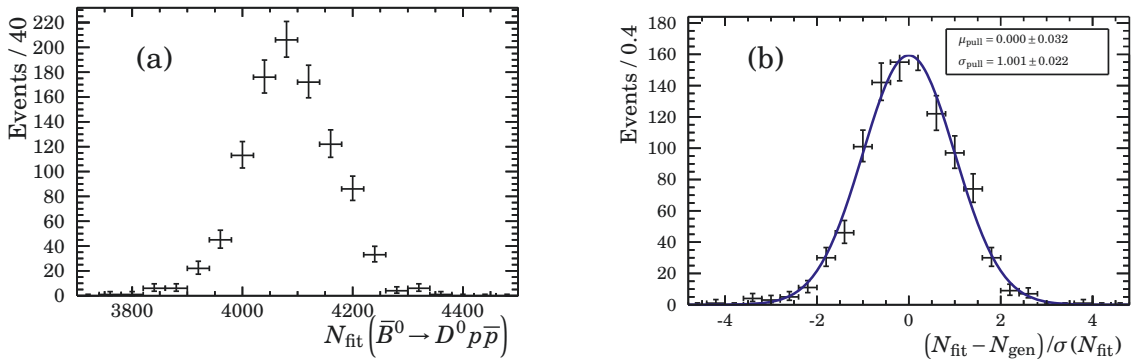

Figure 4.16: Variation of the number of events of the $\overline{B}^0 \to D^0 p\overline{p}$ fit using 1000 Monte Carlo experiments (a) and the pull-distribution $(N_{\rm fit} - N_{\rm gen})/\sigma(N_{\rm fit})$ on these Monte Carlo experiments (b). The blue line is a Gaussian fit to the distribution.

$\overline{B}^0_s \to D^0 K^+ \pi^-$ decays, the description for the partially reconstructed backgrounds of $\overline{B}^0 \to D^{*0} \pi^+ \pi^-$ events with $D^{*0} \to D^0 \gamma$ and $D^{*0} \to D^0 \pi^0$ and an exponential function to describe the combinatorial background. The functions for the B decays are allowed to shift along the x-axis. The $\overline{B}^0 \to D^0 \pi^+ \pi^-$ signal function and the functions for the misidentified background components are assumed to have the same shift since the kinematics of kaons and pions is very similar. The non-parametric PDFs for the partially reconstructed background components are allowed to have a different shift value. The background from $\Lambda^0_b \to D^0 p \pi^-$ and $\overline{B}^0_s \to D^{*0} K^+ \pi^-$ decays is not included in the fit function since their contributions are negligible. The total number of $\overline{B}^0 \to D^0 \pi^+ \pi^-$ signal events found in the fit region $[5120, 5900]\,\text{MeV}/c^2$ is 50283 ± 391.

4.4.1 Toy Monte Carlo study

In general, maximum likelihood fits do not provide a measurement of the goodness of the fit as χ^2-fits do. One way to validate the goodness of the unbinned maximum likelihood fit is to compare the fit result with a binned histogram of data as shown in the pull-plots of Figure 4.14. For both fits, the fit function and the binned data histogram are in good agreement. The red lines in the plot indicate a 2σ deviation between the fit function and the data points in the histogram. It is also possible to calculate the χ^2 of the binned histogram with respect to the fit function. However, both methods depend on the binning of the data.

Another possibility to validate the likelihood fit is to simulate samples according to the estimated PDF in data where the number of events per sample equals the number of events in the fit region. For the $\overline{B}^0 \to D^0 p\overline{p}$ fit to data, 1000 samples are simulated to validate the fit; for the $\overline{B}^0 \to D^0 \pi^+ \pi^-$ fit to data, 700 samples are generated. The result can be seen in Figures 4.16 and 4.17. The number of signal events is important for the branching fraction measurement. Figures 4.16(a) and

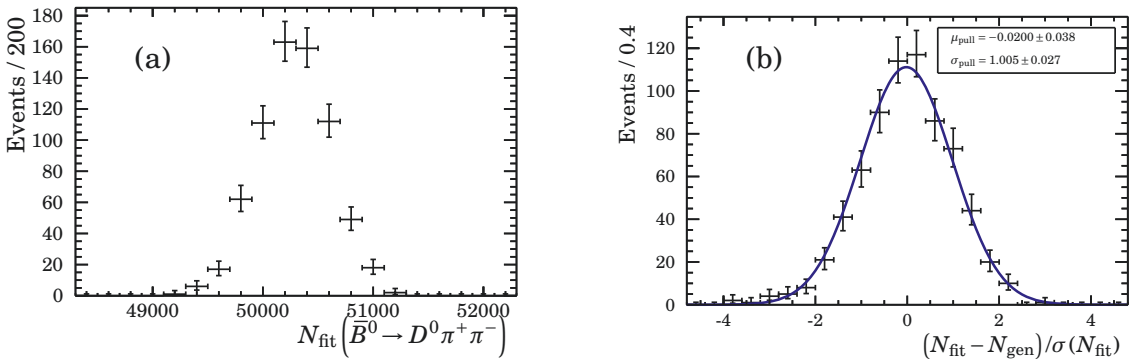

Figure 4.17: Variation of the number of events of the $\bar{B}^0 \to D^0\pi^+\pi^-$ fit using 700 Monte Carlo experiments (a) and the pull-distribution $\left(N_{\rm fit} - N_{\rm gen}\right)/\sigma\left(N_{\rm fit}\right)$ on these Monte Carlo experiments (b). The blue line is a Gaussian fit to the distribution.

4.17(a) show the variation of fitted number of signal events in the fit. The result is comparable with the result from the fit to data. The shape of the number of signal events distribution is expected to be Gaussian. The pull-distribution for the number of signal events in the Monte Carlo experiments is defined as

$$f_{\rm pull}\left(N_{\rm sig}\right) = \frac{N_{\rm fit} - N_{\rm gen}}{\sigma\left(N_{\rm fit}\right)}. \tag{4.23}$$

The mean of this distribution should be 0 if the fit is not biased and the width should be 1 if the error is correctly determined. Figures 4.16(b) and 4.17(b) show these distributions. The fits do not seem to be biased, and the errors seem to be correctly determined within the statistical precision of the Monte Carlo study.

4.5 Efficiencies and efficiency corrections

When reconstructing decays, not all produced decays can be reconstructed and observed. This might be, *e.g.* due to the limits of the detector volume or the selections applied. The efficiency determination is necessary for the calculation of the branching fraction. This Section will describe the determination of the efficiency and their correction over the Dalitz plane. The efficiency is determined using simulated events, calibration samples, where simulated events do not describe the data correctly, and data. The total efficiency can be factorised as follows

$$\epsilon = \epsilon_{\rm acc|gen} \times \epsilon_{\rm sel|acc} \times \epsilon_{\rm PID|sel} \times \epsilon_{L0|\rm PID} \tag{4.24}$$

Each term $\epsilon_{\rm x|y}$ describes the efficiency of events selected under the condition x relative to the events selected under condition y. Here,

- $\epsilon_{\text{acc|gen}}$ is the fraction of simulated events decaying inside the detector acceptance,
- $\epsilon_{\text{sel|acc}}$ is the fraction of events, that are stripped and fully reconstructed, and pass the HLT trigger requirement, the offline selection, and the selection on the Fisher discriminant,
- $\epsilon_{\text{PID|sel}}$ is the fraction of events passing selection on the particle identification.
- $\epsilon_{L0|\text{PID}}$ is the fraction of events which pass the L0 trigger requirement,

The determination of these terms will be explained below.

4.5.1 Kinematic selection

Particles are produced within a 4π solid angle. Due to the geometry of the detector, only particles inside the detector volume can be detected. The efficiency of the detector acceptance is listed in Tables A.1 to A.4, where $\epsilon_{\text{acc|gen}} = N_{\text{acc}}/N_{\text{gen}}$ is the fraction of candidates with all daughter particles inside the detector acceptance. During the simulation of events, flipping of backward signal events is used to increase the result of simulated signal events. This makes the simulation of events equivalent to a 2π solid angle. For the decays used to measure the branching fraction in this thesis, the efficiencies at the generator-level with all daughters within the LHCb acceptance are

- $\epsilon_{\text{acc|gen}}\left(\overline{B}^0 \to D^0 p\overline{p}\right) = (18.22 \pm 0.03)\%$,
- $\epsilon_{\text{acc|gen}}\left(\overline{B}^0 \to D^0 \pi^+\pi^-\right) = (15.81 \pm 0.03)\%$.

The efficiency of the detector acceptance is slightly larger for $\overline{B}^0 \to D^0 p\overline{p}$ decays than for $\overline{B}^0 \to D^0 \pi^+\pi^-$ decays.

The fraction of selected events generated within the LHCb detector acceptance is described by $\epsilon_{\text{sel|acc}}$. Selected events are stripped, and fully reconstructed with offline and BDTG selection and HLT1 and HLT2 trigger selection applied. Unlike the L0 hadron trigger, the high-level triggers use fully reconstructed events. Therefore the efficiency determination for simulated events is considered to be trustable. A PID selection is not applied to these events, as the modelled PID variables in simulation do not describe the behaviour correctly. The selection efficiency calculated from simulated events is $(1.834 \pm 0.012)\%$ for $\overline{B}^0 \to D^0 p\overline{p}$ events and $(2.234 \pm 0.015)\%$ for $\overline{B}^0 \to D^0 \pi^+\pi^-$ events. The selection efficiency also includes the track reconstruction efficiency. The track reconstruction efficiency corrects the efficiency obtained for simulated events for differences in the track reconstruction between data and simulated

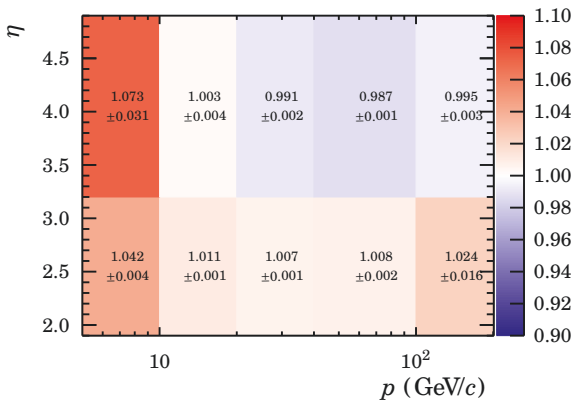

Figure 4.18: Track reconstruction efficiency correction table for 2012 data obtained from $J/\psi \to \mu^+\mu^-$ decays.

events. The LHCb physics performance working group *Tracking, Alignment and Vertexing* provides tables to correct simulated events for the tracking efficiency [125,126]. These tables list weights in dependence of the particle's momentum and pseudorapidity as shown in Figure 4.18. The track reconstruction efficiencies have been measured using clean high-statistics samples of $J/\psi \to \mu^+\mu^-$ decays. The correction table for data taken in 2012 is used to correct the differences since the same reconstruction software was used in 2012 and 2011. Furthermore, the correction factors for the track reconstruction are quite small and the difference in the efficiency ratio between both years should be negligible. The correction for the track reconstruction has to be calculated for every track in the final state according to their p-η distribution. The tracking efficiency correction is 1.031 ± 0.007 for $\overline{B}^0 \to D^0 p\overline{p}$ events and 1.041 ± 0.007 for $\overline{B}^0 \to D^0\pi^+\pi^-$ events. The selection efficiency $\epsilon_{\text{sel|acc}}$ is therefore $(1.891 \pm 0.018)\%$ for $\overline{B}^0 \to D^0 p\overline{p}$ events and $(2.324 \pm 0.022)\%$ for $\overline{B}^0 \to D^0\pi^+\pi^-$ events.

4.5.2 Particle identification

The particle identification variables are not well modelled in simulated events. Therefore, weights from calibration samples are used to obtain the PID efficiency. LHCb provides a tool called PIDCalib [127] (see Appendix D for a summary) which allows determining the PID efficiency per track in dependence of momentum, pseudorapidity, data taking period, and magnet polarity. The efficiency per track of $\overline{B}^0 \to D^0[h_1 h_2]h_3 h_4$ is then combined to an efficiency per event as follows

$$\epsilon_{\text{PID}}^{\text{evt}} = \prod_{i=1}^{4} \epsilon_i \,. \tag{4.25}$$

Table 4.10: PID efficiency for $\overline{B}^0 \to D^0 p\overline{p}$ and $\overline{B}^0 \to D^0\pi^+\pi^-$ events.

	$\overline{B}^0 \to D^0 p\overline{p}$		$\overline{B}^0 \to D^0\pi^+\pi^-$	
magnet polarity	*MagUp*	*MagDown*	*MagUp*	*MagDown*
2011	$(71.18 \pm 0.94)\%$	$(71.52 \pm 0.96)\%$	$(91.71 \pm 1.20)\%$	$(91.82 \pm 1.22)\%$
2012	$(74.38 \pm 0.98)\%$	$(76.22 \pm 1.01)\%$	$(91.47 \pm 1.20)\%$	$(91.93 \pm 1.22)\%$
total	$(74.15 \pm 0.98)\%$		$(91.72 \pm 1.21)\%$	

For pions and kaons, the PIDCalib tool uses a $D^* \to D^0\pi$ calibration sample. The calibration sample for protons contains either $\Lambda \to p\pi^-$ or $\Lambda_c^+ \to pK^-\pi^+$ events. Since the kinematics of the protons from the Λ_c^+ sample are in better agreement with the kinematic characteristics of the protons from $\overline{B}^0 \to D^0 p\overline{p}$ decays; this sample is used. The results for the PID efficiency are listed in Table 4.10. To get the overall PID efficiency, the efficiencies are weighted by their fraction to the total luminosity multiplied by the integrated production cross-section for $\overline{B}^0$ mesons

$$\epsilon_{\text{PID}} = f_{2011}\,\epsilon_{\text{PID}}^{2011} + f_{2012}\,\epsilon_{\text{PID}}^{2012}\,, \tag{4.26}$$

with $f_{2011}+f_{2012} = 1$. For $\overline{B}^0$ mesons, the integrated production cross-section is $\sigma\left(\sqrt{s} = 8\,\text{TeV}\right)/\sigma\left(\sqrt{s} = 7\,\text{Te}\right.$ 1.2 [128], the luminosities are listed in Table 4.1. The efficiency $\epsilon_{\text{PID|sel}}$ is $(74.15 \pm 0.98)\%$ for $\overline{B}^0 \to D^0 p\overline{p}$ events and $(91.72 \pm 1.21)\%$ for $\overline{B}^0 \to D^0\pi^+\pi^-$ events.

4.5.3 L0 trigger efficiency

In this analysis, the L0 trigger decisions `L0Hadron_TOS` or `L0Global_TIS` is used. It has been found that the simulation does not reproduce the trigger performance for the `L0Hadron` trigger correctly. Therefore, efficiency tables for the `L0Hadron_TOS` efficiency are provided by the *Calorimeter Objects Tools Group* [129] which allow reweighting simulated events to account for differences in the `L0Hadron` trigger performance between simulation and data. The available tables depend on the particle type, the charge of the particle, the year of the data taking period and the magnet polarity, storing the `L0Hadron` trigger efficiency as a function of p_{T} or E_{T} for individual tracks. The calibration samples for pions and kaons come from D^0 meson decays of D^* decays and the samples for protons from Λ decays. A problem with the efficiency tables for protons had been observed during the analysis of $\Lambda_b^0 \to D^0 p\pi^-$ decays. Therefore, efficiency tables for protons are also available from $\Lambda_b^0 \to \Lambda_c^+\pi^-$ decays, covering a larger p_{T} range. The efficiency for triggering on the event is calculated as follows, *e.g.* for a

Table 4.11: L0Hadron_TOS efficiency for $\overline{B}^0 \to D^0 p\overline{p}$ and $\overline{B}^0 \to D^0\pi^+\pi^-$ events using correction tables.

	$\overline{B}^0 \to D^0 p\overline{p}$		$\overline{B}^0 \to D^0\pi^+\pi^-$	
magnet polarity	*MagUp*	*MagDown*	*MagUp*	*MagDown*
2011	$(53.19 \pm 0.63)\%$	$(55.05 \pm 0.65)\%$	$(57.72 \pm 0.67)\%$	$(58.03 \pm 0.68)\%$
2012	$(51.09 \pm 0.60)\%$	$(51.65 \pm 0.61)\%$	$(52.61 \pm 0.61)\%$	$(52.77 \pm 0.62)\%$
$\epsilon_{\text{L0}}^{\text{TOS}}$	$(52.21 \pm 0.62)\%$		$(54.21 \pm 0.63)\%$	

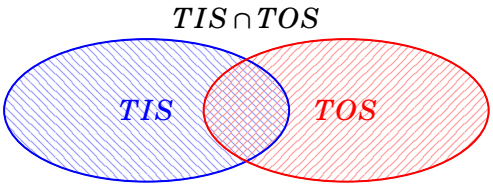

Figure 4.19: Schematic diagram of the TIS and TOS trigger decision.

two-body decay $B \to p_1 p_2$

$$\epsilon^{\text{TOS}} = \epsilon(p_{\text{T}}, p_1) * [1 - \epsilon(p_{\text{T}}, p_2)] + \epsilon(p_{\text{T}}, p_2) * [1 - \epsilon(p_{\text{T}}, p_1)] + \epsilon(p_{\text{T}}, p_1) * \epsilon(p_{\text{T}}, p_2) \,. \tag{4.27}$$

The first term describes the efficiency of triggering on p_1 and not on p_2, the second the efficiency of triggering on p_2 and not on p_1, and the third the efficiency for triggering on both p_1 and p_2. Transferring this procedure to a decay of four final state particles, the L0Hadron_TOS efficiency can be calculated as

$$\epsilon^{\text{TOS}} = 1 - \prod_{4}^{i=1} (1 - \epsilon(p_{\text{T}}, p_i)) \,, \tag{4.28}$$

where the product term describes the efficiency that none of the final state particles fired the trigger. This procedure works well for two-body decays as they fire the trigger independently but cannot account for overlap in multi-body decays. Therefore, the L0Hadron_TOS efficiency is calculated using the correction tables and then compared to the efficiency obtained from data.

Assuming a negligible contribution of overlapping and using the Λ_b^0 efficiency tables for protons results in Table 4.11, the L0Hadron_TOS trigger efficiency is determined using 2011 and 2012 efficiency tables. The overall L0Hadron_TOS trigger efficiency for both years is then calculated as for the PID efficiency (see equation 4.26). The $\epsilon_{\text{L0}}^{\text{TOS}}$ efficiency is $(52.21 \pm 0.62)\%$ for $\overline{B}^0 \to D^0 p\overline{p}$ decays and $(54.21 \pm 0.63)\%$ for $\overline{B}^0 \to D^0\pi^+\pi^-$ decays.

The L0Hadron_TOS efficiency can be calculated from data using the so-called TIS-

TOS method [130]. The efficiency for the TOS trigger is then calculated as $\epsilon^{\text{TOS}} = N(\text{TOS\&TIS})/N(\text{TIS})$, where the TIS sample satisfies the `L0Hadron_TIS` trigger selection but not the TIS trigger selection of the HLT1 and the HLT2. For $\overline{B}^0 \to D^0 p\overline{p}$ decays, the number of events satisfying the `L0Hadron_TOS&L0Global_TIS` trigger decision is 734 ± 32, and the number of events for the `L0Global_TIS` trigger selection is 2464 ± 58. The number of events that fulfil the `L0Hadron_TOS&&L0Global_TIS` trigger decision for $\overline{B}^0 \to D^0\pi^+\pi^-$ decays is 9903 ± 121, for the `L0Global_TIS` trigger requirement 29209 ± 213. That gives a `L0Hadron_TOS` trigger efficiency of $(29.79 \pm 1.48)\%$ for $\overline{B}^0 \to D^0 p\overline{p}$ decays and $(33.91 \pm 0.48)\%$ for $\overline{B}^0 \to D^0\pi^+\pi^-$ decays. As the values for the `L0Hadron_TOS` efficiency obtained from efficiency tables and those obtained from data differ significantly, the trigger efficiency obtained from data is taken for the branching fraction measurement.

A schematic diagram for the L0 trigger decision is shown in Figure 4.19. An event can be triggered on the signal and is `L0Hadron_TOS` or independent of the signal and is `L0Global_TIS`, but it can also trigger on both and is `L0Hadron_TOS&&L0Global_TIS`. The trigger efficiency for `L0Hadron_TOS` or `L0Global_TIS` is

$$\epsilon_{\text{L0}}^{\text{TIS||TOS}} = \frac{N_{\text{TIS}} + N_{\text{TOS\&\&!TIS}}}{N_0} = \epsilon^{\text{TIS}} + \epsilon^{\text{TOS\&\&!TIS}} \tag{4.29}$$

$$= \frac{N_{\text{TIS}}}{N_{\text{TOS}}} \times \frac{N_{\text{TOS}}}{N_0} + \frac{N_{\text{TOS\&\&!TIS}}}{N_{\text{TOS}}} \times \frac{N_{\text{TOS}}}{N_0} \tag{4.30}$$

$$= \frac{N_{\text{TIS}}}{N_{\text{TOS}}} \times \epsilon^{\text{TOS}} + \frac{N_{\text{TOS\&\&!TIS}}}{N_{\text{TOS}}} \times \epsilon^{\text{TOS}} \tag{4.31}$$

$$= (g + f) \times \epsilon^{\text{TOS}}, \tag{4.32}$$

with

$$f = \frac{N_{\text{TOS\&\&!TIS}}}{N_{\text{TOS}}}, \tag{4.33}$$

and

$$g = \frac{N_{\text{TIS}}}{N_{\text{TOS}}}. \tag{4.34}$$

The values for f and g can be determined by extracting the values for N_{TIS}, N_{TOS} and $N_{\text{TOS\&\&!TIS}}$ from data. The results are shown in Table 4.12. The total L0 trigger efficiency is then $(51.63 \pm 2.87)\%$ for $\overline{B}^0 \to D^0 p\overline{p}$ decays and $(55.03 \pm 0.91)\%$ for $\overline{B}^0 \to D^0\pi^+\pi^-$ decays.

Table 4.12: Parameters $f = N_{\text{TOS\&\&!TIS}}/N_{\text{TOS}}$ and $g = N_{\text{TIS}}/N_{\text{TOS}}$ for both decay modes

	$\overline{B}^0 \to D^0 p\overline{p}$	$\overline{B}^0 \to D^0 \pi^+\pi^-$
f	0.688 ± 0.026	0.680 ± 0.008
g	1.045 ± 0.035	0.943 ± 0.010

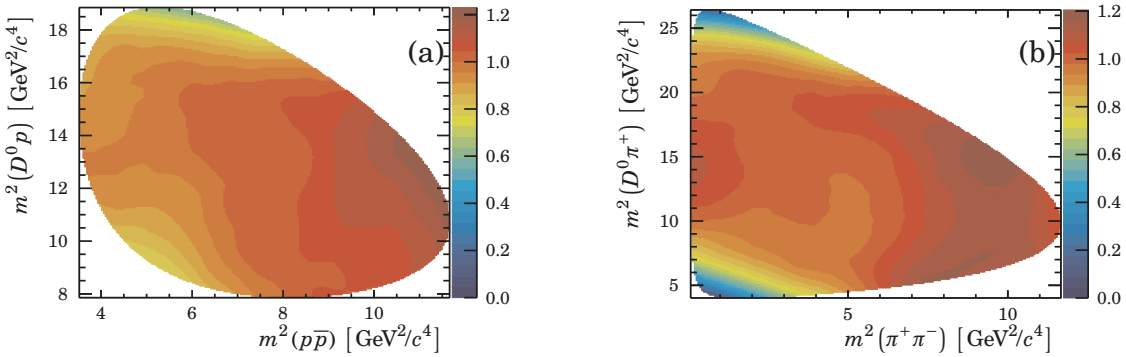

Figure 4.20: Distribution of the total efficiency over the Dalitz plane for (a) $\overline{B}^0 \to D^0 p\overline{p}$ decays and (b) $\overline{B}^0 \to D^0\pi^+\pi^-$ decays without L0 trigger efficiency.

4.5.4 Efficiency distribution in the Dalitz plane

The efficiency of an event can depend on the position of the Dalitz plane. The distribution of the total efficiency as a function of the Dalitz plane $\epsilon\left(m^2_{D^0h}, m^2_{hh}\right)$ is shown in Figure 4.20. To produce the Figure, the `Meerkat` package [131] is used. It uses a kind of kernel density estimation technique to describe the Dalitz plane. The efficiency over the Dalitz plane is normalised that way that the average efficiency over the Dalitz plane is equal to one. Additional plots for the efficiency distribution over the Dalitz plane can be found in Appendix F. Note, that the trigger efficiency has been calculated from data and is not included in Figure 4.20

$$\epsilon\left(m^2_{D^0h}, m^2_{hh}\right) = \epsilon_{\text{acc|gen}}\left(m^2_{D^0h}, m^2_{hh}\right) \times \epsilon_{\text{sel|acc}}\left(m^2_{D^0h}, m^2_{hh}\right) \times \epsilon_{\text{PID|sel}}\left(m^2_{D^0h}, m^2_{hh}\right). \tag{4.35}$$

4.5.5 Efficiency correction according to the Dalitz distribution

Simulated events were produced with a uniform distribution over the Dalitz plane. The *sPlot* method [106] (see Appendix E.2) is a tool to visualise the signal component in a fit with signal and one or more background components. The *sWeighted*

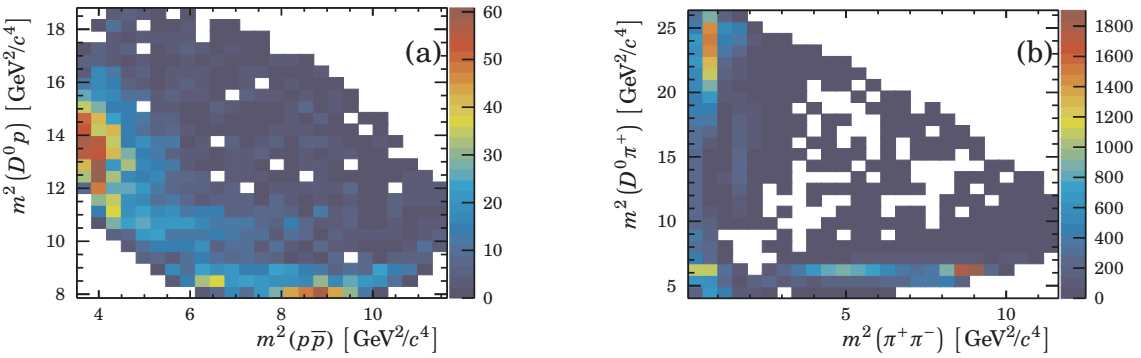

Figure 4.21: Dalitz distribution of *sweighted* events for (a) $\overline{B}^0 \to D^0 p\overline{p}$ decays and (b) $\overline{B}^0 \to D^0\pi^+\pi^-$ decays.

Dalitz planes for $\overline{B}^0 \to D^0 p\overline{p}$ decays and $\overline{B}^0 \to D^0\pi^+\pi^-$ decays, produced using the *sPlot* technique with `RooStats` [132], show some structures as can be seen in Figure 4.21. Detailed information about the resonances in $\overline{B}^0 \to D^0\pi^+\pi^-$ decays can be found elsewhere [61, 105, 133]. Structures in the Dalitz plane of $\overline{B}^0 \to D^0 p\overline{p}$ decays will be discussed in Chapter 5. The correction factor will not include a correction for the distribution of the trigger efficiency as this efficiency was calculated from data.

The total efficiency as a function of the Dalitz plane can be used to calculate the average efficiency over the Dalitz plane

$$\bar{\epsilon} = \frac{\sum_{i=0}^{n} w_i}{\sum_{i=0}^{n} w_i/\epsilon\left(m^2_{D^0h}, m^2_{hh}\right)} \tag{4.36}$$

$$= \epsilon \times < C_{\mathrm{DP}} > , \tag{4.37}$$

where n is the number of events in the fit range and w_i the signal *sWeight* assigned to each candidate in the fit range. The correction factor for the efficiencies calculated from simulation is $(97.48 \pm 2.44)\%$ for $\overline{B}^0 \to D^0 p\overline{p}$ events and $(78.47 \pm 0.64)\%$ for $\overline{B}^0 \to D^0\pi^+\pi^-$ events. The error only includes the statistical error of the *sWeights*.

4.5.6 Total efficiency

All efficiencies are summarised in Table 4.13. The total efficiency with correction for the Dalitz structures is $(12.85 \pm 0.81) \times 10^{-4}$ for the $\overline{B}^0 \to D^0 p\overline{p}$ decays and $(14.53 \pm 0.38) \times 10^{-4}$ for $\overline{B}^0 \to D^0\pi^+\pi^-$ decays.

Table 4.13: Summary of the efficiencies for $\overline{B}^0 \to D^0 p\overline{p}$ and $\overline{B}^0 \to D^0\pi^+\pi^-$ events.

efficiency	$\overline{B}^0 \to D^0 p\overline{p}$	$\overline{B}^0 \to D^0\pi^+\pi^-$
$\epsilon_{\text{acc\|gen}}$	$(18.22 \pm 0.03)\%$	$(15.81 \pm 0.03)\%$
$\epsilon_{\text{sel\|acc}}$	$(1.89 \pm 0.02)\%$	$(2.32 \pm 0.03)\%$
$\epsilon_{\text{PID\|sel}}$	$(74.15 \pm 0.98)\%$	$(91.72 \pm 1.21)\%$
$\epsilon_{L0\text{\|PID}}$	$(51.63 \pm 2.87)\%$	$(55.03 \pm 0.91)\%$
ϵ	$(13.18 \pm 0.77) \times 10^{-4}$	$(18.51 \pm 0.46) \times 10^{-4}$
C_{DP}	$(97.48 \pm 2.44)\%$	$(78.47 \pm 0.64)\%$
ϵ_{tot}	$(12.85 \pm 0.81) \times 10^{-4}$	$(14.53 \pm 0.38) \times 10^{-4}$

4.6 Systematic uncertainties

In general, every measurement is affected by statistical and systematic errors. Statistical errors arise randomly and lead to a distribution of results that can be observed by repeating the experiment. Systematic errors can occur, *e.g.* from the measurement instruments or the methods of observation. As the branching fraction of $\overline{B}^0 \to D^0 p\overline{p}$ decays is measured relative to the branching fraction of $\overline{B}^0 \to D^0\pi^+\pi^-$ decays some uncertainties, like the error on the cross-section measurement or on the luminosity measurement, cancel out. This Section will summarise the systematic uncertainties on the efficiency ratio that arise in the measurement of the branching fraction of $\overline{B}^0 \to D^0 p\overline{p}$ decays relative to $\overline{B}^0 \to D^0\pi^+\pi^-$ decays.

4.6.1 Tracking

The efficiency ratio tables for the track reconstruction used to correct for differences in the track reconstruction efficiency between data and simulation are determined using a clean sample of $J/\psi \to \mu^+\mu^-$ decays. The efficiency ratios shown in Figure 4.18 have an overall systematic uncertainty of 0.4% [125] coming from the differences in the efficiency ratios when reweighting the simulated events in parameters where the parameter distribution differs for data and simulation. Such parameters are, *e.g.* the number of primary vertices or the number of hits or tracks in the different subdetectors. The method to calculate the track reconstruction efficiency uses long track muons reaching the muon stations which are not sensitive to effects of the hadronic interaction. However, hadrons are mostly affected by the hadronic interaction and therefore 1.4% systematic uncertainty has to be added for kaons and pions to take into account interactions with the material so that the systematic uncertainty is 1.5%. The description of the hadronic interaction with material in simulation is less accurate for baryons than for mesons. The systematic uncertainty for protons is therefore 4% as

used in the analyses of $B^+ \to p\overline{\Lambda}$ [134] and $B^0_{(s)} \to p\overline{p}hh'$ [135].

The track efficiency correction factor was used in Section 4.5.1 to correct the selection efficiency. The correction factor used for the tracking efficiency in simulation was calculated to be 1.031 ± 0.007 for simulated events of $\overline{B}^0 \to D^0 p\overline{p}$ decays and 1.041 ± 0.007 for simulated events of $\overline{B}^0 \to D^0 \pi^+ \pi^-$ decays. The total systematic uncertainty is calculated by adding the uncertainties per track linearly. The total systematic uncertainty for the track reconstruction efficiency is therefore 11% for $\overline{B}^0 \to D^0 p\overline{p}$ decays and 6% for $\overline{B}^0 \to D^0 \pi^+ \pi^-$ decays. For the branching fraction measurement, only the ratio of these values is relevant as these values correct the selection efficiencies and the $\overline{B}^0 \to D^0 p\overline{p}$ branching fraction is measured relative to the $\overline{B}^0 \to D^0 \pi^+ \pi^-$ branching fraction. The systematic uncertainty can be estimated using following assumption

$$\frac{r_1}{r_2} = \frac{1+\delta_1}{1+\delta_2} \simeq (1+\delta_1) \times (1-\delta_2) \simeq 1 + (\delta_1 - \delta_2) = 1 + (r_1 - r_2)\,, \tag{4.38}$$

where r_i is the efficiency ratio. The maximal deviation from the ratio taken for the branching fraction measurement obtained by varying the tracking efficiency correction factor within their systematic uncertainty is 0.0522. The systematic uncertainty is therefore taken as 5.22%.

4.6.2 Selection

The variables used as input for the multivariate analysis of the decays $\overline{B}^0 \to D^0 p\overline{p}$ and $\overline{B}^0 \to D^0 \pi^+ \pi^-$ have a good data-simulation agreement. To achieve this agreement the variables for $\overline{B}^0 \to D^0 p\overline{p}$ phase-space simulated events were weighted according to the Dalitz distribution observed in data. No systematic uncertainty is assigned to the training of the multivariate analysis.

Data were used to find the best cut values of the PID variables and the FisherG response. To check whether this method biases the branching ratio measurement, the datasets are pseudo-randomly divided into two samples which are then used to repeat the procedure for finding the best cut value. The results are shown in Figure 4.22. The obtained values are in agreement with the ones derived from Figure 4.8. The decay $\overline{B}^0 \to D^0 p\overline{p}$ has less statistics which leads to larger fluctuations in the bins. The results obtained are similar to those obtained in Section 4.2.5.

As a next step, the FisherG response cut is increased from to greater than -0.2 to greater than 0.1 in steps of 0.1 while the PID cut is kept constant. First, the cut for $\overline{B}^0 \to D^0 \pi^+ \pi^-$ decays is kept constant and the cut for the $\overline{B}^0 \to D^0 p\overline{p}$ FisherG response is changed and then the cut for $\overline{B}^0 \to D^0 p\overline{p}$ decays is kept constant and the cut for the $\overline{B}^0 \to D^0 \pi^+ \pi^-$ FisherG response is increased stepwise. This affects the branch-

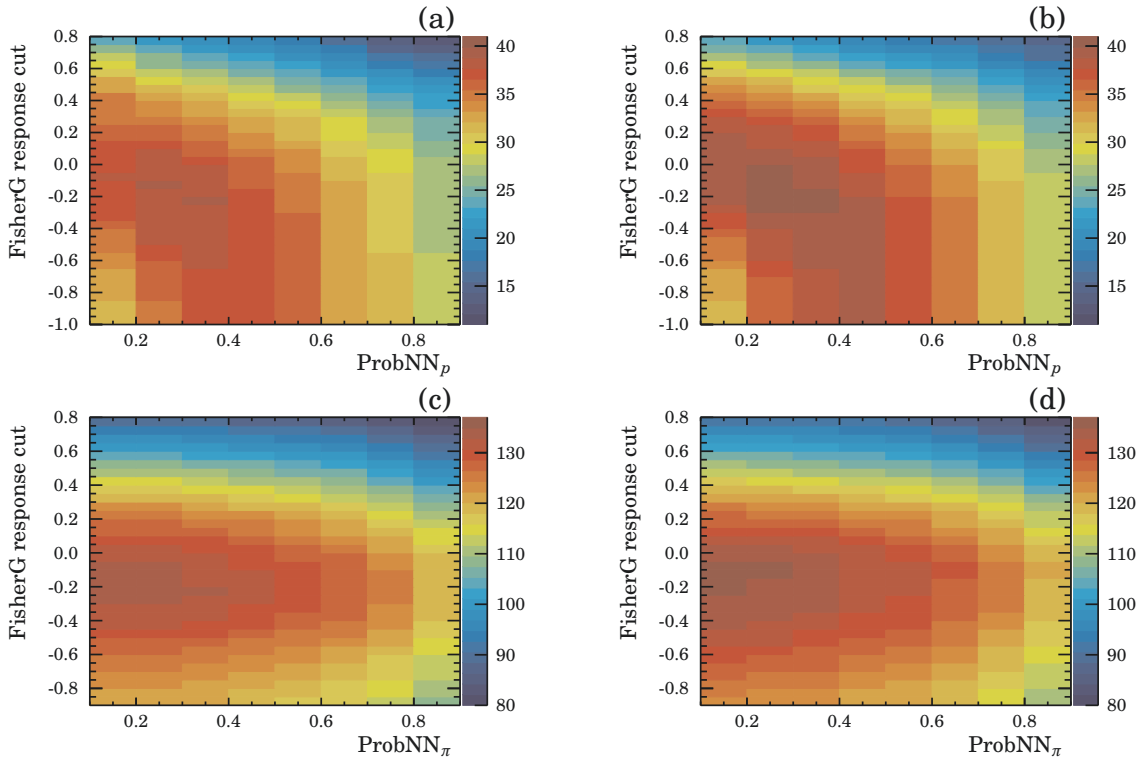

Figure 4.22: Selection optimization for (a-b) $\overline{B}^0 \to D^0 p\overline{p}$ events and (c-d) $\overline{B}^0 \to D^0\pi^+\pi^-$ events using two pseudo-randomly divided samples.

ing ratio measurement by less than 0.4%. Then, the PID cut is increased to ProbNN$_p$ (ProbNN$_\pi$) greater than 0.3 while the FisherG response cut is kept constant. The systematic uncertainty is less than 0.2%. A systematic uncertainty of 0.60% is assigned to the selection efficiency.

No systematic uncertainty is assigned to the selection efficiency accounting for differences in the variables used to select the decays $\overline{B}^0 \to D^0 p\overline{p}$ and $\overline{B}^0 \to D^0\pi^+\pi^-$ in the datasets of 2011 and 2012 as they are in good agreement (see Appendix A.2).

4.6.3 Trigger

As stated before, simulated events are known not to describe the trigger efficiency correctly. Trigger efficiency tables obtained from data are therefore available to determine the trigger efficiency. As the TOS trigger efficiency obtained with the trigger efficiency tables and data differ significantly, it has been decided to obtain the trigger efficiency completely from data. Therefore, no systematic error is assigned to the trigger efficiency.

4.6.4 Particle identification

The systematic uncertainty for the particle identification efficiency has to be considered for the relative branching fraction measurement when one or more final state particles have a different type. Since the D^0 decay mode for both decays is the same and the same PID selection criteria are applied, this systematic uncertainty cancels out. Only the systematic uncertainty for the baryons (pions) originating directly from the $\overline{B}^0$ meson has to be considered.

There are two sources for systematic uncertainties coming from the method to derive the particle identification efficiencies. The first source comes from the *sWeighting* method used in the PIDCalib package. This systematic uncertainty is at least 0.1% [136]. The second source for systematic uncertainties is the choice of the binning scheme and the variables used. In this thesis p and η were used to derive the particle identification efficiency because the statistics for the $\Lambda_c^+ \to pK^-\pi^+$ calibration sample is limited. For smaller calibration sample sizes the systematic uncertainty might be larger since the binning has to be wider. The systematic uncertainty is determined using a higher number of bins to determine the efficiencies in the p-η plane and by comparing the result to the former bining schema. A systematic uncertainty for the binning scheme of 0.7% is assigned to the protons and of 0.2% to the pions. The systematic uncertainty of 1.80% is derived by adding the uncertainties linearly.

4.6.5 Fit model

The toy study done in Section 4.4.1 shows that the fit is not biased. Largest influence on the branching ratio measurement has the determination of the signal events. To get the number of signal events, simulated events were fitted to get the shape of the signal candidates, and four parameters of the signal shape were fixed in the fit to data. This can affect the number of signal events found in the fit to data.

The systematic uncertainty will be determined by rerunning the fit without fixed parameters. The number of signal events changes to 4035 ± 89 for $\overline{B}^0 \to D^0 p\overline{p}$ decays and to 49152 ± 468 for $\overline{B}^0 \to D^0\pi^+\pi^-$ decays. For the branching fractions measurement, the important value is the change of the ratio of the number of events. Letting the values for the signal shape float changes the ratio of the number of events by less than 0.2%. The shape of background events is taken from simulation, which might not be perfect. To account for shape differences of mass shifts, the background shapes are shifted along the B mass. For $\overline{B}^0 \to D^0 p\overline{p}$ decays the $\overline{B}^0 \to D^{*0} p\overline{p}$ are allowed to have unequal shifts to higher or lower B mass values. The highest observed number of events for $\overline{B}^0 \to D^0 p\overline{p}$ decays is 4119 ± 83. A similar procedure is applied for the fit of $\overline{B}^0 \to D^0\pi^+\pi^-$ decays. Background shapes are allowed to shift individually along

Table 4.14: Summary of systematic uncertainties.

source	systematic uncertainty
tracking	5.22%
selection	0.60%
PID	1.80%
fit model	0.23%
total systematic uncertainty	5.56%

the x-axis, only $\overline{B}^0 \to D^0 K^- \pi^+$ and $\overline{B}^0_s \to D^0 K^+ \pi^-$ background shapes are expected to have the same shift. The number of events for $\overline{B}^0 \to D^0 \pi^+ \pi^-$ decays changes then to 50663 ± 459. The ratio of the number of events can maximally change by less than 0.1%. The total systematic uncertainty for the fit model is obtained by adding the uncertainties in quadrature, which results in a total systematic uncertainty of 0.23%.

4.6.6 Total systematic uncertainty

All systematic uncertainties which will be considered in the branching fraction measurement of $\overline{B}^0 \to D^0 p\overline{p}$ decays relative to $\overline{B}^0 \to D^0 \pi^+ \pi^-$ decays are listed in Table 4.14. The total systematic uncertainty is 5.56%.

4.7 Branching fraction calculation

In conclusion to this Chapter, the branching fraction of $\overline{B}^0 \to D^0 p\overline{p}$ decays relative to $\overline{B}^0 \to D^0 \pi^+ \pi^-$ decays can be calculated from data taken by the LHCb experiment during the years 2011 and 2012 with an integrated luminosity of $3\,\text{fb}^{-1}$. The branching fraction can be determined using equation 4.5. Since the *Stripping* selections of both decays have different *Stripping* versions and a small difference in the luminosity (see Tables 4.1 and 4.2) can be observed. This difference needs to be taken into account

$$\frac{\mathcal{B}\left(\overline{B}^0 \to D^0 p\overline{p}\right)}{\mathcal{B}\left(\overline{B}^0 \to D^0 \pi^+ \pi^-\right)} = \frac{N\left(\overline{B}^0 \to D^0 p\overline{p}\right) \times \epsilon_{\text{tot}}\left(\overline{B}^0 \to D^0 \pi^+ \pi^-\right)}{N\left(\overline{B}^0 \to D^0 \pi^+ \pi^-\right) \times \epsilon_{\text{tot}}\left(\overline{B}^0 \to D^0 p\overline{p}\right)} \times \frac{\mathcal{L}_{\overline{B}^0 \to D^0 \pi^+ \pi^-}}{\mathcal{L}_{\overline{B}^0 \to D^0 p\overline{p}}} . \tag{4.39}$$

The relative branching fraction is then

$$\frac{\mathcal{B}\left(\overline{B}^0 \to D^0 p\overline{p}\right)}{\mathcal{B}\left(\overline{B}^0 \to D^0 \pi^+ \pi^-\right)} = (9.2 \pm 0.7\,(\text{stat}) \pm 0.6\,(\text{syst})) \times 10^{-2} , \tag{4.40}$$

where the first uncertainty is the statistical uncertainty and the second uncertainty the systematic uncertainty.

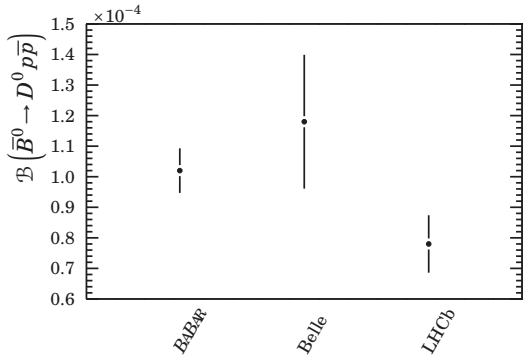

Figure 4.23: Comparison of the branching fraction measurement from *BABAR*, Belle and the result of this thesis.

The branching fraction for $\overline{B}^0 \to D^0 p\overline{p}$ decays can then be calculated using the measured branching fraction of $\overline{B}^0 \to D^0\pi^+\pi^-$ decays. The LHCb result $\mathcal{B}\left(\overline{B}^0 \to D^0\pi^+\pi^-\right) = (8.46 \pm 0.14\,(\text{stat}) \pm 0.29\,(\text{syst}) \pm 0.40(\text{norm})) \times 10^{-4}$ [61] measured in the kinematic region $m\left(D^0\pi\right) > 2.1\,\text{GeV}/c^2$ is currently the most precise value for this branching fraction. The first uncertainty is statistical, the second is systematic, and the last arises from the normalisation channel $\overline{B}^0 \to D^*(2010)^+\pi^-$. The approximation to the full phase-space is $\mathcal{B}\left(\overline{B}^0 \to D^0\pi^+\pi^-\right) = (8.95 \pm 0.15\,(\text{stat}) \pm 0.52\,(\text{syst})) \times 10^{-4}$ [4]. The world average for the branching fraction of $\overline{B}^0 \to D^0\pi^+\pi^-$ decays is at the moment $\mathcal{B}\left(\overline{B}^0 \to D^0\pi^+\pi^-\right) = (8.8 \pm 0.5) \times 10^{-4}$ [4]. The branching fraction of $\overline{B}^0 \to D^0 p\overline{p}$ decays, using the world's average for the $\overline{B}^0 \to D^0\pi^+\pi^-$ branching fraction, is

$$\mathcal{B}\left(\overline{B}^0 \to D^0 p\overline{p}\right) = (0.81 \pm 0.06\,(\text{stat}) \pm 0.06\,(\text{syst}) \pm 0.05(\text{norm})) \times 10^{-4}\,, \tag{4.41}$$

where the last uncertainty comes from the normalisation channel. Previous measurements from the *BABAR* experiment resulted in $\mathcal{B}\left(\overline{B}^0 \to D^0 p\overline{p}\right) = (1.02 \pm 0.04\,(\text{stat}) \pm 0.06\,(\text{syst})) \times 10^{-4}$ (*BABAR*) [6]; Belle's measurement is $\mathcal{B}\left(\overline{B}^0 \to D^0 p\overline{p}\right) = (1.18 \pm 0.15\,(\text{stat}) \pm 0.16\,(\text{syst})) \times 10^{-4}$ (Belle) [19]. Figure 4.23 visualised the different branching fraction measurements for $\overline{B}^0 \to D^0 p\overline{p}$ decays. The branching fraction measurement of this thesis deviates by about 2σ from the measurement of the *BABAR* experiment. This result will be further discussed in Chapter 6.

CHAPTER 5

Dalitz structures

This Chapter discusses the structures in the Dalitz plane in $\overline{B}^0 \to D^0 p\overline{p}$ decays visible in the data from the first physics run of the LHCb experiment.

5.1 Kinematics of the three-body decay

Heavy meson decays to three-body final states are often dominated by intermediate resonances which can be described by the Dalitz plot technique [137, 138]. In contrast to two-body decays, which can be completely determined in the centre-of-mass frame by using the conservation of energy and momentum, three-body decays are more complex. The particle decay $\overline{B}^0 \to D^0 p\overline{p}$ in the rest frame of the $\overline{B}^0$ meson can be expressed by four four-vectors: $p_{\overline{B}^0}(m_{\overline{B}^0}, \vec{0})$, $p_{D^0}(E_{D^0}, \vec{p}_{D^0})$, $p_p(E_p, \vec{p}_p)$, and $p_{\overline{p}}(E_{\overline{p}}, \vec{p}_{\overline{p}})$. Twelve parameters describe the three-body decay but can be reduced using information about the particle system:

- the masses of the final state particles m_{D^0}, m_p, and $m_{\overline{p}}$ are known, removing three degrees of freedom
- energy and momentum are conserved. This removes four degrees of freedom.
- The $\overline{B}^0$ meson has spin 0; the final state particles decay in the same plane. This fact removes three additional degrees of freedom.

There are then two remaining degrees of freedom, which can be chosen to be the invariant mass squared of the final state particles. These variables are called Dalitz variables, and their distribution is called the Dalitz plot. The invariant masses squared of the $\overline{B}^0 \to D^0 p\overline{p}$ final state particles are defined as

$$\begin{aligned} &m^2_{D^0 p} \equiv \left(p_{D^0} + p_p\right)^2, \quad m^2_{D^0\overline{p}} \equiv \left(p_{D^0} + p_{\overline{p}}\right)^2 \\ &\text{and} \quad m^2_{p\overline{p}} \equiv \left(p_p + p_{\overline{p}}\right)^2 . \end{aligned} \tag{5.1}$$

They are related to each other by the following equation

$$m^2_{p\overline{p}} = m^2_{B^0} + m^2_{D^0} + m^2_p + m^2_{\overline{p}} - \left(m^2_{D^0 p} + m^2_{D^0\overline{p}}\right) . \tag{5.2}$$

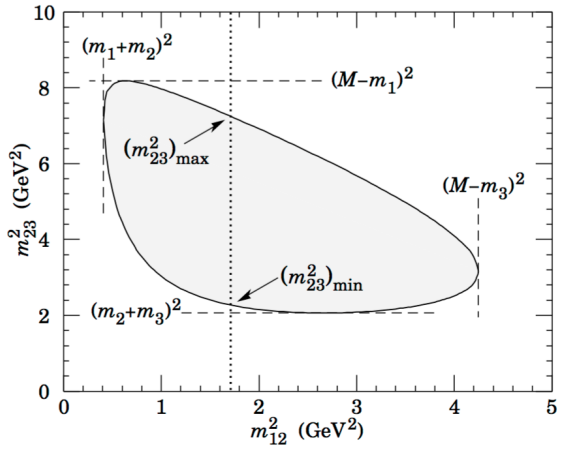

Figure 5.1: Dalitz plot for a three-body final state. In this example, the state is $\pi^+\overline{K}^0 p$ at 3 GeV. Four-momentum conservation restricts events to the shaded region. Taken from [4].

An example of the Dalitz plot boundaries of a three-body decay is shown in Figure 5.1.

The partial decay rate of the three-body decay can be written as

$$\mathrm{d}\Gamma = \frac{(2\pi)^4}{2m_{B^0}} |\mathcal{A}|^2 \, \mathrm{d}\Phi_3 \left(p_{B^0}, p_{D^0}, p_p, p_{\overline{p}}\right) , \tag{5.3}$$

where $\mathcal{A}$ is the matrix element describing the decay amplitude and $\mathrm{d}\Phi_3$ is an element that describes the three-body phase space

$$\mathrm{d}\Phi_3 \left(p_{B^0}, p_{D^0}, p_p, p_{\overline{p}}\right) = \delta\left(m_{B^0} - \left(E_{D^0} + E_p + E_{\overline{p}}\right)\right) \frac{\mathrm{d}^3 p_{D^0}}{E_{D^0}} \frac{\mathrm{d}^3 p_p}{E_p} \frac{\mathrm{d}^3 p_{\overline{p}}}{E_{\overline{p}}} . \tag{5.4}$$

The invariant masses of the three-body decay $\overline{B}^0 \to D^0 p \overline{p}$ can also be used to rewrite the decay rate

$$\mathrm{d}\Gamma = \frac{1}{(2\pi)^3} \frac{1}{32 m^3_{B^0}} |\mathcal{A}|^2 \, \mathrm{d}m^2_{D^0 p} \, \mathrm{d}m^2_{p\overline{p}} . \tag{5.5}$$

This relation indicates that the population of the Dalitz plane depends on the matrix element $\mathcal{A}$. A constant matrix element will uniformly populate the Dalitz plane, because the matrix element $\mathcal{A}$ describes the underlying dynamic of the decay. If the decay has more than one resonant contribution, the decay amplitudes are usually described using the isobar model [139, 140]. The total amplitude is approximated as a coherent sum of complex amplitudes and dynamical functions of resonant and nonres-

onant terms. This relation can be written as

$$\left|\mathcal{A}\left(m^2_{D^0p}, m^2_{p\overline{p}}\right)\right|^2 = \left|\sum_n c_n F_n\left(m^2_{D^0p}, m^2_{p\overline{p}}\right)\right|^2 = \left|\sum_n a_n e^{i\phi_n} F_n\left(m^2_{D^0p}, m^2_{p\overline{p}}\right)\right|^2 , \quad (5.6)$$

where c_n is a complex coefficient with its relative magnitude a_n and its phase ϕ_n, also called the isobar parameters of the component n. The function F_n is a spin-dependent dynamical function which can be decomposed in an invariant mass term and an angular distribution as follows

$$F_n\left(m^2_{D^0p}, m^2_{p\overline{p}}\right) = R_n(M) \times A_n , \quad (5.7)$$

where $R_n(M)$ is the mass term for the resonance n and A_n its function for the angular distribution. The dynamics of a quasi-two-body B^0 decay is described by a modified relativistic Breit-Wigner function $R_n(M)$. The modified relativistic Breit-Wigner function is a relativistic Breit-Wigner function multiplied by angular barrier factors and corrected by Blatt-Weisskopf form factors [141]. The angular distribution term is explained in the next section.

5.1.1 Angular distribution

Various descriptions for the decay amplitudes are available for particles decaying into final states with nonzero spins, as the covariant description [142] or the helicity formalism developed by Jacob and Wick [143–145]. In the helicity formalism, the angular distribution of the decay is modelled using the helicity angle.

The helicity is the projection of the spin s of the particle along the direction of its momentum. It is also the projection of the total angular momentum $\vec{J} = \vec{L} + \vec{s}$ along the direction of the momentum with $\vec{L} = \vec{r} \times \vec{p}$. Here, $\vec{L}$ is the orbital angular momentum, $\vec{r}$ the position of the particle, $\vec{p}$ the momentum of the particle, and $\vec{s}$ the spin angular momentum. The quantum number of the helicity is denoted λ. For a particle of spin s, there are $2s+1$ possible eigenvalues for the helicity $\lambda = -s, -s+1, \ldots, s$. The helicities for the particles of the decay $\overline{B}^0 \to D^0 p\overline{p}$ are $\lambda_{\overline{B}^0} = 0$ and $\lambda_{D^0} = 0$ for the $\overline{B}^0$ meson and the D^0 meson and $\lambda_p = \pm 1/2$ and $\lambda_{\overline{p}} = \pm 1/2$ for the proton and the antiproton. The angle between the direction of the daughter in the parent particle rest frame and the direction of the grandparent particle is called the helicity angle θ (see Figure 5.2). The distribution of $\cos\theta$ depends on the spin and the orbital angular momentum of the decaying resonance. The helicity angle can be calculated by boosting the particle and the grandparent particle into the parent particle rest frame or using following

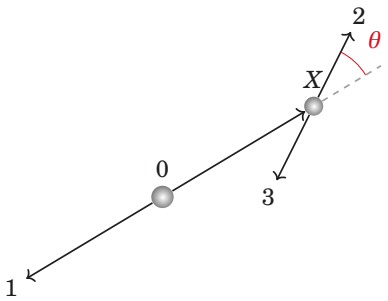

Figure 5.2: Simple decay model $0 \to 1X$ and $X \to 23$ to define the helicity angle.

equation

$$\cos(\theta)_{ij} = \frac{\left(m^2_{jk}\right)_{\max} + \left(m^2_{jk}\right)_{\min} - 2m^2_{jk}}{\left(m^2_{jk}\right)_{\max} - \left(m^2_{jk}\right)_{\min}} . \tag{5.8}$$

In the helicity basis, the amplitude of a two-body decay $p_M \to p_1 p_2$ is

$$\mathcal{A}\left(\theta,\phi,M,\lambda_1,\lambda_2\right) = a\, D^{J*}_{M,\lambda_1-\lambda_2}\left(\phi,\theta,0\right) F^J_{\lambda_1,\lambda_2} , \tag{5.9}$$

where a is a complex number, $F^J_{\lambda_1,\lambda_2}$ is the helicity-coupling Amplitude including a function which describes the dynamics of the decay, usually with a modified Breit-Wigner function, and $D^{J*}_{M,\lambda_1-\lambda_2}$ is Wigner's rotation matrix

$$D^{J*}_{M,\lambda_1-\lambda_2}\left(\phi,\theta,0\right) = e^{i\phi M}\, d^J_{M,\lambda_1-\lambda_2}(\theta) , \tag{5.10}$$

where $d^J_{M,\lambda_1-\lambda_2}(\theta)$ is Wigner's small d-function [146]. In the isobar model, the total amplitude is approximated as a coherent sum of complex amplitudes and dynamical functions of resonant and non-resonant terms. This relation can be written as

$$|\mathcal{A}|^2 = \left|\sum_n \mathcal{A}_n\left(\theta,\phi,M,\lambda_1,\lambda_2\right)\right|^2 . \tag{5.11}$$

When the experiment does not measure the helicities, the differential decay rate is

$$d\Gamma \propto \sum_{\lambda_1,\lambda_2} \left|\sum_n \mathcal{A}_n\left(\theta,\phi,M,\lambda_1,\lambda_2\right)\right|^2 . \tag{5.12}$$

5.2 Expected resonances in $\overline{B}^0 \to D^0 p\overline{p}$ decays

The Feynman diagrams that describe the decay $\overline{B}^0 \to D^0 p\overline{p}$ are shown in Figure 2.6. Figure 2.6 (a) shows the colour-suppressed quark subprocess $b\overline{d} \to (c\overline{u})_{D^0} d\overline{d}$, with a subsequent fragmentation of the $d\overline{d}$ pair into the $p\overline{p}$ pair through the creation of two

additional $u\overline{u}$ pairs. Since the $\overline{d}$ of the antiproton is a spectator quark and the d of the proton is produced in a weak decay, this diagram type can explain an enhancement at the low $p\overline{p}$ mass threshold. Another colour-suppressed mechanism with the $b \to c\overline{u}d$ quark process is shown in Figure 2.6 (c), where the $\overline{u}$ is part of the antiproton and the d part of the proton. It is not expected, that this process could contribute to structures in the $p\overline{p}$ invariant mass, but this diagram can contribute to the creation of a $D^0 p$ resonance. The exchange process $b\overline{d} \to c\overline{u}$ followed by the fragmentation of the $c\overline{u}$ into $D^0 p\overline{p}$ is shown in Figure 2.6 (b), where the $\overline{u}$ is incorporated into the antiproton while the d is incorporated into the proton. This diagram type can be used to describe the creation of a $D^0 p$ resonance. Figure 2.6 (d) shows a different kind of $b\overline{d} \to c\overline{u}$ exchange process where the $p\overline{p}$ pair is produced from the vacuum. This type of diagram could explain a glueball production.

An enhanced rate at the threshold of the baryon-antibaryon mass, the threshold enhancement, has been observed in many baryonic decays as in $B \to D^* N\overline{N}'$ [6, 19, 147], $B^- \to K^- p\overline{p}$ [148, 149], and $\overline{B}^0 \to \Lambda\overline{p}\pi^-$ [150]. The same effect of an enhanced invariant mass spectrum for baryon-antibaryon pairs has been observed from radiative decays of $J/\psi \to \gamma p\overline{p}$ [151]. Several theories try to explain the threshold enhancement. The pole model explains the threshold enhancement with the existence of an intermediate state [9, 10, 152]. Another way to explain the baryon-antibaryon threshold enhancement in the final-state-interaction between the baryon pairs [15–18]. For $p\overline{p}$ pairs, there also exists the idea of forming a bound state like a baryonium or $X(1835)$ [11, 12, 153, 154]. The $X(1835)$ is a candidate for a $N\overline{N}$ bound state. A hint of its existence came up after the observation of the $p\overline{p}$ threshold enhancement in the decay $J/\psi \to \gamma p\overline{p}$ [151]. For the $\overline{B}^0 \to D^0 p\overline{p}$ decay exists the prediction of a glueball in the $p\overline{p}$ mass [155]. This gluonic state of an isoscalar $p\overline{p}$ pair can also be used to explain the threshold enhancement [12, 13].

Known charmed baryons decaying into $D^0 p$ are the $\Lambda_c^+(2880)$ and $\Lambda_c^+(2940)$ baryons. The Belle experiment measured the spin-parity assignment for the $\Lambda_c^+(2880)$ baryon to be $5/2^+$ [156], whereas the spin-parity assignment of the $\Lambda_c^+(2940)$ is unknown. Lately, the LHCb experiment published new results where they set new constraints to the spin and parity of the $\Lambda_c^+(2940)$ [157]. A measurement of the spin-parity assignment of the $\Lambda_c^+(2940)$ is very interesting since relativistic quark model calculations [158–160] predict three excited Λ_c baryons with different spin-parity assignments near a mass of $2.94\,\mathrm{GeV}/c^2$. Since the mass of the $\Lambda_c^+(2940)$ is barely below the threshold of the $D^{*0} p$ production, theories of an exotic molecular state of D^{*0} and p exist for this charmed baryon [161]. The *BABAR* publication of charmed baryon decaying into $D^0 p$ also shows, besides the $\Lambda_c^+(2880)$ and $\Lambda_c^+(2940)$, an unknown structure near $2.84\,\mathrm{GeV}/c^2$ [162]. Such a structure has also been seen by the LHCb experiment.

Table 5.1: Allowed LS-couplings for $p\overline{p}$ resonances and corresponding Wigner d-function.

$++/-$			$+-/-+$		
$^{2s+1}L_j$	J^P	$d^j_{0,\lambda_p-\lambda_{\overline{p}}}(\theta)$	$^{2s+1}L_j$	J^P	$d^j_{0,\lambda_p-\lambda_{\overline{p}}}(\theta)$
$^1S_0$	0^-	$d^0_{0,0}(\theta)=1$	$^3S_1$	1^-	$d^1_{0,\pm1}(\theta)=\mp\sqrt{1/2}\sin\theta$
$^3P_0$	0^+	$d^0_{0,0}(\theta)=1$	$^3P_1$	1^+	$d^1_{0,\pm1}(\theta)=\mp\sqrt{1/2}\sin\theta$
$^1P_1$	1^+	$d^1_{0,0}(\theta)=\cos\theta$	$^3P_2$	2^+	$d^2_{0,\pm1}(\theta)=\mp\sqrt{3/2}\sin\theta\cos\theta$
$^3S_1$	1^-	$d^1_{0,0}(\theta)=\cos\theta$			
$^3P_2$	2^+	$d^2_{0,0}(\theta)=(3\cos^2\theta-1)/2$			

They found a new resonance $\Lambda_c^+(2860)$ with spin 3/2 and positive parity [157].

5.3 The Dalitz plane of $\overline{B}^0 \to D^0 p\overline{p}$ decays

Figure 5.3 (a) shows a scatter plot for the $\overline{B}^0 \to D^0 p\overline{p}$ events selected in Chapter 4. A cut on the B mass $m(D^0 p\overline{p}) \in [5250;5310]\,\text{MeV}/c^2$ is applied to reduce the background events in the Dalitz plot. The scatter plot contains 4013 ± 75 signal events and 1082 ± 8 background events. The grey shaded region represents the kinematically allowed region for $\overline{B}^0 \to D^0 p\overline{p}$ decays. The same plot with other invariant masses on the x-y axis is shown in Appendix G.1. Visible, and not a result of the background events as can be seen in Figures 5.3 (b)-(c), are enhancements at the boundary of the invariant mass squared of the $p\overline{p}$ system and at the boundary of the invariant mass squared of the $D^0 p$ system.

Figure 5.3 shows the expected threshold enhancement behaviour for baryon-antibaryon masses. The maximum of the $p\overline{p}$ enhancement is near $m_{p\overline{p}} = 2\,\text{GeV}/c^2$, also observed in the *BABAR* data for this decay [6]. The graphs in Figure 5.3 are not efficiency corrected since the efficiency distribution over the Dalitz plane is not known for the L0 trigger efficiency as it was derived from data (see Chapter 4). The spin of a $p\overline{p}$ resonance can be either $s \geq 0$ or $s \geq 1$, depending on the helicity combination of the proton and the antiproton. The allowed LS-couplings in the spectroscopic notation and their corresponding Wigner d-function are listed in Table 5.1, including their parity for a mesonic state. In the spectroscopic notation $^{2s+1}L_j$ is s the total spin quantum number, j the total angular momentum quantum number, and L the orbital angular momentum quantum number l written as $S,P,D\ldots$ for $l = 0,1,2\ldots$. The helicity combination $\lambda_p\,\lambda_{\overline{p}}$ is shortened to $++/-$ for $+1/2+1/2/-1/2-1/2$ and to $+-/-+$ for $+1/2-1/2/-1/2+1/2$. The non-resonant contribution of the $p\overline{p}$ system and the resonant part with $j = 0$ result in a flat distribution of the cosine of the helicity angle. Therefore, the asymmetric behaviour of the angular distribution of the $p\overline{p}$ sys-

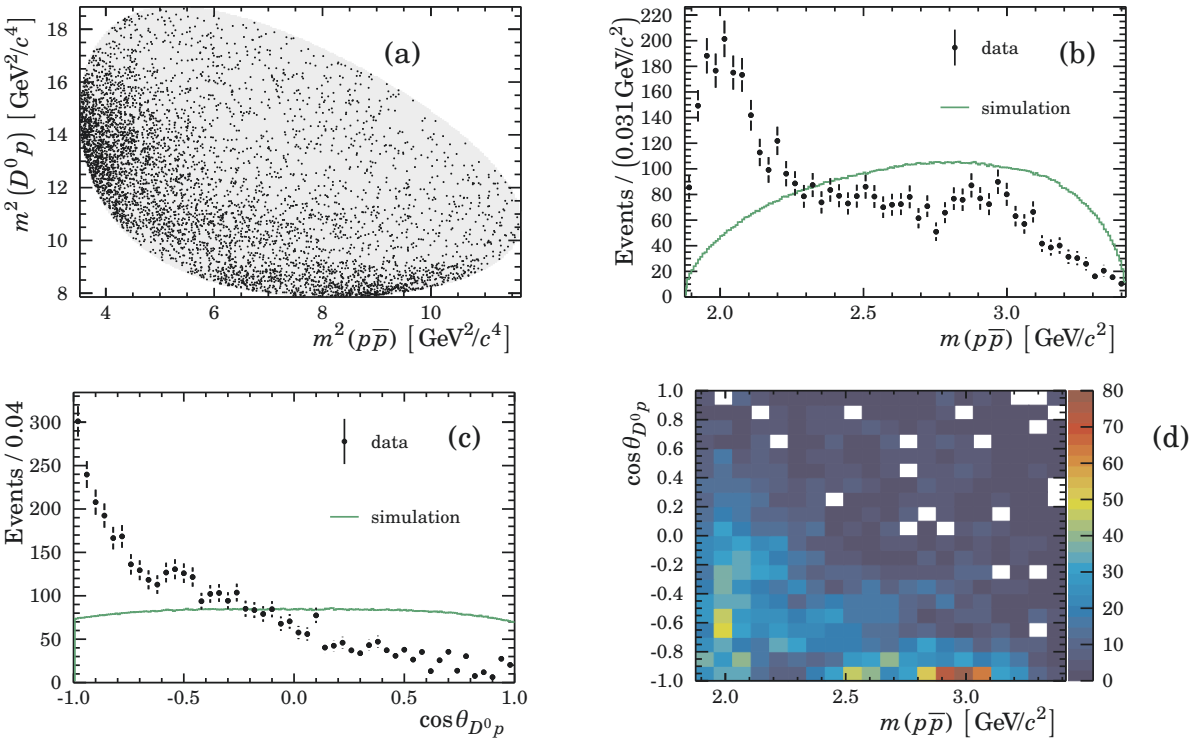

Figure 5.3: (a): Invariant mass squared of the $p\overline{p}$ versus D^0p for events with $m(D^0p\overline{p}) \in [5250;5310]\,\text{MeV}/c^2$. The grey area shows the kinematically allowed region. (b)-(d): Background subtracted distributions for $\overline{B}^0 \to D^0p\overline{p}$ decays using *sWeights*. (b): Projection of the invariant $p\overline{p}$ mass. (c): Angular distribution of the D^0p system in the $p\overline{p}$ rest frame. The green line is the expected shape of phase-space simulated events including selections. (d): Invariant $p\overline{p}$ mass versus $\cos\theta_{D^0p}$ for signal events.

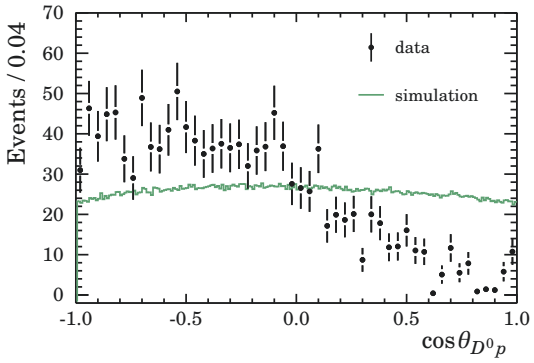

Figure 5.4: Angular distribution of the D^0p system in the $p\overline{p}$ rest frame for events with $m^2_{p\overline{p}} \leq 4.5\,\mathrm{GeV}^2/c^4$. The green line is the expected shape from phase-space simulated events including selections.

tem must result from the interference of resonances with different quantum numbers, different parity. Figure 5.3 (d) suggests that a large contribution in the helicity angle distribution at $\theta_{D^0p} = \pi$ in Figure 5.3 (c) comes from structures at $m^2_{p\overline{p}} > 5\,\mathrm{GeV}^2/c^4$. Figure 5.4 shows the angular distribution of the $p\overline{p}$ system in rest where the $p\overline{p}$ invariant mass is $m^2_{p\overline{p}} \leq 4.5\,\mathrm{GeV}^2/c^4$. A large asymmetry in the angular distribution is still visible.

The angular asymmetry can be calculated as

$$A_{\mathrm{FB}} = \frac{N_{\mathrm{pos}} - N_{\mathrm{neg}}}{N_{\mathrm{pos}} + N_{\mathrm{neg}}} = \frac{N^{\mathrm{raw}}_{\mathrm{pos}} - f N^{\mathrm{raw}}_{\mathrm{neg}}}{N^{\mathrm{raw}}_{\mathrm{pos}} + f N^{\mathrm{raw}}_{\mathrm{neg}}}\,, \tag{5.13}$$

where $N_{\mathrm{pos}} = N(\cos\theta_{D^0p} > 0)$, $N_{\mathrm{neg}} = N(\cos\theta_{D^0p} < 0)$ and $f = <\epsilon_{\mathrm{pos}}> / <\epsilon_{\mathrm{neg}}>$ is the ratio of the average efficiencies in each region, considering only events with $m^2_{p\overline{p}} \leq 4.5\,\mathrm{GeV}^2/c^4$. The efficiencies are determined as described in Section 4.5. The fit procedure to determine $N^{\mathrm{raw}}_{\mathrm{pos}}$ and $N^{\mathrm{raw}}_{\mathrm{neg}}$ is the same as described in Chapter 4. The fit to data and the fit results are shown in Figure 5.5; The parameter α_i and n_i are fixed as done for the branching fraction measurement. The ratio of the average efficiency is $f = 0.977 \pm 0.106$, where the large error results from the correction of the efficiency according to the observed distribution in data and the limited statistics in the region of interest. The reweighting method is the largest contribution to the systematic uncertainties. As it is dominated by the statistical uncertainties no additional systematic uncertainty is added to account for this method. A systematic uncertainty of 5% is added due to the fit method. The observed angular asymmetry for $\overline{B}^0 \to D^0 p\overline{p}$ decays in the region $m^2_{p\overline{p}} \leq 4.5\,\mathrm{GeV}^2/c^4$ is

$$A_{\mathrm{FB}}\left(\overline{B}^0 \to D^0 p\overline{p}\right) = -0.487 \pm 0.098\,(\mathrm{stat}) \pm 0.024\,(\mathrm{syst})\,. \tag{5.14}$$

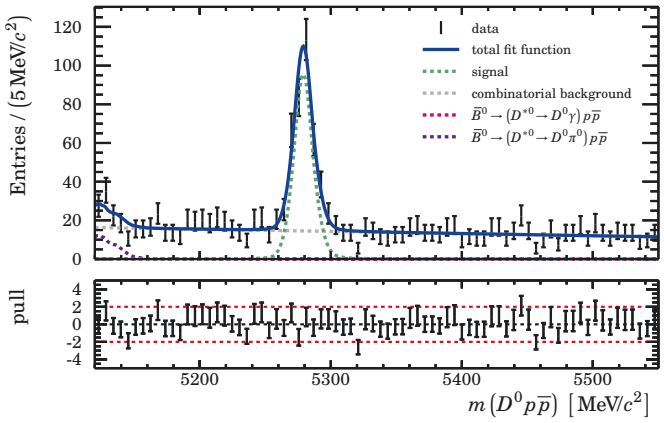

	$\bar{B}^0 \to D^0p\bar{p}$
$\Delta m_{\bar{B}^0 \to D^0hh}$ [MeV/c^2]	-0.7 ± 0.6
σ_1 [MeV/c^2]	8.4 ± 1.7
σ_2 [MeV/c^2]	5.3 ± 1.8
r_{CB}	0.71 ± 0.35
a_{comb}	-0.18 ± 0.06
$\Delta m_{\bar{B}^0 \to D^{*0}hh}$ [MeV/c^2]	-4.3 ± 4.1
$N_{\bar{B}^0 \to D^0hh}$	318 ± 25
$N_{comb.bkg}$	1056 ± 39
$N_{\bar{B}^0 \to D^{*0}hh, D^{*0} \to D^0\gamma}$	0 ± 20
$N_{\bar{B}^0 \to D^{*0}hh, D^{*0} \to D^0\pi^0}$	40 ± 12

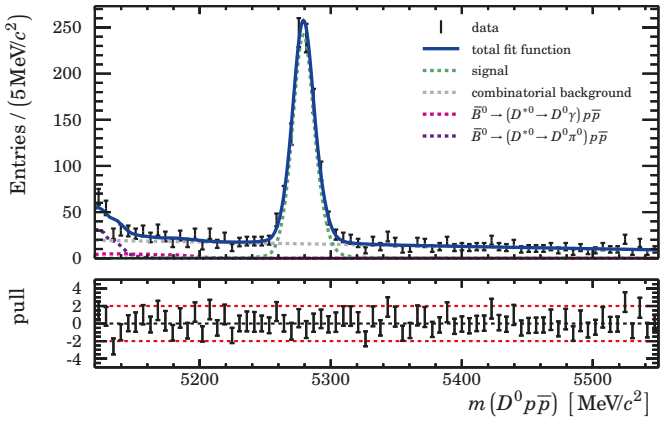

	$\bar{B}^0 \to D^0p\bar{p}$
$\Delta m_{\bar{B}^0 \to D^0hh}$ [MeV/c^2]	-0.6 ± 0.4
σ_1 [MeV/c^2]	9.6 ± 0.7
σ_2 [MeV/c^2]	6.3 ± 1.5
r_{CB}	0.72 ± 0.16
a_{comb}	-0.37 ± 0.07
$\Delta m_{\bar{B}^0 \to D^{*0}hh}$ [MeV/c^2]	-4.9 ± 3.3
$N_{\bar{B}^0 \to D^0hh}$	943 ± 37
$N_{comb.bkg}$	1087 ± 54
$N_{\bar{B}^0 \to D^{*0}hh, D^{*0} \to D^0\gamma}$	59 ± 35
$N_{\bar{B}^0 \to D^{*0}hh, D^{*0} \to D^0\pi^0}$	98 ± 17

Figure 5.5: Top: Fit and fit result for events with $\cos\theta_{D^0p} < 0$ and $m^2_{p\bar{p}} \leq 4.5\,\text{GeV}^2/c^4$. Bottom: Fit and fit result for events with $\cos\theta_{D^0p} > 0$ and $m^2_{p\bar{p}} \leq 4.5\,\text{GeV}^2/c^4$

Structures in the D^0p system are observed for $m_{D^0p} < 3.1\,\text{GeV}/c^2$, and there is also a peak around $m_{D^0p} = 3.3\,\text{GeV}/c^2$ (see Figure 5.6). Baryons decaying into a D^0 meson and a proton are barely known. The narrow resonances $\Lambda_c^+(2880)$ and $\Lambda_c^+(2940)$ are observed to decay into D^0p final states, but these charmed baryons itself cannot explain the structures in $\bar{B}^0 \to D^0p\bar{p}$ decays. A new broad charmed baryon at a mass of about $m_{D^0p} = 3.3\,\text{GeV}/c^2$ is needed to explain the peak in this region. It could even be an interference of more than one charmed baryon as already stated in [7].

5.4 Summary

The structures observed in the Dalitz plane of $\bar{B}^0 \to D^0p\bar{p}$ decays using LHCb date agree with the structures the *BABAR* experiment observed [6]. The threshold enhancement in the $p\bar{p}$ invariant mass must be an interference of resonances so

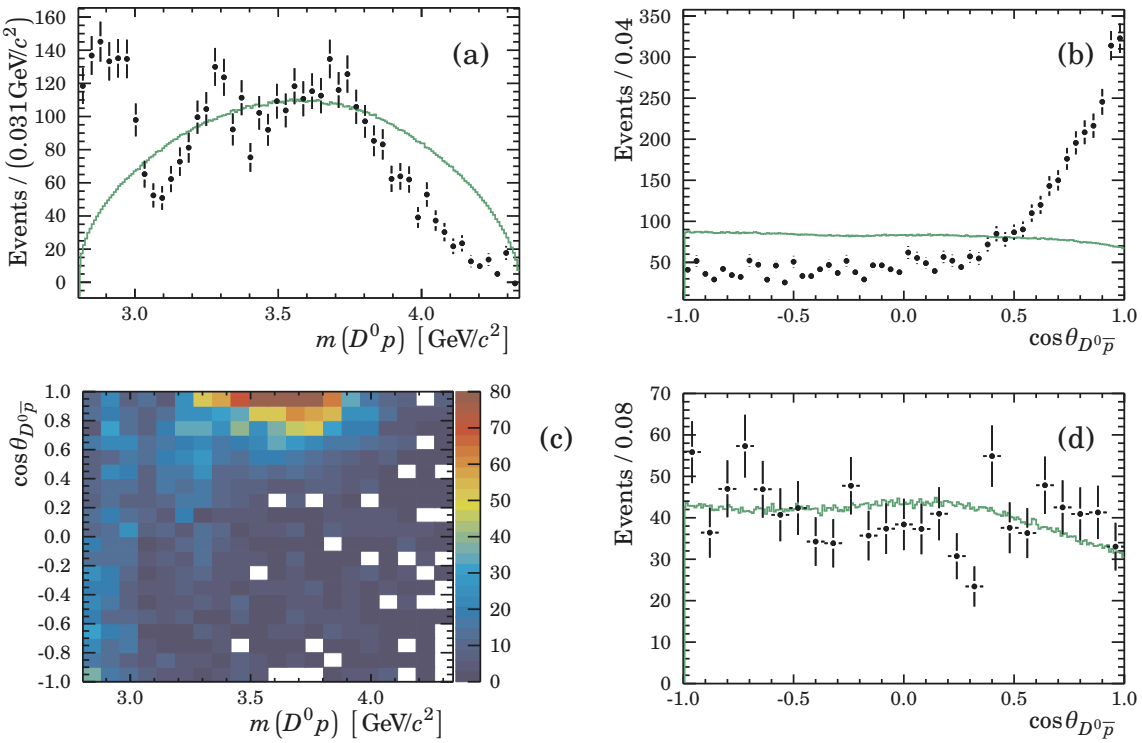

Figure 5.6: (a)-(c): Background subtracted distributions for $\overline{B}^0 \to D^0 p\overline{p}$ decays using *sWeights*. (a): Projection of the invariant D^0p mass. (b): Angular distribution of the $D^0\overline{p}$ system in the D^0p rest frame. The green line is the expected shape from phase-space simulated events including selections. (c): Invariant D^0p mass versus $\cos\theta_{D^0\overline{p}}$ for signal events. (d): Angular distribution of the $D^0\overline{p}$ system in the D^0p rest frame for events with $m^2_{D^0p} \leq 9.5\,\text{GeV}^2/c^4$.

that the angular distribution in the $p\overline{p}$ system becomes asymmetric. The angular asymmetry in the region $m^2_{p\overline{p}} \leq 4.5\,\mathrm{GeV}^2/c^4$ is measured to be $A_{\mathrm{FB}}\left(\overline{B}^0 \to D^0 p\overline{p}\right) = -0.487 \pm 0.098\,(\mathrm{stat}) \pm 0.024\,(\mathrm{syst})$. The observed angular asymmetry is on the order of the one observed in $B^+ \to p\overline{p}\pi^+$ decays $A_{\mathrm{FB}}(B^+ \to p\overline{p}\pi^+, m_{p\overline{p}} < 2.85\,\mathrm{GeV}/c^2) = 0.409 \pm 0.033\,(\mathrm{stat}) \pm 0.006\,(\mathrm{syst})$ and $B^+ \to p\overline{p}K^+$ decays $A_{\mathrm{FB}}(B^+ \to p\overline{p}K^+, m_{p\overline{p}} < 2.85\,\mathrm{GeV}/c^2) = 0.495 \pm 0.012\,(\mathrm{stat}) \pm 0.007\,(\mathrm{syst})$ [8], not accounting for the direction of the asymmetry. The helicity angle for the angular asymmetry measurement in $B^+ \to p\overline{p}\pi^+$ and $B^+ \to p\overline{p}K^+$ is defined as the angle between the charged meson and the oppositely charged baryon in the $p\overline{p}$ rest frame. Transferring this definition to the $\overline{B}^0 \to D^0 p\overline{p}$ decay, the helicity angle has to be calculated between the D^0 meson and the antiproton in the rest frame of the $p\overline{p}$ system. The relation between the angles of the $\overline{B}^0 \to D^0 p\overline{p}$ decay for $p\overline{p}$ at rest is $\theta^{p\overline{p}}_{D^0 p} = \pi - \theta^{p\overline{p}}_{D^0\overline{p}}$. This then results in a sign flip for $A_{\mathrm{FB}}\left(\overline{B}^0 \to D^0 p\overline{p}\right)$. The angular asymmetry is observed to behave like the one observed in $B^+ \to p\overline{p}K^+$ decays. This observation is contrary to what theorists predicted [163]. The predicted the asymmetry to be $A_{\mathrm{FB}}\left(\overline{B}^0 \to D^0 p\overline{p}\right) = 0.04 \pm 0.01$ using a simple relation between $\overline{B}^0 \to D^0 p\overline{p}$ decays and $B^+ \to p\overline{p}\pi^+$ decays as both are dominated by tree-level contributions.

Additionally to the threshold enhancement in the $p\overline{p}$ system, resonant structures in the $D^0 p$ system are observed. These structures cannot only result from the yet known baryons decaying into $D^0 p$ final states so that $\overline{B}^0 \to D^0 p\overline{p}$ decays have the potential to establish new charmed baryons with $D^0 p$ final states.

CHAPTER 6

Conclusion

In this thesis, the branching fraction for $\overline{B}^0 \to D^0 p\overline{p}$ decays has been measured, and the structures in the Dalitz plane have been discussed. The results from the previous Chapters will be summarised below.

The first physics run of the LHCb experiment collected data with an integrated luminosity of about $3\,\text{fb}^{-1}$ in 2011 and 2012 which was used for the measurements in this thesis. The branching fraction of $\overline{B}^0 \to D^0 p\overline{p}$ decays relative to $\overline{B}^0 \to D^0\pi^+\pi^-$ decays is measured to be

$$\frac{\mathcal{B}\left(\overline{B}^0 \to D^0 p\overline{p}\right)}{\mathcal{B}\left(\overline{B}^0 \to D^0\pi^+\pi^-\right)} = (9.2 \pm 0.7\,(\text{stat}) \pm 0.6\,(\text{syst})) \times 10^{-2}\,. \tag{6.1}$$

Substituting the branching fraction of $\overline{B}^0 \to D^0\pi^+\pi^-$ decays by the world's average of the $\overline{B}^0 \to D^0\pi^+\pi^-$ branching fraction, results in

$$\mathcal{B}\left(\overline{B}^0 \to D^0 p\overline{p}\right) = (0.81 \pm 0.06\,(\text{stat}) \pm 0.06\,(\text{syst}) \pm 0.05(\text{norm})) \times 10^{-4}\,, \tag{6.2}$$

which deviates about 2σ from *BABAR*'s measurement [6]

$$\mathcal{B}(\overline{B}^0 \to D^0 p\overline{p}) = (1.02 \pm 0.04\,(\text{stat}) \pm 0.06\,(\text{syst})) \times 10^{-4}\,. \tag{6.3}$$

The statistical uncertainty for the branching fraction measurement with LHCb data is still larger than the statistical uncertainty for *BABAR*'s measurement. It could be reduced using the data of the second physics run. By the end of 2018, the LHCb experiment will have collected between $5\,\text{fb}^{-1}$ and $6\,\text{fb}^{-1}$ of proton-proton collisions at $\sqrt{s} = 13\,\text{TeV}$ [164]. Improvements to the relative branching fraction measurement could also be achieved using simulated events with resonant structures instead of phase-space simulated events, but for that, the appearing resonances in the decay need to be known. Having high statistics would also allow using *sWeighted* signal events as input for the MVA which might lead to a better discriminating power signal candidate selection.

The structures in the Dalitz plane observed for $\overline{B}^0 \to D^0 p\overline{p}$ decays using LHCb data can verify the resonant structures observed by the *BABAR* experiment. The decay

shows a significant enhancement at the low mass threshold of the $p\overline{p}$ mass which is observed in many other three-body decays with a baryon-antibaryon pair in the final state. The angular distribution of the $p\overline{p}$ system at rest is observed to be asymmetric. The angular asymmetry for $m^2_{p\overline{p}} \leq 4.5\,\mathrm{GeV}^2/c^4$ is measured to be

$$A_{\mathrm{FB}}\left(\overline{B}^0 \to D^0 p\overline{p}\right) = -0.487 \pm 0.098\,(\mathrm{stat}) \pm 0.024\,(\mathrm{syst})\,, \tag{6.4}$$

where the helicity angle is calculated between the D^0 meson and the proton. The observed asymmetry is larger than the predicted one of $A_{\mathrm{FB}}\left(\overline{B}^0 \to D^0 p\overline{p}\right) = 0.04 \pm 0.01$ [163], and agrees more with the one observed in $B^+ \to p\overline{p}K^+$ decays $A_{\mathrm{FB}}(B^+ \to p\overline{p}K^+, m_{p\overline{p}} < 2.85\,\mathrm{GeV}/c^2) = 0.495 \pm 0.012\,(\mathrm{stat}) \pm 0.007\,(\mathrm{syst})$, rather than with the one observed in $B^+ \to p\overline{p}\pi^+$ decays $A_{\mathrm{FB}}(B^+ \to p\overline{p}\pi^+, m_{p\overline{p}} < 2.85\,\mathrm{GeV}/c^2) = 0.409 \pm 0.033\,(\mathrm{stat}) \pm 0.006\,(\mathrm{syst})$ [8], where the helicity angle is calculated between the charged meson and the oppositely charged baryon. Note, that there is a sign flip due to the calculation of the helicity angle. The asymmetry in the $p\overline{p}$ system can only be caused by an interference of non-resonant and resonant parts where the resonant part also has contributions from resonances with $j \geq 1$ and different parity. The threshold enhancement in the $p\overline{p}$ invariant mass could therefore be a baryonium as stated by Suzuki [165]. Studying three-body baryonic B decays more intensively with high statistics can help to get a better understanding of the baryon-antibaryon threshold enhancement and the angular asymmetry. LHCb, as well as Belle II, have the potential to contribute to improve the understanding of the threshold enhancement in baryon-antibaryon masses. The decays $B^- \to K^- p\overline{p}$ and $B^- \to \pi^- p\overline{p}$ seem to be a good starting point to understand the threshold enhancement as there seem to be no other structures interfering with the threshold enhancement [8]. The structure in $\overline{B}^0 \to D^0 p\overline{p}$ decays seems to be more complex, and constraints to the composition of the threshold enhancement could simplify the Dalitz analysis.

The enhancement for low $D^0 p$ invariant masses suggests contributions from charmed baryons which might be $\Lambda_c^+(2880)$ and $\Lambda_c^+(2940)$ resonances. Furthermore, a charmed baryon with $m_{D^0 p} \approx 3.3\,\mathrm{GeV}/c^2$ or an interference of more than one charmed baryon will be needed to explain the peak in this mass region. A Dalitz analysis has not been done in this thesis but will be interesting to get more information about the composition of the threshold enhancement and the occurring resonances in the $D^0 p$ invariant mass.

The decay $\overline{B}^0 \to D^0 p\overline{p}$ is dominated by resonant rather than non-resonant structures. A deeper understanding of the resonances in $\overline{B}^0 \to D^0 p\overline{p}$ is essential for the next step toward a time-dependent CPV analysis. Besides the lack of knowledge about the resonant structures in the Dalitz plane, the statistics for $\overline{B}^0 \to D^0{}_{CP} p\overline{p}$ is at the moment too small to compete with the precise measurement of $\sin 2\beta$ and to make a

conclusion about New Physics. It will take more years of data taking and analysis to completely understand the decay $\overline{B}^0 \to D^0 p\overline{p}$ and be able to use it for a time-dependent CPV measurement to search for New Physics.

APPENDIX A

Data and simulation

This Chapter summarises information about samples of data and simulated events. Data and simulation are compared to test the data-simulation agreement.

A.1 Samples of simulated events

The following Tables (Tables A.1 to A.4) show all samples of simulated events that are used to analyse the decay $\overline{B}^0 \to D^0 p\overline{p}$ and to measure its branching fraction. All tables list the decay itself, the generator option, the number of available events (N_{acc}), and the efficiencies for the final state particles in the LHCb acceptance, called generator level efficiency ($\epsilon_{\text{acc|gen}}$). The generator option can be either `PHSP` or `spDalitz`. `PHSP` means that the events are generated uniformly in the phase space, whereas `spDalitz` implies that the events are generated uniformly in the square Dalitz plane (m', θ') (see Sections 4.1.2 and 5.1). Both generator options were used because generated samples of simulated events had different generator options. Every mode uses the Cabibbo favoured D^0 decay $D^0 \to K^-\pi^+$ and $\overline{D}^0 \to K^+\pi^-$ respectively. Table A.1 shows the signal modes, Tables A.2, A.3, and A.4 list all background modes.

Table A.1: Simulated signal events used for the analysis. The D^0 decay mode is the Cabibbo favoured one $D^0 \to K^-\pi^+$. All final state particles are generated within the LHCb acceptance.

Decay	Option	N_{acc}	$\epsilon_{\text{acc\|gen}}$
$\overline{B}^0 \to D^0 p\overline{p}$	PHSP	1287993	$(18.22 \pm 0.03)\%$
$\overline{B}^0 \to D^0 \pi^+\pi^-$	PHSP	1040000	$(15.81 \pm 0.03)\%$

Table A.2: Simulated $\overline{B}^0$ decays used to study the backgrounds of this analysis. The D^0 decay mode is the Cabibbo favoured one $D^0 \to K^-\pi^+$. All final state particles are generated within the LHCb acceptance.

Decay	Option	N_{acc}	$\epsilon_{\text{acc\|gen}}$
$\overline{B}^0 \to (D^{*0} \to D^0\pi^0)\, p\overline{p}$	PHSP	659680	$(15.64 \pm 0.04)\%$
$\overline{B}^0 \to (D^{*0} \to D^0\gamma)\, p\overline{p}$	PHSP	620141	$(18.33 \pm 0.04)\%$
$\overline{B}^0 \to D^0 K^-\pi^+$	spDalitz	2013496	$(16.67 \pm 0.02)\%$
$\overline{B}^0 \to (D^{*0} \to D^0\pi^0)\, \pi^+\pi^-$	PHSP	563000	$(13.96 \pm 0.04)\%$
$\overline{B}^0 \to (D^{*0} \to D^0\gamma)\, \pi^+\pi^-$	PHSP	553500	$(15.88 \pm 0.04)\%$

Table A.3: Simulated $\overline{B}^0_s$ decays used to study backgrounds of the analysis. The D^0 decay mode is the Cabibbo favoured one $D^0 \to K^-\pi^+$. The D^{*0} in the $\overline{B}^0_s \to D^{*0}K^+\pi^-$ decay can either decay to $D^0\pi^0$ or to $D^0\gamma$ weighted by their branching fractions. All final state particles are generated within the LHCb acceptance.

Decay	Option	N_{acc}	$\epsilon_{\text{acc\|gen}}$
$\overline{B}^0_s \to D^0 K^+\pi^-$	spDalitz	2003492	$(16.65 \pm 0.02)\%$
$\overline{B}^0_s \to D^{*0} K^+\pi^-$	spDalitz	539247	$(15.46 \pm 0.04)\%$

Table A.4: Simulated Λ^0_b decays used to study the backgrounds of this analysis. The D^0 decay mode is the Cabibbo favoured one $D^0 \to K^-\pi^+$. All final state particles are generated within the LHCb acceptance.

Decay	Option	N_{acc}	$\epsilon_{\text{acc\|gen}}$
$\Lambda^0_b \to D^0 p\pi^-, D^0 \to K^-\pi^+$	spDalitz	542499	$(16.93 \pm 0.04)\%$
$\Lambda^0_b \to D^0 pK^-, D^0 \to K^-\pi^+$	spDalitz	535000	$(17.38 \pm 0.04)\%$

A.2 Comparison of 2011 and 2012 data

Here, data taken in 2012 are compared with data taken in 2011. To get the signal and background behaviour of different variables, data is fitted with a signal and a background component. The shape of the signal component is obtained using simulated events; the background component is a first order polynomial. The *sPlot* technique [106] allows reweighting the data by using information from the fit model and the fit result (see Appendix E.2).

A.2.1 Comparison of RunI data for $\overline{B}^0 \to D^0 p\overline{p}$ decays

To get the signal behaviour for variables of $\overline{B}^0 \to D^0 p\overline{p}$ decays, data are fitted in the range $m \in [5235;5550]\,\text{MeV}/c^2$ to apply the *sPlot* technique. The fit function for the signal is obtained using simulated $\overline{B}^0 \to D^0 p\overline{p}$ events. These events are generated according to the phase space model and selected so that only `true` $\overline{B}^0 \to D^0 p\overline{p}$ events remain in the dataset. These events are fitted with a double Crystal Ball function (see Section E.1) and the results are listed in Table A.5 and shown in Figure A.1(c). Five of the fitted parameters from the double Crystal Ball function are fixed in the fit to data to have a converging fit. The background function is a first order polynomial. The fit results for the fit to data taken in 2011 and 2012 can be found in Figure A.1 and Table A.5. The comparison of the *sWeighted* variables with simulated events is shown in Figure A.2 for variables of the $\overline{B}^0$ meson, the D^0 meson, and the number of tracks in the event; in Figure A.3 and A.4 for the variables of the final state particles. There are small differences in the variables between both configurations due to the increased centre-of-mass energy in 2012, clearly visible in the comparison of the number of tracks in an event. The higher centre-of-mass energy in 2012 led to a higher track multiplicity.

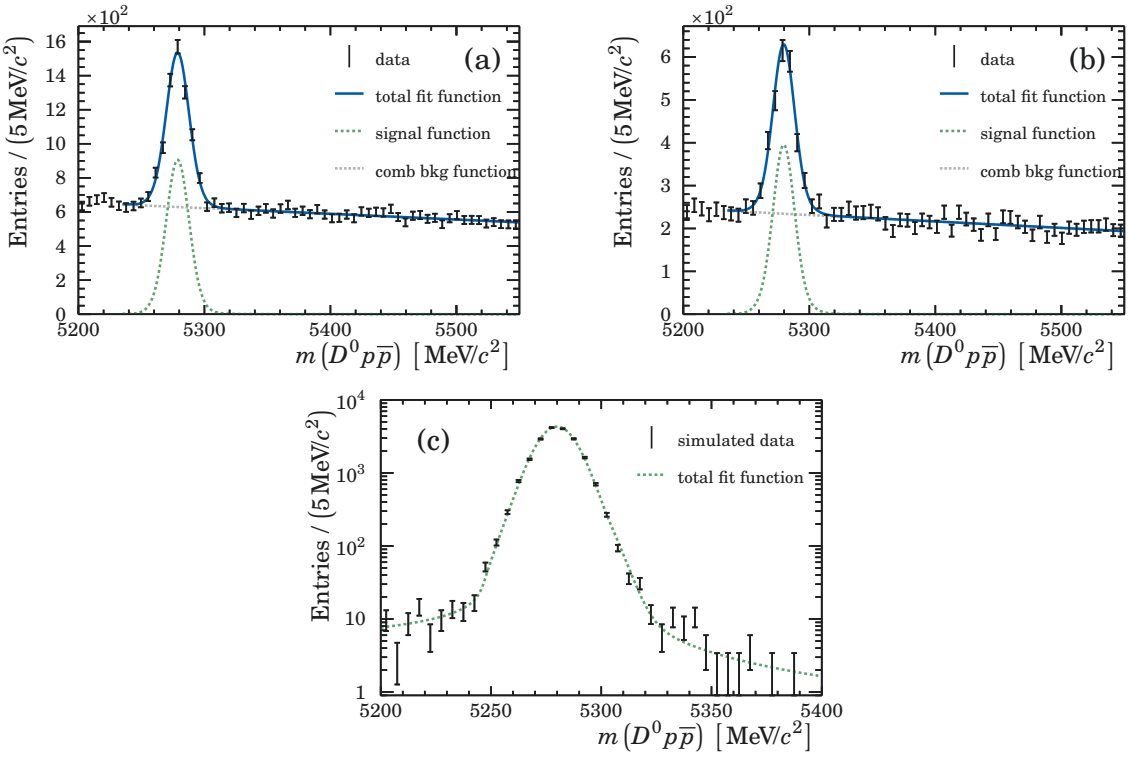

Figure A.1: Extended maximum likelihood fit to $\overline{B}^0 \to D^0 p\overline{p}$ data (a) taken in 2012, (b) taken in 2011, and (c) simulated $\overline{B}^0 \to D^0 p\overline{p}$ events. Fit parameters are listed in Table A.5.

Table A.5: Fit parameters from the fit to simulated $\overline{B}^0 \to D^0 p\overline{p}$ events and data taken in 2012 and 2011. The fits are shown in Figure A.1

parameter	simulation	2012 data	2011 data
$\bar{m}$ [MeV/c^2]	5279.93 ± 0.07	5278.76 ± 0.29	5279.7 ± 0.5
σ_1 [MeV/c^2]	11.7 ± 1.9	11.3 ± 2.3	12.1 ± 2.6
α_1	2.7 ± 0.5	2.7 (fixed)	2.7 (fixed)
n_1	0.4 ± 1.0	0.4 (fixed)	0.4 (fixed)
σ_2 [MeV/c^2]	8.5 ± 0.6	8.5 ± 0.8	8.0 ± 0.7
α_2	-2.73 ± 0.29	-2.73 (fixed)	-2.73 (fixed)
n_2	1.12 ± 0.32	1.12 (fixed)	1.12 (fixed)
r_{CB}	0.34 ± 0.17	0.34 (fixed)	0.34 (fixed)
a	–	-0.097 ± 0.013	-0.120 ± 0.026
N_{signal}	–	3665 ± 131	1546 ± 84
N_{bkg}	–	$35828pm258$	13204 ± 159

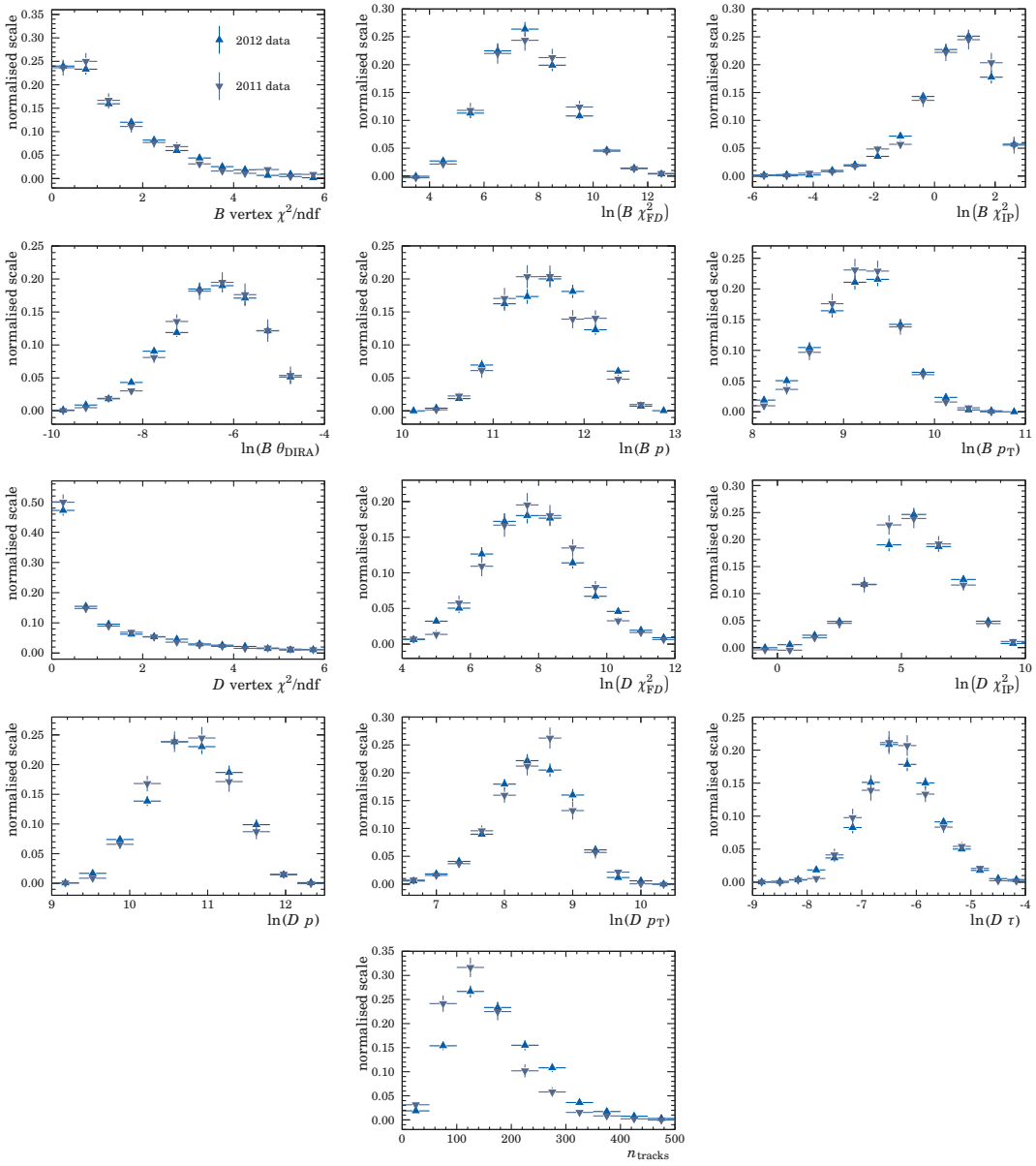

Figure A.2: Comparison of variables from the $\overline{B}^0$ meson and D^0 meson and the number of tracks in the event of *sWeighted* $\overline{B}^0 \to D^0 p\overline{p}$ signal events from 2012 data (light blue) and 2011 data (dark blue). The distributions are normalised to unit area.

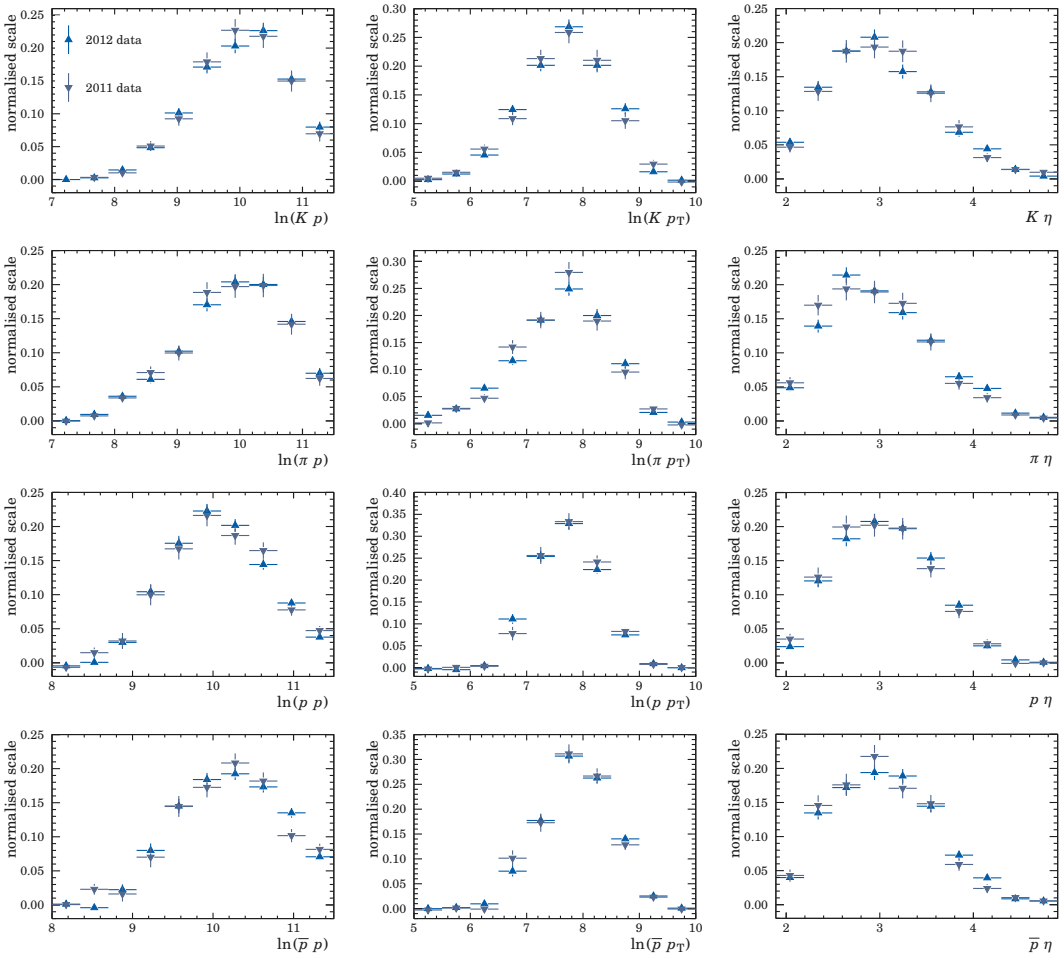

Figure A.3: Comparison of variables from the final state particles in the event of *sWeighted* $\overline{B}^0 \to D^0 p\overline{p}$ signal events from 2012 data (light blue) and 2011 data (dark blue). The distributions are normalised to unit area.

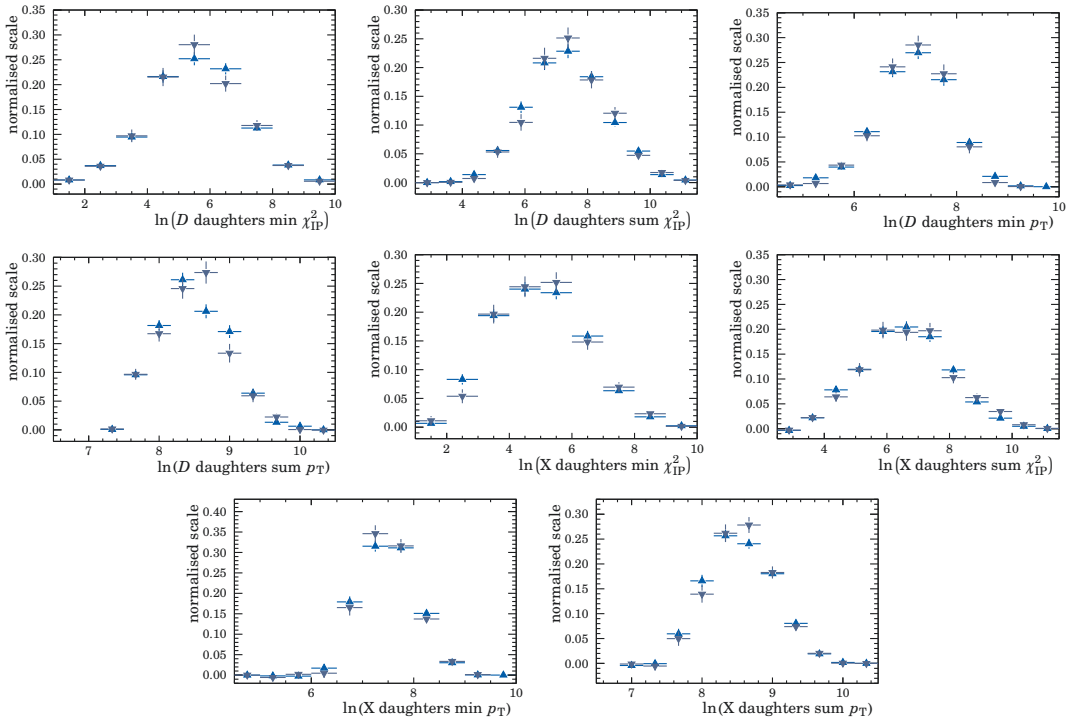

Figure A.4: Comparison of variables from the final state particles in the event of *sWeighted* $\overline{B}^0 \to D^0 p\overline{p}$ signal events from 2012 data (light blue) and 2011 data (dark blue). The distributions are normalised to unit area.

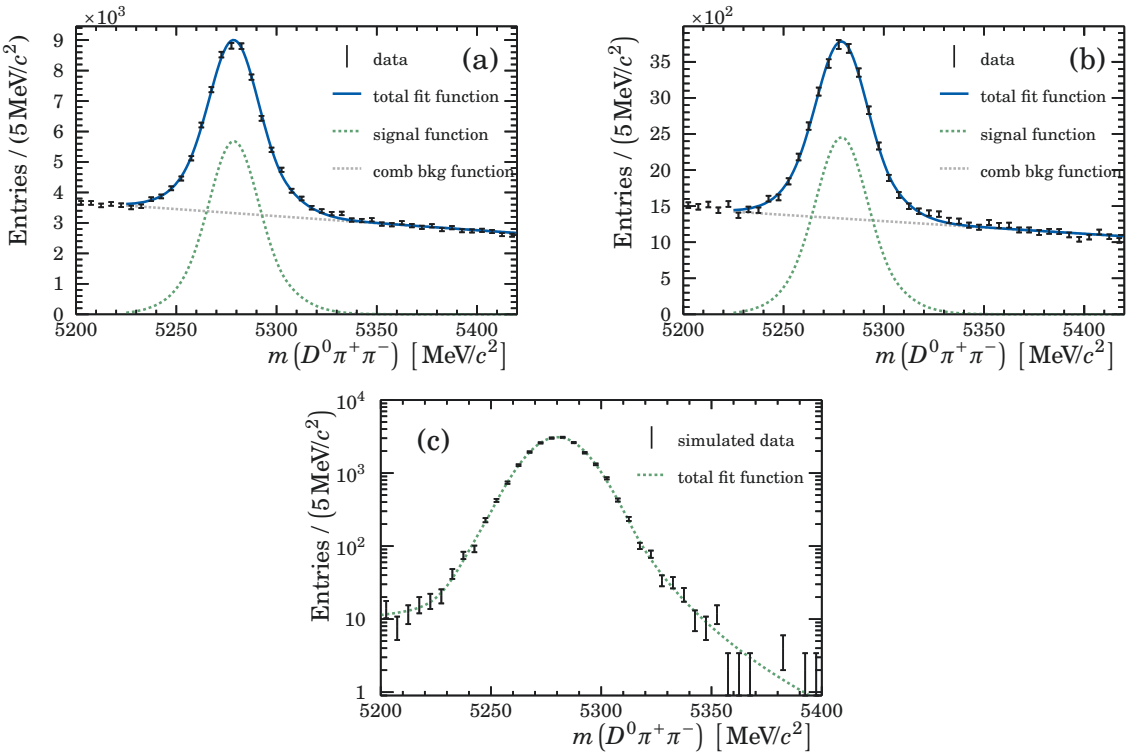

Figure A.5: Extended maximum likelihood fit to $\bar{B}^0 \to D^0\pi^+\pi^-$ data (a) taken in 2012, (b) taken in 2011, and simulated $\bar{B}^0 \to D^0\pi^+\pi^-$ events. Fit parameters are listed in Table A.6.

A.2.2 Comparison of RunI data for $\bar{B}^0 \to D^0\pi^+\pi^-$ decays

The same method as described in Section A.2.1 is applied to get the *sWeighted* distribution of $\bar{B}^0 \to D^0\pi^+\pi^-$ variables. Selected simulated $\bar{B}^0 \to D^0\pi^+\pi^-$ candidates are fitted with a double Crystal Ball function to get the shape of the signal candidates (see Figure A.5(c) and Table A.6). Mean and widths of the double Crystal Ball function are allowed to float in the fit to data, while the other parameters of the signal fit function are fixed to avoid a non-converging fit. The function to describe the combinatorial background is a first order polynomial. The total fit is shown in Figure A.5, and the fit parameters can be found in Table A.6. The comparisons for *sWeighted* data and simulated events (see Figure A.6, A.7 and A.8) show very small differences between the data-taking periods except for the number of tracks in the event.

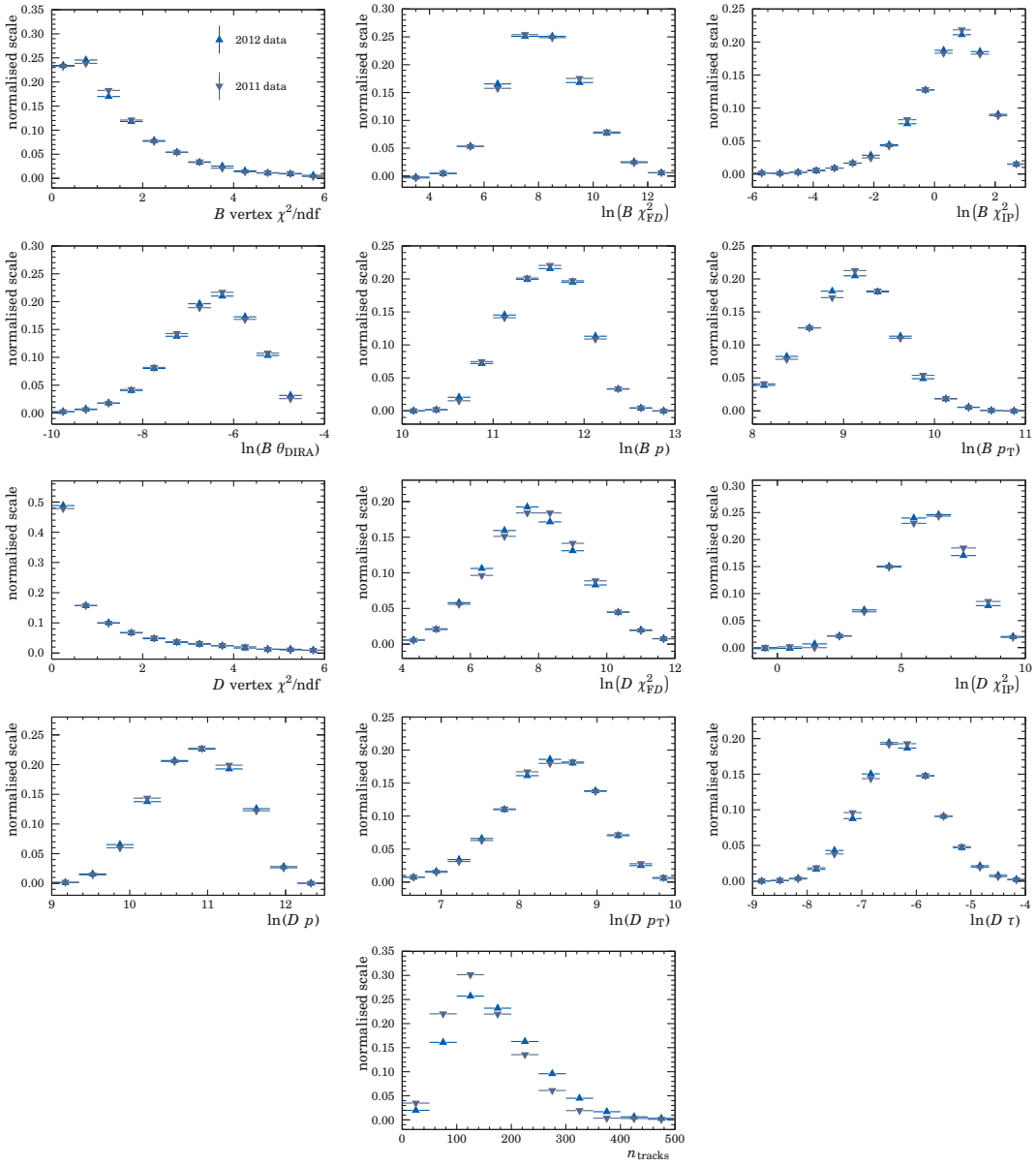

Figure A.6: Comparison of variables from the $\overline{B}^0$ meson and D^0 meson and the number of tracks in the event of *sWeighted* $\overline{B}^0 \to D^0\pi^+\pi^-$ signal events from 2012 data (light blue) and 2011 data (dark blue). The distributions are normalised to unit area.

Table A.6: Fit parameters from the fit to simulated $\overline{B}^0 \to D^0\pi^+\pi^-$ events and data taken in 2012 and 2011. The fits are shown in Figure A.5

parameter	simulation	2012 data	2011 data
$\bar{m}$ $[\mathrm{MeV}/c^2]$	5280.18 ± 0.10	5278.75 ± 0.14	5279.19 ± 0.20
σ_1 $[\mathrm{MeV}/c^2]$	11.4 ± 0.6	19.6 ± 1.2	15.2 ± 1.8
α_1	2.69 ± 0.22	2.69 (fixed)	2.69 (fixed)
n_1	0.43 ± 0.31	0.43 (fixed)	0.43 (fixed)
σ_2 $[\mathrm{MeV}/c^2]$	16.3 ± 0.8	11.11 ± 0.21	12.41 ± 0.95
α_2	-1.99 ± 0.15	-1.99 (fixed)	-1.99 (fixed)
n_2	4.7 ± 1.3	4.7 (fixed)	4.7 (fixed)
r_{CB}	0.47 ± 0.12	0.47 (fixed)	0.47 (fixed)
a	–	-0.156 ± 0.014	-0.198 ± 0.017
N_{signal}	–	39294 ± 1052	15905 ± 475
N_{bkg}	–	112389 ± 1087	46707 ± 506

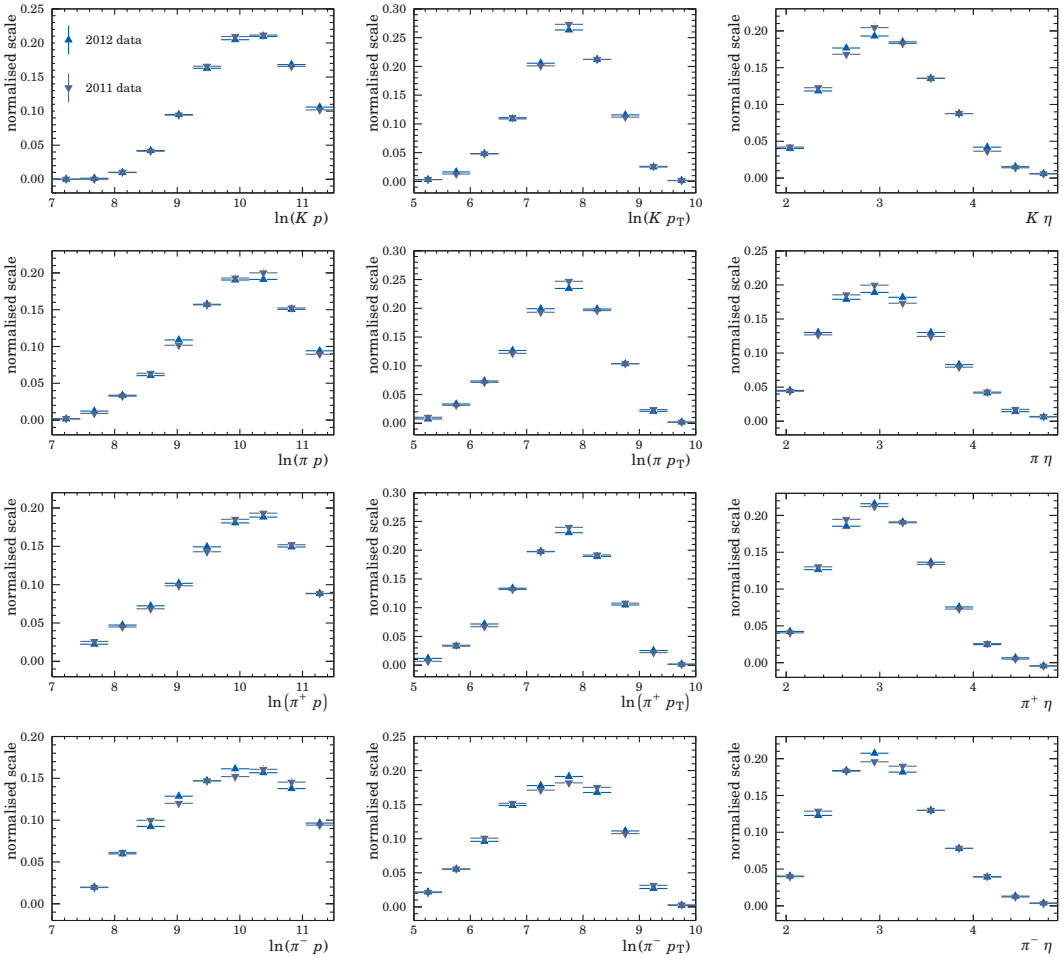

Figure A.7: Comparison of variables from the final state particle and number of tracks in the event of *sWeighted* $\overline{B}^0 \to D^0\pi^+\pi^-$ signal events from 2012 data (light blue) and 2011 data (dark blue). The distributions are normalised to unit area.

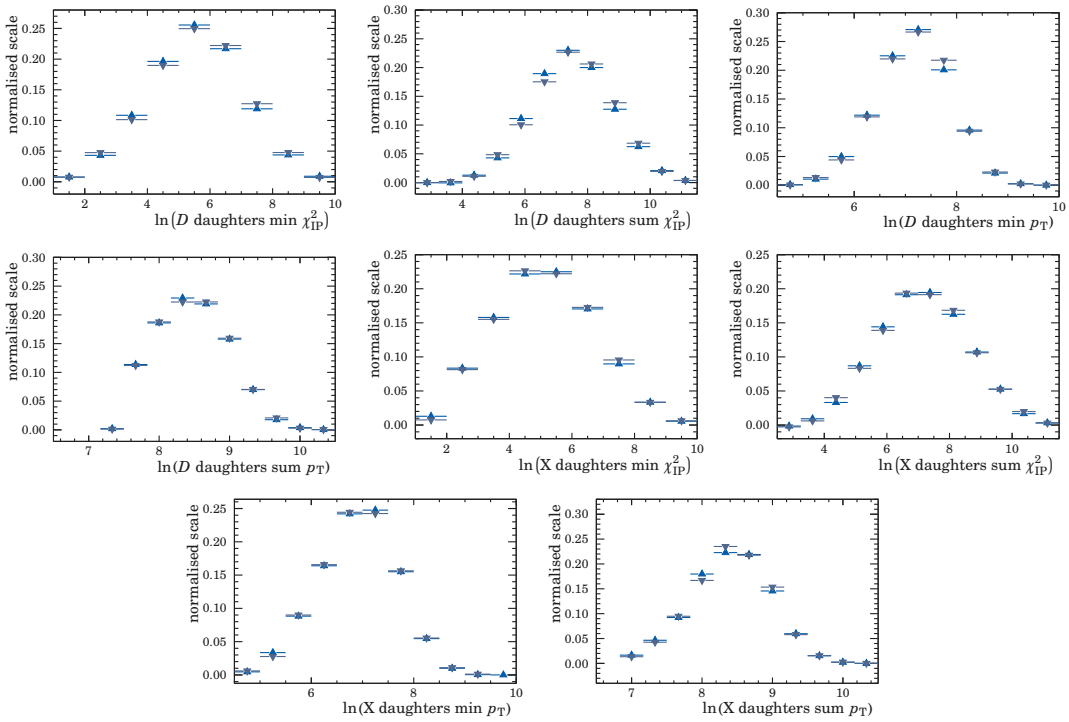

Figure A.8: Comparison of variables from the final state particles in the event of *sWeighted* $\bar{B}^0 \to D^0\pi^+\pi^-$ signal events from 2012 data (light blue) and 2011 data (dark blue). The distributions are normalised to unit area.

A.3 Comparison of 2012 data and simulation

Here, simulated events are compared with data taken in 2012. To get the signal and background behaviour of different variables in data, the data are fitted with a signal and background component as described in Appendix A.2. The truth-matched signal behaviour in simulation is obtained by using the BKGCAT tool (see Section A.4). Figures A.9, A.10 and A.11 show the comparison of data and simulation for $\overline{B}^0 \to D^0 p\overline{p}$ decays; Figures A.12, A.13 and A.14 the comparison for $\overline{B}^0 \to D^0\pi^+\pi^-$ decays. Not all variables used for the multivariate analysis described in Section 4.2.4 or *e.g.* the variables used to determine the particle identification efficiency (p, η) have a good data-simulation agreement. A reason can be that certain variables are poorly described by the simulation. Another reason can be the distribution of events in the Dalitz plane. The simulations used here are generated with a uniform distribution over the Dalitz plane while in data the distribution is not uniform as can be seen in Figure A.15. Therefore, the events are reweighted according to their Dalitz distribution. The histograms used to reweight the events have smoothed bin contents using ROOT's TH2::Smooth-function. The Dalitz distributions with smoothed bin contents are shown in Figure A.16. The structures seen in the $\overline{B}^0 \to D^0 p\overline{p}$ Dalitz plane are relatively broad compared to the resonances of the $\overline{B}^0 \to D^0\pi^+\pi^-$ decay (for more information on the Dalitz analysis of $\overline{B}^0 \to D^0\pi^+\pi^-$ decays see [61, 105, 133]). Even though the reweighting cannot reproduce the structures in the Dalitz plane for $\overline{B}^0 \to D^0\pi^+\pi^-$ decays correctly, Figures A.17 to A.20 show that reweighting improves the variable's data-simulation agreement for the particle's momentum and transverse momentum in particular. Reweighted variables will be used for the multivariate analysis of $\overline{B}^0 \to D^0 p\overline{p}$ decays. An additional scale factor is applied to the B χ^2_{IP} variable for a better data-simulation agreement. The scale factor is 1.2. The data-simulation agreement is sufficient for $\overline{B}^0 \to D^0\pi^+\pi^-$ decays without reweighting for the variables used in the multivariate analysis.

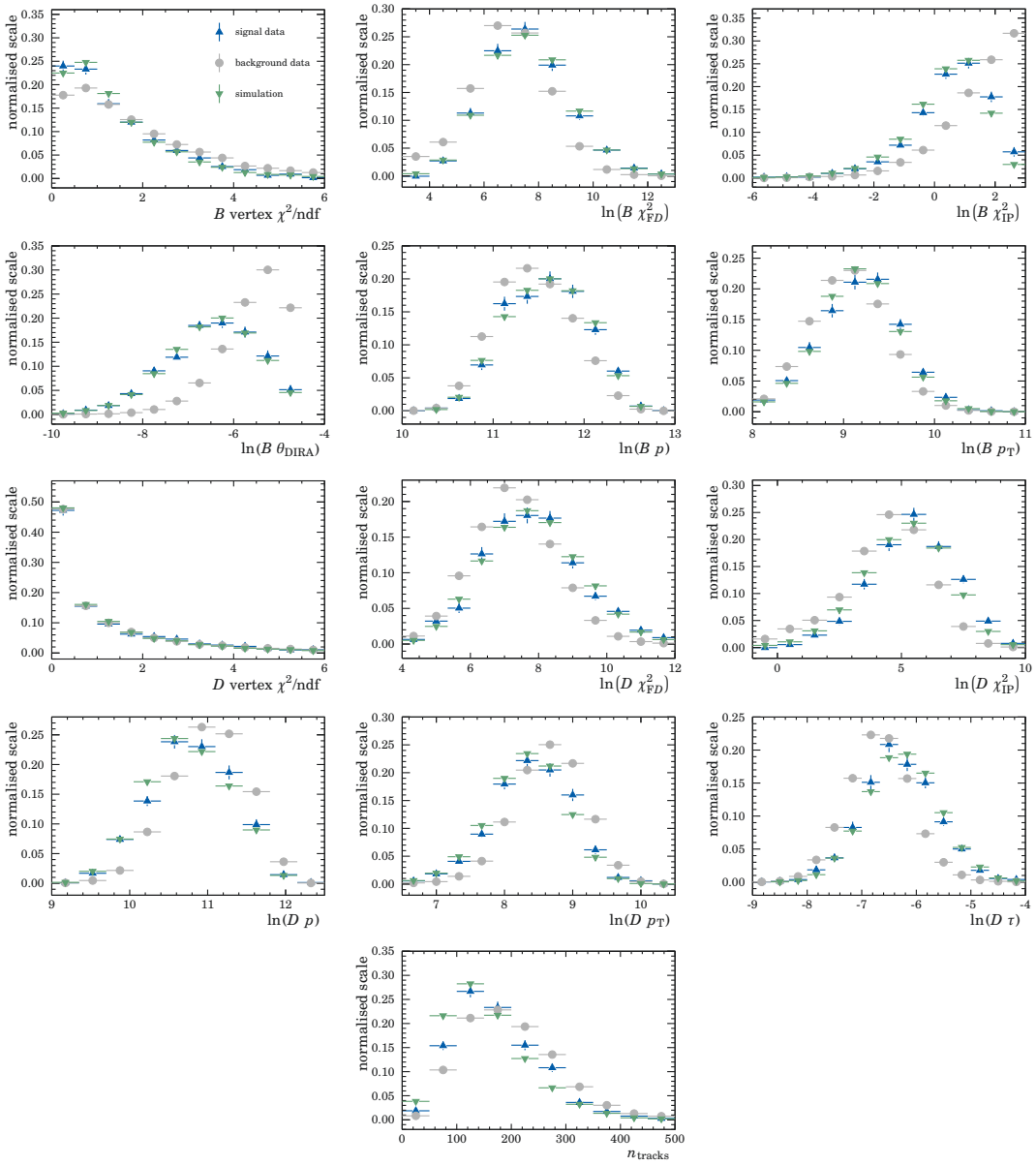

Figure A.9: Comparison of variables from the $\overline{B}^0$ meson and D^0 meson and the number of tracks in the event of simulated events (green), *sWeighted* $\overline{B}^0 \to D^0 p\overline{p}$ signal events from 2012 data (light blue) and *sWeighted* $\overline{B}^0 \to D^0 p\overline{p}$ background events from 2012 data (grey). The distributions are normalised to unit area.

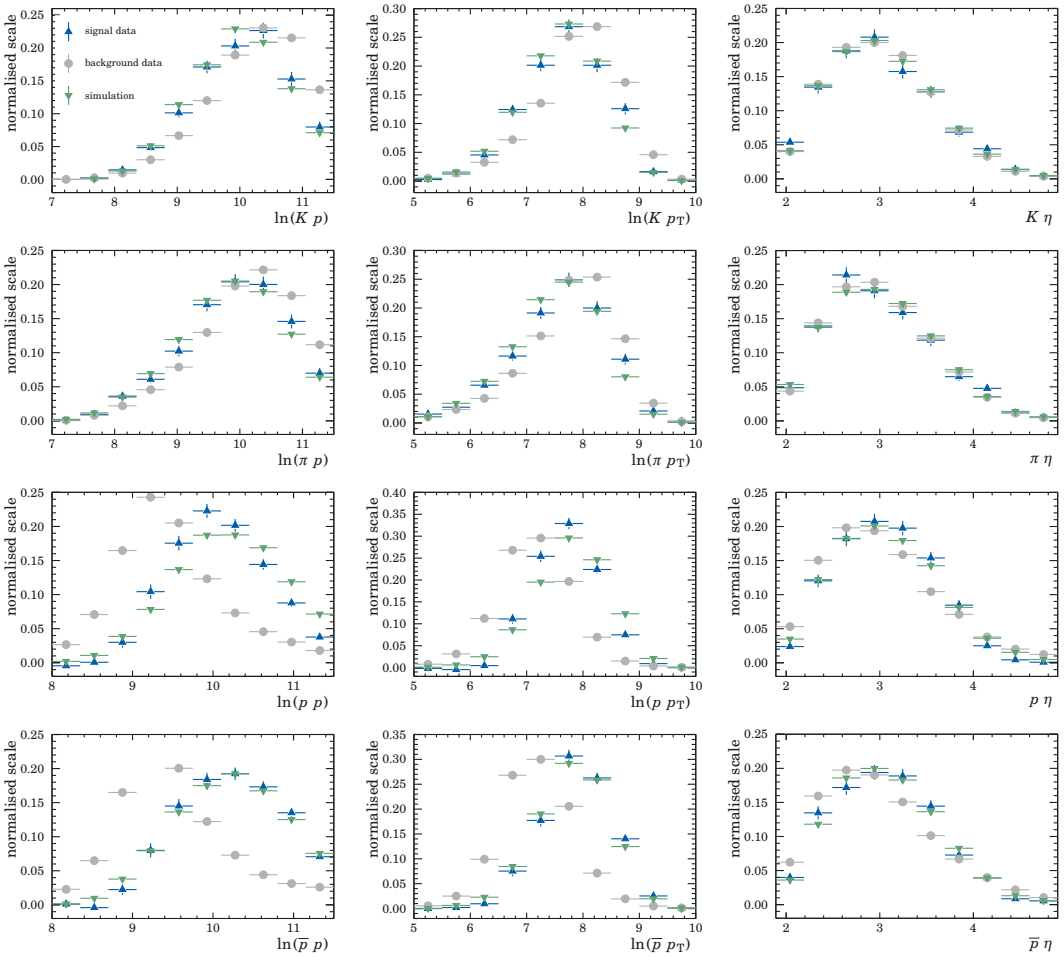

Figure A.10: Comparison of variables from the final state particles of simulated events (green), *sWeighted* $\overline{B}^0 \to D^0 p\overline{p}$ signal events from 2012 data (light blue) and *sWeighted* $\overline{B}^0 \to D^0 p\overline{p}$ background events from 2012 data (grey). The distributions are normalised to unit area.

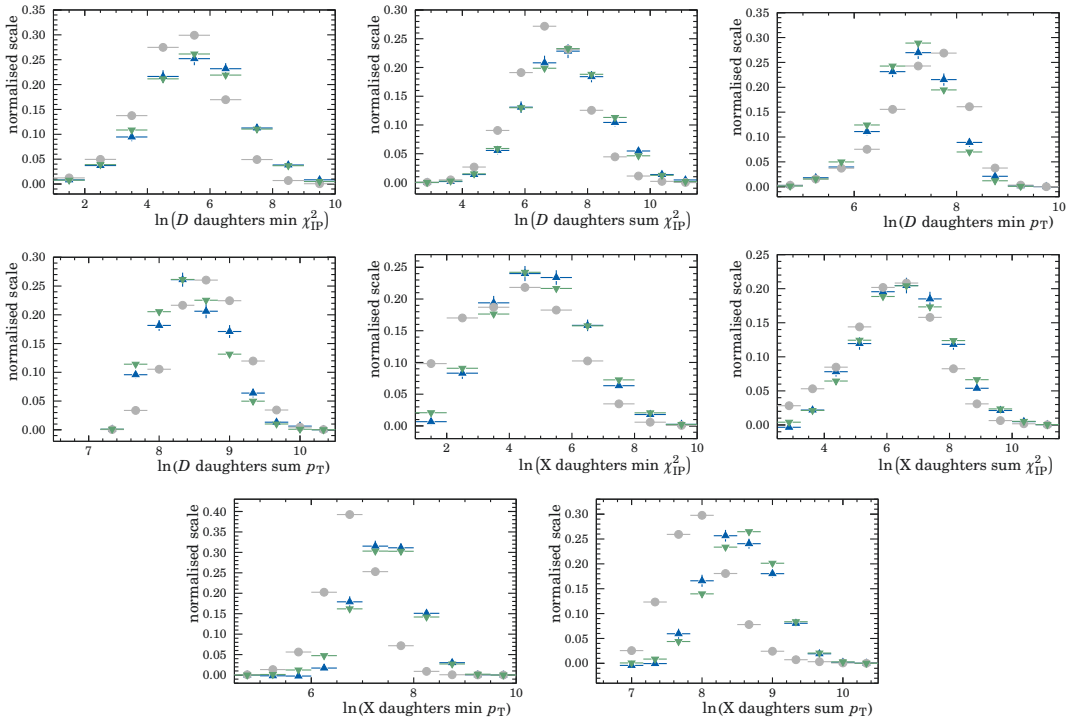

Figure A.11: Comparison of variables from the final state particles of simulated events (green), *sWeighted* $\overline{B}^0 \to D^0 p\overline{p}$ signal events from 2012 data (light blue) and *sWeighted* $\overline{B}^0 \to D^0 p\overline{p}$ background events from 2012 data (grey). The distributions are normalised to unit area.

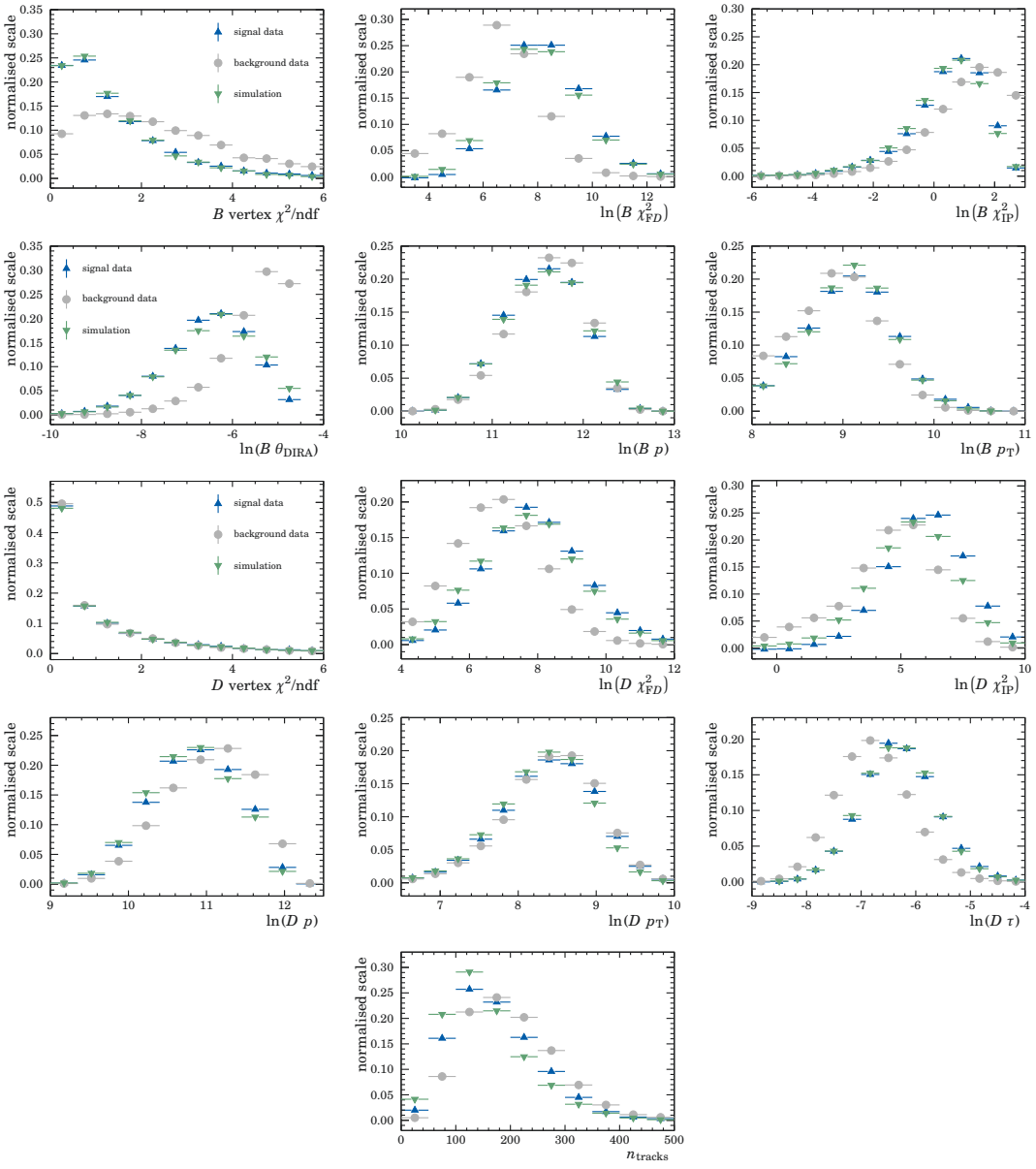

Figure A.12: Comparison of variables from the $\overline{B}^0$ meson and D^0 meson and the number of tracks in the event of simulated events (green), *sWeighted* $\overline{B}^0 \to D^0\pi^+\pi^-$ signal events from 2012 data (light blue) and *sWeighted* $\overline{B}^0 \to D^0\pi^+\pi^-$ background events from 2012 data (grey). The distributions are normalised to unit area.

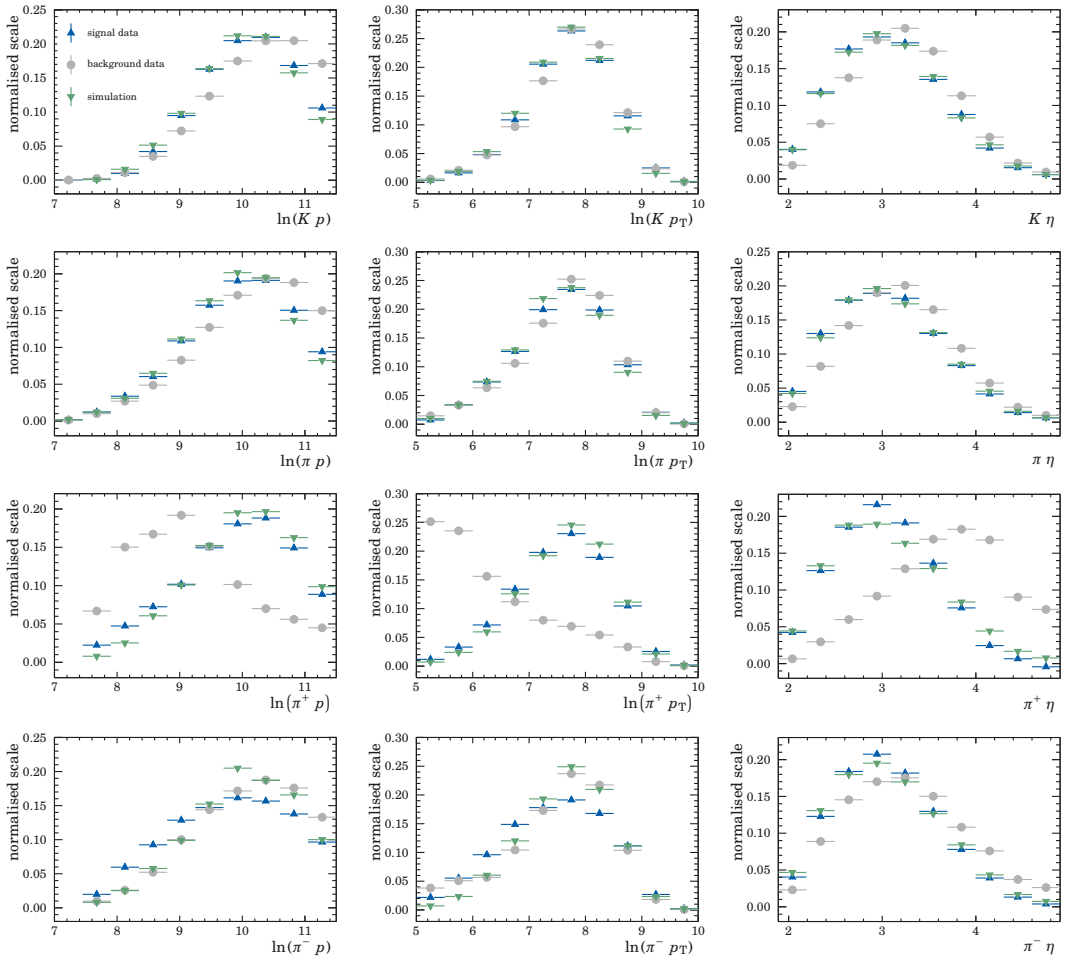

Figure A.13: Comparison of variables from the final state particle of simulated events (green), *sWeighted* $\overline{B}^0 \to D^0\pi^+\pi^-$ signal events from 2012 data (light blue) and *sWeighted* $\overline{B}^0 \to D^0\pi^+\pi^-$ background events from 2012 data (grey). The distributions are normalised to unit area.

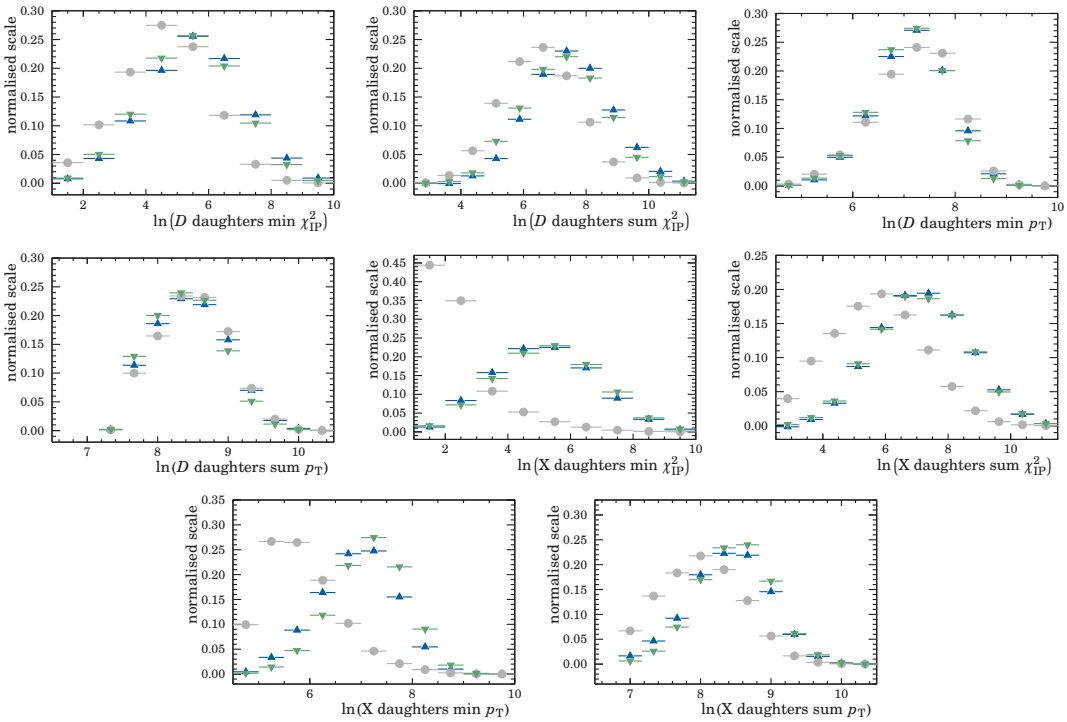

Figure A.14: Comparison of variables from the final state particle of simulated events (green), *sWeighted* $\overline{B}^0 \to D^0\pi^+\pi^-$ signal events from 2012 data (light blue) and *sWeighted* $\overline{B}^0 \to D^0\pi^+\pi^-$ background events from 2012 data (grey). The distributions are normalised to unit area.

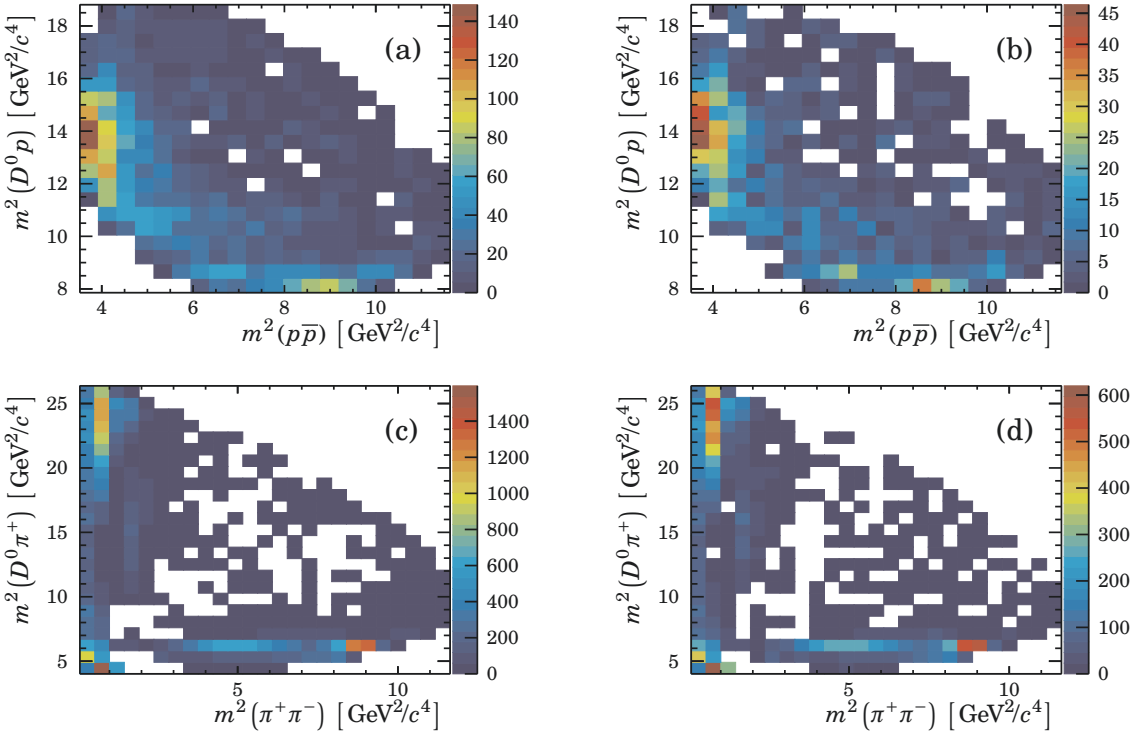

Figure A.15: *sWeighted* Dalitz distribution for data taken in 2012 (left) and data taken in 2011 (right). The top row shows the Dalitz distribution for $\overline{B}^0 \to D^0 p\overline{p}$ decays ((a) and (b)); the bottom row the Dalitz distribution for $\overline{B}^0 \to D^0\pi^+\pi^-$ decays ((c) and (d)).

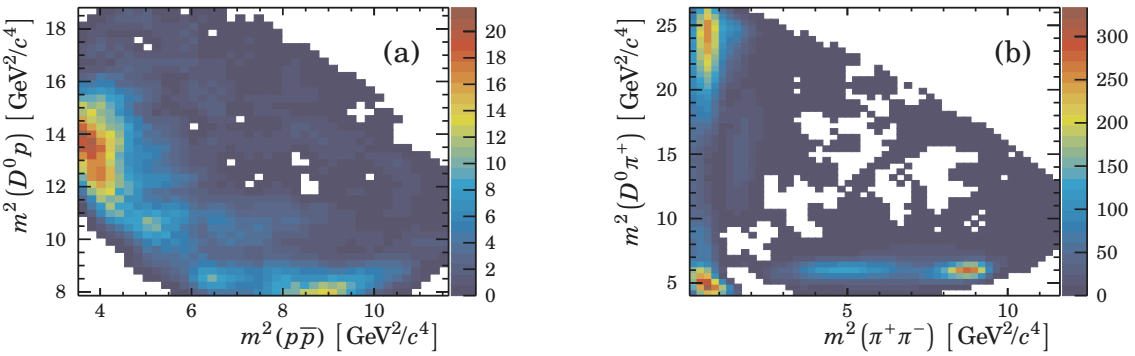

Figure A.16: *sWeighted* Dalitz distribution for data taken in 2012 with smoothed bin contents for (a) $\overline{B}^0 \to D^0 p\overline{p}$ decays and (b) $\overline{B}^0 \to D^0\pi^+\pi^-$ decays.

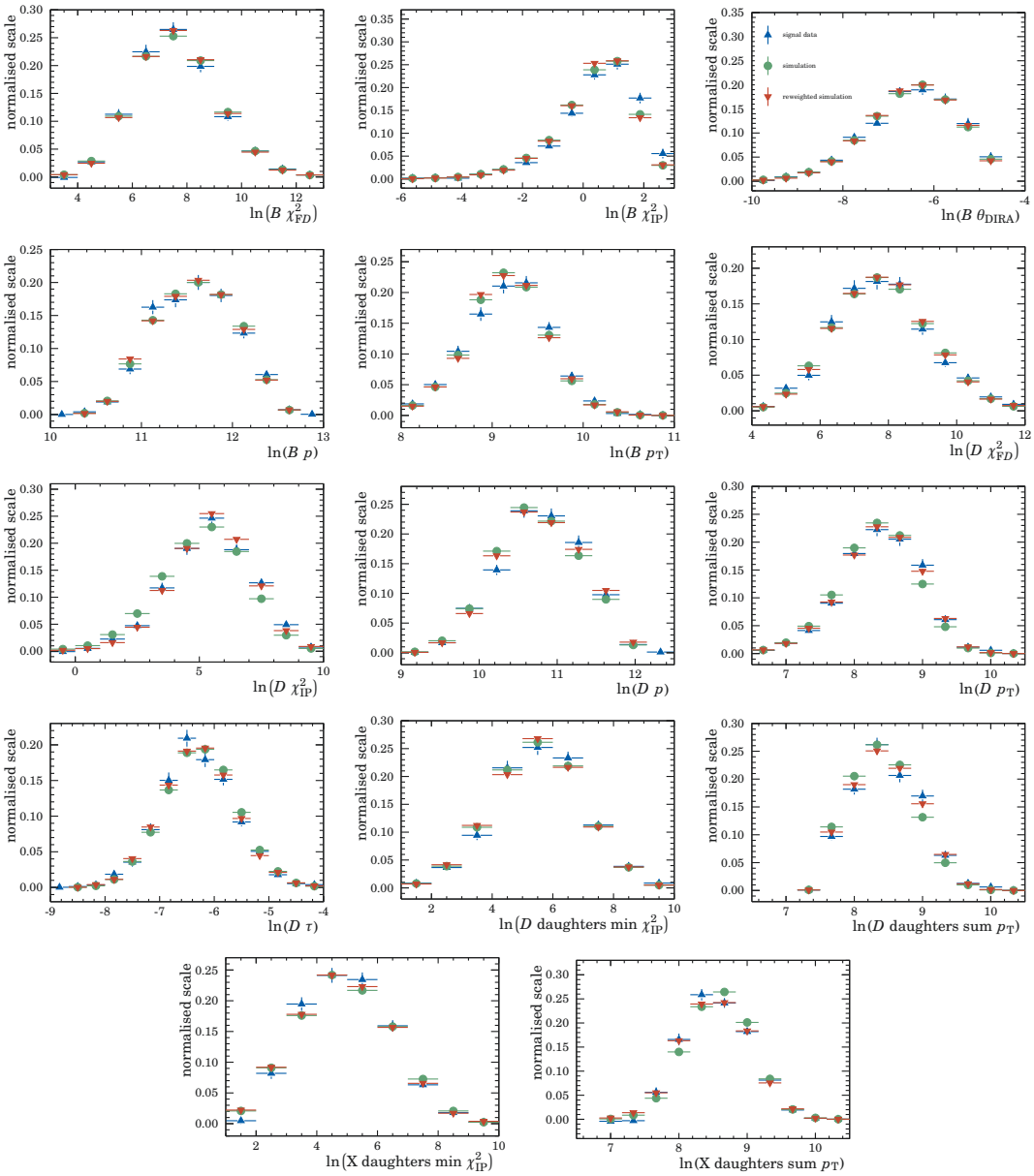

Figure A.17: Comparison of variables of simulated events (green), *sWeighted* $\overline{B}^0 \to D^0 p\overline{p}$ signal events from 2012 data (light blue) and reweighted simulated events (red) used for the multivariate analysis. The distributions are normalised to unit area.

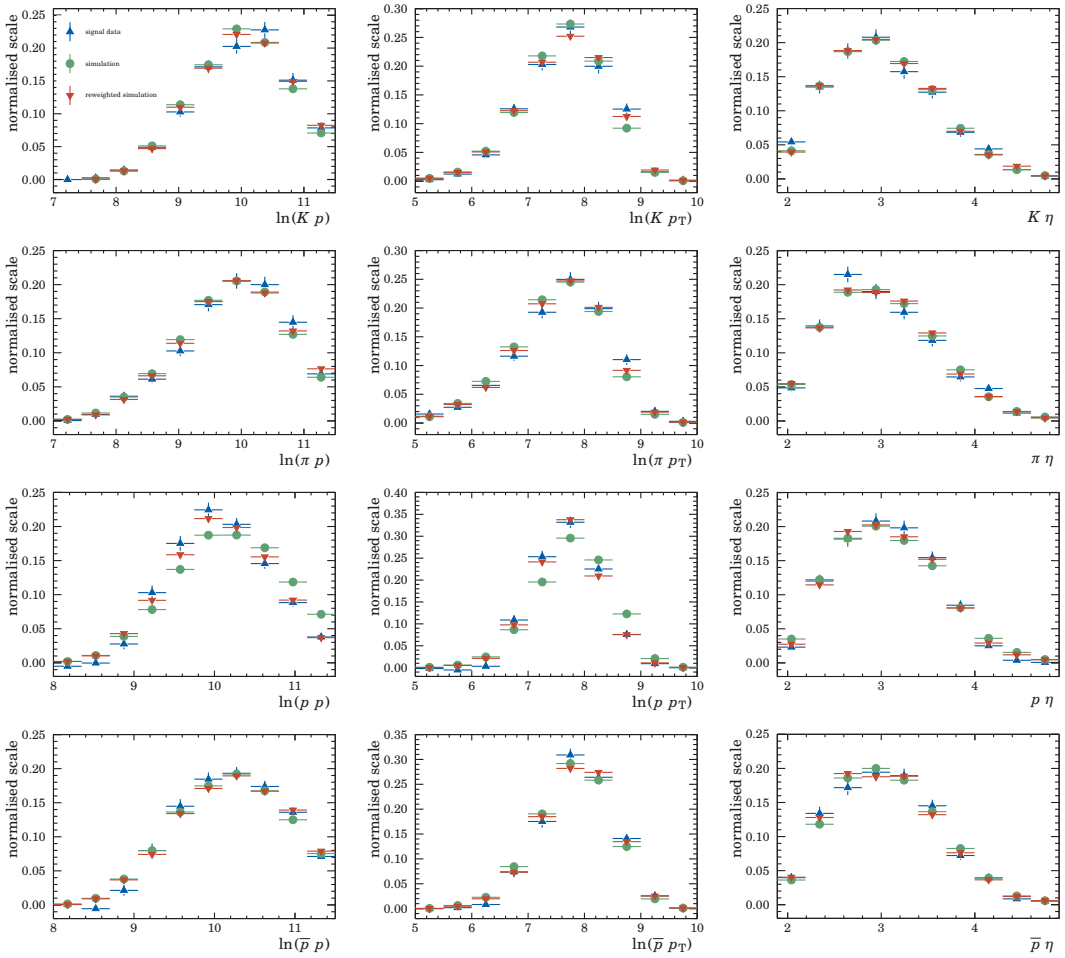

Figure A.18: Comparison of variables from the final state particles of simulated events (green), *sWeighted* $\overline{B}^0 \to D^0 p\overline{p}$ signal events from 2012 data (light blue) and reweighted simulated events (red). The distributions are normalised to unit area.

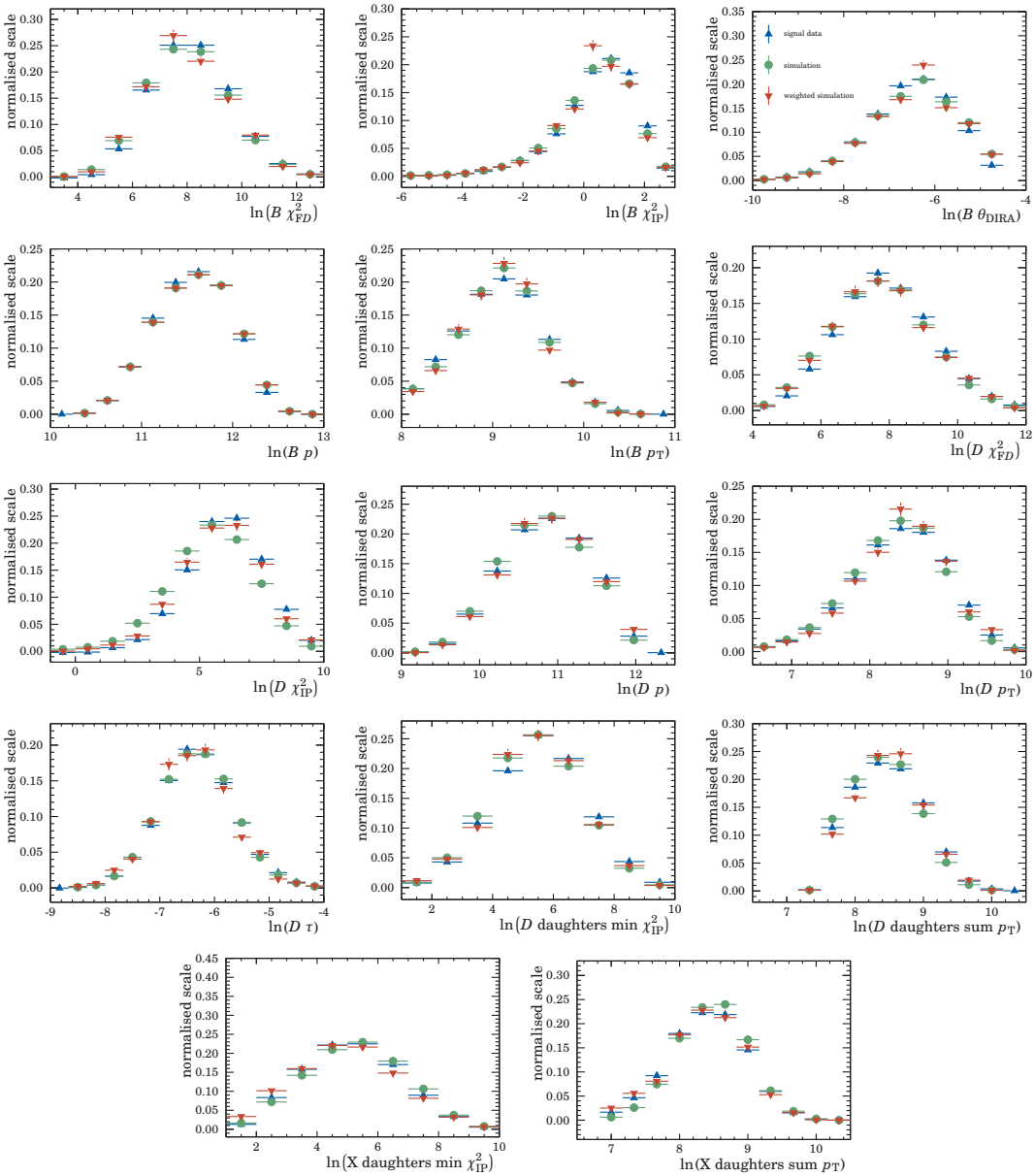

Figure A.19: Comparison of variables of simulated events (green), *sWeighted* $\overline{B}^0 \to D^0\pi^+\pi^-$ signal events from 2012 data (light blue) and reweighted simulated events (red) used for the multivariate analysis. The distributions are normalised to unit area.

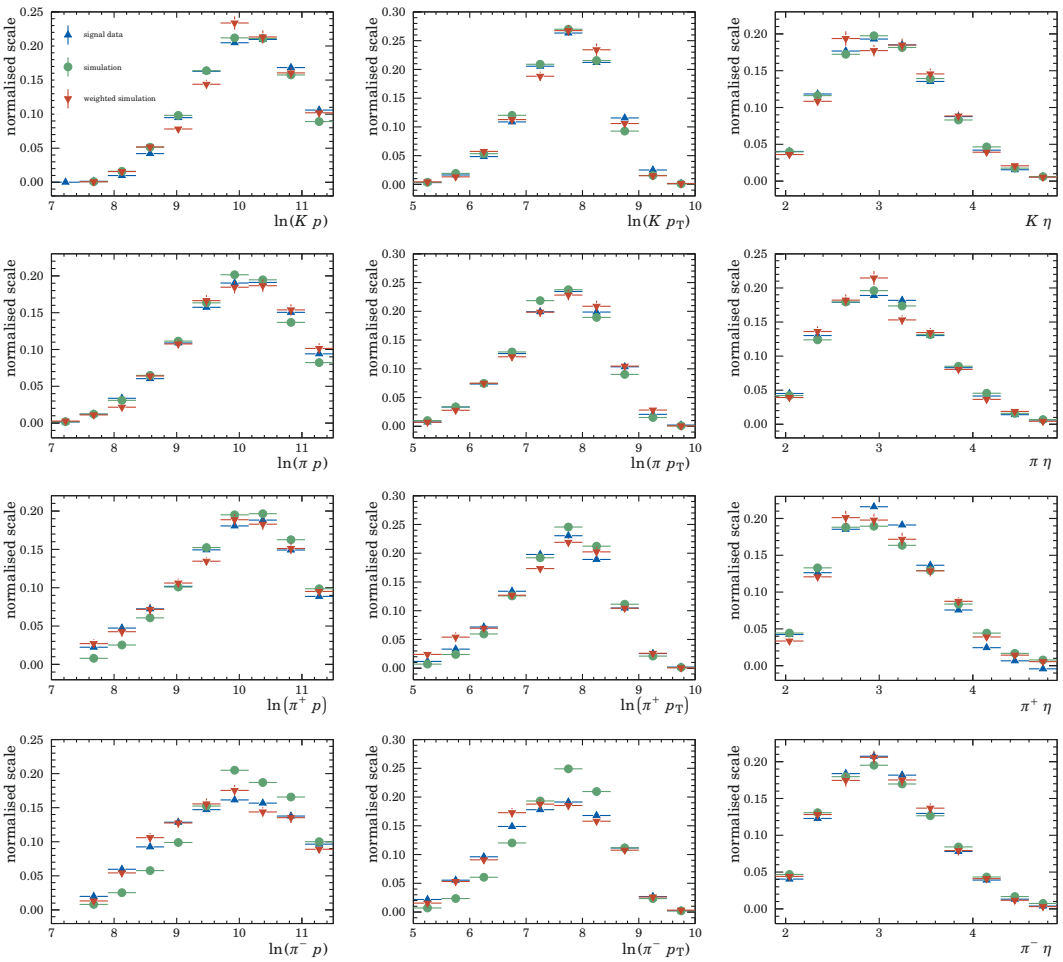

Figure A.20: Comparison of variables from the final state particles of simulated events (green), *sWeighted* $\overline{B}^0 \to D^0\pi^+\pi^-$ signal events from 2012 data (light blue) and reweighted simulated events (red). The distributions are normalised to unit area.

A.4 Background category tool

The background category (BKGCAT) tool is a tool to classify simulated events. The relevant categories are the following [110]:

- 0: Signal. The decay can be reconstructed according to the decay descriptor, and all final state particle have their associated Monte Carlo truth particle (MC particle). The conditions for the signal are:
  (a) Each final state particle has an MC particle associated to it with the same particle type.
  (b) All such MC particles have a common MC particle mother.
  (c) There is a one-to-one correspondence between the final state particles and final state MC particle daughters of the MC particle mother in (b).
  (d) The MC particle mother in (b) has the same particle type as the reconstructed decay mother.
  (e) All intermediate states of this decay are correctly reconstructed (as listed in the decay descriptor).
- 10: Quasi-signal. The decay fulfils the criteria of a signal, but not all intermediate states of this decay are correctly reconstructed (as listed in the decay descriptor). This is the case for the reconstruction of $\overline{B}^0 \to D^0 p\overline{p}$ and $\overline{B}^0 \to D^0\pi^+\pi^-$ decay because the *Stripping*-line uses a pseudo-particle X to reconstruct the full decay.

Physics backgrounds:

- 20: Fully reconstructed physics background. The decay topology is fully and correctly reconstructed, but the mother particle is incorrectly identified.
- 30: Reflection. One or more of the final state particles are misidentified. For example, the decay $D^0 \to K^-\pi^+$ can be mistaken as $D^0 \to K^-K^+$ if the pion is misidentified as a kaon.
- 40: Partially reconstructed physics background. A fragment of the decay is incorrectly identified as a signal decay.
- 50: Low-mass background. The low-mass background is a special case of the partially reconstructed physics background. There is no misidentification, and the reconstructed particle is found to have a mass systematically below the signal peak. This can be caused by radiative emission.

Technical and combinatorial background:

- 60: Ghost background. One or more of the final state particles from the decay are a ghost and have no associated MC particle.
- 63: Clone background. Two final state particles are associated to the same MC particle.
- 66: Hierarchy background. One of the final state particles has an associated MC particle which is also the mother of an MC particle associated to one of the other final state particles.
- 70: PV background. One or more of the final state particles come from the same PV or a short-lived resonance, and the event is not a PileUp.
- 80: Badly reconstructed PV background. All final state particles come from the same PV, or from short-lived resonances from the same PV. It is possible that the PV is not reconstructed correctly and particles coming from such vertex can seem to originate from a secondary vertex.
- 100: PileUp background/from different PV. The final state particles come, directly or indirectly, from more than one PV.
- 110: $b\bar{b}$ background. The background does not fit into any previous category, but at least one of the final state particles has a mother with bottom content.
- 120: $c\bar{c}$ background. The background does not fit into any previous category, but at least one of the final state particles has a mother with charm content.
- 130: Light-flavour background. The background does not fit into any previous category.

Truth-matched events refer to events in category 10 due to the structure of the *Stripping*-line. Although the signal identification is good, the `BKGCAT` tool is not perfect. There are also badly reconstructed signal events in other categories than the signal or quasi-signal category as can be seen in Figure A.21. Therefore, these categories are also included in the efficiency determination, but multiple candidates are removed.

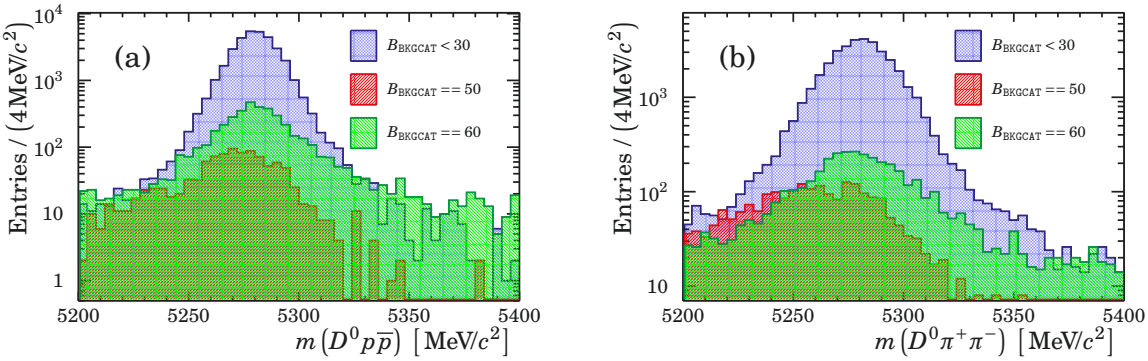

Figure A.21: B mass distribution for simulated (a) $\overline{B}^0 \to D^0 p\overline{p}$ and (b) $\overline{B}^0 \to D^0\pi^+\pi^-$ events in different BackgroundCategories.

APPENDIX B

LHCb variables

This Appendix summarises all variables used for the selection of candidates of interest. The selection sequence starts with the *Stripping* selection followed by the offline selection, a loose selection tightening the *Stripping* selection a bit further. The last selection step is the application of a multivariate analysis. The variables are listed in the order they appear in Chapter 4:

- n_{tracks}: The total number of trajectories reconstructed in the event.
- # long track: The number of long tracks in the event. Long tracks are those which pass the full tracking system from the VELO to the T-stations.
- # PV: The number of primary vertices (PV), proton-proton vertices, in the event.
- `Hlt2Topo.*Decision` or `Hlt2IncPhi.*Decision`: Either the topological lines of the HLT2 trigger for 2-, 3- and 4-body decays, or the inclusive HLT2 ϕ lines have triggered. The HLT2 ϕ lines search for detached ϕ mesons built from pairs of oppositely charged tracks identified as kaons by making use of the RICH detectors and is part of the B2OC *Stripping*-lines. For the decays analysed in this thesis, the `Hlt2Topo.*Decision` trigger decision is important.
- IP: The impact parameter (IP) is defined as the length of the vector from the fixed point to the nearest point on the particle trajectory:

$$\vec{i} = \vec{\mathbf{v}}_p - \vec{\mathbf{v}}_0 - \vec{\mathbf{p}}\frac{(\vec{\mathbf{v}}_p - \vec{\mathbf{v}}_0)\,\vec{\mathbf{p}}}{\vec{\mathbf{p}}^2}\,, \tag{B.1}$$

  where the particle's trajectory is parametrised as $\vec{\mathbf{v}}(t) = \vec{\mathbf{v}}_p + \vec{\mathbf{p}}t$ and $\vec{\mathbf{v}}_0$ stands for the position of the fixed point.
- Min χ^2_{IP}: The minimum χ^2 of the impact parameter of a track which is the minimum χ^2 distance of a particles trajectory to any set of primary vertices. The χ^2-value for the IP is defined as the increase of the χ^2 of the PV vertex fit when one adds the track into the vertex. The χ^2-value behaves almost like $(\text{IP}/\sigma_{\text{IP}})^2$ [166]. It can be used to check for the inconsistency with originating from a PV. Its value is small for particles coming from the PV as the B meson

whereas the value is larger for the D meson because of its separated production vertex.

- ghost probability: The ghost probability is the probability that the particle track is a fake track. Fake tracks compared to real tracks have fewer hits in the detector, and their χ^2/ndf of the track fit is worse [167].

- $\sum p_{\mathrm{T}}$: The sum of the transverse momenta of the daughter particles can be used to reduce background events.

- $\delta M\left(D^0\right)$: The difference between the measured mass of the D^0 and the PDG value [4] is used to reduce the background of random track combinations but is chosen to be large enough to be able to do background studies on the D^0 mass sidebands.

- DOCA: The distance of closest approach (DOCA) of two tracks coming from the same vertex is the minimal distance between these tracks and used to reduce the background. This variable can give information about the quality of the reconstructed vertex.

- Vertex χ^2/ndf (χ^2_{vtx}/ndf): The χ^2 per degree of freedom of the particle's vertex is used to ensure a good quality vertex.

- BPV (best PV): There are two different ways to define the best PV. For online reconstruction, the best PV is the one with the smallest IP. For offline reconstruction, the best PV is the one with the smallest IPχ^2.

- BPVVD χ^2 (χ^2_{VS}): The vertex separation (VS) is the geometrical distance from the particle's end vertex to the related best PV; χ^2_{VS} denotes its χ^2-separation of the vertex to its associated best PV. The end vertex is the decay vertex position for the reconstructed particle. Particles coming from a secondary vertex are well separated from the PV.

- BPVDDIRA ($\cos(\theta_{\mathrm{DIRA}})$): The direction angle ($cos(\theta_{\mathrm{DIRA}})$) is the cosine of the angle between the momentum of the particle and the direction of flight from the best PV to the decay vertex. The θ_{DIRA} value is close to zero for signal candidates.

- Track χ^2/ndf: The χ^2 per degree of freedom of the track fit is a variable to describe the quality of the track fit.

- p_{T}: The particle's transverse momentum (p_{T}) is the momentum component perpendicular to the beam axis.

- p: The particle's total momentum (p) and its transverse component are used to reject particles that do not come from meson decays.

- n-body invariant mass: The mass of the n-body system calculated as

$$m_{\text{inv}} = \left(\sum_n p_n\right)^2 , \tag{B.2}$$

  where p_n is the four-momentum of the nth particle.

- BPVLTIME (τ): The proper lifetime (τ) of the particle is given in units of time. B mesons and D mesons fly a certain distance before they decay.

- BPVIPCHI2 (χ^2_{IP}): The χ^2-separation of the distance of closest approach of a track to the best PV. The way of the χ^2 calculation is the same as for the Min χ^2_{IP}, but for the Min χ^2_{IP} the χ^2 is calculated for a set of primary vertices and only the smallest χ^2 is returned, whereas here only the χ^2 for the best PV is calculated and returned. The χ^2-separation for the IP of the best PV is used to reduce the combinatorial background as most of the particles come from the PV.

- Min IPDV: The minimum distance of a particles trajectory to any set of PVs is as well used to reduce the combinatorial background.

- FD: The flight distance (FD) of a particle with respect to its PV can be used to distinguish prompt D^0 mesons from D^0 mesons produced in the B^0 decay as D^0 mesons from B^0 decays have a longer distance to the B^0 decay vertex.

- η: The pseudorapidity (η) describes the angle of a particle relative to the beam axis

$$\eta = \frac{1}{2} \ln\left(\frac{p + p_{\text{L}}}{p - p_{\text{L}}}\right) , \tag{B.3}$$

  where p is the magnitude of the particle's three-momentum and p_{L} the momentum component along the beam axis.

- ProbNN$_x$: The particle identification variable for the particle x, trained using a Bayesian neural-network (see Appendix D).

- χ^2_{FD}: The measured flight distance divided by its uncertainty. The χ^2-value of the particle's flight distance can be used to distinguish prompt produced particles from non-prompt particles.

- daughters min χ^2_{IP}: The smallest χ^2_{IP} of the daughter particles.

APPENDIX C

Multivariate Analysis

Simple cut-based techniques can be extended to multivariate algorithms using machine learning algorithms such as Neural Networks (NNs), boosted decision trees (BDTs) or Fisher discriminants. They are widely used for the classification of events of different types. A toolkit for the ROOT framework, used to analyse data, is TMVA [112, 113], which has several machine learning techniques implemented. Two multivariate techniques will be explained in the following: the Fisher discriminant and the boosted decision tree.

C.1 Fisher discriminant

The Fisher discriminant [114, 115] is a linear classifier for pattern classification. It is often referred to as linear discriminant analysis (LDA). In linear discriminant analyses, the component axes in the hyperspace of the input variables are chosen to maximise the class separation as can be seen in Figure C.1.

For the classification of *e.g.* signal (S) and background (B) events with a Fisher discriminant following characteristics are needed: the overall sample of mean values $\bar{x}_k$ of each input variable $k = 1, \ldots, n_{\text{var}}$, the mean values of the class-specific samples $\bar{x}_{\text{S(B)},k}$, and the total covariance matrix $\mathbf{C}$ of the sample. The total covariance matrix can be decomposed into the sum of two matrices; the within-class matrix $\mathbf{W}$ and the between-class matrix $\mathbf{B}$: $\mathbf{C} = \mathbf{W} + \mathbf{B}$. The within-class matrix describes the dispersion of events to the means of their own class:

$$\mathbf{W}: \quad W_{k,l} = \sum_{U=\text{S,B}} \langle \left(x_{U,k} - \bar{x}_{U,k}\right) \left(x_{U,l} - \bar{x}_{U,l}\right) \rangle = C_{\text{S},kl} + C_{\text{B},kl} \, . \tag{C.1}$$

Whereas the between-class matrix describes the dispersion of events relative to the overall sample means:

$$\mathbf{B}: \quad B_{k,l} = \frac{1}{2} \sum_{U=\text{S,B}} \left(\bar{x}_{U,k} - \bar{x}_k\right) \left(\bar{x}_{U,l} - \bar{x}_l\right) \, . \tag{C.2}$$

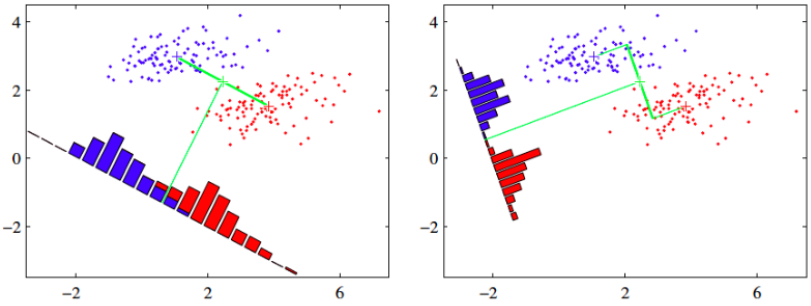

Figure C.1: LDA examples: The left plot shows samples from two classes (depicted in red and blue) along with the histograms resulting from projection onto the line joining the class means. Note that there is considerable class overlap in the projected space. The right plot shows the corresponding projection based on the Fisher linear discriminant, showing the greatly improved class separation. Taken from [168].

The Fisher coefficients F_k are then defined as

$$F_k = \frac{\sqrt{N_S N_B}}{N_S + N_B} \sum_{l=1}^{n_{var}} W_{kl}^{-1} \left(\bar{x}_{S,l} - \bar{x}_{B,l} \right) , \tag{C.3}$$

where N_S and N_B are the number of signal and background events in the training sample, respectively. The Fisher discriminant $y_{Fi}(i)$ for event i is calculated by

$$y_{Fi}(i) = F_0 + \sum_{k=1}^{n_{var}} F_k x_k(i) , \tag{C.4}$$

where F_0 is the offset that centres the sample mean $\bar{y}_{Fi}$ of all events at zero.

C.2 Boosted decision tree

Another way to classify a dataset is to use a decision tree [116] as shown in Figure C.2, where S means signal and B means background. A decision tree is a sequence of binary splits to the dataset. The top of the decision tree is called root node. From this node on, the decision tree algorithm usually works from top to bottom and divides the problems into subproblems. The two resulting nodes after the root node are then further classified until a given number of final nodes are obtained, or until all end nodes of the tree (leaves) are pure or until a node has too few events. A separation criterion for signal and background can be the *Gini Index* defined by

$$Gini = p \times (1 - p) , \tag{C.5}$$

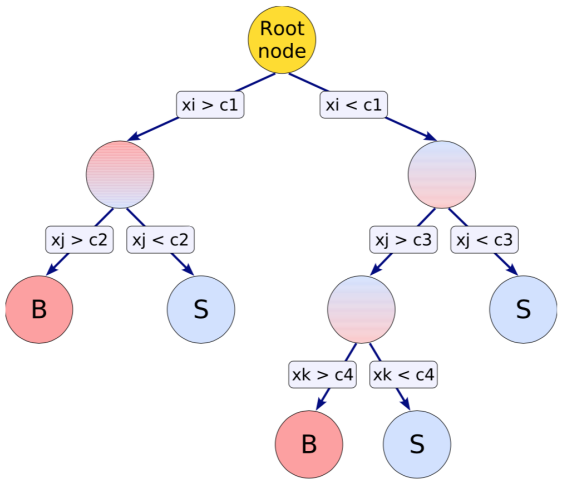

Figure C.2: Schematic of a decision tree. Figure taken from [112].

where $p = S/(S+B)$ is the purity of the sample. The Gini indices have maximum values when the sample is mixed entirely with signal and background events. The purer the sample becomes in either signal or background, the more the Gini indices decrease. If the leave has a purity greater than a certain value, then the leave is called signal leave; otherwise a background leave.

To make the powerful algorithm of the decision tree less vulnerable for small changes in the training data and even more powerful, a boosting algorithm [169–171] can be applied. Boosting algorithms allow transforming weak or base learners into strong learners. There are many different boosting algorithms available which in principle only vary in their way to weight the training data points and hypotheses. One of these boosting algorithms is the gradient boosting. When using gradient boosting many models are trained sequentially, and each model minimises the so-called loss function applying the gradient descent method. The local minimum is found using the negative gradient of the loss function.

C.3 Kolmogorov-Smirnov test

The Kolmogorov-Smirnov test (KS-test) [172] can be used to determine the significance of the difference between two datasets. It is non-parametric and makes no assumption about the data distribution. To compare two datasets, the KS-test uses

empirical distribution functions (EDFs) $F_n(x)$ defined as:

$$\begin{aligned} F_n(x) &= 0 && x < X_1 \\ F_n(x) &= \frac{k}{n} && X_k \le x < X_{k+1} \qquad k = 1,2,\ldots,n-1; \\ F_n(x) &= 1 && X_n \le x\,, \end{aligned} \tag{C.6}$$

where X_i are n values with $X_1 \le X_2 \le \ldots \le X_n$. For a given cumulative distribution function $F(x)$ is the Kolmogorov-Smirnov statistic defined as

$$D_n = \sup_x |F_n(x) - F(x)|\,. \tag{C.7}$$

For large samples ($n \to \infty$), the sampling distribution of D_n can be approximated as follows

$$\lim_{n\to\infty} P\left(D_n \le d/\sqrt{n}\right) = L(d)\,, \tag{C.8}$$

where

$$L(d) = 1 - 2\sum_{k=1}^{\infty} (-1)^{k-1} \mathrm{e}^{-2k^2d^2}\,. \tag{C.9}$$

The function $L(d)$ converges slowly for small d.

For two random EDFs $F_n(x)$ and $G_m(x)$ of sizes n and m, the Kolmogorov-Smirnov statistic is based on the maximum absolute difference between both empirical distributions

$$D_{m,n} = \sup_x |F_n(x) - G_m(x)|\,. \tag{C.10}$$

The asymptotic distribution of equation C.8 is also valid for two random EDFs

$$\lim_{m,n\to\infty} P\left(\sqrt{\frac{mn}{m+n}} D_{m,n} \le d\right) = L(d)\,. \tag{C.11}$$

The p-value is

$$P\left(D_{m,n} \ge D_O | H_0\right)\,, \tag{C.12}$$

where D_O is the observed value of the KS test statistic, and H_0 is the null hypothesis $F = G$.

C.4 Additional Figures from the MVA training

This section will show additional Figures for Section 4.2.4. Figures C.3 and C.4 show the correlation matrices for signal and background training samples for $\overline{B}^0 \to D^0 p\overline{p}$ and $\overline{B}^0 \to D^0 \pi^+ \pi^-$ decays, respectively.

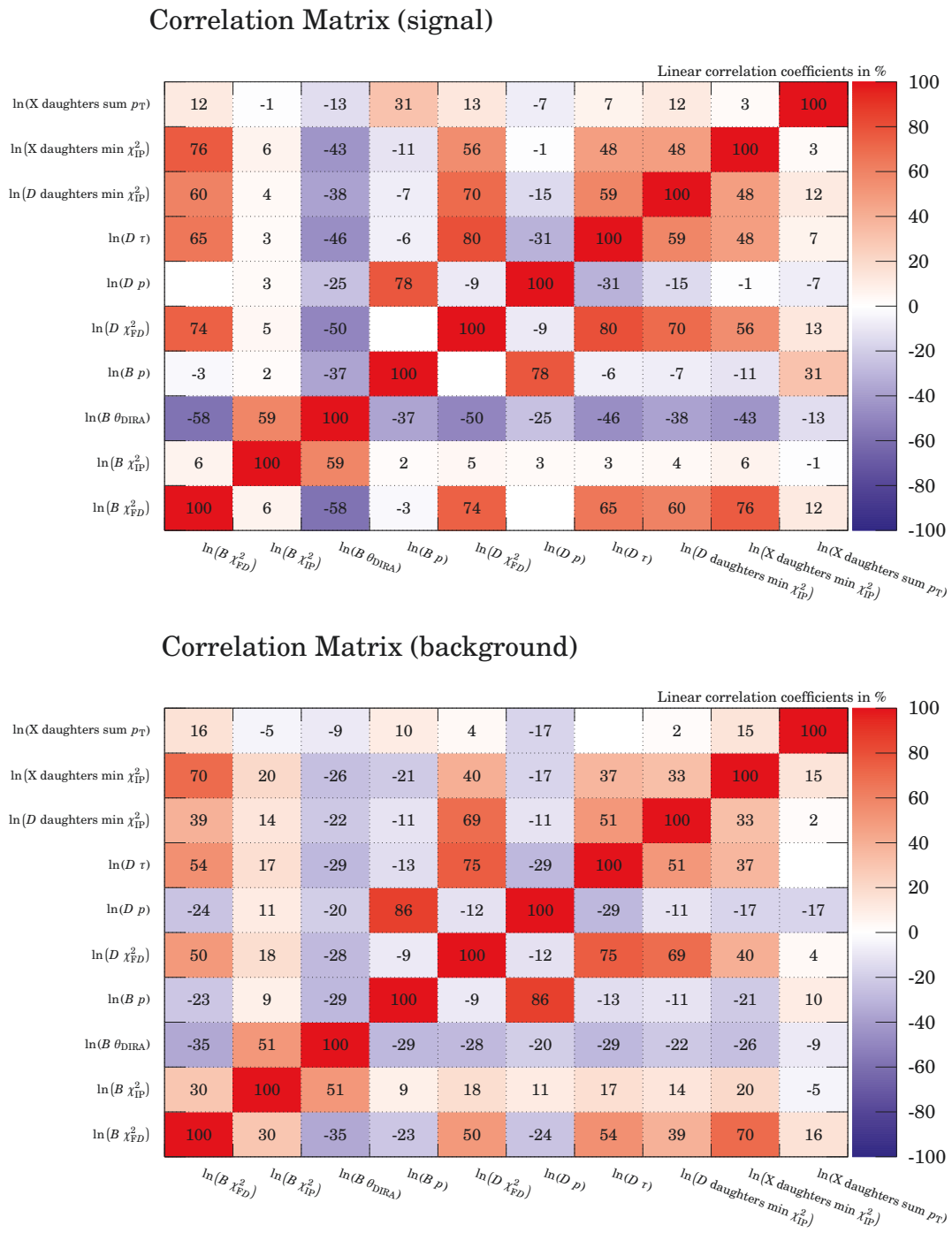

Figure C.3: Correlation matrix of the discriminator variables of the training samples for signal (top) and background (bottom) events of $\overline{B}^0 \to D^0 p\overline{p}$ decays.

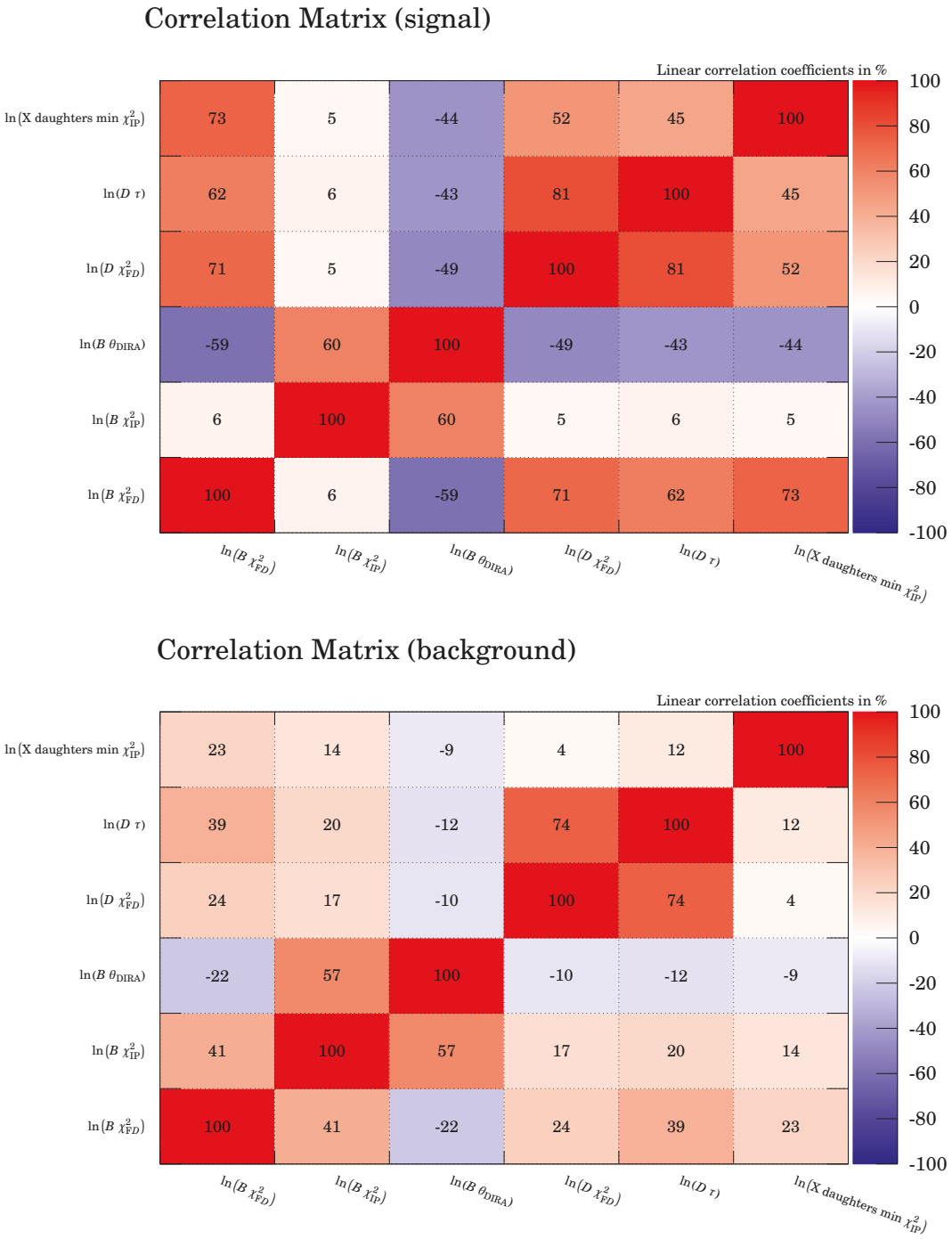

Figure C.4: Correlation matrix of the discriminator variables of the training samples for signal (top) and background (bottom) events of $\bar{B}^0 \to D^0\pi^+\pi^-$ decays.

APPENDIX D

PIDCalib package

The PIDCalib package [127] is a tool that provides access to calibration samples of different particle types and allows to use a data-driven technique for the calculation of particle identification efficiencies.

D.1 Particle identification variables

Particle identification [70] is primarily used to distinguish charged particle types. The LHCb experiment has two main versions of PID variables, those based on likelihood values $\mathrm{DLL}_{hh'}$ and those based on a Bayesian neural network $\mathrm{ProbNN}_{h^{(\prime)}}$, where $h^{(\prime)}$ stands for the particle hypothesis.

Information from the RICH detectors, the calorimeters and the muon stations are combined to provide the particle identification of charged tracks in terms of log-likelihood differences ($\mathrm{DLL}_{h\pi}$). As a reference, the likelihood value is always compared to the pion hypothesis. The global likelihood value is defined as:

$$\mathrm{DLL}_{h\pi} = \ln L(h) - \ln L(\pi) = \ln\left[\frac{L(h)}{L(\pi)}\right], \tag{D.1}$$

where $L(h)$ stands for the likelihood of a hadron track. The global likelihood hypothesis for kaons, pions and protons is formed by multiplying the different subdetector contributions:

$$L(K/\pi/p) = L^{RICH}(K/\pi/p) \times L^{\mathrm{CALO}}(\mathrm{non}\, e) \times L^{\mathrm{MUON}}\left(\mathrm{non}\,\mu\right). \tag{D.2}$$

The Bayesian neural-network-based variables $\mathrm{ProbNN}_{h^{(\prime)}}$ use as input information from the RICH detectors, the calorimeters and the muon stations, as for the likelihood values, but also additional information, *e.g.* the track's p and p_{T}. The neural networks are trained using simulated events of inclusive B decays. As the output of the neural networks depends on the arrangement and the tuning of the input samples, different versions of neural-network-based PID variables exist.

D.2 PIDCalib principle

The simulation of the detectors that contribute to the particle identification is non-trivial for various reasons. Therefore a data-driven technique is preferred for the measurement of the particle identification selection efficiency. The LHCb package that allows the determination of the efficiency is called PIDCalib (Particle Identification Calibration). The calibration samples are samples of decays with high statistics without any PID requirement applied. To provide a clear signal behaviour, the *sPlot* technique [106] is used for background subtraction. The efficiency ϵ_i can then be calculated using the number of signal events before N_i and after N_i' the PID selection:

$$\epsilon_i = \frac{N_i'}{N_i} \,. \tag{D.3}$$

To calculate the PID efficiency for a reference sample, which is a sample that is not the calibration sample, the parametrising variables (*e.g.* p, η) in the calibration sample can be weighted to look like those in the reference sample. The weights are defined as:

$$w_i = \frac{R_i}{C_i} \times \frac{C}{R} \,, \tag{D.4}$$

where R_i (C_i) is the number of tracks in the ith subset of the reference (calibration) sample, and R (C) is the total number of tracks in the reference (calibration) sample. The average efficiency per subset is then

$$\bar{\epsilon} = \frac{\sum_i \epsilon_i w_i C_i}{\sum_i w_i C_i} \,. \tag{D.5}$$

The PIDCalib tool allows mapping the PID efficiency as a function of the track's p, p_{T}, and η, the data taking conditions (data taking period, magnet polarity), and the number of tracks in the event. In this thesis calibration samples for kaons, pions and protons are needed. The calibration sample for kaons and pions is a clear sample of $D^*(2010)^+ \to D^0[K^-\pi^+]\pi_s^+$ decays. As calibration sample for protons the decays $\Lambda \to p\pi^-$ and $\Lambda_c^+ \to pK^-\pi^+$ can be taken.

APPENDIX E

Fit functions and the *sPlot* technique

This Chapter summarises all fit functions used in Chapter 4 to fit data points and gives a summary of the *sPlot* technique.

E.1 Definition of fit functions

Different functions, especially probability density functions are used in this thesis to describe data points. This section describes all functions that are used to fit data.

E.1.1 Gaussian function

The Gaussian function f_G with mean value μ and variance σ^2 is defined as

$$f_G\left(m;\mu,\sigma\right) = N \times \exp\left(-\frac{\left(m-\mu\right)^2}{2\sigma^2}\right), \tag{E.1}$$

where N is the function's normalisation factor. The normalisation factor

$$N = \frac{1}{\sigma\sqrt{2\pi}} \tag{E.2}$$

makes the Gaussian function a probability density function (PDF). The Gaussian function is shown in Figure E.1. The double Gaussian function used to fit the data is defined as

$$\begin{aligned} &f_{2G}\left(m;\mu,\sigma_1,r_G,\sigma_2\right) \\ &\quad = r_G \times f_G\left(m;\mu,\sigma_1\right) + \left(1-r_G\right) \times f_G\left(m;\mu,\sigma_2\right). \end{aligned} \tag{E.3}$$

E.1.2 Crystal Ball function

The Crystal Ball function f_{CB} [173–175], named after the Crystal Ball Collaboration, is a PDF consisting of a modified Gaussian function with a power-law tail. The power-law tail can be on the low end of the Gaussian function ($\alpha > 0$) or at the high

end ($\alpha < 0$). The Crystal Ball function is defined as

$$f_{CB}\left(m;\mu,\sigma,\alpha,n\right)_{\alpha>0} = N \times \begin{cases} \exp\left(-\frac{(m-\mu)^2}{2\sigma^2}\right) & \text{for } \frac{m-\mu}{\sigma} \geq -|\alpha| \\ A(\alpha,n) \times \left(B(\alpha,n) - \frac{m-\mu}{\sigma}\right)^{-n} & \text{for } \frac{m-\mu}{\sigma} < -|\alpha| \end{cases} \tag{E.4}$$

with

$$A(\alpha,n) = \left(\frac{n}{|\alpha|}\right)^n \times \exp\left(-\frac{|\alpha|^2}{2}\right) \quad \text{and} \quad B(\alpha,n) = \frac{n}{|\alpha|} - |\alpha| \,. \tag{E.5}$$

The parameters α and n describe the power-law tail. The fitting parameters μ and σ are the mean value and the standard deviation of the Gaussian core, respectively. In case of $\alpha < 0$ is $(m-\mu)/\sigma = -(m-\mu)/\sigma$. The normalisation factor N is defined as

$$N = \frac{1}{\sigma(C+D)} \tag{E.6}$$

with

$$C = \frac{n}{|\alpha|} \times \frac{1}{n-1} \times \exp\left(-\frac{|\alpha|^2}{2}\right) \quad \text{and} \quad D = \sqrt{\frac{\pi}{2}} \times \left(1 + \operatorname{erf}\left(\frac{|\alpha|}{\sqrt{2}}\right)\right) . \tag{E.7}$$

The error function erf is defined as

$$\operatorname{erf}(x) = \frac{2}{\sqrt{\pi}} \int_0^x e^{-\tau^2} \, \mathrm{d}\tau \,. \tag{E.8}$$

The Crystal Ball function with variation of the parameters α and n can be seen in Figure E.1. The double Crystal Ball function used to fit the data is defined as

$$\begin{aligned} &f_{2CB}(m;\mu,\sigma_1,\alpha_1,n_1,r_{CB},\sigma_2,\alpha_2,n_2) \\ &\quad = r_{CB} \times f_{CB}(m;\mu,\sigma_1,\alpha_1,n_1) + (1-r_{CB}) \times f_{CB}(m;\mu,\sigma_2,\alpha_2,n_2) \,. \end{aligned} \tag{E.9}$$

E.1.3 RooKeysPDF

Data distributions can be approximated using kernel estimation. It is an unbinned and non-parametric estimate of the PDF. RooFit [118] allows estimating PDFs using *RooKeysPdf*. It is an implemented one-dimensional kernel estimation which models the distribution as a superposition of Gaussian kernels. More about the kernel estimation algorithm can be found in [176].

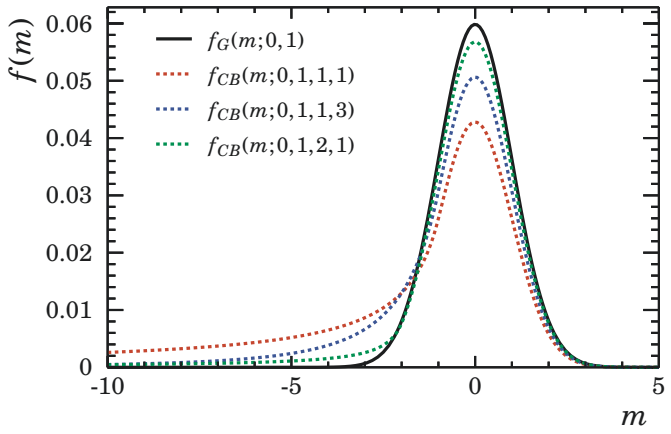

Figure E.1: Gaussian PDF and Crystal Ball PDF with variation of the α and n parameters.

E.2 *sPlot* technique

The *sPlot* technique [106] is a powerful tool to visualise signal behaviour. This likelihood-based background subtraction approach allows reconstructing distributions for control variables. The *sPlot* technique assumes that the control variable is uncorrelated with the discriminating variables.

The *sPlot* technique can be applied to unbinned maximum likelihood analysis of samples with several components, *e.g.* signal and background events. The log-likelihood can be expressed as:

$$\mathcal{L} = \sum_{e=1}^{N} \ln\left(\sum_{i=1}^{\mathrm{N_c}} N_i f_i(y_e)\right) - \sum_{i=1}^{\mathrm{N_c}} N_i \,, \tag{E.10}$$

where N is the total number of events, $\mathrm{N_c}$ is the number of components in the data sample, N_i is the number of events expected on average for the i^{th} component, y represents the set of discriminating variables (which can be correlated with each other), and $f_i(y_e)$ is the value of the PDF of y for the i^{th} component and for event e. Assuming an unknown set of control variables x and discriminating variables y, the two sets of variables x and y are uncorrelated. The so-called *sWeight* for the component n for each event e is then given as:

$${}_s\mathcal{P}_{\mathrm{n}}(y_e) = \frac{\sum_{j=1}^{\mathrm{N_c}} \mathbf{V}_{\mathrm{n}j} f_j(y_e)}{\sum_{k=1}^{\mathrm{N_c}} N_k f_k(y_e)} \,, \tag{E.11}$$

where $\mathbf{V}_{\mathrm{n}j}$ is the covariance matrix obtained from the likelihood fit. The inverse of the covariance matrix, given by the second derivatives of $-\mathcal{L}$:

$$\mathbf{V}_{\mathrm{n}j}^{-1} = \frac{\partial^2(-\mathcal{L})}{\partial N_{\mathrm{n}} \partial N_j} = \sum_{e=1}^{N} \frac{f_{\mathrm{n}}(y_e) f_j(y_e)}{\left(\sum_{k=1}^{\mathrm{N_c}} N_k f_k(y_e)\right)^2} \,. \tag{E.12}$$

The distribution of the control variable x can then be derived from the *sPlot* histogram:

$$N_{\mathrm{n}}\, {}_s\tilde{\mathrm{M}}_{\mathrm{n}}(\bar{x})\delta x \equiv \sum_{e \subset \delta x} {}_s\mathcal{P}_{\mathrm{n}}(y_e) \,, \tag{E.13}$$

where $\sum_{e \subset \delta x}$ runs over $N_{\delta x}$ events and each interval is centred around $\bar{x}$ and has a total width of δx. The *sPlot* technique has following properties:

- Each distribution of the control variable x is properly normalised. The sum over the x-bins of $N_{\mathrm{n}}\, {}_s\tilde{\mathrm{M}}_{\mathrm{n}}\delta x$ is equal to N_{n}

$$\sum_{e=1}^{N} {}_s\mathcal{P}_{\mathrm{n}}(y_e) = N_{\mathrm{n}} \,. \tag{E.14}$$

- The sum over all components of expected numbers of events in each bin equals to the number of events actually observed. For any event is:

$$\sum_{l=1}^{\mathrm{N_c}} {}_s\mathcal{P}_l(y_e) = 1 \,. \tag{E.15}$$

- The statistical uncertainty on $N_{\mathrm{n}}\, {}_s\tilde{\mathrm{M}}_{\mathrm{n}}(x)\delta x$ can be defined in each bin by

$$\sigma\left[N_{\mathrm{n}}\, {}_s\tilde{\mathrm{M}}_{\mathrm{n}}(x)\delta x\right] = \sqrt{\sum_{e \subset \delta x} ({}_s\mathcal{P}_{\mathrm{n}})^2} \tag{E.16}$$

In the case of a fit to the invariant mass m with a signal and background component, the log-likelihood is:

$$\mathcal{L} = \sum_{e=1}^{N} \ln(\mathrm{N_s} f_{\mathrm{s}}(m_e) + \mathrm{N_b} f_{\mathrm{b}}(m_e)) - \mathrm{N_s} - \mathrm{N_b} \,, \tag{E.17}$$

where N, $\mathrm{N_s}$, $\mathrm{N_b}$ are the number of events and the number of signal and background events, respectively. The PDF for signal (background) is f_{s} (f_{b}). And the inverse covariance matrix would be defined as:

$$\mathbf{V}_{\mathrm{n}j}^{-1} = \sum_{e=1}^{N} \frac{f_{\mathrm{n}}(m_e) f_j(m_e)}{(\mathrm{N_s} f_{\mathrm{s}}(m_e) + \mathrm{N_b} f_{\mathrm{b}})^2} \,. \tag{E.18}$$

The *sWeight* for the signal $w_{\mathrm{s},e}$ and the *sWeight* for the background $w_{\mathrm{b},e}$ is then:

$$w_{\mathrm{s},e} = \frac{\mathbf{V}_{\mathrm{ss}} f_{\mathrm{s}}(m_e) + \mathbf{V}_{\mathrm{sb}} f_{\mathrm{b}}(m_e)}{\mathrm{N_s} f_{\mathrm{s}} + \mathrm{N_b} f_{\mathrm{b}}}\,, \tag{E.19}$$

$$w_{\mathrm{b},e} = \frac{\mathbf{V}_{\mathrm{bs}} f_{\mathrm{s}}(m_e) + \mathbf{V}_{\mathrm{bb}} f_{\mathrm{b}}(m_e)}{\mathrm{N_s} f_{\mathrm{s}} + \mathrm{N_b} f_{\mathrm{b}}}\,. \tag{E.20}$$

Note that the *sPlot* technique is valid for uncorrelated or almost uncorrelated variables. A comparison of *sWeighted* data with simulation is not trivial if the discriminating variable y is correlated with the control variable x.

APPENDIX F

Efficiency

This Chapter summarises additional plots and information to the efficiency determination, especially the distribution of the efficiency over the Dalitz plane.

The efficiency in this thesis is factorised as follows

$$\epsilon = \epsilon_{\text{acc|gen}} \times \epsilon_{\text{sel|acc}} \times \epsilon_{\text{PID|sel}} \times \epsilon_{L0|\text{PID}} \,, \tag{F.1}$$

where

- $\epsilon_{\text{acc|gen}}$ is the fraction of simulated events decaying inside the detector acceptance,
- $\epsilon_{\text{sel|acc}}$ is the fraction of events, that are stripped and fully reconstructed, and pass the HLT trigger requirement, the offline selection, and the selection on the Fisher discriminant,
- $\epsilon_{\text{PID|sel}}$ is the fraction of events passing selection on the particle identification,
- $\epsilon_{L0|\text{PID}}$ is the fraction of events which pass the L0 trigger requirement.

A detailed description of how the efficiency is determined can be found in Section 4.5. Figures F.1 to F.7 show the all determined efficiencies distributed over the Dalitz plane. They are normalised so that the integral over the Dalitz plane is one. Figure F.1 shows the distribution of fully reconstructed and stripped simulated events and Figure F.2 the change in the efficiency distribution from fully reconstructed and stripped events to events that are fully reconstructed and stripped with HLT trigger requirement and further selection cuts applied. The correction factor for the track reconstruction from correction tables is close to one. Its distribution over the Dalitz plane is shown in Figure F.3. Figure F.4 shows the distribution of the PID efficiency derived from efficiency tables using the PIDCalib package (see Appendix D). Selected events are inside the detector acceptance, stripped and fully reconstructed with HLT trigger requirements applied as well as offline selection and a cut on the Fisher discriminant. These events can either be `L0Hadron_TOS` or `L0Global_TIS`. The distribution of the `L0Hadron_TOS` efficiency obtained using the TISTOS method for simulated events is shown in Figure F.5. The distribution of selected events weighted with the

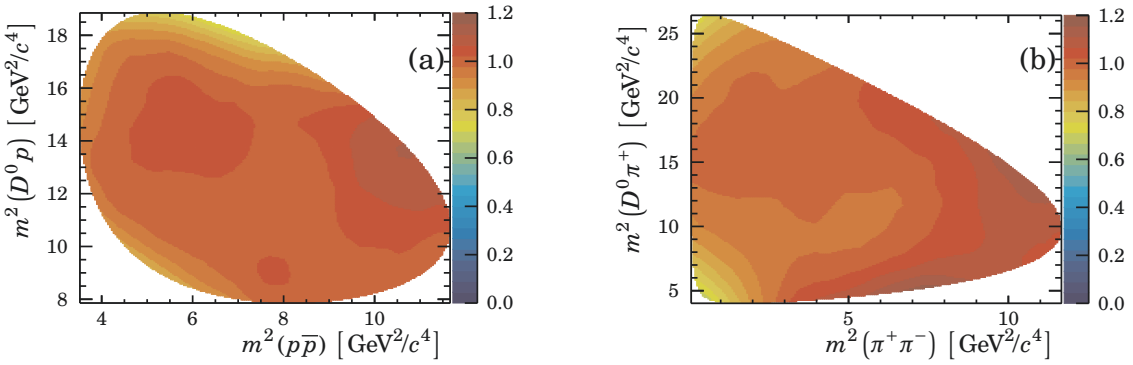

Figure F.1: Distribution of $\epsilon_{\text{sel}*|\text{gen}}$ over the Dalitz plane for (a) $\overline{B}^0 \to D^0 p\overline{p}$ decays and (b) $\overline{B}^0 \to D^0\pi^+\pi^-$ decays.

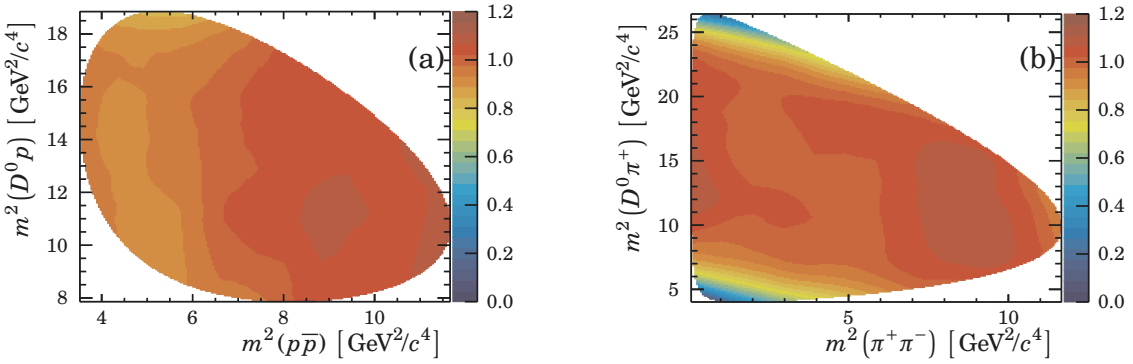

Figure F.2: Distribution of $\epsilon_{\text{sel}|\text{sel}*}$ over the Dalitz plane for (a) $\overline{B}^0 \to D^0 p\overline{p}$ decays and (b) $\overline{B}^0 \to D^0\pi^+\pi^-$ decays without track reconstruction efficiency correction.

`L0Hadron_TOS` efficiency from data is shown in Figure F.6. The overall efficiency distribution used for the branching fraction measurement is visualised in Figure F.7. It does not include the L0 trigger efficiency as it was derived from data.

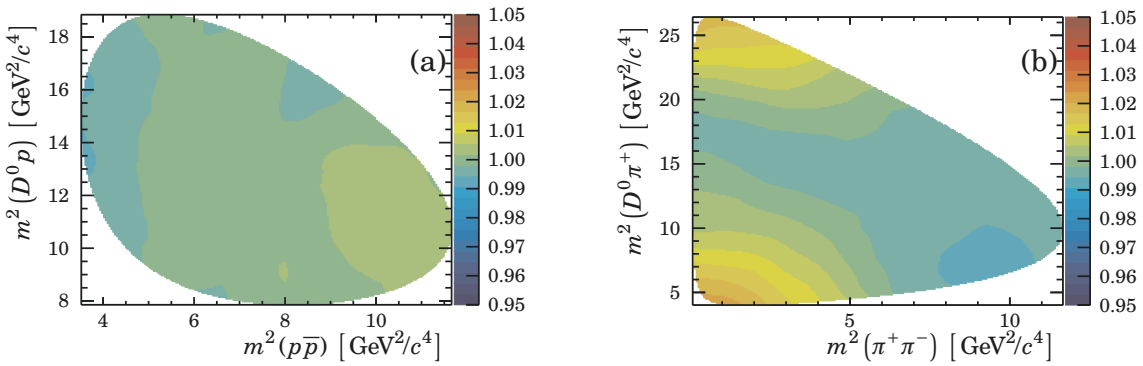

Figure F.3: Distribution of track reconstruction efficiency over the Dalitz plane for (a) $\overline{B}^0 \to D^0 p\overline{p}$ decays and (b) $\overline{B}^0 \to D^0\pi^+\pi^-$ decays.

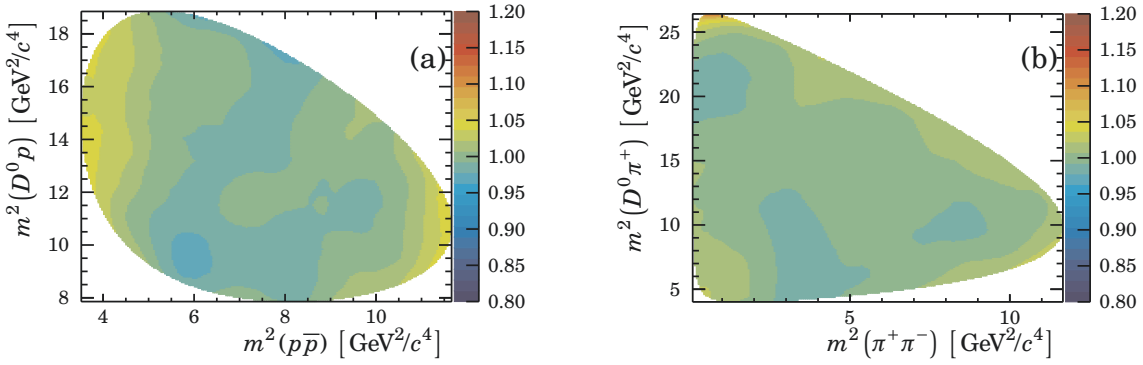

Figure F.4: Distribution of $\epsilon_{\text{PID}|\text{sel}}$ over the Dalitz plane for (a) $\overline{B}^0 \to D^0 p\overline{p}$ decays and (b) $\overline{B}^0 \to D^0\pi^+\pi^-$ decays using PID efficiency tables.

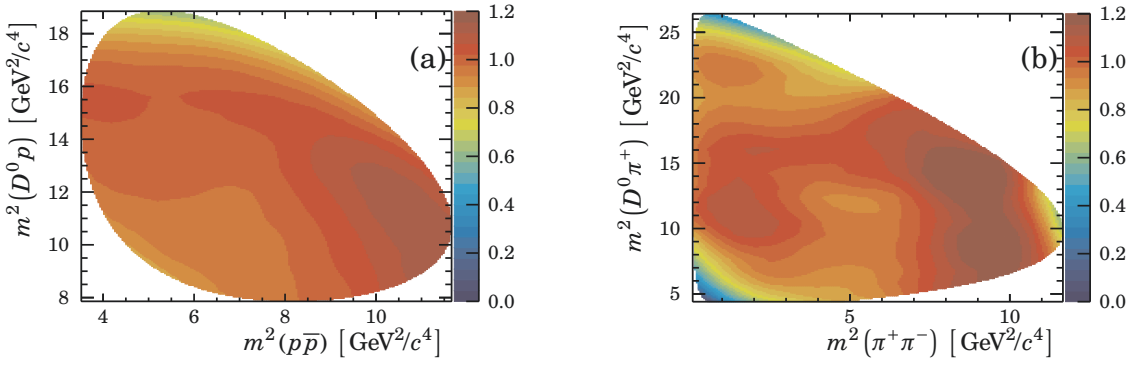

Figure F.5: Distribution of the TOS trigger efficiency derived from simulated events with the TISTOS method over the Dalitz plane for (a) $\overline{B}^0 \to D^0 p\overline{p}$ decays and (b) $\overline{B}^0 \to D^0\pi^+\pi^-$.

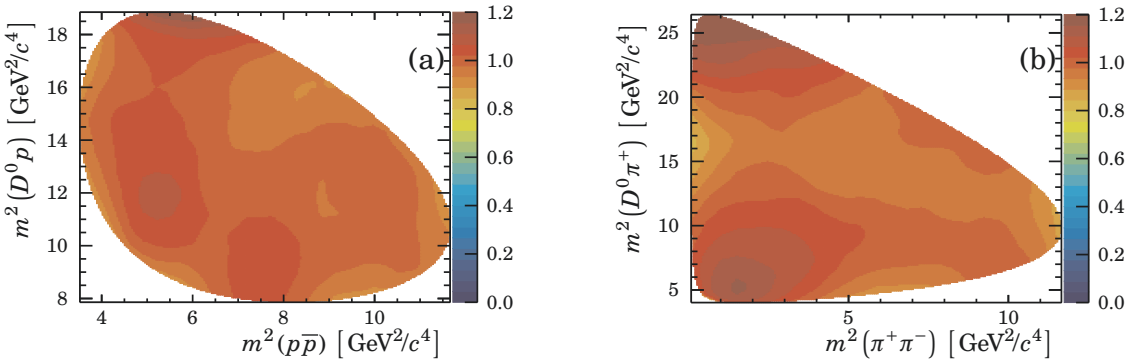

Figure F.6: Distribution of the `L0Hadron_TOS` efficiency (a) $\overline{B}^0 \to D^0 p\overline{p}$ decays and (b) $\overline{B}^0 \to D^0\pi^+\pi^-$ decays obtained by weighting the events using `L0Hadron_TOS` efficiency tables.

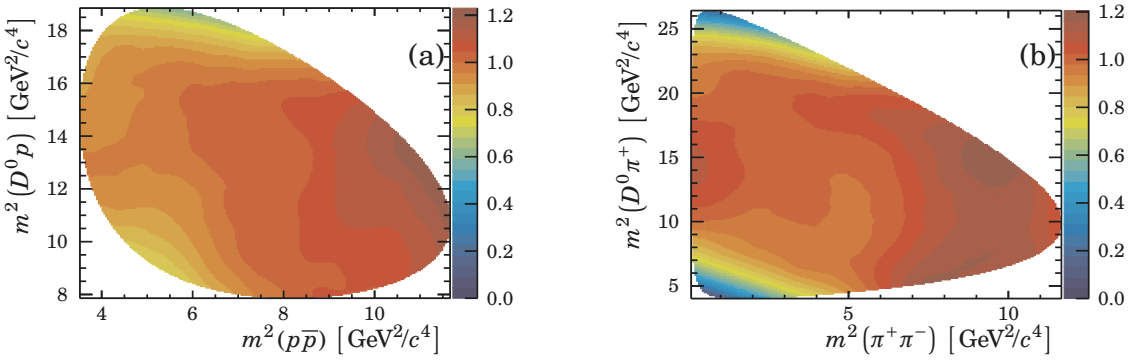

Figure F.7: Total efficiency distribution over the Dalitz plane for (a) $\overline{B}^0 \to D^0 p\overline{p}$ decays and (b) $\overline{B}^0 \to D^0\pi^+\pi^-$ decays.

APPENDIX G

Supplementary material containing Dalitz structures

This Appendix collects supplementary to Chapter 5.

G.1 Data distributions

Figure G.1 shows the data in the signal region $m(D^0 p\overline{p}) \in [5250;5310]\text{MeV}/c^2$ for the invariant mass squared of the $D^0\overline{p}$ versus $D^0 p$, the $D^0\overline{p}$ versus $p\overline{p}$, and the $p\overline{p}$ versus $D^0 p$. Structures, where the Dalitz plane is highly populated, are visible near the lower invariant mass squared boundaries for the $D^0 p$ and the $p\overline{p}$, whereas other parts of the Dalitz plane are less populated. Note, that the Figures also include background events in the region $m(D^0 p\overline{p}) \in [5250;5310]\text{MeV}/c^2$. The projections for the invariant mass of the $D^0 p$ system, the $p\overline{p}$ system, and the $D^0\overline{p}$ system are shown in Figure G.2 compared the distribution of a uniformly populated Dalitz plane including efficiency effects. Similarly, the projections of data onto the cosine of the helicity angle compared to simulated events are shown in Figure G.3. Each value of the cosine of the helicity angle corresponds to a slice in the Dalitz plane.

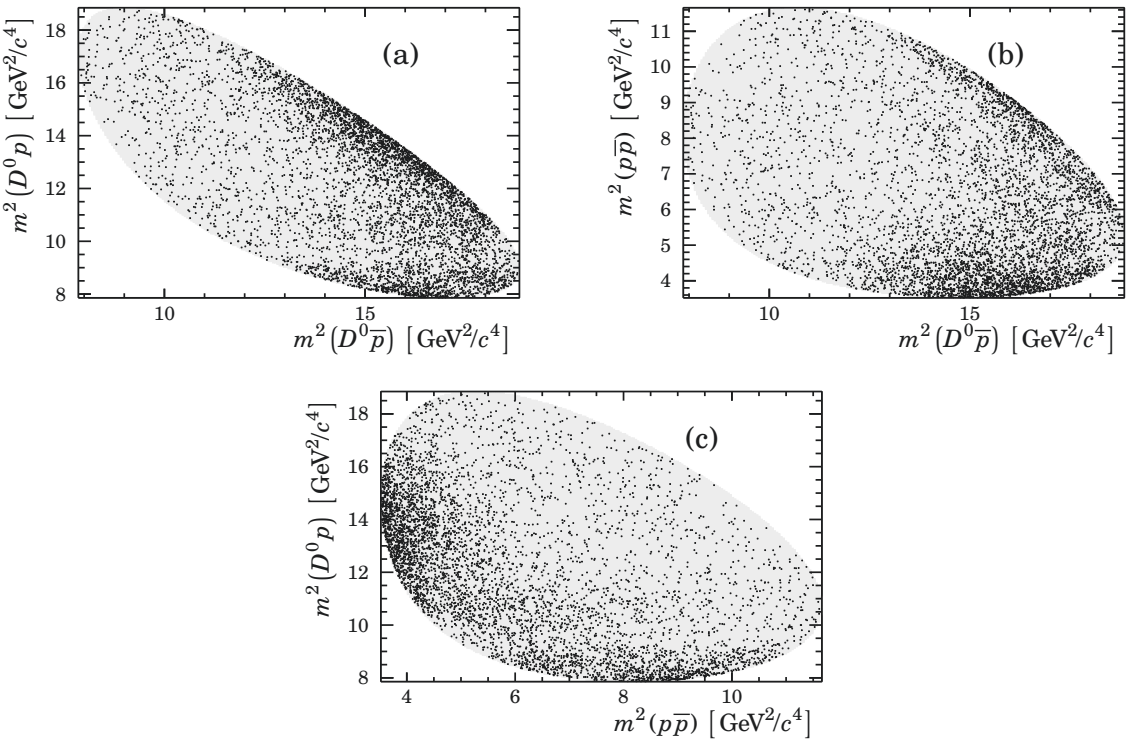

Figure G.1: Invariant mass squared of (a) the $D^0\overline{p}$ versus D^0p, (b) the $D^0\overline{p}$ versus $p\overline{p}$, and (c) the $p\overline{p}$ versus D^0p. The grey area shows the kinematically allowed region.

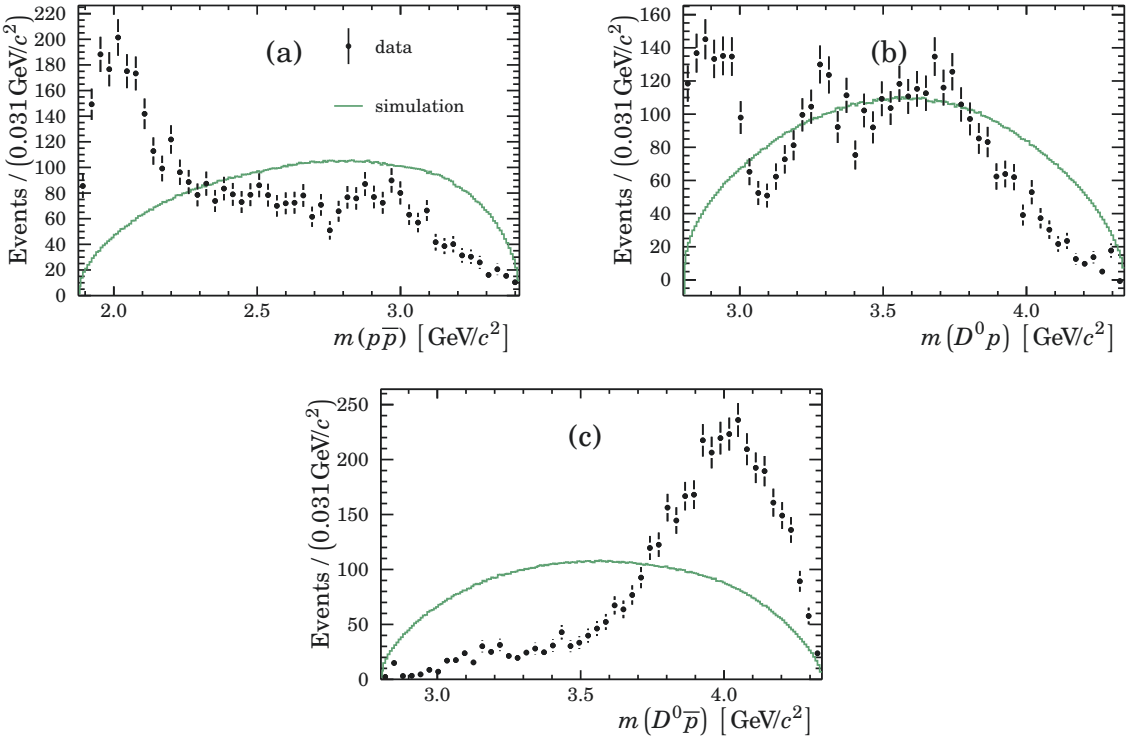

Figure G.2: Projections of the invariant mass of (a) the D^0p, (b) the $p\overline{p}$, and (c) the $D^0\overline{p}$ combination from $\overline{B}^0 \to D^0p\overline{p}$ decays. The background is subtracted using the *sPlot* technique. The solid (green) curve shows the expected distribution from phase space simulated events including efficiencies.

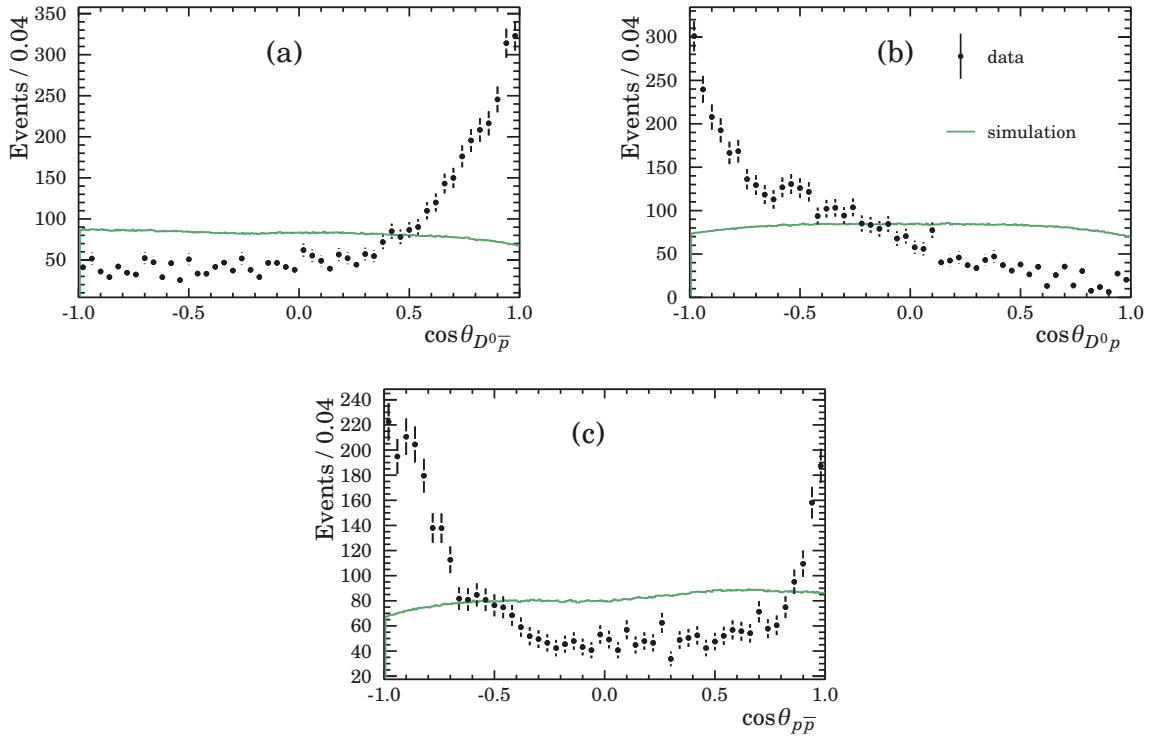

Figure G.3: Projections of data onto the cosine of the helicity angle of (a) the $D^0 p$ system, (b) the $p\overline{p}$ and (c) the $D^0\overline{p}$ system. The background is subtracted using the *sPlot* technique. The solid (green) curve shows the expected distribution from phase space simulated events including efficiencies.

Bibliography

[1] ARGUS Collaboration, H. Albrecht *et al.*, *Measurement of Inclusive B Meson Decays Into Baryons*, Z. Phys. **C42** (1989) 519.

[2] CLEO Collaboration, G. D. Crawford *et al.*, *Measurement of baryon production in B meson decay*, Phys. Rev. **D45** (1992) 752.

[3] ARGUS Collaboration, H. Albrecht *et al.*, *Measurement of Inclusive Baryon Production in B Meson Decays*, Z. Phys. **C56** (1992) 1.

[4] K. A. Olive, *Review of Particle Physics*, Chin. Phys. **C40** (2016) 100001.

[5] Belle Collaboration, *BABAR* Collaboration, A. J. Bevan *et al.*, *The Physics of the B Factories*, Eur. Phys. J. **C74** (2014) 3026, arXiv:1406.6311.

[6] *BABAR* Collaboration, P. del Amo Sanchez *et al.*, *Observation and study of the baryonic B-meson decays* $B \to D^{(*)} p\overline{p}(\pi)(\pi)$, Phys. Rev. **D85** (2012) 092017, arXiv:1111.4387.

[7] H.-Y. Cheng, C. Q. Geng, and Y. K. Hsiao, *Possibly New Charmed Baryon States from* $\overline{B}^0 \to p\overline{p}D^{(*)0}$ *Decays*, Phys. Rev. **D89** (2014) 034005, arXiv:1205.0117.

[8] LHCb Collaboration, R. Aaij *et al.*, *Evidence for CP Violation in* $B^+ \to p\overline{p}K^+$ *Decays*, Phys. Rev. Lett. **113** (2014) 141801, arXiv:1407.5907.

[9] H.-Y. Cheng and K.-C. Yang, *Charmless exclusive baryonic B decays*, Phys. Rev. **D66** (2002) 014020, arXiv:hep-ph/0112245.

[10] W.-S. Hou and A. Soni, *Pathways to rare baryonic B decays*, Phys. Rev. Lett. **86** (2001) 4247, arXiv:hep-ph/0008079.

[11] A. Datta and P. J. O'Donnell, *A New state of baryonium*, Phys. Lett. **B567** (2003) 273, arXiv:hep-ph/0306097.

[12] J. L. Rosner, *Low mass baryon anti-baryon enhancements in B decays*, Phys. Rev. **D68** (2003) 014004, arXiv:hep-ph/0303079.

[13] C.-K. Chua, W.-S. Hou, and S.-Y. Tsai, *Charmless three-body baryonic B decays*, Phys. Rev. **D66** (2002) 054004, arXiv:hep-ph/0204185.

[14] C.-K. Chua and W.-S. Hou, *Three body baryonic $\overline{B} \to \Lambda\overline{p}\pi$ decays and such*, Eur. Phys. J. **C29** (2003) 27, arXiv:hep-ph/0211240.

[15] J. Haidenbauer, U.-G. Meissner, and A. Sibirtsev, *Near threshold $p\overline{p}$ enhancement in B and J/ψ decay*, Phys. Rev. **D74** (2006) 017501, arXiv:hep-ph/0605127.

[16] B. Kerbikov, A. Stavinsky, and V. Fedotov, *Model independent view on the low mass proton anti-proton enhancement*, Phys. Rev. **C69** (2004) 055205, arXiv:hep-ph/0402054.

[17] V. Laporta, *Final state interaction enhancement effect on the near threshold $p\overline{p}$ system in $B^{\pm} \to p\overline{p}\pi^{\pm}$ decay*, Int. J. Mod. Phys. **A22** (2007) 5401, arXiv:0707.2751.

[18] A. Sibirtsev *et al.*, *Near threshold enhancement of the $p\overline{p}$ mass spectrum in J/ψ decay*, Phys. Rev. **D71** (2005) 054010, arXiv:hep-ph/0411386.

[19] Belle Collaboration, K. Abe *et al.*, *Observation of $\overline{B}^0 \to D^{(*)0}p\overline{p}$*, Phys. Rev. Lett. **89** (2002) 151802, arXiv:hep-ex/0205083.

[20] S. L. Glashow, *Partial Symmetries of Weak Interactions*, Nucl. Phys. **22** (1961) 579.

[21] S. Weinberg, *A Model of Leptons*, Phys. Rev. Lett. **19** (1967) 1264.

[22] A. Salam, *Weak and Electromagnetic Interactions*, Conf. Proc. **C680519** (1968) 367.

[23] S. Weinberg, *The Making of the Standard Model*, Eur. Phys. J. **C34** (2004) 5, arXiv:hep-ph/0401010, [,99(2005)].

[24] J. J. Thomson, *Cathode rays*, Phil. Mag. **44** (1897) 293.

[25] E. Rutherford, *The scattering of alpha and beta particles by matter and the structure of the atom*, Phil. Mag. **21** (1911) 669.

[26] J. Chadwick, *Possible Existence of a Neutron*, Nature **129** (1932) 312.

[27] C. M. G. Lattes, G. P. S. Occhialini, and C. F. Powell, *Observations on the Tracks of Slow Mesons in Photographic Emulsions. 1*, Nature **160** (1947) 453, ; C. M. G. Lattes, G. P. S. Occhialini, and C. F. Powell, *Observations on the Tracks of Slow Mesons in Photographic Emulsions. 2*, Nature **160** (1947) 486, .

[28] C. L. Cowan *et al.*, *Detection of the free neutrino: A Confirmation*, Science **124** (1956) 103.

[29] ATLAS Collaboration, G. Aad *et al.*, *Observation of a new particle in the search for the Standard Model Higgs boson with the ATLAS detector at the LHC*, Phys. Lett. **B716** (2012) 1, arXiv:1207.7214.

[30] CMS Collaboration, S. Chatrchyan *et al.*, *Observation of a new boson at a mass of* 125 GeV *with the CMS experiment at the LHC*, Phys. Lett. **B716** (2012) 30, arXiv:1207.7235.

[31] A. Einstein, *The Foundation of the General Theory of Relativity*, Annalen Phys. **49** (1916) 769, [Annalen Phys.14,517(2005)].

[32] S. T. Petcov, *The Nature of Massive Neutrinos*, Adv. High Energy Phys. **2013** (2013) 852987, arXiv:1303.5819.

[33] L. Canetti, M. Drewes, and M. Shaposhnikov, *Matter and Antimatter in the Universe*, New J. Phys. **14** (2012) 095012, arXiv:1204.4186.

[34] L. Sadeghian, *Star Clusters and Dark Matter as Probes of the Spacetime Geometry of Massive Black Holes*, PhD thesis, Washington University in St. Louis, 2013, arXiv:1308.5378.

[35] Planck Collaboration, R. Adam *et al.*, *Planck 2015 results. IX. Diffuse component separation: CMB maps*, arXiv:1502.05956.

[36] S. Weinberg, *Implications of Dynamical Symmetry Breaking*, Phys. Rev. **D13** (1976) 974.

[37] R. D. Peccei, *The Strong CP problem and axions*, Lect. Notes Phys. **741** (2008) 3, arXiv:hep-ph/0607268, [,3(2006)].

[38] M. E. Peskin and D. V. Schroeder, *An Introduction to Quantum Field Theory*, Westview Press, 1995.

[39] W. Greiner, S. Schramm, and E. Stein, *Quantum chromodynamics*, Springer-Verlag Berlin Heidelberg, 2007.

[40] Wikipedia, *Standard model — Wikipedia, the free encyclopedia*, 2016. [Accessed on 13/07/2016].

[41] F. Englert and R. Brout, *Broken Symmetry and the Mass of Gauge Vector Mesons*, Phys. Rev. Lett. **13** (1964) 321.

[42] P. W. Higgs, *Broken Symmetries and the Masses of Gauge Bosons*, Phys. Rev. Lett. **13** (1964) 508.

[43] A. D. Sakharov, *Violation of CP Invariance, C Asymmetry, and Baryon Asymmetry of the Universe*, Pisma Zh. Eksp. Teor. Fiz. **5** (1967) 32, [Usp. Fiz. Nauk **161** (1991) 61]; A. D. Sakharov, *Violation of CP invariance, C asymmetry, and baryon asymmetry of the universe*, Soviet Physics Uspekhi **34** (1991) 392.

[44] J. H. Christenson, J. W. Cronin, V. L. Fitch, and R. Turlay, *Evidence for the* 2π *Decay of the* K_2^0 *Meson*, Phys. Rev. Lett. **13** (1964) 138.

[45] N. Cabibbo, *Unitary Symmetry and Leptonic Decays*, Phys. Rev. Lett. **10** (1963) 531, .

[46] M. Kobayashi and T. Maskawa, *CP Violation in the Renormalizable Theory of Weak Interaction*, Prog. Theor. Phys. **49** (1973) 652.

[47] A. B. Carter and A. I. Sanda, *CP Violation in B Meson Decays*, Phys. Rev. **D23** (1981) 1567.

[48] *BABAR* Collaboration, B. Aubert *et al.*, *The BABAR detector*, Nucl. Instrum. Meth. **A479** (2002) 1, arXiv:hep-ex/0105044.

[49] A. Abashian *et al.*, *The Belle Detector*, Nucl. Instrum. Meth. **A479** (2002) 117.

[50] *BABAR* Collaboration, B. Aubert *et al.*, *Observation of CP violation in the* B^0 *meson system*, Phys. Rev. Lett. **87** (2001) 091801, arXiv:hep-ex/0107013.

[51] Belle Collaboration, K. Abe *et al.*, *Observation of large CP violation in the neutral B meson system*, Phys. Rev. Lett. **87** (2001) 091802, arXiv:hep-ex/0107061.

[52] L.-L. Chau and W.-Y. Keung, *Comments on the Parametrization of the Kobayashi-Maskawa Matrix*, Phys. Rev. Lett. **53** (1984) 1802.

[53] L. Wolfenstein, *Parametrization of the Kobayashi-Maskawa Matrix*, Phys. Rev. Lett. **51** (1983) 1945.

[54] *The CKM matrix and the unitarity triangle. Workshop, CERN, Geneva, Switzerland, 13-16 Feb 2002: Proceedings*, 2003. doi: 10.5170/CERN-2003-002-corr.

[55] J. Charles *et al.*, *Current status of the Standard Model CKM fit and constraints on* $\Delta F = 2$ *New Physics*, Phys. Rev. **D91** (2015) 073007, arXiv:1501.05013, updated results and plots available at: http://ckmfitter.in2p3.fr.

[56] E. Noether, *Invariant Variation Problems*, Gott. Nachr. **1918** (1918) 235, arXiv:physics/0503066, [Transp. Theory Statist. Phys. **1** (1971) 186].

[57] M. Chaichian, A. D. Dolgov, V. A. Novikov, and A. Tureanu, *CPT Violation Does Not Lead to Violation of Lorentz Invariance and Vice Versa*, Phys. Lett. **B699** (2011) 177, arXiv:1103.0168.

[58] ARGUS Collaboration, H. Albrecht *et al.*, *Observation of B^0–$\overline{B}^0$ Mixing*, Phys. Lett. **B192** (1987) 245, .

[59] J. R. Ellis, M. K. Gaillard, D. V. Nanopoulos, and S. Rudaz, *The Phenomenology of the Next Left-Handed Quarks*, Nucl. Phys. **B131** (1977) 285, [Erratum: Nucl. Phys. **B132** (1978) 541].

[60] P. Koppenburg, *CP violation and CKM studies*, PoS **EPS-HEP2015** (2015) 028, arXiv:1510.01923.

[61] LHCb Collaboration, R. Aaij *et al.*, *Dalitz plot analysis of $B^0 \to \overline{D}^0\pi^+\pi^-$ decays*, Phys. Rev. **D92** (2015) 032002, arXiv:1505.01710.

[62] T. Latham and T. Gershon, *A Method to Measure* $\cos(2\beta)$ *Using Time-Dependent Dalitz Plot Analysis of $B^0 \to D_{CP}\pi^+\pi^-$*, J. Phys. **G36** (2009) 025006, arXiv:0809.0872.

[63] J. Charles *et al.*, *${B^0}_d(t) \to DPP$ time–dependent Dalitz plots, CP–violating angles 2β, $2\beta+\gamma$, and discrete ambiguities*, Phys. Lett. **B425** (1998) 375, arXiv:hep-ph/9801363, [Erratum: Phys. Lett.B433,441(1998)].

[64] A. Birnkraut, *b-flavour tagging in pp collisions*, PoS **EPS-HEP2015** (2015) 544.

[65] LHCb, R. Aaij *et al.*, *B flavour tagging using charm decays at the LHCb experiment*, JINST **10** (2015) P10005, arXiv:1507.07892.

[66] LHCb, R. Aaij *et al.*, *A new algorithm for identifying the flavour of B_s^0 mesons at LHCb*, JINST **11** (2016) P05010, arXiv:1602.07252.

[67] LHCb, R. Aaij *et al.*, *Opposite-side flavour tagging of B mesons at the LHCb experiment*, Eur. Phys. J. **C72** (2012) 2022, arXiv:1202.4979.

[68] M. Gronau, A. Nippe, and J. L. Rosner, *Method for flavor tagging in neutral B meson decays*, Phys. Rev. **D47** (1993) 1988, arXiv:hep-ph/9211311.

[69] L. R. Evans and P. Bryant, *LHC Machine*, J. Instrum. **3** (2008) S08001. 164 p, This report is an abridged version of the LHC Design Report (CERN-2004-003).

[70] LHCb Collaboration, A. A. Alves, Jr. *et al.*, *The LHCb Detector at the LHC*, JINST **3** (2008) S08005.

[71] LHCb Collaboration, R. Aaij *et al.*, *LHCb Detector Performance*, Int. J. Mod. Phys. **A30** (2015) 1530022, arXiv:1412.6352.

[72] J. Haffner, *The CERN accelerator complex. Complexe des accélérateurs du CERN*, OPEN-PHO-ACCEL-2013-056, General Photo.

[73] CERN, *The Large Hadron Collider: Conceptual design*, 1995.

[74] ATLAS Collaboration, G. Aad *et al.*, *The ATLAS Experiment at the CERN Large Hadron Collider*, JINST **3** (2008) S08003.

[75] CMS Collaboration, S. Chatrchyan *et al.*, *The CMS experiment at the CERN LHC*, JINST **3** (2008) S08004.

[76] ALICE Collaboration, K. Aamodt *et al.*, *The ALICE experiment at the CERN LHC*, JINST **3** (2008) S08002.

[77] B. Muratori and T. Pieloni, *Luminosity levelling techniques for the LHC*, in *Proceedings, ICFA Mini-Workshop on Beam-Beam Effects in Hadron Colliders (BB2013): CERN, Geneva, Switzerland, March 18-22 2013*, pp. 177–181, 2014. arXiv:1410.5646. doi: 10.5170/CERN-2014-004.177.

[78] F. Follin and D. Jacquet, *Implementation and experience with luminosity levelling with offset beam*, in *Proceedings, ICFA Mini-Workshop on Beam-Beam Effects in Hadron Colliders (BB2013): CERN, Geneva, Switzerland, March 18-22 2013*, pp. 183–187, 2014. arXiv:1410.3667. doi: 10.5170/CERN-2014-004.183.

[79] B. L. Combridge, *Associated Production of Heavy Flavor States in pp and $\overline{p}p$ Interactions: Some QCD Estimates*, Nucl. Phys. **B151** (1979) 429.

[80] E. Norrbin and T. Sjostrand, *Production and hadronization of heavy quarks*, Eur. Phys. J. **C17** (2000) 137, arXiv:hep-ph/0005110.

[81] LHCb Collaboration, R. Aaij *et al.*, *Measurement of B meson production cross-sections in proton-proton collisions at $\sqrt{s} = 7$ TeV*, JHEP **08** (2013) 117, arXiv:1306.3663.

[82] LHCb VELO Group, R. Aaij *et al.*, *Performance of the LHCb Vertex Locator*, JINST **9** (2014) 09007, arXiv:1405.7808.

[83] LHCb Silicon Tracker Group, J. Luisier, *Performance of LHCb Silicon Tracker Detector in the LHC*, Phys. Procedia **37** (2012) 851.

[84] LHCb Outer Tracker Group, R. Arink *et al.*, *Performance of the LHCb Outer Tracker*, JINST **9** (2014) P01002, arXiv:1311.3893.

[85] LHCb RICH Group, M. Adinolfi *et al.*, *Performance of the LHCb RICH detector at the LHC*, Eur. Phys. J. **C73** (2013) 2431, arXiv:1211.6759.

[86] LHCb Collaboration, P. Perret and X. Vilasís-Cardona, *Performance of the LHCb calorimeters during the period 2010-2012*, J. Phys. Conf. Ser. **587** (2015) 012012.

[87] A. A. Alves, Jr. *et al.*, *Performance of the LHCb muon system*, JINST **8** (2013) P02022, arXiv:1211.1346.

[88] R. Aaij *et al.*, *The LHCb Trigger and its Performance in 2011*, JINST **8** (2013) P04022, arXiv:1211.3055.

[89] LHCb HLT project, J. Albrecht, V. V. Gligorov, G. Raven, and S. Tolk, *Performance of the LHCb High Level Trigger in 2012*, J. Phys. Conf. Ser. **513** (2014) 012001, arXiv:1310.8544.

[90] A. Puig, *The LHCb trigger in 2011 and 2012*, tech. rep., CERN, Geneva, Nov, 2014.

[91] LHCb Speakers' Bureau, *Material for Presentations*, https://twiki.cern.ch/twiki/bin/view/LHCb/LHCbTriggerConferenceDiagramsPlots. (Accessed on 21/06/2016).

[92] LHCb Collaboration, R. Aaij *et al.*, *Absolute luminosity measurements with the LHCb detector at the LHC*, JINST **7** (2012) P01010, arXiv:1110.2866.

[93] A. Martin Sanchez, P. Robbe, and M.-H. Schune, *Performances of the LHCb L0 Calorimeter Trigger*, tech. rep., CERN, Geneva, Jun, 2012.

[94] G. Corti *et al.*, *Software for the LHCb experiment*, IEEE Trans. Nucl. Sci. **53** (2006) 1323.

[95] M. Williams *et al.*, *The HLT2 Topological Lines*, tech. rep., CERN, Geneva, Jan, 2011.

[96] V. V. Gligorov and M. Williams, *Efficient, reliable and fast high-level triggering using a bonsai boosted decision tree*, JINST **8** (2013) P02013, arXiv:1210.6861.

[97] G. Barrand *et al.*, *GAUDI - A software architecture and framework for building HEP data processing applications*, Comput. Phys. Commun. **140** (2001) 45.

[98] LHCb Collaboration, R. Antunes-Nobrega *et al.*, *LHCb computing: Technical Design Report*, Technical Design Report LHCb, CERN, Geneva, 2005. Submitted on 11 May 2005.

[99] R. Brun and F. Rademakers, *ROOT: An object oriented data analysis framework*, Nucl. Instrum. Meth. **A389** (1997) 81.

[100] I. Antcheva *et al.*, *ROOT: A* C++ *framework for petabyte data storage, statistical analysis and visualization*, Comput. Phys. Commun. **182** (2011) 1384.

[101] LHCb Collaboration, M. Clemencic *et al.*, *The LHCb simulation application, Gauss: Design, evolution and experience*, J. Phys. Conf. Ser. **331** (2011) 032023.

[102] T. Sjöstrand, S. Mrenna, and P. Skands, *PYTHIA 6.4 physics and manual*, JHEP **05** (2006) 026, arXiv:hep-ph/0603175; T. Sjöstrand, S. Mrenna, and P. Skands, *A brief introduction to PYTHIA 8.1*, Comput. Phys. Commun. **178** (2008) 852, arXiv:0710.3820.

[103] D. J. Lange, *The EvtGen particle decay simulation package*, Nucl. Instrum. Meth. **A462** (2001) 152.

[104] J. Allison *et al.*, *Geant4 developments and applications*, IEEE Trans. Nucl. Sci. **53** (2006) 270; GEANT4 Collaboration, S. Agostinelli *et al.*, *GEANT4: A Simulation toolkit*, Nucl. Instrum. Meth. **A506** (2003) 250.

[105] Belle Collaboration, A. Kuzmin *et al.*, *Study of* $\overline{B}^0 \to D^0\pi^+\pi^-$ *decays*, Phys. Rev. **D76** (2007) 012006, arXiv:hep-ex/0611054.

[106] M. Pivk and F. R. Le Diberder, *SPlot: A Statistical tool to unfold data distributions*, Nucl. Instrum. Meth. **A555** (2005) 356, arXiv:physics/0402083.

[107] LHCb Collaboration, W. Baldini *et al.*, *Overview of LHCb alignment*, .

[108] M. Needham, *Momentum scale calibration using resonances*, tech. rep., CERN, Geneva, Jul, 2008.

[109] LHCb Collaboration, R. Aaij *et al.*, *Measurement of b–hadron masses*, Phys. Lett. **B708** (2012) 241, arXiv:1112.4896.

[110] V. V. Gligorov, *Reconstruction of the Channel* $B^0_d \to D^+\pi^-$ *and Background Classification at LHCb (revised)*, tech. rep., CERN, Geneva, Jun, 2007. revised version submitted on 2008-01-24 12:46:44; V. V. Gligorov, *TupleToolMCBackgroundInfo*, https://twiki.cern.ch/twiki/bin/view/LHCb/TupleToolMCBackgroundInfo. (Accessed on 04/11/2016).

[111] W. D. Hulsbergen, *Decay Chain Fitting with a Kalman Filter*, Nucl. Instrum. Methods Phys. Res. , A **552** (2005) 566.

[112] A. Hoecker *et al.*, *TMVA: Toolkit for Multivariate Data Analysis*, PoS **ACAT** (2007) 040, arXiv:physics/0703039; A. Hoecker *et al.*, *TMVA website*, http://tmva.sourceforge.net/. (Accessed on 21/06/2016).

[113] P. Speckmayer, A. Hocker, J. Stelzer, and H. Voss, *The toolkit for multivariate data analysis, TMVA 4*, J. Phys. Conf. Ser. **219** (2010) 032057.

[114] R. A. Fisher, *The use of multiple measurements in taxonomic problems*, Annals Eugen. **7** (1936) 179.

[115] T. W. Anderson, *R. A. Fisher and Multivariate Analysis*, Stat. Sci. **11** (1996) 20.

[116] L. Breiman, J. Friedman, R. A. Olshen, and C. J. Stone, *Classification and regression trees*, Chapman and Hall/CRC, 1984.

[117] Y. Freund and R. E. Schapire, *A decision-theoretic generalization of on-line learning and an application to boosting*, Journal of Computer and System Sciences **55** (1997) 119 .

[118] W. Verkerke and D. P. Kirkby, *The RooFit toolkit for data modeling*, eConf **C0303241** (2003) MOLT007, arXiv:physics/0306116, .

[119] LHCb Collaboration, R. Aaij *et al.*, *Measurement of the branching fractions of the decays* $B_s^0 \to \overline{D}^0 K^- \pi^+$ *and* $B^0 \to \overline{D}^0 K^+ \pi^-$, Phys. Rev. **D87** (2013) 112009, arXiv:1304.6317.

[120] LHCb Collaboration, B. Storaci, *Updated average* f_s/f_d *b–hadron production fraction ratio for* 7 *TeV* pp *collisions*, 2013.

[121] LHCb Collaboration, R. Aaij *et al.*, *Measurement of b–hadron production fractions in* 7 *TeV* pp *collisions*, Phys. Rev. **D85** (2012) 032008, arXiv:1111.2357.

[122] LHCb Collaboration, R. Aaij *et al.*, *Study of the kinematic dependences of* Λ_b^0 *production in* pp *collisions and a measurement of the* $\Lambda_b^0 \to \Lambda_c^+ \pi^-$ *branching fraction*, JHEP **08** (2014) 143, arXiv:1405.6842.

[123] LHCb Collaboration, R. Aaij *et al.*, *Studies of beauty baryon decays to* $D^0 p h^-$ *and* $\Lambda_c^+ h^-$ *final states*, Phys. Rev. **D89** (2014) 032001, arXiv:1311.4823.

[124] R. J. Barlow, *Extended maximum likelihood*, Nucl. Instrum. Meth. **A297** (1990) 496.

[125] LHCb Collaboration, R. Aaij *et al.*, *Measurement of the track reconstruction efficiency at LHCb*, JINST **10** (2015) P02007, arXiv:1408.1251.

[126] Tracking, Alignment and Vertexing Physics Performance Working Group, *Tracking Efficiencies*, https://twiki.cern.ch/twiki/bin/view/LHCb/LHCbTrackingEfficiencies. (Accessed on 18/11/2016).

[127] L. Anderlini *et al.*, *The PIDCalib package*, tech. rep., CERN, Geneva, Jul, 2016.

[128] LHCb, R. Aaij *et al.*, *Study of the production of Λ_b^0 and $\overline{B}^0$ hadrons in pp collisions and first measurement of the $\Lambda_b^0 \to J/\psi p K^-$ branching fraction*, Chin. Phys. **C40** (2016) 011001, arXiv:1509.00292.

[129] Calorimeter Objects Tools Group, *L0 Hadron trigger efficiencies*, https://twiki.cern.ch/twiki/bin/view/LHCbPhysics/CalorimeterObjectsToolsGroupDOC#L0_Hadron_trigger_efficiencies. (Accessed on 18/11/2016).

[130] S. Tolk, J. Albrecht, F. Dettori, and A. Pellegrino, *Data driven trigger efficiency determination at LHCb*, tech. rep., CERN, Geneva, May, 2014.

[131] A. Poluektov, *Kernel density estimation of a multidimensional efficiency profile*, JINST **10** (2015) P02011, arXiv:1411.5528.

[132] L. Moneta *et al.*, *The RooStats Project*, PoS **ACAT2010** (2010) 057, arXiv:1009.1003.

[133] *BABAR* Collaboration, P. del Amo Sanchez *et al.*, *Dalitz–plot Analysis of $B^0 \to \overline{D}^0 \pi^+ \pi^-$*, PoS **ICHEP2010** (2010) 250, arXiv:1007.4464.

[134] LHCb Collaboration, R. Aaij *et al.*, *Evidence for the two-body charmless baryonic decay $B^+ \to p\overline{\Lambda}$*, arXiv:1611.07805; J. Beddow *et al.*, *Search for the Rare Two-body Charmless Baryonic decay $B^+ \to p\overline{\Lambda}$*, LHCb-ANA-2014-094.

[135] G. Dujany, G. Lafferty, and E. Rodrigues, *Analysis of the decays $B_{(s)} \to p\overline{p}hh^{(\prime)}$*, LHCb-ANA-2015-054.

[136] Particle Identification and CALO Obejcts Physics Performance Working Group, *PIDCalib*, https://twiki.cern.ch/twiki/bin/view/LHCb/PIDCalibPackage. (Accessed on 30/11/2016).

[137] R. H. Dalitz, *On the analysis of tau-meson data and the nature of the tau-meson*, Phil. Mag. Ser. 7 **44** (1953) 1068.

[138] R. H. Dalitz, *Decay of tau mesons of known charge*, Phys. Rev. **94** (1954) 1046.

[139] G. N. Fleming, *Recoupling Effects in the Isobar Model. 1. General Formalism for Three-Pion Scattering*, Phys. Rev. **135** (1964) B551.

[140] D. Herndon, P. Soding, and R. J. Cashmore, *A GENERALIZED ISOBAR MODEL FORMALISM*, Phys. Rev. **D11** (1975) 3165.

[141] J. M. Blatt and V. F. Weisskopf, *Theoretical nuclear physics*, Springer, New York, 1952. doi: 10.1007/978-1-4612-9959-2.

[142] W. Rarita and J. Schwinger, *On a theory of particles with half integral spin*, Phys. Rev. **60** (1941) 61.

[143] M. Jacob and G. C. Wick, *On the general theory of collisions for particles with spin*, Annals Phys. **7** (1959) 404, [Annals Phys.281,774(2000)].

[144] J. D. Richman, *An Experimenter's Guide to the Helicity Formalism*, .

[145] H. Chen and R.-G. Ping, *Coherent helicity amplitude for sequential decays*, Phys. Rev. **D95** (2017) 076010, arXiv:1704.05184.

[146] S. M.B̃erman and M. Jacob, *Systematics of angular and polarization distributions in three-body decays*, .

[147] CLEO Collaboration, S. Anderson *et al.*, *First observation of the decays $B^0 \to D^{*-} p\overline{p}\pi^+$ and $B^0 \to D^{*-} p\overline{n}$*, Phys. Rev. Lett. **86** (2001) 2732, arXiv:hep-ex/0009011.

[148] Belle Collaboration, K. Abe *et al.*, *Observation of $B^\pm \to p\overline{p}K^\pm$*, Phys. Rev. Lett. **88** (2002) 181803, arXiv:hep-ex/0202017.

[149] Belle Collaboration, J. T. Wei *et al.*, *Study of $B^+ \to p\overline{p}K^+$ and $B^+ \to p\overline{p}\pi^+$*, Phys. Lett. **B659** (2008) 80, arXiv:0706.4167.

[150] Belle Collaboration, M. Z. Wang *et al.*, *Observation of $B^0 \to p\overline{\Lambda}\pi^-$*, Phys. Rev. Lett. **90** (2003) 201802, arXiv:hep-ex/0302024.

[151] BES Collaboration, J. Z. Bai *et al.*, *Observation of a near threshold enhancement in the $p\overline{p}$ mass spectrum from radiative $J/\psi \to \gamma p\overline{p}$ decays*, Phys. Rev. Lett. **91** (2003) 022001, arXiv:hep-ex/0303006.

[152] M. Jarfi *et al.*, *Decays of b mesons into baryon - anti-baryon*, Phys. Rev. **D43** (1991) 1599.

[153] C. B. Dover and M. Goldhaber, *Possibility of $\overline{N}N$, $\overline{\Lambda}\Lambda$, $\overline{\Sigma}\Sigma$, and $\overline{\Xi}\Xi$ Quasinuclear States*, Phys. Rev. **D15** (1977) 1997.

[154] I. S. Shapiro, *The Physics of Nucleon-Antinucleon Systems*, Phys. Rept. **35** (1978) 129.

[155] Y. K. Hsiao and C. Q. Geng, *Identifying Glueball at* 3.02 GeV *in Baryonic B Decays*, Phys. Lett. **B727** (2013) 168, arXiv:1302.3331.

[156] Belle Collaboration, K. Abe *et al.*, *Experimental constraints on the Spin and Parity of the* $\Lambda_c^+(2880)$, Phys. Rev. Lett. **98** (2007) 262001, arXiv:hep-ex/0608043.

[157] LHCb, R. Aaij *et al.*, *Study of the* D^0p *amplitude in* $\Lambda_b^0 \to D^0 p\pi^-$ *decays*, JHEP **05** (2017) 030, arXiv:1701.07873.

[158] T. Yoshida *et al.*, *Spectrum of heavy baryons in the quark model*, Phys. Rev. **D92** (2015) 114029, arXiv:1510.01067.

[159] S. Migura, D. Merten, B. Metsch, and H.-R. Petry, *Charmed baryons in a relativistic quark model*, Eur. Phys. J. **A28** (2006) 41, arXiv:hep-ph/0602153.

[160] D. Ebert, R. N. Faustov, and V. O. Galkin, *Spectroscopy and Regge trajectories of heavy baryons in the relativistic quark-diquark picture*, Phys. Rev. **D84** (2011) 014025, arXiv:1105.0583.

[161] X.-G. He, X.-Q. Li, X. Liu, and X.-Q. Zeng, $\Lambda_c^+(2940)$*: A Possible molecular state?*, Eur. Phys. J. **C51** (2007) 883, arXiv:hep-ph/0606015.

[162] BaBar Collaboration, B. Aubert *et al.*, *Observation of a charmed baryon decaying to* D^0p *at a mass near* 2.94 GeV/c^2, Phys. Rev. Lett. **98** (2007) 012001, arXiv:hep-ex/0603052.

[163] Y. K. Hsiao and C. Q. Geng, *Factorization and angular distribution asymmetries in charmful baryonic B decays*, Phys. Rev. **D93** (2016) 034036, arXiv:1601.03804.

[164] A. Hicheur, *Review of recent LHCb results and prospects for Run II*, in *International School on High Energy Physics: Session C: Workshop in HEP (LISHEP 2015) Manaus, Amazonas, Brazil, August 2-9, 2015*, 2015. arXiv:1509.07708.

[165] M. Suzuki, *Partial waves of baryon-antibaryon in three-body B meson decay*, J. Phys. **G34** (2007) 283, arXiv:hep-ph/0609133.

[166] LHCb collaboration, *LHCb*, https://gitlab.cern.ch/lhcb, 2017.

[167] M. Needham, *Performance of the LHCb track reconstruction software*, CERN-LHCB-2007-144, LPHE-2008-01.

[168] C. Li and B. Wang, *Fisher Linear Discriminant Analysis*, 2014.

[169] Y. Freud and R. E. Schapire, *A short introduction to boosting*, Journal of Japanese Society for Artificial Intelligence **14** (1999) 771, In Japanese, translation by Naoki Abe.

[170] R. E. Schapire, *The boosting approach to machine learning: An overview*, MSRI Workshop on Nonlinear Estimation and Classification (2002).

[171] J. H. Friedman, *Recent advances in predictive (machine) learning*, J. Classif. **23** (2006) 175.

[172] J. D. Gibbons and S. Chakraborti, *Nonparametric Statistical Inference*, Dekker, 4 ed., 2003.

[173] M. J. Oreglia, *A Study of the Reactions $\psi' \to \gamma\gamma\psi$*, PhD thesis, SLAC, 1980.

[174] J. E. Gaiser, *Charmonium Spectroscopy From Radiative Decays of the J/ψ and ψ'*, PhD thesis, SLAC, 1982.

[175] T. Skwarnicki, *A study of the radiative CASCADE transitions between the Upsilon-Prime and Upsilon resonances*, PhD thesis, Cracow, INP, 1986.

[176] K. S. Cranmer, *Kernel estimation in high-energy physics*, Comput. Phys. Commun. **136** (2001) 198, `arXiv:hep-ex/0011057`.

List of Figures

List of Tables